University of Cambridge
Department of Chemical Engineering

The Effects of Natural Convection on Low Temperature Combustion

by

Alasdair Neil Campbell
Pembroke College

A dissertation submitted for the degree of Doctor of Philosophy
at the University of Cambridge

December 2006

Preface

The work in this dissertation was undertaken in the Department of Chemical Engineering at the University of Cambridge, between October 2003 and December 2006. It is the original work of the author, except where specifically acknowledged in the text, and includes nothing that is the outcome of work done in collaboration. No part of the dissertation has been submitted for a degree to any other University.

This dissertation is approximately 60,000 words in length, including references, tables, equations and appendices, and contains precisely 65 figures and 7 tables.

Alasdair Neil Campbell
Pembroke College
December 2006

Publications Arising from this Work

Much of the material presented in this dissertation has been published previously. Specifically, the work in Chapter 3 appears in:

Campbell A.N., Cardoso S.S.S., Hayhurst A.N., 2005. A scaling analysis of Sal'nikov's reaction, P → A → B, in the presence of natural convection and the diffusion of heat and matter. *Proceedings of the Royal Society A*, **461**, 1999 – 2020,

and

Campbell A.N., Cardoso S.S.S., Hayhurst A.N., 2006. A scaling analysis of the effects of natural convection, when Sal'nikov's reaction: P → A → B occurs, together with diffusion and heat transfer in a batch reactor. *Chemical Engineering Research and Design*, **84**(A7), 553 – 561.

The material in Chapter 4 appears in:

Campbell A.N., Cardoso S.S.S., Hayhurst A.N., 2006. The behaviour of Sal'nikov's reaction, P → A → B, in a spherical batch reactor with the diffusion of heat and matter. *Physical Chemistry Chemical Physics*, **8**, 2866 – 2878.

Chapter 6 contains material previously published in:

Campbell A.N., Cardoso S.S.S., Hayhurst A.N., 2005. The influence of natural convection on the temporal development of the temperature and concentration fields for Sal'nikov's reaction, P → A → B, occurring batchwise in the gas phase in a closed vessel. *Chemical Engineering Science*, **60**, 5705 – 5717.

In addition to these published papers, the work presented in Chapter 2 has been submitted for publication in Chemical Engineering Science:

Campbell A.N., Cardoso S.S.S., Hayhurst A.N., 2006. A comparison of measured temperatures with those calculated numerically and analytically for an exothermic chemical reaction inside a spherical reactor with natural convection. *Chemical Engineering Science*, submitted November 2006.

Acknowledgements

I would like to thank my supervisor, Dr. Silvana Cardoso for her advice and guidance in my research over the past three years. I would also like to thank Prof. Allan Hayhurst for many very helpful discussions over the past three years. In addition, I would like to thank the computing officers in the Department of Chemical Engineering, Dr. Jim Thompson, Vanessa Blake and Barrie Goddard, for their help with technical issues.

I would like to thank Dr. Brian Tyler for pointing us in the direction of some very useful experimental work, which was used to validate the numerical and theoretical methods used in this work.

Finally, financial support from the Engineering and Physical Sciences Research Council and Society of Chemical Industry, is gratefully acknowledged.

Alasdair Neil Campbell

Summary

The effects of natural convection on low temperature combustion

by

Alasdair Neil Campbell

When a gas undergoes an exothermic reaction in a closed vessel, spatial temperature gradients can develop. If these gradients become sufficiently large, the resulting buoyancy forces will move the gas, *i.e.* there is natural convection. The nature of the resulting flow is determined by the Rayleigh number, $Ra = (\beta\, g\, \Delta T\, L^3) / (\kappa\ \nu)$. The evolution of such a system will depend on the interactions of natural convection, diffusion of both heat and chemical species, and chemical reaction. This study is concerned with a gas-phase system undergoing Sal'nikov's reaction: P → A → B, in the presence of natural convection. This kinetic scheme is used as a simplified representation of a cool flame, which is a feature of the low temperature combustion of a hydrocarbon vapour. Sal'nikov's reaction is one of the simplest to display thermokinetic oscillations, such as those seen in cool flames.

The behaviour of Sal'nikov's reaction in the presence of natural convection was investigated using a combination of analytical and numerical techniques. First, a numerical model was developed to compute the temperature, velocity and concentrations when a simple exothermic reaction occurs in a spherical batch reactor, the results of which could be compared with previous experimental measurements. Subsequently, a scaling analysis of Sal'nikov's reaction proceeding in a spherical reactor was performed. This yielded significant insight into the general behaviour of this and similar systems. The forms of the analytical scales were confirmed through comparison with the results from numerical simulations. These scales were used to predict how the system responds to changes in certain key process variables, such as the pressure and the size of the reactor.

It was shown that the behaviour of this system is governed by the ratios of the characteristic timescales for diffusion, reaction and natural convection. These ratios were used to define a regime diagram describing the system. The behaviour in different parts of this regime diagram was characterised and regions in which oscillations occur were identified.

Table of Contents

List of Figures

List of Tables

Nomenclature

Roman

a	concentration of the intermediate A
a'	dimensionless concentration of the intermediate A, $a' = a / a_0$
a_0	characteristic concentration of the intermediate A
c	concentration of azomethane
c'	dimensionless concentration of azomethane, $c' = c / c_0$
c_0	initial concentration of azomethane
C_P	specific heat at constant pressure
C_V	specific heat at constant volume
D_A	diffusion coefficient of the intermediate A
D_C	diffusion coefficient of azomethane
D_P	diffusion coefficient of the precursor P
E	activation energy
E_i	activation energy of step i of Sal'nikov's reaction
g	acceleration due to gravity
Gr	Grashof number, $Gr = Ra / Pr$
h	heat transfer coefficient
k	rate constant
k_0	rate constant evaluated at $T = T_0$
k_i	rate constant of step i of Sal'nikov's reaction
$k_{2,0}$	rate constant of step 2 evaluated at $T = T_0$
k_T	thermal conductivity
L	characteristic length (radius) of the reactor
l_0	width of the box considered by Gray and Scott (1990*b*)
Le	Lewis number, $Le = \kappa / D_i$
m	constant of order unity
n	order of the chemical reaction
Nu	Nusselt number, $Nu = h\,L / k_T$
p	concentration of precursor P
p'	dimensionless concentration of P, $p' = p / p_0$
p_0	initial concentration of P
$\mathscr{P}$	pressure

$\mathscr{P}_0$	initial pressure
$\mathscr{P}'$	dimensionless pressure, $\mathscr{P}' = \mathscr{P} - \mathscr{P}_0 / \rho_0\, U^2$
$\mathscr{P}_i$	partial pressure of component i
Pr	Prandtl number, $Pr = \nu / \kappa$
q	exothermicity of the reaction
q_i	exothermicity of step i of Sal'nikov's reaction
r	radial coordinate
r'	dimensionless radial coordinate
R	universal gas constant
Ra	Rayleigh number, $Ra = \beta\, g\, L^3\, \Delta T / \kappa\, \nu$
t	time
t'	dimensionless time, $t' = U\, t / L$
$\underline{u}$	velocity
$\underline{u}'$	dimensionless velocity, $\underline{u}' = \underline{u} / U$
U	characteristic velocity
T	temperature
T'	dimensionless rise in temperature, $T' = (T - T_0) / \Delta T$
T_0	constant wall temperature
$\underline{x}$	spatial coordinates
$\underline{x}'$	dimensionless spatial coordinates, $\underline{x}' = \underline{x} / L$
y	coordinate measuring the vertical distance from the bottom of the reactor
Z	pre-exponential factor in the Arrhenius term
Z_2	pre-exponential factor in Arrhenius expression for k_2

Greek

β	coefficient of thermal expansion
$\beta_{G\,\&\,S}$	Gray and Scott dimensionless parameter
γ	ratio of principal specific heats
$\gamma_{G\,\&\,S}$	Gray and Scott dimensionless parameter
δ	Frank-Kamenetskii parameter, $\delta = qEL^2 k_0 c_0^n \big/ \rho_0 C_P \kappa R T_0^2$
δ_{cr}	critical Frank-Kamenetskii parameter for explosion
ΔT	characteristic temperature increase

ΔT_{ad}	adiabatic temperature rise, $\Delta T_{ad} = q / C_V$
ε	small parameter in perturbation analysis
ε_1	convergence criterion in numerical scheme
ε_2	convergence criterion in numerical scheme
η	dimensionless parameter, $\eta = \Delta T / T_0$
ϕ	dimensionless activation energy, $\phi = E\,\Delta T / R\,T_0^2$
ϕ_{ad}	adiabatic dimensionless activation energy, $\phi = E\,q_2 / C_P\,R\,T_0^2$
κ	thermal diffusivity
$\kappa_{G\,\&\,S}$	Gray and Scott dimensionless parameter
μ	viscosity
$\mu_{G\,\&\,S}$	Gray and Scott dimensionless parameter
ν	kinematic viscosity
ρ	density
ρ_0	density at $T = T_0$
$\tau_{convection}$	timescale for convection
$\tau_{diffusion}$	timescale for diffusion of heat
τ_i	induction period for natural convection
$\tau_{reaction}$	timescale for the reaction
$\tau_{step\ i}$	timescale for step *i* of Sal’nikov’s reaction
ω	stretching coordinate, $\omega = t' / \varepsilon$
ω_0	angular frequency

Superscripts

c	composite solution
i	inner solution
o	outer solution

Abbreviations

CFD	computational fluid dynamics
CSTR	continuous stirred tank reactor

1 Introduction and Literature Survey

1.1 Cool Flames

When a hydrocarbon vapour reacts with oxygen at low pressures inside a closed vessel, different types of behaviour can be observed. The reaction can proceed very slowly, with the fuel being gently oxidised without any significant emission of heat or visible light. In contrast to this, the system can also proceed rapidly to explosion, where the reaction is very violent and liberates a great deal of heat. Between these two extreme behaviours there lies a region in which cool flames occur. Cool flames arise due to the complex interaction of chemical and thermal feedback, and also heat loss to the surroundings. Cool flames were first observed by Sir Humphry Davy in the early 19th Century (Davy, 1817). Davy observed that when the slow combustion of ether was performed in a dark laboratory, a pale phosphorescent light could be seen. This feeble luminescence is characteristic of cool flames. Perkin (1882) found that these weak flames were visible when many different fuels were used, and he observed that the blue flames produced by different substances had similar properties. The emission spectra obtained for cool flames produced by different fuels is similar, and is quite different from that seen during ‘hot’ combustion (Emeléus, 1926, 1929). The spectrum consists of a series of bands shaded toward the red, the intensity of which is greatest in the blue and near-ultraviolet regions (Pekalski *et al.*, 2002). The blue luminescence was found to be emission from electronically excited formaldehyde (CH_2O^*) (Sheinson and Williams, 1973; Ubbelohde, 1935); the weakness of the emission is because only about one in every 10^6 formaldehyde molecules emits radiation (Griffiths and Sykes, 1989; Knox, 1967).

As the name suggests, cool flames occur at lower temperatures than hot ignitions. Generally these flames occur at temperatures of 500 – 800 K and slightly sub-atmospheric pressures. In addition to the weak blue flames, cool flames are associated with small increases in temperature, with associated increases in pressure. The temperature increases can be as small as 2 K and as large as 200 K (Griffiths and Scott, 1987). After the short-lived increase in temperature, the system settles back to near its starting temperature. Cool flames were initially thought to be single events, until the pioneering work of Newitt and Thornes (1937), who studied propane oxidation in a closed vessel. They observed that cool flames were, in fact, periodic and observed up to five cool flames occurring in series. When multiple cool flames are observed, the temperature increases, before settling back to near its starting value. After a short while, there would be another, similar spike in the temperature. Each of these temperature spikes is associated with the appearance of a weak blue flame. The time between these individual cool flames is approximately constant, which led to the phenomenon being dubbed the ‘lighthouse effect’. The ignition diagram produced by Newitt and Thornes (1937) is shown in Figure 1.1, and is typical for a hydrocarbon reacting with oxygen. A clearly defined region where cool flames occur is shown at the transition between slow combustion and ignition. The observed periodicity is an important aspect of cool flames, and indeed, up to 11 successive flames have been reported in the low temperature oxidation of propane. The number of flames seen depends on a number of factors, most notably the depletion of reactants (Griffiths and Scott, 1987), and so is not particularly significant, but instead merely highlights the limitations of studies using closed vessels.

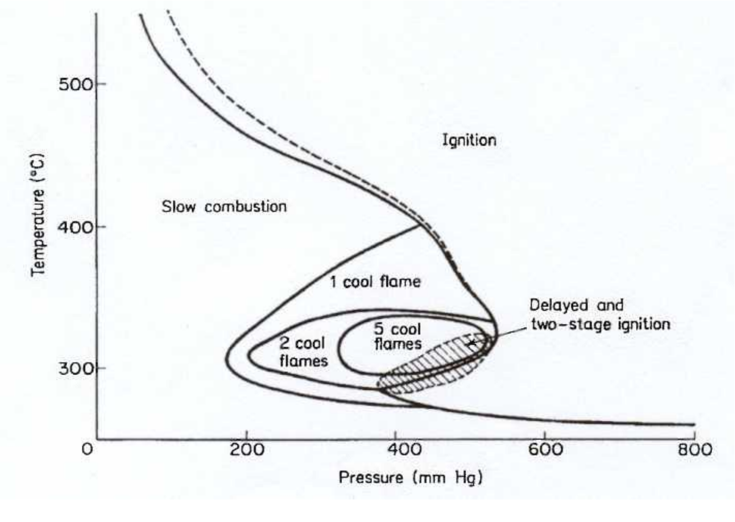

Figure 1.1. Ignition diagram for a mixture of propane and oxygen (equimolar mixtures) (Newitt and Thornes, 1937).

Another interesting feature of slow combustion is the existence of a negative temperature coefficient (ntc) in the rate of reaction. This is a very unusual phenomenon, and is closely associated with cool flames. Over a temperature range of ~ 50 K the overall rate of reaction actually decreases when the temperature is increased. It is widely believed that the negative temperature coefficient arises by switching from a low temperature mechanism producing mainly oxygenated products, to a high temperature mechanism producing cracking products (Knox, 1967). Given the close association between the ntc and cool flames, this explanation of a switch between mechanisms seems attractive, in that a similar switching between mechanisms could account for the periodicity of cool flames.

In addition, another important behaviour is highlighted in Figure 1.1. Delayed and two-stage ignition occur when a system is below the explosion limit initially; however, the changes in temperature, pressure and composition due to cool flames cause the system to move across the boundary between slow and fast reaction and accordingly ignite. This mechanism is important in automotive engines, both for compression ignition engines where the fuel autoignites by design and in spark ignition engines where autoignition is undesired and results in ‘knock’, which can impair the efficiency, and ultimately damage the engine. Indeed, the majority of early studies of cool flames were motivated by a desire to understand the origins of knock in automotive engines, and to help in its mitigation (Griffiths, 1985*a*). It was observed that the knocking tendency of a fuel was related to its ability to produce cool flames (Lignola and Reverchon, 1987).

Interest in cool flames has also developed more recently in a number of different fields. Perhaps the most obvious of these is in process safety, because cool flames are found at the transition from slow to fast reactions (Figure 1.1), and hence explosion. It is widely known that gas and vapour explosions are a significant risk in the process industries, and can cause significant damage. For an example of this, one only has to look back to the explosion at the Buncefield fuel depot in Hertfordshire in December 2005. This event underlined the destructive effect of vapour explosions. For this reason, a great deal of money and effort is invested in the prevention and understanding of explosions. Autoignition poses a significant risk of causing an explosion, and Richardson *et al.* (1990) even explore this as a possible cause of the explosion on the Piper Alpha platform in the North Sea in 1988. Autoignition usually arises when a fuel/air mixture is heated above its autoignition temperature (AIT);

however, it can also occur *via* a cool flame mechanism. It is widely believed that a fuel-rich, flammable mixture kept below its AIT cannot ignite and therefore cannot explode (Pekalski *et al.*, 2002). This is, however, not the case, since delayed or two-stage ignitions can occur at temperatures well below the AIT. As Buda *et al.* (2006) and Pekalski *et al.* (2002) both point out, cool flames can occur at temperatures several hundred degrees below the AIT. These flames themselves might not present a great threat due to their gentle nature, but they can lead to the accumulation of intermediates and by-products. These would at best impair efficiency and contaminate final products, but they could also lead to additional safety problems. For example, peroxides could build up within the system, and these could potentially decompose explosively. Peroxides are more likely to accumulate in dead spaces or cold spots within equipment; therefore any inhomogeneity in the flow field or temperature field within equipment could be problematic. Hot spots will also occur in real systems under the influence of natural convection. These hot zones can promote oxidation reactions and therefore could lead to explosions. Pekalski *et al.* (2002) speculate that a review of 'unexplained' industrial loses would uncover many instances where incidents occurred due to the transition from cool flames to hot ignition. They cite an example of an explosion caused by a cool flame in a distillation column. This event resulted in human injury, damage to plant and also significant interruption in production. Figure 1.1 shows that cool flames, and therefore delayed and two-stage ignitions, occur at pressures below atmospheric; however, Griffiths (1985*a*) states that when air is used instead of oxygen, significantly higher pressures are required to induce cool flames. This means the problem of autoignition *via* cool flames is not limited to low pressure systems.

As well as research into the problems caused by cool flames, significant attention has recently focussed on using cool flame reactors in industrial processes. Such processes exploit the unique chemistry of cool flames. Naidja *et al.* (2003) examined the use of a cool flame reactor for producing fuel for fuel cells. The fuel is partially oxidised in the reactor and then some of the products passed to a reformer, where hydrogen is produced. The use of a stabilised cool flame reactor as part of the process for diesel or gasoline reforming has also been studied (Hartman *et al.*, 2003; Matos da Silva *et al.*, 2004). Such a reactor exploits the negative temperature coefficient as a barrier to autoignition to stabilise a cool flame in an open system. The reactor is used to vaporise the liquid fuel, and also partially oxidise it. The use of cool flames as vaporisers is also discussed by Griffiths (2004) in the context of oil-fired boilers. A cool flame system is used to vaporise the oil before it is introduced into the burner, which can therefore operate like a gas-fired, rather than an oil-fired unit, thus increasing efficiency. In addition, the more homogeneous fuel mix leads to a reduction in emissions; the unit described produces half the nitrogen oxide emissions of a conventional oil-fired system. The vaporisation of the fuel also allows a greater variety of fuels to be used, such as recycled cooking oil and biofuels.

1.2 Cool Flames with Natural Convection

When an exothermic reaction occurs in any fluid within a closed vessel, spatial temperature gradients are induced. If these gradients become sufficiently large, the resulting buoyancy forces will cause the gas to move. This natural convection can have a significant influence on the progress of the reaction. The nature of the induced flow is determined by the Rayleigh number, $Ra = (\beta\ g\ L^3\ \Delta T)\ /\ (\kappa\ \nu)$. Natural convection becomes significant when Ra increases above a threshold value of $\approx 10^3$ (Turner, 1979). The temperature rises associated with cool flames, described above, mean that in most cases, Ra will be sufficiently large for natural convection to play a role. Most experimental measurements on cool flames have, however, been made in unstirred vessels, so the effects of buoyancy have not been accounted for (Griffiths, 1995). Indeed, in many of these studies the experiments were carried out without *e.g.* a thermocouple measuring the temperature in the reaction vessel. Even when a temperature was measured, this often consisted of a single thermocouple at the centre of the vessel. Given the asymmetric distribution of the temperature and reactant within the vessel, conclusions based on these observations can be misleading (Griffiths and Scott, 1987). This asymmetry in the temperature distribution can be seen by interferometry.

Figure 1.2 shows a series of interferograms for cool flames occurring in a horizontal cylinder for an equimolar mixture of propane and oxygen (Melvin, 1969). These images show changes in the refractive index in the vessel, and therefore, to a first approximation, changes in the temperature distribution. It is clear from these images that the development of cool flames in such a system is very complex. There is clearly a hot zone above the centre of the reactor. Near the bottom of the reactor there appears to be very little change in the temperature and a degree of stratification in the temperature field is evident. This is a classic feature of a system in which natural convection is significant. As the reaction proceeds, the temperature in the hot zone of the reactor increases, as also do the temperature gradients. Eventually, a point is reached where a flame front develops near the centre of the reactor. This is evident in frame 5 in Figure 1.2. This flame front is horizontal and flat, and propagates downwards at ~ 3 cm s^{-1}. Evidence of this progress can be seen in frames 6 and 7 in Figure 1.2. The complexity of the temperature profile shown in Figure 1.2 underlines the fact that conventional methods of following the progress of the reaction, by monitoring the pressure or by chemical analysis of the contents of the reactor, would be misleading, because the reaction is largely localised to the hot zone at the top of the reactor. Melvin (1969) even speculated that the existence of multiple cool flames is, in fact, due to the influence of natural convection, rather than the complex chemistry. It would be useful to be able to visualise the flow field induced by convection, as well as the temperature field. Melvin, however, also points out that visualisation and measurement of the velocity field by particle tracking methods is not possible, because the introduction of these particles into the vessel quenches the reaction.

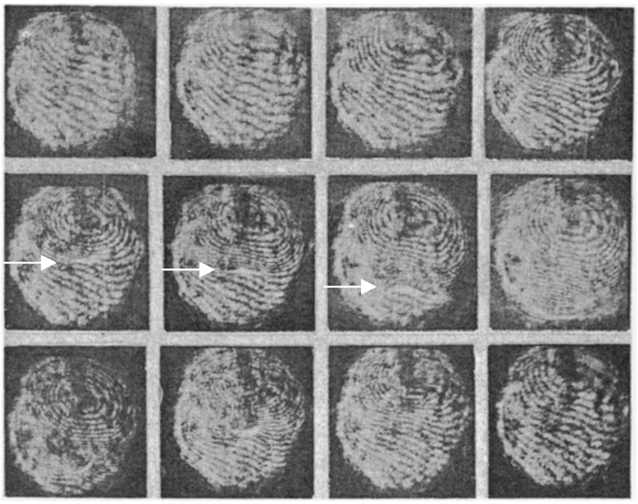

Figure 1.2. Sequence of interferograms from a study of cool flames in equimolar mixtures of propane and oxygen at 580 K in a horizontal cylinder (Melvin, 1969). The order of the frames is from top left to bottom right. A very weak horizontal flame front is just visible in the fifth, sixth and seventh frames, moving downwards from the centre of the vessel (this is shown by the arrows).

Very little work has been done to follow-up on Melvin's initial insight into the effects of natural convection on cool flames. Bull *et al.* (1977) did, however, use similar techniques to study cool flames in a parallel plate system under the influence of natural convection. Convection was generated in their system both by the reaction itself, and by heating the bottom plate in a similar fashion to the classic Rayleigh-Bénard system. The top plate of the reactor could also be heated to inhibit convection; thus the results in the presence and absence of convection could be compared. They found that in the purely conductive system, the results were very reproducible, whereas when convection was significant, the appearance of cool flames was far more random, both temporally and spatially. It was also noted that the hot zones, from which the cool flames emerged, occurred near the top of the reactor, away from the hot plate. Such an effect can only be due to natural convection. The formation of these hot zones due to natural convection is highly significant, because explosions could potentially be initiated in these regions, as described above. Finally, Bull *et al.* (1977) noted that the boundary between slow combustion and two-stage ignition in the presence of natural convection lies above that found in the purely conductive studies. This is unsurprising, given that heat loss to the surroundings plays an important role in thermal explosion theory, and heat transfer is significantly better in the presence of natural convection.

Whilst the convective effects described by Melvin (1969) and Bull *et al.* (1977) are very interesting, most workers have tried to suppress convection in an attempt to avoid the complications introduced by a flowing fluid, therefore gaining a better insight into the underlying chemistry. There are three techniques which have been used to eliminate convection. The first is to perform experiments at very low pressures, because *Ra* is proportional to the square of the pressure, thus eliminating natural convection at sufficiently low pressures. This method has proved successful studying of thermal ignition in gases; however, cool flames generally do not occur at pressures below ~ 0.2 bar, at which point the Rayleigh number is likely to be sufficiently high that natural convection is significant.

The second approach has been to use a mechanical stirrer in the vessel to induce spatial homogeneity. This technique has been applied successfully to systems exhibiting both spontaneous ignition (Griffiths and Phillips, 1990) and cool flames (Gray *et al.*, 1974; Griffiths *et al.*, 1971; Griffiths *et al.*, 1973). These studies were, in fact, the first to confirm the non-isothermal oscillatory nature of cool flames, thus refuting the hypothesis of Melvin (1969) that multiple cool flames could be caused solely by natural convection. Whilst the stirred vessel experiments give a good insight into cool flames, all spatial information about the development of the flames is lost.

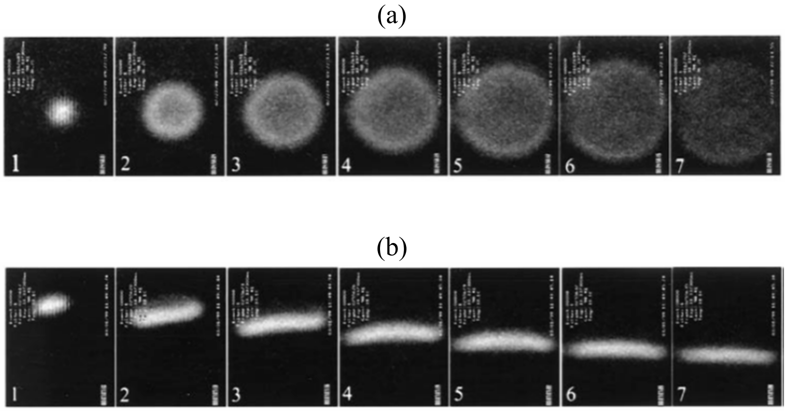

Figure 1.3. Development of a butane and oxygen cool flame in (a) microgravity, and (b) terrestrial gravity (Pearlman, 2000). The pictures are for a mixture of 66.7% butane and 33.3% oxygen, and the interval between neighbouring images is 0.1 s.

The most recent approach to the suppression of natural convection has been to study the combustion of gases in microgravity. Microgravity can be achieved in a number of different ways, such as performing experiments in drop towers, sounding rockets and also, of course, in orbit. Perhaps the most striking results however, are those presented by Pearlman (2000), who studied cool flames both at terrestrial gravity, and in simulated microgravity. The microgravity experiments were carried out aboard the NASA KC-135 microgravity aircraft, which follows a parabolic flight-plan to achieve microgravity for ~ 20 s. The gravity levels during such a manoeuvre are typically reduced to 10^{-2} g, thus achieving a reduction in Ra of two orders of magnitude. Figure 1.3 shows the development of a cool flame in butane and oxygen inside a spherical reactor with a diameter of 10.2 cm, under: (a) microgravity, and (b) terrestrial gravity. The different structure of the cool flame under the influence of natural convection from that in microgravity, where diffusion is the principal transport mechanism, is obvious. In microgravity, the flame initiates at the centre of the reactor, where the temperature would be at a maximum within the vessel, and then propagates outwards with spherical symmetry. By contrast, when convection is significant ($Ra \sim 10^4$ in Figure 1.3(b)) the flame initiates at the top of the reactor, which would again be the hottest part of the vessel, then propagates vertically downwards in a horizontal flame front. This horizontal flame front is similar to that observed by Melvin (1969), weakly visible in Figure 1.2, and is consistent with other experimental observations

(Sawerysyn *et al.*, 1973). It is evident from Figure 1.3 that natural convection has a significant effect on the spatial and temporal development of a cool flame and from Figure 1.2 that the temperature field is very complex. Despite this interesting, and highly significant behaviour, virtually no studies, experimental, numerical or theoretical, have been carried out to try and elucidate the effects of the interaction of the complex chemical phenomena and the flow due to natural convection. This was a major factor motivating this work.

1.3 Modelling Cool Flames

"Rich and varied patterns are always possible when heat release accompanies even the simplest reaction, and until the properties of the simplest systems are clearly understood, one cannot proceed confidently to the fundamental interpretation of behaviour in more complicated reactions." Griffiths (1985*b*)

1.3.1 The Thermal Switch Mechanism

As mentioned previously, cool flames occur due to chemical and thermal feedback interacting with heat loss. The chemical mechanism can be described as a 'thermal switch' and is outlined for a general hydrocarbon RH in Figure 1.4 below (Griffiths and Scott, 1987; Lignola and Reverchon, 1987). At lower temperatures the top mechanism operates, generating branching agents, and because it is an exothermic process, liberating heat. This release of heat causes the gas to increase in temperature. This heating has at least two consequences. The first is that RO_2 decomposes back to R and O_2. Also, the bottom mechanism, which is endothermic, with a relatively large activation energy, becomes more active and will eventually dominate. The progress of the endothermic reaction will then, in conjunction with heat loss to the walls, lower the temperature until the endothermic reaction effectively switches off, and the top reaction starts again. This cycle can then repeat itself until the fuel is depleted. This switching between high and low temperature mechanisms explains the oscillations; the system can also potentially proceed to explosion, because chain branching occurs. This would be *via* a two-stage ignition process. Oscillations can be produced because of this switching mechanism, which provides the chemical feedback mentioned above. In addition to this, oscillations can also arise due to thermal feedback. This occurs due to the non-linear temperature dependence of the rates of the reactions, coupled with heat loss to the surroundings.

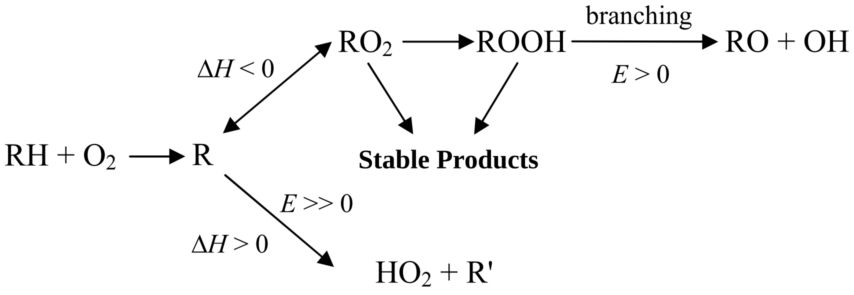

Figure 1.4. Outline of the thermal switch mechanism explaining oscillatory cool flames. R' is a stable unsaturated hydrocarbon formed with no branching. RO_2 and ROOH are degenerate branching agents.

1.3.2 Reduction of Comprehensive Mechanisms

Typical schemes describing combustion reactions can be very large, even for $H_2 + O_2$ (Dixon-Lewis, 1979). Buda *et al.* (2005) report reaction schemes generated by a computer package (EXGAS) for the combustion of several short chain hydrocarbons at temperatures of 600 – 1200 K. For *n*-butane, their mechanism contains 128 species in 731 separate reactions. These numbers are typical of the mechanisms produced by Buda *et al.* (2005) for other hydrocarbons. In fact, the largest kinetic schemes produced nowadays can consist of many thousands of elementary steps (Griffiths, 1995). Whilst these comprehensive schemes can be used to simulate behaviour in a spatially homogeneous system, it would, of course, be impractical to use such complex chemical mechanisms in a CFD code for complex geometries and flow patterns. Consequently, some reduced mechanism is required. In a comprehensive review on reduced kinetic schemes for combustion systems, Griffiths (1995) states the general rule of thumb that for any fluid mechanical calculation of reactive systems, the kinetics must be reduced to their simplest form. In addition, many of the kinetic schemes developed for hydrocarbon combustion are for high temperatures, and so have not necessarily been formulated to describe low temperature phenomena, such as cool flames. Several different approaches to reducing the kinetics are possible, and these are outlined below. There are however two distinct approaches to this problem.

The first is to take the comprehensive model and select the most important steps of the reaction to use as a reduced model. The second approach is to build up a kinetic model of oxidation to describe the observed effects. Most of the development has focussed on the latter approach of 'building up' a reaction mechanism.

The primary technique used in the reduction of large scale comprehensive models is sensitivity analysis. This is very similar to stability analysis, which can be used to explore the stability of steady-states in non-linear problems, and also identify the potential for oscillations. Sensitivity analysis is used to study how a system will respond to perturbations in parameter space. In effect, this means that rate constants are varied for each individual reaction at a given set of conditions, and the effect on the overall reaction quantified. The magnitude of the calculated sensitivity coefficient determines the importance of a reaction to the overall scheme. If the coefficient is small, then the reaction is redundant and can be discarded from the scheme. This method provides a rigorous and systematic mathematical approach to reducing kinetic mechanisms. By using sensitivity analysis it is possible to achieve significant reductions in the number of reactions. For example, Griffiths (1995) cites the kinetic scheme derived by Müller *et al.* (1992) for heptane oxidation. Those authors began with a mechanism consisting of 1011 reactions with 171 species; they reduced it to 79 reactions with 40 species. Whilst this reduction is considerable, it highlights a shortcoming of sensitivity analysis. As Griffiths (1995) points out, it is almost certainly the case that the reduced schemes produced in this way still contain too many variables to be used in multi-dimensional calculations including *e.g.* flow and temperature fields. Other procedures therefore have to be used, but sensitivity analysis does give an excellent starting point for these methods. However, as of yet, no reduced schemes describing low temperature combustion, derived through these rigorous mathematical methods are sufficiently small enough to be used in multi-dimensional simulations. That said, it is interesting to note that in a recent study, Fairlie *et al.* (2005) simulated cool flames in microgravity (*i.e.* a spatially non-homogeneous case but without any fluid flow), using a reduced mechanism comprising 58 species in 378 reactions. This is an impressive achievement given the likely computational cost involved; however, it seems unlikely that such a scheme could yet be used in conjunction with a flow solver due to the prohibitive computational cost. The use of such a reduced scheme does have one other attraction. Through following the product of species concentrations, [OH][CH_3O], it was possible to approximate the intensity of light output from CH_2O^* (this species is produced primarily by the reaction $OH + CH_3O \rightarrow CH_2O^* + H_2O$), and hence track the development of the flame, which oftentimes is the only experimental observation made. Such methods have also been employed to study the development of a cool flame in a well-mixed system (Griffiths and Sykes, 1989).

Given that a reduced mechanism is usually too large to be used in conjunction with CFD, an alternative approach is necessary, using relatively simple kinetic models to match experimental observations. Of course, using a handful of reactions raises the question of whether such simple models are truly representative of a combustion system. It should be remembered though, that the very simple reaction $A \rightarrow B$ forms the basis of thermal explosion theory and has played an important role in the history of combustion. There are many skeleton schemes to represent cool flames; several are discussed in detail by Griffiths (1995). In the following sections, some of the more significant examples are discussed.

1.3.3 Sal’nikov’s Reaction

Sal’nikov (1949) was the first to demonstrate that a simple chemical mechanism can produce oscillations. Sal’nikov considered a closed vessel in which a product B is formed from a precursor P, *via* an active intermediate A:

$$\mathrm{P} \xrightarrow{1} \mathrm{A} \xrightarrow{2} \mathrm{B}\,. \tag{1.1}$$

There are two consecutive, first-order steps, the first of which is taken to be thermoneutral, and the second is exothermic. The reaction was initially considered to occur in a well-mixed, and therefore spatially homogeneous, reactor. This reaction scheme is the simplest to display the thermokinetic oscillations which characterise cool flames. In this case, the oscillations occur due to purely thermal feedback, which arises due to the Arrhenius temperature dependence (non-linear) of the second step and heat loss to the surroundings. For a well-mixed reactor, the heat loss to the surroundings can be assumed to be *via* Newtonian cooling. Sal’nikov’s analysis was both powerful and elegant and shows that even a very simple exothermic reaction can exhibit very complicated behaviour. The lack of chemical feedback, through chain branching, in this model limits its direct applicability to cool flames, because phenomena such as delayed and two-stage ignition are not predicted. Despite this, Bardwell and Hinshelwood (1951) did show that the general behaviour predicted by Sal'nikov's reaction was qualitatively similar to what was observed experimentally for cool flames of methyl ethyl ketone. Another weakness of this model is the lack of a purely combustion or other analogue to Sal'nikov's reaction; therefore it is difficult to compare the analytical analyses of the reaction to experimental results. However, Griffiths *et al.* (1988), Gray and Griffiths (1989) and Coppersthwaite *et al.* (1991) have devised an experimental procedure whereby the first step of the reaction is modelled by the slow addition of one of the reactants into a well-stirred reactor. Griffiths (1995) suggests that this experimental procedure has relevance in the context of process safety, because it could describe a slow leak, through a faulty valve, into a reactive atmosphere. These experimental studies showed that oscillations occurred in closed regions of parameter space, as predicted by theory.

The behaviour of Sal'nikov's reaction in the spatially uniform, well-mixed system has been extensively studied (*e.g.* Forbes, 1990; Gray *et al.*, 1988; Gray and Roberts, 1988; Gray and Scott, 1990*a;* Kay and Scott, 1988). Many of these workers have studied the stability of Sal'nikov's reaction to identify the regions where oscillatory behaviour occurs, and, in fact, the system is now well understood in this respect. Regions of stability can be defined by examining the stability of steady states. For steady states to be possible, the concentration of the precursor P has been assumed to remain constant spatially and temporally. This is the so-called 'pool chemical approximation', and is widely used in the study of Sal'nikov's reaction. This approximation is valid because step 1 of reaction (1.1) is always taken to be very slow, so the concentration of P only varies very slightly as time progresses. One weakness common to all these stability studies is the choice of dimensionless groups. They have been borrowed from thermal explosion theory and chosen for mathematical economy. Whilst this leads to more elegant equations, the physical interpretation of the results can be difficult. This is discussed in greater detail in Chapter 4.

Some initial work has also been done for Sal'nikov's reaction in systems, which are not perfectly mixed. Gray and Scott (1990*b*) and Forbes (1993) analysed the stability of Sal'nikov's reaction, with respect to spatial and temporal oscillations, in a purely diffusive system, *i.e.* spatial variations in the temperature and the concentration were possible, but natural convection was ignored. The situation they considered was of the reaction occurring in a long, thin box in which diffusion of heat and mass was only possible in one dimension. Forbes (1996) extended this work to look at reaction in circular geometry. The geometries used in these studies are somewhat contrived, in an effort to achieve a set of equations, which can be examined for stability analytically; however, Forbes's (1996) study for circular geometry corresponds to the experimentally observed formation of target and spiral patterns in uniformly propagating planar flames (Pearlman, 1997; Pearlman and Ronney, 1994*a*, *b*) and indeed Scott *et al.* (1997) have used Sal'nikov's reaction as a model to simulate these phenomena in pre-mixed flames. The theoretical studies of Sal'nikov's reaction occurring in a purely diffusive system have been augmented with numerical studies by Fairlie and Griffiths (2001, 2002), who examined Sal'nikov's reaction occurring in a spherical reactor and in a planar system. They showed that oscillations in the temperature and the concentration of the intermediate A were possible in this more complex geometry, and they examined the effects of varying certain key parameters, such as the thermal diffusivity and the Lewis number. More recently, some preliminary numerical results have been presented by Cardoso *et al.* (2004*a*, *b*) for Sal'nikov's reaction occurring in the presence of natural convection. These results will be discussed in section 1.4.

1.3.4 Gray and Yang's Model

As mentioned above, Sal'nikov's reaction does not capture some possibly important aspects of a cool flame. This is due to the omission of any chemical feedback through chain branching. A model taking account of chain branching as well as thermal effects was proposed by Gray and Yang in the 1960's (Gray and Yang, 1965; Yang and Gray, 1969*a*, *b, c*) in an attempt to unify the thermal and chain branching theories of thermal explosion, and account for spontaneous ignitions and oscillatory cool flames, occurring in a region in which a negative temperature coefficient for the reaction rate was observed. This was a first attempt at proposing a model, which could reproduce the form of an experimentally measured ignition diagram (*e.g.* Figure 1.1). The model they proposed is:

$\mathrm{A} \xrightarrow{k_1} \mathrm{X}$ initiation, (1.2 a)

$\mathrm{X} \xrightarrow{k_2} 2\mathrm{X}$ branching, (1.2 b)

$\mathrm{X} \xrightarrow{k_3} \mathrm{P}_1$ termination 1, (1.2 c)

$X \xrightarrow{k_4} P_2$ termination 2. (1.2 d)

This mechanism consists simply of an initiation step, followed by chain branching and two parallel termination reactions. It is generally assumed (implicitly), that the decay in the concentration of the precursor, A, is ignored, *i.e.* the pool chemical approximation is applied. The only constraint on the kinetic parameters is that the activation energies are such that $E_3 < E_2 < E_4$. This ensures that there is an overall negative temperature dependence of the reaction rate over a limited range of temperature. Yang and Gray (1969*a, b*) performed a stability analysis for their reaction occurring in a well-mixed reactor and were able to identify regions in which oscillatory cool flames and two stage ignitions would occur. Further, more detailed, stability analyses were also presented (Gray, 1969*a*, *b*; Yang, 1969). Indeed, by numerical simulation, Yang and Gray (1969*a, b*) were able to produce the main thermokinetic features of a real ignition diagram. They identified single- and two-stage ignitions, the negative temperature coefficient and oscillatory cool flames. It should be noted though, that the kinetic parameters used were selected on an empirical basis. The results of the simulations can therefore be tuned to give the desired thermokinetic behaviours. Another point to be borne in mind is that it is difficult to relate the reaction steps of Gray and Yang's model to the elementary reactions, which are known to occur in hydrocarbon oxidation. Nevertheless, Gray and Yang's model is attractive, given its elegance and simplicity. It is still being investigated (*e.g.* Foster and Pearlman, 2006; Sidhu *et al.*, 1995) and used as a basis for developing new reduced schemes.

1.3.5 Wang and Mou's Model

Whilst Gray and Yang's model does capture many of the features of low temperature combustion, it fails to account for the multiple-stage ignitions, observed in the oxidation of many fuels. To account for this effect, Wang and Mou's (1985) new model, based on Gray and Yang's model, replaces the branching reaction in Gray and Yang's model (Eq. (1.2 b)) with two branching reactions, one at high temperatures, and one at low temperatures. Wang and Mou's model can be written as:

$A \xrightarrow{k_1} X$ initiation, (1.3 a)

$X \xrightarrow{k_2} 2X$ low temperature branching, (1.3 b)

$X + A \xrightarrow{k_3} 2X$ high temperature branching, (1.3 b)

$X \xrightarrow{k_4} P_1$ termination 1, (1.3 c)

$X \xrightarrow{k_5} P_2$ termination 2, (1.3 d)

subject to the constraint on activation energies of $E_3 > E_1 > E_4 > E_2 > E_5$. The model was formulated to describe acetaldehyde combustion in a CSTR. However, the model did not take account of heat flowing out of the reactor in the outlet stream; it merely accounted for heat loss through the walls of the reactor. Whilst this may seem like a glaring oversight, there is in fact experimental evidence to suggest that heat removal from the reactor by the out-flowing gas is considerably lower than the heat lost through the walls at the conditions of interest. Thus, Gray *et al.* (1984) showed that over 95% of the heat generated by the oxidation of ethane would be lost through the walls of a continuous reactor, rather than in the outflow. Once again, through careful tuning of the kinetic parameters, numerical simulations of Wang and Mou's model showed very good agreement with experimental results, and were able to predict multiple-stage ignitions. Five characteristic regimes of behaviour have been identified and explored numerically (Liang *et al.*, 2003), namely: (i) low temperature steady state, (ii) oscillatory two-stage ignitions, (iii) complex oscillations, (iv) oscillatory cool flames and (v) the high temperature steady state.

1.3.6 The 'Shell' Model

The 'Shell' model describes a series of models developed by Halstead and co-workers at Shell's Thornton Research centre in the 1970's. The initial development of the model was based on a reduced mechanism for acetaldehyde oxidation (Halstead *et al.*, 1970, 1971, 1973) and was tested against experimental studies of cool flames and two-stage ignitions in a closed vessel. The model was further developed (Halstead *et al.*, 1975) for the oxidation of a general alkane, and then further simplified (Halstead *et al.*, 1977) to a scheme with eight reactions:

$RH + O_2 \rightarrow 2R$ initiation, (1.4 a)

$R \rightarrow R + \text{heat}$ propagation, (1.4 b)

$R \rightarrow R + B$ propagation, (1.4 c)

$\mathrm{B} \rightarrow 2\mathrm{R}$ branching. (1.4 d)

$\mathrm{R} + \mathrm{Q} \rightarrow \mathrm{B} + \mathrm{R}$ propagation, (1.4 e)

$\mathrm{R} \rightarrow \mathrm{R} + \mathrm{Q}$ propagation, (1.4 f)

$\mathrm{R} \rightarrow \text{products}$ termination, (1.4 g)

$\mathrm{R} + \mathrm{R} \rightarrow \text{products}$ termination, (1.4 h)

Care has to be taken when applying this model to CFD codes to ensure conservation of mass. The ‘Shell’ model has often been used as a basis for development of further models, such as Cox and Cole’s (1985) model. Other models have developed from the ‘Shell’ model, with increasing complexity and including more explicit representation of the elementary reactions seen in the low temperature combustion of alkanes. The inclusion of these reactions brings the reduced kinetic schemes closer to reality, meaning there is less need to tune the kinetic parameter inputs. That said, the inclusion of an increasing number of reactions does limit the applicability of these reduced schemes to CFD modelling.

1.3.7 Choice of Reduced Kinetic Scheme

This work is concerned with understanding the effect of natural convection on cool flames. Given the complexity of the behaviour of cool flames in the presence of natural convection, and the difficulties of integrating complex reaction schemes into a CFD code, the logical choice for gaining an insight into the effects of natural convection is to use Sal’nikov’s reaction. This choice is principally motivated by the lack of knowledge of the interaction between cool flames and natural convection. Since Sal’nikov’s reaction is the simplest to display thermokinetic oscillations, it can yield significant insight into the fundamentals of the interaction between oscillations induced by thermal feedback and the fluid mechanics, whilst not being prohibitively computationally expensive. In reference to the quotation from Griffiths (1985*b*) at the start of the section, it is vitally important that an understanding of this simplest reaction is gained before any attempt is made to examine more complex reaction schemes. This work therefore aims to provide a strong foundation upon which all future work can be built. A sound understanding of how Sal’nikov’s reaction behaves in the presence of natural convection will allow deductions to be made as to whether thermal or chemical effects are more important under different conditions when the results are compared with those for a more detailed reaction mechanism.

1.4 Natural Convection with Exothermic Reaction

In contrast to a well-mixed system, the behaviour of Sal'nikov's reaction, or any other exothermic reaction, in the presence of natural convection has received surprisingly little attention. In the classical work of Frank-Kamenetskii (1955) describing thermal explosion in a purely conductive system (for heat and mass transfer), it was suggested that in a gaseous system, natural convection becomes significant when $Ra > 10^4$ (*n.b.* the condition actually states that natural convection will be significant when the Grashof number, Gr, exceeds 10^4. Since Ra is the product of Gr and the Prandtl number, Pr, and $Pr \sim 1$ for a gas, then Ra and Gr are equivalent in this case). Further studies have shown that natural convection becomes important when Ra is at least an order of magnitude lower than this. The first of these to appear was that of Tyler (1966), who presented very compelling experimental results for nitric oxide reacting with oxygen in a spherical vessel. Measured temperature profiles along the vertical axis of the reactor were presented; they showed the symmetrical temperature distributions expected for low Ra and also revealed that the temperature profiles for higher Ra (~ 9000) were skewed. In fact, the maximum temperature in the vessel occurred well above the centre of the vessel. Tyler (1966) also compared the temperature increase predicted by the purely conductive theory of Frank-Kamenetskii and the measured temperature rise at the centre of the reactor, over a range of values of Ra. This comparison showed that convection becomes significant when $Ra \sim 500$, a value considerably lower than the 10^4 postulated by Frank-Kamenetskii, and one which is certainly attainable in experimental systems. Such a value is of similar order to that predicted for the onset of convection in a parallel plate system heated from below in the absence of reaction ($Ra = 1708$). As an interesting aside, Tyler and Tuck (1967) also showed that even in the absence of reaction, natural convection could cause oscillations in the temperature inside a vessel. Experiments were performed wherein an inert gas was admitted to a preheated vessel. The gas would then heat up to the wall temperature. Tyler and Tuck (1967) showed that when Ra rose above $\sim 10^4$, the temperature measured at the centre of a spherical vessel would exhibit small-scale oscillations as it approached the wall temperature. Tyler's initial study (1966) was expanded by Ashmore *et al.* (1967), who included further measurements for the reaction between hydrogen and chlorine inside a sphere. These measurements followed the same trend as those for the reaction between nitric oxide and oxygen. Ashmore *et al.* (1967) also showed that previous measurements by Gerri and Kaufman (1965) for the thermal decomposition of azomethane in a spherical reactor were consistent with natural convection influencing the measured temperature. Gerri and Kaufman (1965) observed that the Arrhenius plot of their kinetic measurements was curved. They speculated that this effect was due to a change in mechanism; however, Ashmore *et al.* (1967) showed that this change in apparent activation energy was consistent with natural convection developing in the reactor and skewing the temperature profile. Thus, an understanding of when natural convection becomes important, and the effects it has, is crucial in the interpretation of experimental work. Further experiments by Archer (1977) on the thermal decomposition of azomethane inside a spherical reactor revealed various effects of natural convection on the development of the temperature field. These measurements will be discussed in Chapter 2.

The experimental studies of Tyler and co-workers investigating the effects of natural convection on exothermic reactions inspired a series of theoretical and experimental studies of the effect of natural convection on thermal explosion. Much of the early work on this problem was performed by Merzhanov and co-workers in the early 1970's. Merzhanov and Shtessel (1971) presented experimental results for liquid systems in cylindrical and flat vessels. They compared these results with the theory of Frank-Kamenetskii, based on an effective heat transfer coefficient due to convection. Their results showed good agreement with the theory. Merzhanov and Shtessel (1971) also presented measured temperature profiles in a flat vessel; these are qualitatively similar to those measured by Tyler (1966) in a spherical reactor. Shtessel *et al.* (1971) presented a numerical solution to the governing equations for a zeroth-order reaction occurring in a square cavity. They investigated the effect of increased Ra on the critical Frank-Kamenetskii parameter, δ_{cr}, for explosion, and found that increasing the Rayleigh number increased the threshold to explosion. This is unsurprising, because thermal explosion depends on the balance between heat generated by the reaction, and heat lost to the walls. When Ra is increased, heat transfer from the reacting fluid becomes faster, resulting in more heat being lost to the surroundings, thereby suppressing explosion. The numerical computations of Shtessel *et al*. (1971) also showed that the critical Rayleigh number for the onset of convection was ~ 500, agreeing well with the experimental observations of Tyler (1966) and Ashmore *et al.* (1967). This conclusion was backed up by the theoretical work of Jones (1973), who performed a stability analysis for a zeroth-order reaction occurring between two infinite parallel plates. Jones (1973) showed that the critical Rayleigh number for the onset of convection was ~ 500. It is interesting that Jones (1973) suggests that inside a horizontal cylinder or a sphere, there will always be some degree of convection, because of the existence of temperature gradients perpendicular to the gravity vector, and that the observed 'onset' of convection is in fact merely the point where the effects of this flow become observable. In a seminal work on the interaction of thermal explosion and natural convection, Merzhanov and Shtessel (1973) presented a detailed numerical and experimental analysis of explosion in a liquid system. They identified four distinct regions of behaviour, namely: (i) a region where neither convection nor explosion arises, (ii) there is convection present but no explosion occurs, (iii) there is both convection and explosion and (iv) there is explosion but no convection. Merzhanov and Shtessel (1973) showed that natural convection suppresses explosion, and that when explosion does occur, the ignition delay is longer in the presence of natural convection. The computations of Merzhanov and Shtessel (1973), whilst powerful were limited to a two-dimensional system, and were for a zeroth-order reaction, ignoring any effects of varying concentration. The square cavity in which a zeroth-order reaction occurs, analysed by Merzhanov and Shtessel (1973), has more recently been studied numerically by Dumont *et al.* (2002). As well as examining the four regions described above, they found regions where oscillations occurred. Dumont *et al.* (2002) also did a stability analysis which showed a critical Rayleigh number for the onset of natural convection of 500 – 1000. Also identified were conditions for which natural convection actually enhanced explosion, rather than suppressing it. Similar observations were made by Kagan *et al.* (1997) for a parallel plate system. These latter authors showed that the formation of hot spots due to convection could promote explosion; however, this observation was based on calculations made for an imposed flow pattern, with eddies similar in form to those produced by natural convection, and the scale of the eddies required to promote explosion would not physically occur simply through natural convection.

In addition to the numerical and theoretical studies in parallel plate reactors, there has been some limited work examining the effect of natural convection on an exothermic reaction in reactors with other geometries. Jones (1974) studied numerically, the effect of natural convection on δ_{cr} in a horizontal cylinder, and was able to show that increasing the Rayleigh number increased the explosion threshold, as is the case with parallel plates. Mitachi and co-workers (Mitachi *et al.*, 1986; Mitachi and Igarashi, 1987) compared numerical simulations in a horizontal cylinder with experiments in which the exothermicity of the reaction was mimicked by electrical heating. In these comparisons zeroth-order kinetics were once again assumed in the simulations, thereby neglecting any effects of variation in composition in the reactor. These studies compared the average Nusselt number for heat transfer measured experimentally with those found numerically, and found good agreement. Mitachi and Igarashi (1987) also used interferometry to make a qualitative comparison between the simulated and actual temperature fields. The temperature field they observed experimentally was qualitatively similar to that shown in Figure 1.2 for cool flames occurring in a cylindrical reactor.

Virtually all previous numerical and theoretical studies of an exothermic reaction in the presence of natural convection have considered zeroth-order reactions, so neglecting any effects due to the composition changing in the reactor. Stiles and Fletcher (2001) and Stiles *et al.* (2001) reported a somewhat limited study of first-order reactions occurring in a convective system. They found that the rates of these reactions were significantly altered in the presence of convection. They showed that the average rate of reaction for firstly, a thermoneutral first-order reaction occurring in a heated vessel, and secondly, an endothermic reaction occurring in a heated vessel, were significantly increased by natural convection. These studies are the converse of the case of an exothermic reaction in a cooled vessel considered here; nevertheless, the results do demonstrate the effect that natural convection can have on a simple reaction. Despite this lack of work on reactions with non-zero order, it seems clear from the effects discussed above for zeroth-order reactions that natural convection will have a significant impact on the progress of Sal’nikov’s reaction, and that complex behaviour will be observed. Cardoso *et al.* (2004*a*) have reported some preliminary computations of the development of natural convection in a closed vessel wherein Sal’nikov’s reaction occurs. They found that natural convection influenced the temporal and spatial development of the temperature and concentration fields inside a spherical reactor. The temperature fields they presented were of the same form as those seen in the interferograms in Figure 1.2, and the horizontal stratification in the temperature was similar to the form of the cool flame seen in Figure 1.3. Cardoso *et al.* (2004*b*) proposed the three-dimensional regime diagram, shown in Figure 1.5, to describe the behaviour of such a system. The axes of this diagram are $(\tau_{step\ 2} / \tau_{convection})$, $(\tau_{step\ 2} / \tau_{diffusion})$ and $(\tau_{step\ 2} / \tau_{step\ 1})\ p'$, where each τ is the characteristic timescale for each interacting phenomenon in the system and p' is the dimensionless concentration ($= p / p_0$) of the precursor P. It was assumed when drawing up Figure 1.5 that the Lewis and Prandtl numbers remain constant. The horizontal plane in this diagram, described by the axes $(\tau_{step\ 2} / \tau_{convection})$ and $(\tau_{step\ 2} / \tau_{step\ 1})\ p'$, corresponds to the well-mixed case discussed above, whereas the vertical plane defined by the axes $(\tau_{step\ 2} / \tau_{diffusion})$ and $(\tau_{step\ 2} / \tau_{step\ 1})\ p'$ corresponds to the purely diffusive case. In the generalised Sal'nikov system, both diffusion and natural convection will play a role. Such a system can be represented on Figure 1.5 by a point such as C. If the concentration of P decreases with time, point C will move towards the origin along a line parallel to the $(\tau_{step\ 2} / \tau_{step\ 1})\ p'$ axis. If the concentration of P remains constant, (*e.g.* by constant supply of reactant), point C remains fixed. Straight lines through the origin of the plane described by the $(\tau_{step\ 2} / \tau_{diffusion})$ and $(\tau_{step\ 2} / \tau_{convection})$ axes in fact correspond to a constant value of the Rayleigh number.

Also presented by Cardoso *et al.* (2004*b*) was a simple, preliminary scaling analysis of Sal'nikov's reaction in the presence of natural convection and diffusion. This method allowed analytical predictions for certain parameters, such as the temperature rise and the velocity, to be made through inspection of the governing equations. These predictions, however, remained largely unverified, but are re-examined in detail below.

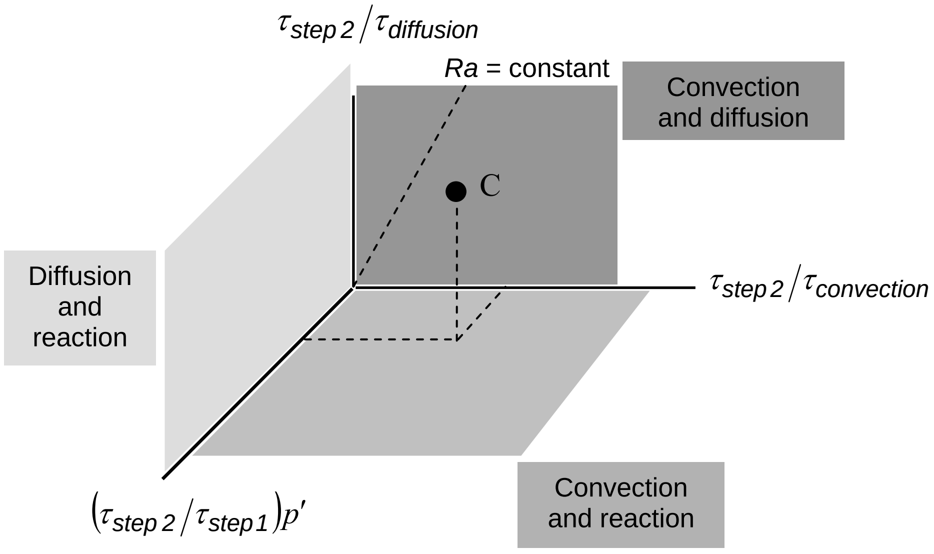

Figure 1.5. Regime diagram showing the planes containing purely diffusive systems and purely convective systems. A system with chemical reaction, diffusion and convection is represented by point C (Cardoso *et al.*, 2004*b*).

1.5 The Present Work

1.5.1 Aims

The work below investigates the effects of natural convection on Sal'nikov's reaction, which is used to model cool flames. The reaction is taken to occur in a closed spherical reactor with a constant wall temperature. Such a system is investigated through a combination of mathematical techniques and numerical simulation in an attempt to gain insight into the critical parameters governing the behaviour, and to discover how natural convection influences any thermokinetic oscillations. An understanding of these properties is vital for any future work on more complex reaction mechanisms.

A numerical algorithm had to be developed for an exothermic reaction occurring in a spherical vessel. The results from this algorithm will be compared with previous experimental measurements for the thermal decomposition of azomethane in a spherical reactor. The experimental measurements are also compared with analytical scales derived through analysis of the governing equations. Comparing these experimental results with the results of scaling and numerical simulation will serve as a validation of both methods.

The numerical method developed is also used to investigate the behaviour of Sal’nikov’s reaction under a number of different conditions, both in the presence, and absence of natural convection. Regions in which oscillations occur are sought, as also are analytical expressions for the characteristic temperature rise, velocity and concentration of the intermediate, A. These expressions can then be used to predict how the system will behave in response to changes in certain key process parameters.

1.5.2 Outline

The remainder of this thesis is divided into six chapters. In Chapter 2 the results of previous experimental work are compared with analytical scales derived by examining the equations governing the progress of a simple, single-step exothermic reaction in a closed vessel. The numerical method for simulating such a reaction is also introduced, and the outputs from these simulations are compared with experimental results. Finally, the developments which have to be made to the numerical scheme to simulate Sal’nikov’s reaction are discussed. A scaling analysis of Sal’nikov’s reaction is presented in Chapter 3, for the two cases where the transport of heat and mass are dominated by diffusion and natural convection, respectively. The form of the scales developed is confirmed through comparison with the results of numerical simulations. The scales are also used to show how the progress of the reaction changes when certain parameters, such as the pressure, are varied. Chapter 4 examines in more detail the behaviour of Sal’nikov’s reaction in the absence of natural convection. A region in parameter space where oscillations occur is identified, and this region is compared with the results of a previous analytical stability analysis. In addition, approximate analytical solutions are sought for two limiting cases of non-oscillatory behaviour. A region of oscillations is also defined in Chapter 5, this time for the case when natural convection does play a role. In addition, the different behaviours exhibited in different parts of the regime diagram are explored. Some unusual aspects of these oscillatory cases are also explored in Chapter 6. Finally, in Chapter 7, the work is summarised and some general conclusions are drawn. In addition, recommendations for future work on this topic are discussed.

2 Comparison of Numerical Methods and Experimental Results for an Exothermic Reaction in the Presence of Natural Convection

2.1 Introduction

In this chapter, a model is developed for simulating a simple exothermic reaction occurring in a spherical batch reactor. Thus, the reactions considered in this chapter are simpler than Sal'nikov's reaction (Eq. (1.1)), which is investigated in later chapters. By studying simpler reaction mechanisms, the results of the analytical and numerical techniques can be compared directly with experimental results to validate the theoretical methods. As mentioned in section 1.3.3, there is no experimental information on Sal'nikov's reaction in a spatially non-homogeneous reactor, so such comparisons are more difficult for that reaction.

When natural convection occurs, it causes a distortion of the spherically symmetric temperature profile achieved when heat is transferred by conduction only. In outline, the system behaves as follows. The walls of the reactor are kept at a constant temperature. Whilst reaction proceeds, heat is released and consequently the temperature of the gas rises, so that heat is removed from the system at the walls. This coupling of heat generation and loss causes a hot zone to form at the centre of the reactor. This in turn results in a gravitationally unstable density distribution in the top section of the reactor and so leads to the development of the familiar Rayleigh-Bénard convection (Turner, 1979), shown schematically in Figure 2.1. Part (a) shows the streamlines of the induced flow, and part (b) gives plots of both the temperature and density along the vertical axis of the reactor. The hot gas near the centre of the reactor rises quickly initially and moves into the hottest part of the reactor (in the top half). However, it slows as it passes through the hot zone, due to the falling density difference and the proximity of the wall at the top of the vessel. The hot gas then contacts the relatively cold walls, where it cools and descends fairly rapidly due to the large density differential between the cool gas at the wall and the much hotter gas near the centreline of the reactor. In the lower half of the reactor the density distribution is intrinsically stable, with the flow being induced by the descending, cooler gas at the wall. This downward flow of cool gas results in a relatively slow upward flow (around the vertical axis of the reactor) of gas displaced from the bottom of the reactor. Whilst this gas rises, it heats up and hence accelerates. The flow patterns typified by Figure 2.1(a) mean that whilst the hottest part of the reactor is initially at the centre of the reactor, for larger times when the flow due to natural convection has developed, the hottest part of the reactor becomes significantly above the centre of the reactor, as shown schematically in Figure 2.1(b). In many experimental studies, only the temperature at the centre of the reactor was measured; whenever natural convection is significant, this temperature can be considerably lower than the maximum temperature in the vessel.

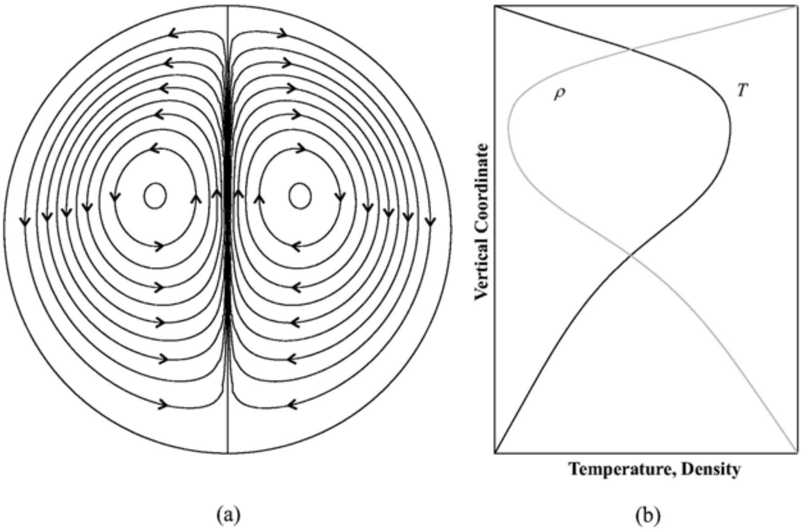

Figure 2.1. (a) Streamlines of the flow due to natural convection in a vertical cross section through the centre of the reactor. The toroidal vortex which typifies the flow (upwards near the axis, downwards near the wall) is shown. (b) Temperature and density profiles along the vertical axis of the reactor, showing the unstable density distribution in the top half of the reactor, which drives the flow, and the stable density distribution in the bottom half of the reactor, where flow is driven by conditions in the boundary layers.

This chapter is concerned with comparing the results of experimental work with numerical simulation and analytical scaling. Such comparisons have seldom been made previously. Merzhanov and Shtessel (1973) made a comparison of liquid-phase systems in planar layers and cylinders, whilst Mitachi and co-workers (Mitachi *et al.*, 1986; Mitachi and Igarashi, 1987) compared numerical simulations in a horizontal cylinder with experiments in which the exothermicity of the reaction was mimicked by electrical heating. In all these comparisons zeroth-order kinetics were assumed in the simulation work, thereby neglecting any effects of composition within the reactor. In addition, only global average parameters, such as the critical Frank-Kamenetskii parameter, δ_{cr}, for explosion or the average Nusselt number for heat transfer, were compared. Mitachi and Igarashi (1987) used interferometry to allow qualitative comparison of the spatial structure of the temperature fields generated experimentally and numerically; however, there has been very little quantitative consideration of the spatial development of *e.g.* the temperature field under the influence of natural convection when the reaction proceeds. In addition to this, no comparisons between experiment and simulation have been made for reactions of any order occurring in a spherical reactor, mainly due to the scarcity of experimental results in such a configuration.

In this chapter, comparison will be made between previous experimental measurements and the theoretical predictions of section 2.3. In addition, the experimental results will be compared with full numerical solutions of the governing equations in section 2.4. The experimental results considered are those of Archer (1977), who studied the thermal decomposition of azomethane in a spherical reactor, and also those of Tyler and co-workers (Ashmore *et al.*, 1967; Tyler, 1966;), who studied the reactions of nitric oxide with oxygen, as well as chlorine with hydrogen, in a spherical reactor. In section 2.5, the alterations to the numerical scheme to simulate Sal'nikov's reaction are discussed.

2.2 Governing Equations

The first reaction considered is the thermal decomposition of azomethane ($CH_3N_2CH_3$); the primary products are methane, ethane and nitrogen. Archer (1977) analysed the kinetics of the reaction at low pressures (up to ~ 0.05 bar) and found that the reaction had an order with respect to azomethane of ~ 1.4. Such a value means that the spatial variation of the rate of reaction, due to the composition varying spatially, ignored in previous zeroth-order numerical studies, is likely to influence this system. Archer (1977) measured the rates of reaction over a temperature range of 612.2 – 652.2 K, with initially pure azomethane, as well as in the presence of diluents (CO_2 and SF_6) and found the rate constant can be written as:

$$k = 1.24\times10^{14}\exp\left(-194\text{ kJ mol}^{-1}/RT\right)\text{ m}^{1.2}\text{ mol}^{-0.4}\text{ s}^{-1}, \tag{2.1}$$

at the pressures of interest. The values of the activation energy, E, and the pre-exponential factor, $Z = 1.24 \times 10^{14}$ $\text{m}^{1.2}$ $\text{mol}^{-0.4}$ s^{-1}, measured by Archer (1977) agree well with previous experimental studies (*e.g.* Camilleri *et al.*, 1975; Riblett and Rubin, 1937; Rice, 1940; Trotman-Dickenson, 1955). However, there is disagreement over the order of the reaction. The decomposition of azomethane was generally considered by these early workers to be quasi-unimolecular. The reaction has been measured to be first-order at ~ 0.4 bar; however, Archer (1977) found the order to be 1.4 at lower pressures, *i.e.* neither at the high pressure limit of unity, nor at the low pressure limit of 2, as expected if the reaction were truly unimolecular. The reaction is evidently complex. In the early studies the reaction was assumed simply to produce either, ethane and nitrogen, or two methyl radicals and nitrogen. The former is unlikely, given that the principal hydrocarbon product of the reaction is methane (Archer, 1977; Riblett and Rubin, 1937), which is likely to be produced by reaction of an azomethane molecule with a methyl radical. Additional decomposition paths of *e.g.* $C_2H_5N_2CH_3$ can explain the deviation from first-order kinetics measured by Archer (1977). Nevertheless, for the purposes of this work, the order of 1.4 and Eq. (2.1) as measured by Archer (1977) are used below.

The equation governing the conservation of the azomethane can be written as:

$$\frac{\partial c}{\partial t} + \underline{u}.\nabla c = D_C\nabla^2 c - k(T)c^n, \tag{2.2}$$

where c is the concentration of azomethane, $\underline{u}$ is the velocity vector, D_C is the molecular diffusivity of azomethane and n is the order of the reaction with respect to azomethane, taken here to be 1.4. It should be noted that the diffusion is assumed to be Fickian, *i.e.* the diffusive flux is proportional to concentration gradients, as opposed to gradients in mole fraction. This is a consequence of the adoption of the Boussinesq approximation, which will be discussed below. The conservation of energy within the reactor is described by:

$$\frac{C_V}{C_P}\frac{\partial T}{\partial t} + \underline{u}.\nabla T = \kappa\nabla^2 T + \frac{qk(T)}{\rho_0 C_P}c^n, \tag{2.3}$$

where C_V and C_P are the mixture's specific heats at constant volume and pressure, T is its temperature, κ is the thermal diffusivity, ρ_0 is the density at the initial temperature T_0 and q is the exothermicity of the reaction. The familiar Navier-Stokes equations:

$$\frac{\partial \underline{u}}{\partial t} + \underline{u}.\nabla \underline{u} = -\frac{1}{\rho_0}\nabla\left(\mathscr{P} - \mathscr{P}_0\right) + \nu\,\nabla^2 \underline{u} + \frac{\rho - \rho_0}{\rho_0}\underline{g}\,, \tag{2.4}$$

describe conservation of momentum, where $\mathscr{P}$ is the pressure in the reactor and ν is the kinematic viscosity. The Boussinesq approximation is adopted, *i.e.* it is assumed that the density only varies in the buoyancy term of Eq. (2.4), in which $\rho = \rho_0[1 - \beta(T - T_0)]$, where β is the coefficient of thermal expansion. The density is assumed constant in all other terms of the governing equations. The Boussinesq approximation requires that the characteristic temperature rise ΔT is such that $\Delta T << T_0$; otherwise full compressibility needs to be taken into account. This approximation is commonly used in the analysis of buoyant flows (Turner, 1979), and was used in all previous numerical studies of natural convection driven by an exothermic reaction, discussed in section 1.4. It should be noted that both the pressure and molar density within the reactor will change due to one mole of azomethane forming more than one mole of products. The molar ratio of the products of the reaction to the reactant has been measured at ~ 2 (Archer, 1977; Riblett and Rubin, 1937). This increase in the number of moles of gas in the reactor, of course, leads to an increase in pressure. This effect has been ignored in this work. This is because over the time period of interest (the first 10 s of reaction), the reaction only proceeds to ~ 5% of completion (Archer, 1977), so any effect of the increased number of moles of gas due to reaction is slight. In addition, for many of the situations considered, a diluent is present in the reactor, thereby minimising the overall increase in the number of moles of gas inside the reactor and hence the consequential changes in pressure and density. The final equation required is the continuity equation. Adoption of the Boussinesq approximation allows the continuity equation to be written in its incompressible form, *i.e.*

$$\nabla.\underline{u} = 0 \tag{2.5}$$

Initially, the reactor is considered to contain either pure azomethane, or a mixture of azomethane and a diluent, when the gases are assumed to be well-mixed initially. The gas is also assumed to be initially motionless and at a uniform temperature T_0; this is the wall temperature, which remains fixed throughout the course of the reaction. This condition, of course, means that heat will be removed from the system at the wall. It is assumed that the no-slip condition applies at the wall and that there is no flux of any species at the wall. The effects of any heterogeneous reactions at the wall have hence been ignored. The initial and boundary conditions can thus be stated:

$$t = 0: \quad c = c_0;\ T = T_0;\ \underline{u} = 0 \quad \forall \underline{x}$$

$$\text{At the wall: } \underline{n}.\nabla c = \underline{u} = 0;\ \ T = T_0\,, \tag{2.6}$$

where $\underline{n}$ is a unit vector perpendicular to the wall of the vessel. It is worth noting that the above formulation requires no information on heat or mass transfer coefficients.

2.3 Scaling Analysis

2.3.1 Development of Scales

By examination of the governing Eqs. (2.2) – (2.5), it is possible to derive analytical expressions describing the behaviour of certain parameters, for example, the temperature rise due to reaction, and the velocity due to convection. The governing equations are first made dimensionless by introducing the following six dimensionless variables:

$$c' = \frac{c}{c_0};\ T' = \frac{T - T_0}{\Delta T};\ \underline{u}' = \frac{\underline{u}}{U};\ \mathscr{P}' = \frac{\mathscr{P} - \mathscr{P}_0}{\rho_0 U^2};\ \underline{x}' = \frac{\underline{x}}{L} \text{ and } t' = \frac{Ut}{L}\,, \tag{2.7 a – f}$$

where c_0 is the initial concentration of azomethane, L is a characteristic length of the reactor, taken to be the radius in the present work, ΔT is the scale or characteristic value of the temperature rise and likewise U is the characteristic magnitude of the velocity. At this stage the form of the scales for velocity and temperature rise are unknown. Using the variables defined in Eq. (2.7), Eqs. (2.2) – (2.5) become:

$$\frac{\partial c'}{\partial t'} + \underline{u}'.\nabla' c' = \frac{D_C}{UL}\nabla'^2 c' - \frac{k_0 L c_0^{n-1}}{U}\exp\left(\frac{\phi T'}{1+\eta T'}\right)c'^n\,, \tag{2.8}$$

$$\frac{C_V}{C_P}\frac{\partial T'}{\partial t'} + \underline{u}'.\nabla' T' = \frac{\kappa}{UL}\nabla'^2 T' + \frac{q k_0 L c_0^n}{\rho_0 C_P U \Delta T}\exp\left(\frac{\phi T'}{1+\eta T'}\right)c'^n\,, \tag{2.9}$$

$$\frac{\partial \underline{u}'}{\partial t'} + \underline{u}'.\nabla' \underline{u}' = -\nabla' \mathscr{P}' + \frac{\nu}{UL}\nabla^2 \underline{u} - \frac{L\beta \Delta T T'}{U^2}\underline{g}\,, \tag{2.10}$$

$$\nabla'.\underline{u}' = 0\,, \tag{2.11}$$

where k_0 is the rate constant k evaluated at the wall temperature, T_0, ∇' is the dimensionless Laplacian operator and

$$\eta = \frac{\Delta T}{T_0} \text{ and } \phi = \frac{E\Delta T}{RT_0^2}. \tag{2.12 a, b}$$

The transport of heat and mass inside the reactor will be controlled by either diffusive or convective processes, depending on the value of Ra. The magnitudes of the unknown scales will depend therefore on which of these mechanisms is dominant for the conditions in the reactor. These regimes are examined below, in turn, to develop the most appropriate form for the unknown scales.

2.3.1.1 Diffusion dominates transport

For Rayleigh numbers less than ≈ 500 (Tyler, 1966), natural convection will be largely absent, so diffusion will be the dominant mechanism for the transfer of heat and mass. In this case the temperature and concentration fields are approximately spherically symmetric, with the maximum occurring near the centre of the vessel. For these low Rayleigh numbers, Eqs. (2.10) and (2.11) for the conservation of momentum can be neglected, as can the convective terms on the left hand side of Eqs. (2.8) and (2.9). In a diffusive system, the characteristic velocity, U, in Eqs. (2.8) and (2.9) is replaced by the ratio κ / L. A scale (*i.e.* an analytical prediction of a characteristic value) for ΔT can be found by assuming the terms for diffusion and the generation of heat dominate Eq. (2.9). This yields

$$\Delta T \sim \frac{q k_0 L^2 c_0^n}{\rho_0 C_P \kappa}. \tag{2.13}$$

It is useful at this stage to define characteristic timescales for diffusion and reaction as:

$$\tau_{diffusion} = \frac{L^2}{\kappa} \text{ and } \tau_{reaction} = \frac{\rho_0}{k_0 c_0^n}. \tag{2.14 a, b}$$

These definitions can be substituted back into Eq. (2.13), which can be rearranged into dimensionless form giving

$$\gamma \frac{\Delta T}{\Delta T_{ad}} \sim \frac{\tau_{diffusion}}{\tau_{reaction}}, \tag{2.15}$$

where ΔT_{ad} is the adiabatic temperature rise ($= q / C_V$) and γ is the ratio of the specific heats, C_P / C_V.

2.3.1.2 Convection dominates transport

When the Rayleigh number rises above ≈ 500, natural convection becomes significant. The flow induced by the reaction causes a distortion of the spherical symmetry observed when diffusion dominates, and leads to the formation of a hot zone above the centre of the reactor (Cardoso *et al.* 2004*a*, *b*), as shown in Figure 2.1(b). It is assumed that the buoyancy and convective terms dominate the Navier-Stokes equations (2.10); therefore the scale for the velocity can be defined as

$$U \sim [\beta g L \Delta T]^{1/2} . \tag{2.16}$$

Similarly, if it is assumed that the convection and generation terms dominate in the energy balance, Eq. (2.9), the scale for ΔT can be defined as

$$\Delta T \sim \frac{q k_0 c_0^n L}{U \rho_0 C_P} , \tag{2.17}$$

and, if Eq. (2.16) is substituted into this expression, it yields

$$\Delta T \sim \left(\frac{q k_0 c_0^n}{\rho_0 C_P} \right)^{2/3} \left(\frac{L}{\beta g} \right)^{1/3} . \tag{2.18}$$

Equation (2.17) can be rewritten in dimensionless form by defining a timescale for natural convection as $\tau_{convection} = L / U$. Thus,

$$\gamma \frac{\Delta T}{\Delta T_{ad}} \sim \frac{\tau_{convection}}{\tau_{reaction}} . \tag{2.19}$$

This should be compared with Eq. (2.15) for the previous case.

2.3.2 Comparison of Scaling with Experimental Results

The forms of the scales developed in Eqs. (2.15) and (2.19) can be compared with Archer's (1977) measurements of the temperature at the centre of the reactor at the time when the temperature in the vessel was at its maximum. For low Rayleigh numbers the maximum temperature is at the centre of the vessel; however, for high Rayleigh numbers the maximum temperature occurs in the top half of the reactor. For these higher Rayleigh numbers, the temperature at the centre of the reactor was measured when the temperature in the hot zone above the centre of the reactor reached its maximum. The forms of Eqs. (2.15) and (2.19) require values of the exothermicity of the reaction, q, and the specific heats for the contents of the reactor. Archer (1977) measured the exothermicity of the reaction, and found it to be weakly dependent on the pressure, according to

$$q = \frac{0.726}{\mathscr{P}} + 116.5, \tag{2.20}$$

where q is in units of kJ mol^{-1} and $\mathscr{P}$ is in bar. This expression gives values for the heat of reaction which are in good agreement with those found elsewhere in the literature (Gerri and Kaufman, 1965; Rice, 1940). The fact that the exothermicity of the reaction depends on pressure suggests that changing the pressure alters the chemistry. Archer (1977) showed that there was a large number of hydrocarbon products when azomethane decomposes, beyond the methane and ethane mentioned above. Even a slight change in the balance of these products alters the heat of reaction. Nevertheless, over the range of pressures considered in this work, there is very little variation in q. Values of other physical parameters are shown in Table 2.1. These values were again chosen to match those used by Archer (1977) and are in good agreement with literature values.

Table 2.1. Physical parameters as estimated for azomethane, CO_2 and SF_6 by Archer (1977).

T / K	k_T / W m^{-1} K^{-1}	$\mu \times 10^5$ / Pa s	C_V / J mol^{-1} K^{-1}
		Azomethane	
612.2	0.0498	1.70	120.9
616.2	0.0502	1.71	121.3
626.2	0.0515	1.73	122.6
636.2	0.0531	1.75	123.8
646.2	0.0544	1.77	125.1
652.2	0.0552	1.78	125.9
		CO_2	
636.2	0.0431	2.84	39.6
		SF_6	
626.2	0.0353	2.91	129.3
636.2	0.0360	2.95	129.7

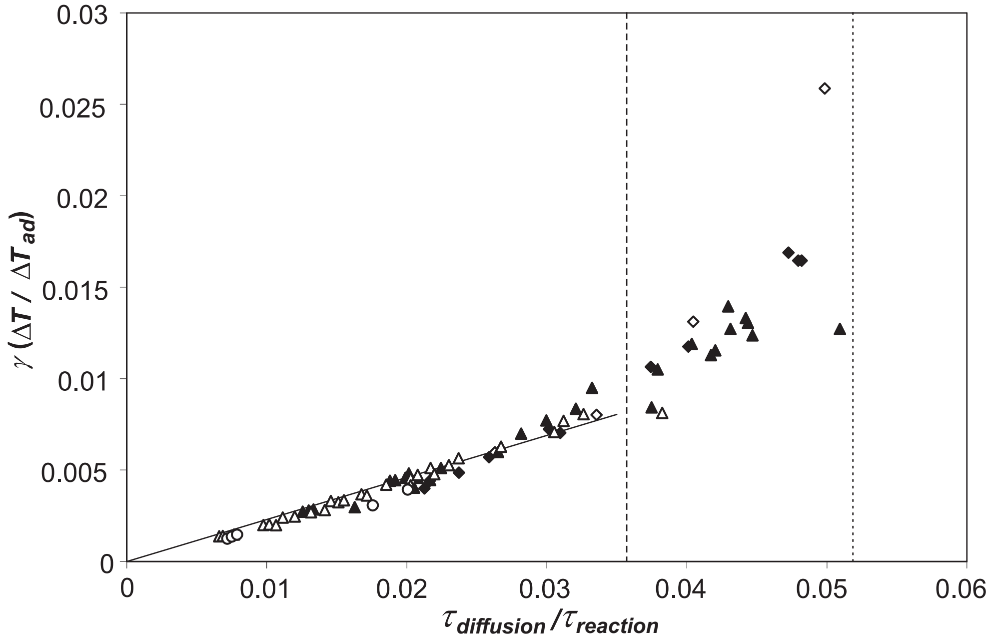

Figure 2.2. Plot of the dimensionless temperature rise at the centre of the reactor against $\tau_{diffusion}$ / $\tau_{reaction}$ for the experimental results of Archer (1977) when diffusion controls transport. Initially, the reactor contained pure azomethane. Results are shown for different values of the wall temperature, T_0. The open diamonds show the results for T_0 = 656.2 K, the filled diamonds show T_0 = 646.2 K, the filled triangles represent T_0 = 636.2 K, the open triangles show T_0 = 626.2 K and the open circles show T_0 = 616.2 K. Also shown are two vertical (dashed) lines representing the approximate transition between slow reaction and explosion, as indicated by Frank-Kamenetskii's (1955) criterion, and a (solid) line representing the scaling result in Eq. (2.23).

Using the physical parameters defined previously, the experimentally measured temperatures can now be compared with the scales developed above. Figure 2.2 shows a plot of the dimensionless temperature rise against $\tau_{diffusion}$ / $\tau_{reaction}$ for Archer's (1977) experiments at low Rayleigh numbers (< 500). According to Eq. (2.15) there should be a linear dependence. It is clear from Figure 2.2 that at low values of $\tau_{diffusion}$ / $\tau_{reaction}$ there is indeed a linear relationship; however, when $\tau_{diffusion}$ / $\tau_{reaction}$ increases above ~ 0.035 there is a clear deviation from linearity. There is therefore a region of slow reaction, with low temperature rises, where the scaling result in Eq. (2.15) is valid; however, beyond $\tau_{diffusion}$ / $\tau_{reaction}$ ~ 0.035, there is a different regime, where the linear form of the scale breaks down. It is interesting to compare the point at which this change in regime occurs in the experimental results in Figure 2.2 with the theoretical prediction of Frank-Kamenetskii (1955), for the transition from a slow reaction to an explosion. Frank-Kamenetskii (1955) showed that this transition depended only on a parameter δ, which is a ratio of the initial rate of heat production by the reaction to the rate of heat loss by conduction. This parameter is defined as

$$\delta = \frac{qEL^2 k_0 c_0^n}{\rho_0 C_P \kappa R T_0^2}. \qquad (2.21)$$

If δ is less than a critical value, δ_{cr}, which was found to be 3.32 for a spherical vessel (Frank-Kamenetskii, 1955), there is a slow reaction, whereas if δ exceeds this critical value there is an explosion. It should be noted that the form of δ defined in Eq. (2.21) is different to the initial definition by Frank-Kamenetskii (1955); it has been modified to take account of the fact that the reaction is not zeroth-order. Equation (2.21) can be rewritten in terms of the timescales defined in Eq. (2.14) as

$$\delta = \frac{qEL^2 k_0 c_0^n}{\rho_0 C_P \kappa R T_0^2} = \frac{E}{RT_0^2}\frac{q}{C_P}\frac{\tau_{diffusion}}{\tau_{reaction}}. \qquad (2.22)$$

Using this definition, and the critical value defined by Frank-Kamenetskii (1955), the value of $\tau_{diffusion} / \tau_{reaction}$ for the transition from slow reaction to explosion can be estimated. Shown in Figure 2.2 are two vertical lines corresponding to the maximum and minimum values of $\tau_{diffusion} / \tau_{reaction}$ for the transition to explosion, based on the physical conditions in Archer's (1977) experiments. Clearly, the region in which δ exceeds the critical value for the onset of explosion corresponds to the change in the experimental results from the linear regime at small $\tau_{diffusion} / \tau_{reaction}$, to the non-linear regime at higher $\tau_{diffusion} / \tau_{reaction}$. The scaling prediction in Eq. (2.15) is therefore valid in the slow reaction regime of the reaction, and breaks down when the transition to thermal explosion approaches. For slow reactions, a numerical factor calculated using the least squares method can be introduced in Eq. (2.15) to give an expression for ΔT in this regime:

$$\gamma \frac{\Delta T}{\Delta T_{ad}} = (0.230 \pm 0.003)\frac{\tau_{diffusion}}{\tau_{reaction}}. \qquad (2.23)$$

The scaling result for the slow reaction regime can be combined with Frank-Kamenetskii's (1955) parameter in Eq. (2.22) to give a condition for the transition from slow reaction to explosion based on a temperature rise. Combining Eqs. (2.22) and (2.23) gives the condition that

$$\frac{E}{RT_0^2}\Delta T < 0.76, \qquad (2.24)$$

for a slow reaction to occur. Taking typical values for the azomethane system considered here, Eq. (2.24) shows that the slow reaction regime occurs for $\Delta T < \sim 13$ K.

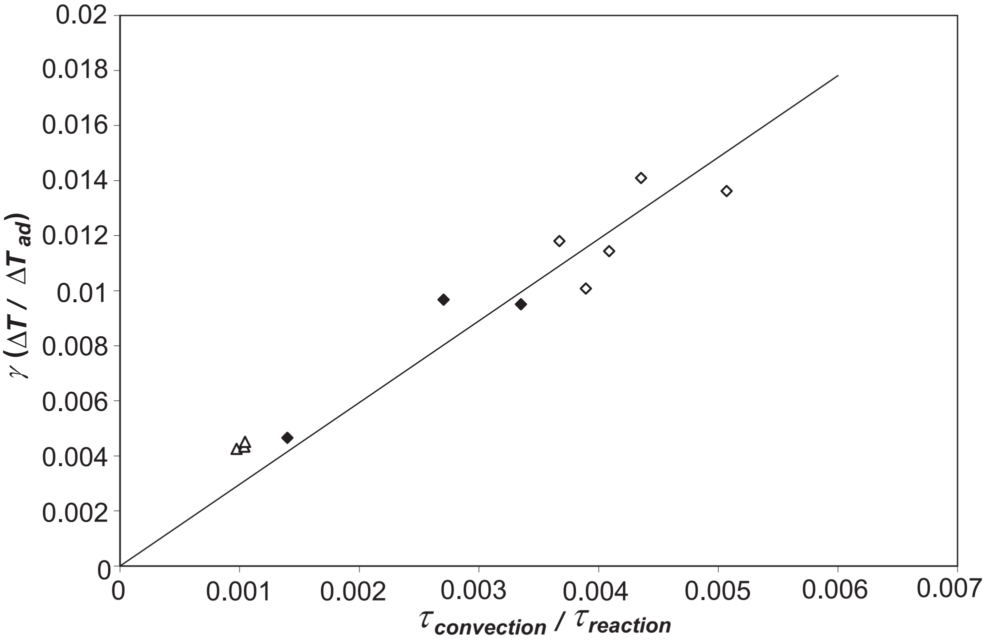

Figure 2.3. Plot of the dimensionless temperature rise at the centre of the reactor against $\tau_{convection} / \tau_{reaction}$ for the experimental results of Archer (1977) when natural convection controls transport. The reactor initially contained azomethane and a diluent. The open triangles correspond to the cases where the initial contents of the reactor were azomethane and CO_2 with $T_0 = 636.2$ K, the filled diamonds represent the cases with azomethane and SF_6 with $T_0 = 636.2$ K and the open diamonds show the cases with azomethane and SF_6 where $T_0 = 626.2$ K. The solid line is Eq. (2.25).

A similar comparison can be made for the experimental results at higher Rayleigh numbers, because Archer (1977) also performed experiments at higher Rayleigh numbers, of ~ 1000 – 2000, *i.e.* when convection becomes significant. At these moderate Rayleigh numbers, diffusion would be expected to still play a role. Figure 2.3 shows the dimensionless temperature rise measured in the reactor plotted against $\tau_{convection} / \tau_{reaction}$; from Eq. (2.19), there should be a linear relationship. Once again there is excellent agreement between the experimental results and the form predicted by scaling. The form of Eq. (2.19) suggests that the experimental measurements should fall on a straight line through the origin in Figure 2.3, and this is indeed the case. As with the diffusive regime, it is possible to include a numerical factor in the expression for the temperature rise. A least squares analysis indicates this can be written as:

$$\gamma \frac{\Delta T}{\Delta T_{ad}} = \left(2.97 \pm 0.12\right) \frac{\tau_{convection}}{\tau_{reaction}}. \qquad (2.25)$$

Clearly Archer’s (1977) experimental measurements agree well with the forms of the analytical scales derived for the cases when diffusion and natural convection, respectively, dominate the transport of heat and mass within the reactor.

2.4 Numerical Modelling

The above comparisons confirm the validity of the analytical scaling analysis. In addition, however, it is desirable to compare the results of numerical simulations with experimental observations. Numerical simulations, of course, can yield a lot more insight into the progress of a reaction inside a vessel. Scaling simply examines characteristic values, whereas simulation can give information on the temporal and spatial development of the temperature, concentration and velocity fields in a reactor. The governing Eqs. (2.2) – (2.6) can be solved numerically for a spherical reactor with a fixed wall temperature. The partial differential equation solver *Fastflo*, which utilises the finite element method, was used for this purpose. An outline of the finite element method is included in the Appendix.

2.4.1 Algorithm

A segregated equation method was used to decouple the governing equations. The equations were solved in their dimensional forms (Eqs. (2.2 – 2.6)). At each time-step, Eq. (2.2) for the conservation of azomethane was solved, by using the velocity and temperature fields at the previous time-step. This newly calculated concentration field was then used to solve the energy Eq. (2.3) for the temperature, using the velocity at the previous time-step. Finally, the momentum and continuity Eqs. (2.4) and (2.5) were solved for the velocity and pressure, using the temperature and concentration at the current time-step.

The coupled momentum and continuity equations have the difficulty that the pressure, $\mathscr{P}$, required in the momentum equation, does not occur explicitly in the continuity equation. Rather, the continuity equation acts as a constraint to the momentum equation, and this constraint determines the pressure. This problem was overcome by employing the Augmented Lagrangian method (CSIRO, 2000), which transforms the continuity equation into $\mathscr{P}_{m,t} - \mathscr{P}_{m-1,t} = -Pen\ \nabla.\underline{u}$, where $\mathscr{P}_{m,t} - \mathscr{P}_{m-1,t}$ is the difference in pressure between consecutive iterations within each timestep, *Pen* is called the penalty parameter, and $\underline{u}$ is the iterative solution for velocity. When the calculation converges, $\mathscr{P}_{m,t} = \mathscr{P}_{m-1,t}$ and continuity is satisfied. Within each time-step, it is necessary to iterate over the momentum and continuity equations until the velocity and pressure converge.

The momentum equations were linearised using Picard's method, *i.e.* a simple successive iteration scheme. A backward difference scheme was used for the time-stepping. The resulting discretised equations are given by:

$$\frac{c_t - c_{t-\Delta t}}{\Delta t} + \underline{u}_{t-\Delta t}.\nabla c_t = D_C \nabla^2 c_t - Z\exp\left(-E/RT_{t-\Delta t}\right)c_t^n\,, \tag{2.26}$$

$$\frac{C_V}{C_P}\frac{T_t - T_{t-\Delta t}}{\Delta t} + \underline{u}_{t-\Delta t}.\nabla T_t = \kappa\nabla^2 T_t + \frac{qZ}{\rho_0 C_P}\exp\left(-E/RT_{t-\Delta t}\right)c_t^n\,, \tag{2.27}$$

$$\frac{\underline{u}_{m,t} - \underline{u}_{t-\Delta t}}{\Delta t} + \underline{u}_{m-1,t}.\nabla\underline{u}_{m,t} = \frac{1}{\rho_0}\left[Pen\,\nabla\left(\nabla.\underline{u}_{m,t}\right) - \nabla\mathscr{P}_{m-1,t}\right] + \nu\,\nabla^2\underline{u}_{m,t} + \underline{g}\left[1 - \beta\left(T_t - T_0\right)\right], \tag{2.28}$$

$$\mathscr{P}_{m,t} = \mathscr{P}_{m-1,t} - Pen\,\nabla.\underline{u}_{m,t}\,, \tag{2.29}$$

where the subscript *m* is the index for iterations of pressure and velocity inside each time-step. Once these equations had been solved, the cycle was repeated until the concentration, temperature and velocity fields converged. The time was then stepped forward and the same series of calculations was performed at the next time-step. The value of the time-step, Δt, used in the calculations was typically fixed at a value of 0.01 s, although this value could be changed to aid convergence. The value of *Pen* was taken as 10 for each run. This value was chosen by trial and error. If the parameter is too small convergence is slow; however, if it is too high, the system can become unstable. With this time-step and penalty parameter, convergence of the coupled momentum and continuity equations was obtained in ~ 5 iterations. It should also be noted that in the course of solving Eqs. (2.26) – (2.29), the physical parameters were assumed to remain constant at their initial values, *i.e.* no account was taken of the effect of temperature and composition on these parameters.

Velocity and pressure were calculated iteratively until two convergence criteria were met. The first convergence criterion is expressed in terms of the difference between the velocities in two consecutive iterations (normalised by the current solution), which should be smaller than a specified tolerance ε_1:

$$\frac{\sum\left|\underline{u}_{m,t}-\underline{u}_{m-1,t}\right|}{\sum\left|\underline{u}_{m,t}\right|}<\varepsilon_1, \tag{2.30}$$

where Σ represents the sum over all nodes. The value of ε_1 was typically set as 0.01. This criterion ensured that the Picard iteration had converged before proceeding to the next time-step. The second convergence criterion

$$\nabla.\underline{u}<\varepsilon_2 \tag{2.31}$$

concerns continuity (and hence pressure). A typical value of ε_2 used in the simulations is 1×10^{-5} s^{-1}.

The discretised equations were solved for a semi-circular mesh of triangular elements. Generally, the mesh contained ~ 2000 corner nodes, arranged in six-noded quadratic elements, but this number could be varied to achieve convergence. The equations for conservation of mass, energy and momentum were solved on this mesh. The equation for pressure was solved on a linear mesh of three-noded elements and interpolated onto the quadratic mesh. This was done to prevent chessboard instabilities in the pressure, which can occur, due to an over-constrained problem, if the continuity equation is solved at full accuracy. An axisymmetric condition was applied to the vertical axis of the reactor. This is a reasonable approximation, as indicated by the temperature measurements made by Melvin (1969) and shown in Figure 1.2. The distributions shown by the interferograms are approximately symmetric. The interferograms presented by Mitachi and Igarashi (1987) for a horizontal cylinder also show a large degree of symmetry about the vertical axis of the reactor. Boundary conditions of a fixed temperature, zero velocity and zero flux were applied to the curved boundary of the mesh, corresponding to the wall of the reactor.

2.4.2 Physical Parameters for Comparison with Experiments

For the numerical simulations, the radius of the reactor was taken to be L = 0.064 m, corresponding to a reactor with a volume of 1100 dm^3, as used in Archer's (1977) experiments. The kinetics of the reaction have been discussed above; the reaction order was taken as 1.4 and the pre-exponential factor and activation energy were taken to be those derived by Archer (1977) in Eq. (2.1). The exothermicity of the reaction was calculated using Eq. (2.20). Various other physical parameters required estimation. These estimates were based on the initial conditions in the reactor and were assumed to remain constant. This assumption is made because the reaction only proceeds to ~ 5% completion in the time simulated (generally 10 s). The specific heat capacities were calculated using a simple weighted average of the components present. The thermal conductivity, and hence thermal diffusivity, of the gas mixture was calculated using Wassiljewa's equation with Mason and Saxena's modification (Reid *et al.*, 1987*b*). The viscosity of the gas mixture was estimated using Wilke's method (Reid *et al.*, 1987*a*). The molecular diffusivity of azomethane in the gas mixture was calculated using the empirical correlation of Fuller *et al.* (1966, 1969), as suggested by Cussler (1984). Table 2.2 lists the physical parameters used in the numerical simulations. In addition, Table 2.2 shows both the simulated temperature rise at the centre of the reactor when the temperature along the vertical axis of the reactor reaches a maximum and the Rayleigh number, based on such a temperature rise at the centre.

Table 2.2. Details of the conditions in the reactor used in the numerical simulations. Also shown are the simulated temperature rise at the centre of the reactor and the corresponding Rayleigh number.

T_0 / K	$\mathscr{P}_{azomethane}$ / Pa	$\mathscr{P}_{CO2}$ / Pa	$\mathscr{P}_{SF6}$ / Pa	$\kappa \times 10^4$ / $m^2\ s^{-1}$	$\mu \times 10^5$ / Pa s	$D_A \times 10^4$ / $m^2\ s^{-1}$	ΔT_{centre} / K	Ra
636.2	1333	0	0	16.0	1.75	19.4	6.2	13
636.2	683	8626	0	4.62	2.72	3.76	1.7	43
636.2	1973	0	0	10.8	1.75	13.1	11.7	54
636.2	2266	0	0	9.38	1.75	11.4	15.8	97
636.2	1029	13159	0	3.03	2.72	2.47	3.2	190
636.2	1733	0	4666	2.47	2.71	3.17	7.8	701
636.2	1733	20932	0	1.89	2.71	1.54	6.1	936
636.2	1760	0	6786	1.80	2.77	2.37	7.0	1173
626.2	4960	0	4960	1.71	2.44	1.99	15.3	2861
636.2	2000	0	13332	0.964	2.84	1.32	6.0	3451
636.2	2000	0	19998	0.658	2.88	0.922	5.0	6130
636.2	3720	0	14399	0.847	2.77	1.12	11.5	8670
636.2	4333	0	12346	0.944	2.72	1.22	15.1	9223
636.2	2066	0	26664	0.499	2.89	0.706	4.4	9461
636.2	3720	0	17332	0.718	2.80	0.964	10.5	10967
636.2	4000	0	15999	0.765	2.78	1.01	11.9	10992
636.2	4666	0	13332	0.875	2.72	1.13	16.2	11492
636.2	5333	0	13332	0.854	2.70	1.09	20.1	15053
636.2	6000	0	13999	0.803	2.68	1.01	25.8	21900

2.4.3 Numerical Results

Numerical simulations were performed for the cases described in Table 2.2, with Rayleigh numbers in the range 13 – 21900. As expected, the fields for the temperature and concentration of azomethane changed as *Ra* increased. Figure 2.4 shows the temporal evolution of the temperature and concentration fields within the reactor at three different Rayleigh numbers, which are typical of the different types of behaviour seen when *Ra* increases. Figure 2.4(a) corresponds to *Ra* = 43 in Table 2.2. This is in the region where natural convection due to the heating effect of the reaction is very weak. Clearly, the temperature field shows the spherical symmetry expected in a system where diffusion is the dominant means of heat transfer. In addition, the radial temperature profile can be shown to be parabolic, as would be expected for a purely diffusive system. It should be noted that the temperature rise in this case is very small (~ 2 K) due to the low initial concentration of azomethane, and hence the low rate of reaction. The maximum temperature is reached relatively quickly, after ~ 4 s; the vessel subsequently cools slowly. Inspection of the evolution of the concentration field in Figure 2.4(a) shows that over the time period considered, the concentration of azomethane remains approximately spatially uniform. The decrease in azomethane concentration is very small (~ 0.01 mol m^{-3}) over the 10 s period of the simulation.

Figure 2.4(b) shows the development for the case with *Ra* = 1173 in Table 2.2, in which natural convection is starting to play a role. The spherical symmetry evident in the temperature field at lower *Ra* has been disrupted by the flow due to natural convection. The toroidal vortex shown in Figure 2.1(a) develops, causing the hottest point in the reactor to shift above the horizontal axis. As a result, the temperature profile along the vertical axis of the reactor becomes skewed. Once again, the concentration field remains virtually spatially uniform over the time period considered, and shows only a very small temporal decrease. There is some slight spatial inhomogeneity evident in the concentration of azomethane in Figure 2.4(b) at *t* = 4.8 – 5.6 s. The concentration of azomethane in the top half of the reactor is marginally lower than in the surrounding fluid. This is unsurprising, given that this region corresponds to the hottest point in the reactor, and thus would have the largest rate of destruction of azomethane. This effect is small, however, due to the relatively low maximum temperature rise.

As the temperature rise due to the reaction increases, natural convection becomes more intense (*i.e. Ra* increases) and the temperature field becomes much more skewed as a result. Under certain conditions, a distinct temperature peak emerges near the top of the reactor. This is shown in Figure 2.4(c), which corresponds to Ra = 21900 in Table 2.2. The temperature peak, confined to the very top of the vessel due to the intensity of the natural convection, can very clearly be identified in Figure 2.4(c). It is also evident that the temperature shows a very high degree of stratification, which is typical of a situation where natural convection is significant. The maximum temperature rise in this case is very large (~250 K); however, this large increase in temperature is confined to a very small region of the reactor. The temperature distribution is therefore similar in form to a planar stabilised flame front. In the bottom section of the vessel, the gas remains relatively cool and, in fact, the rises in temperature are an order of magnitude lower than those in the very hot region at the top of the reactor. The development of the concentration field is also far more complex in this case. It is clear from Figure 2.4(c) that as the hot zone at the top of the reactor develops (at $t \sim 5$ s), the azomethane in this hot region is depleted very rapidly, and in fact decreases to virtually zero. As the reaction proceeds further, this depleted region grows, due to the influence of the toroidal flow pattern (Figure 2.1(a)), and forms a horse-shoe shaped region in Figure 2.4(c) as the gas, which has been depleted of azomethane, flows downwards along the cool walls of the reactor. Meanwhile, at the bottom of the reactor the gas remains relatively cool, and hence is still somewhat rich in azomethane. This, of course, means that there are very large spatial variations in the concentration of azomethane inside the reactor; this is in contrast to the other two cases shown in Figure 2.4, when the concentration remains approximately spatially uniform.

The three types of behaviour described above are in good qualitative agreement with the work of Archer (1977), whose experiments showed similar trends, *i.e.* a spherically symmetric temperature profile was observed at low *Ra*, a skewed temperature profile, along the vertical axis of the reactor, at intermediate *Ra* and a peaked profile at high *Ra*. This qualitative agreement is encouraging. Quantitative agreement was also sought, and this is now described below.

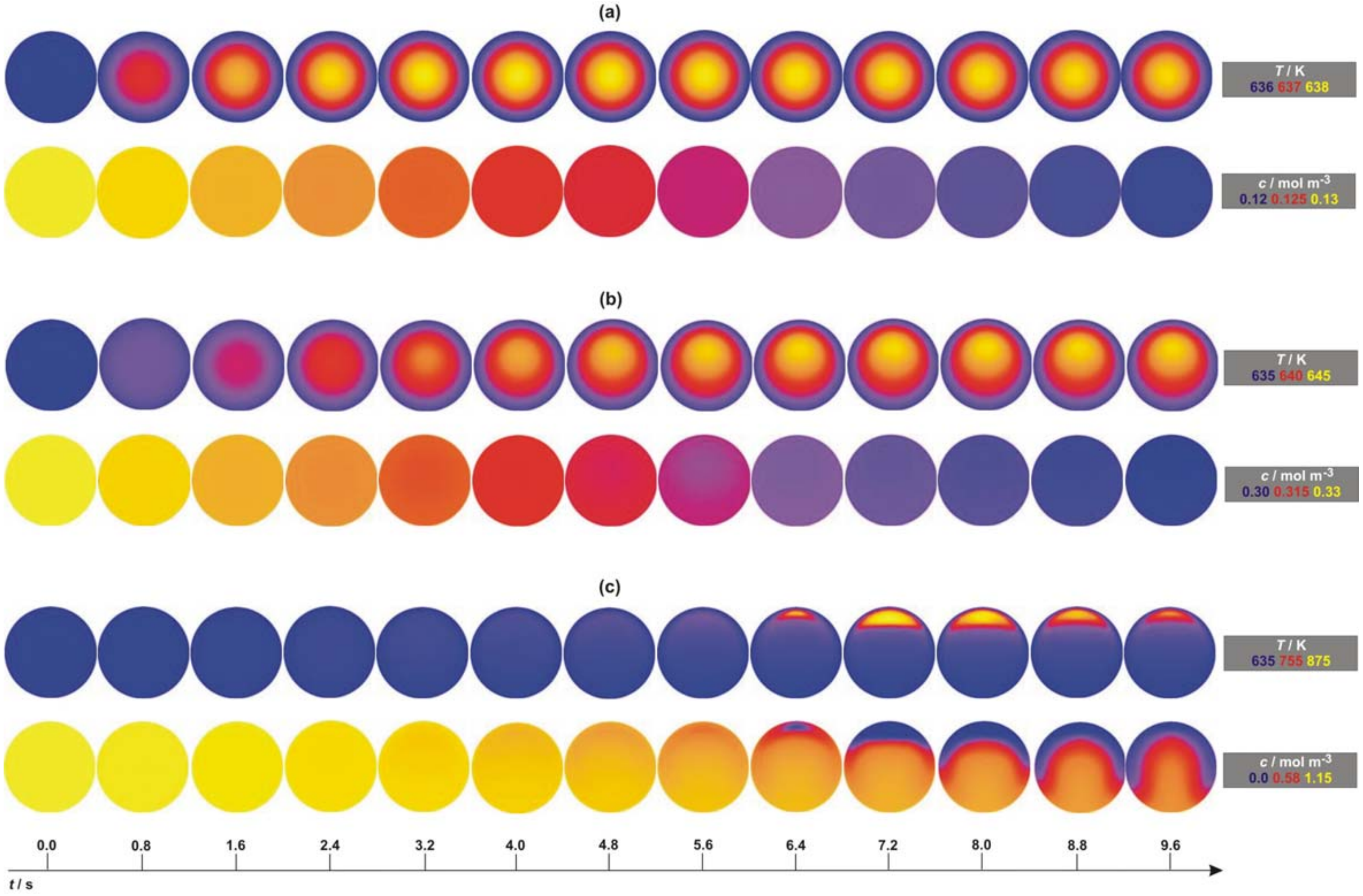

Figure 2.4. Evolution of the temperature field (top) and concentration (of azomethane) field (bottom) over the period $t = 0 – 9.6$ s. The frames occur at regular intervals of 0.8 s. Three cases are shown, corresponding to different values of *Ra*. The details of the cases considered are given in Table 2.2, where (a) shows the $Ra = 43$ case, (b) shows the $Ra = 1173$ case and (c) shows the $Ra = 21900$ case. The temperature and concentration scales appear to the right and it should be noted that these are different for each case presented.

2.4.4 Comparison of experimental and numerical results

Simulations were performed for the cases with *Ra* = 13, 43, 54, 97 and 190 in Table 2.2. The simulated temperature rises at the centre of the reactor were then compared with the experimental results in Figure 2.2.

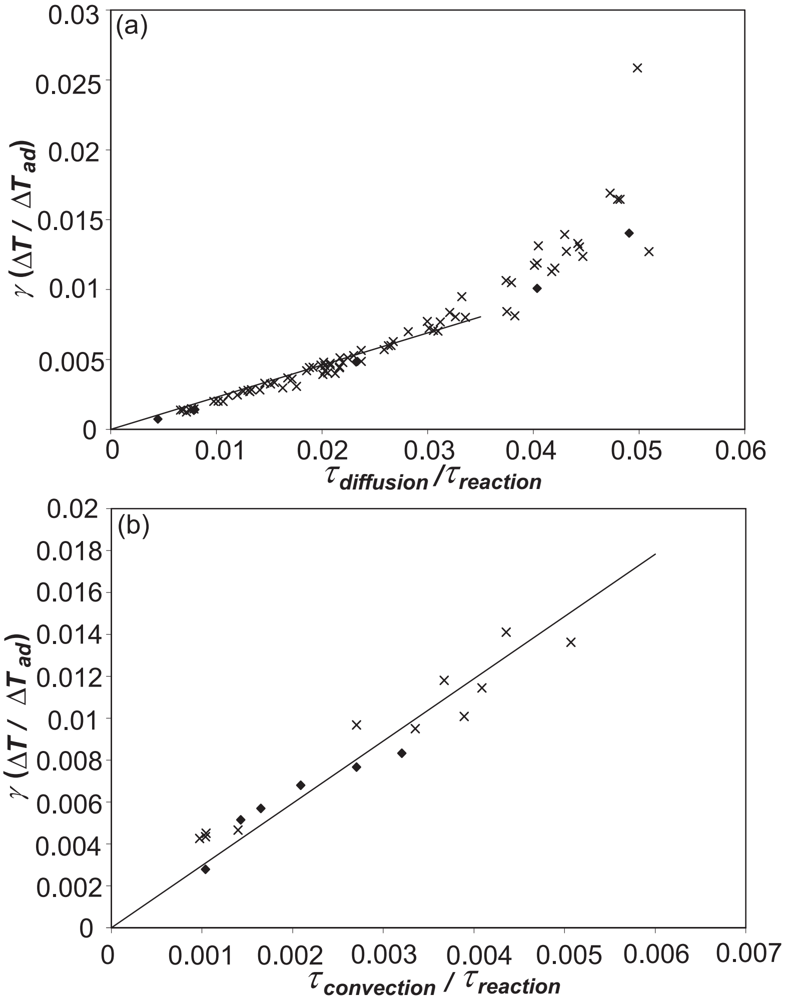

Figure 2.5. (a) Plot of the dimensionless temperature rise at the centre of the reactor against $\tau_{diffusion}$ / $\tau_{reaction}$ for the experimental results of Archer (1977) when diffusion controls transport and the numerical results for the cases with *Ra* = 13, 43, 54, 97 and 190 in Table 2.2. The crosses represent the experimental results and the filled diamonds show the results from the simulations. The line represents Eq. (2.23). (b) Plot of the dimensionless temperature rise at the centre of the reactor against $\tau_{convection}$ / $\tau_{reaction}$ for the experimental results of Archer (1977) when natural convection controls transport and the numerical results for the cases with *Ra* = 701, 936, 1173, 3451, 6130 and 9461 in Table 2.2. The symbols are the same as in (a) and the line corresponds to Eq. (2.25)

Shown in Figure 2.5(a) are the experimental results in Figure 2.2 for the diffusion-controlled regime, as well as a line representing the scaling result in Eq. (2.23). Also plotted are the results of the simulated cases mentioned above. There is clearly excellent agreement between the numerical simulations and both the experimental measurements, and the scaling analysis. A similar comparison is made for the case when natural convection is important in Figure 2.5(b). In this case simulations were performed for $Ra = 701, 936, 1173, 3451, 6130$ and 9461; the results of these simulations appear in Figure 2.5(b) along with the experimental measurements and scaling prediction (Eq. (2.25)). As was the case for the diffusive regime, the agreement is excellent.

In addition to comparing measured temperatures at the centre of the reactor with those found by simulation, it is also possible to compare the computed shapes of the temperature profiles in the reactor with those measured experimentally. As discussed above, when natural convection becomes vigorous, the maximum temperature in the vessel is found in the top half of the reactor. How far above the centre-line the maximum temperature occurs depends on the nature of the flow. Archer (1977) (using very fine thermocouples) measured the location of the maximum temperature along the vertical axis of the reactor and plotted this against the Rayleigh number, calculated using the temperature rise measured at the centre of the reactor at the same time as the maximum temperature along the vertical axis was observed. These measurements are reproduced in Figure 2.6.

Initially, for $Ra < 100$, the maximum temperature occurs very close to the centre of the reactor. When Ra increases beyond ~ 100, the position of the maximum temperature shifts upwards in the reactor. When $Ra \sim 2000$, the maximum temperature is approximately halfway between the centre of the reactor and the wall at the top of the vessel. For further increases of Ra, the position of the maximum temperature rises in the reactor. Above $Ra \sim 10^4$, the location of the maximum temperature no longer moves, but remains at ~ 0.8 L above the centre of the reactor. This upper limit is caused by the boundary layer at the wall, resulting from the wall being maintained at a lower temperature than the reactor's contents. Simulations of the cases shown in Table 2.2 were performed and the position of the maximum temperature for each established. These results are also plotted in Figure 2.6, and the line for the best fit has been drawn through them. There is clearly very good agreement between the results of the simulations and Archer's (1977) measurements. At low Ra (< 2000) the agreement is excellent, and at higher Ra, although there is more of a discrepancy, the agreement is still very good, with the position of the final asymptote agreeing very well with the experimental results.

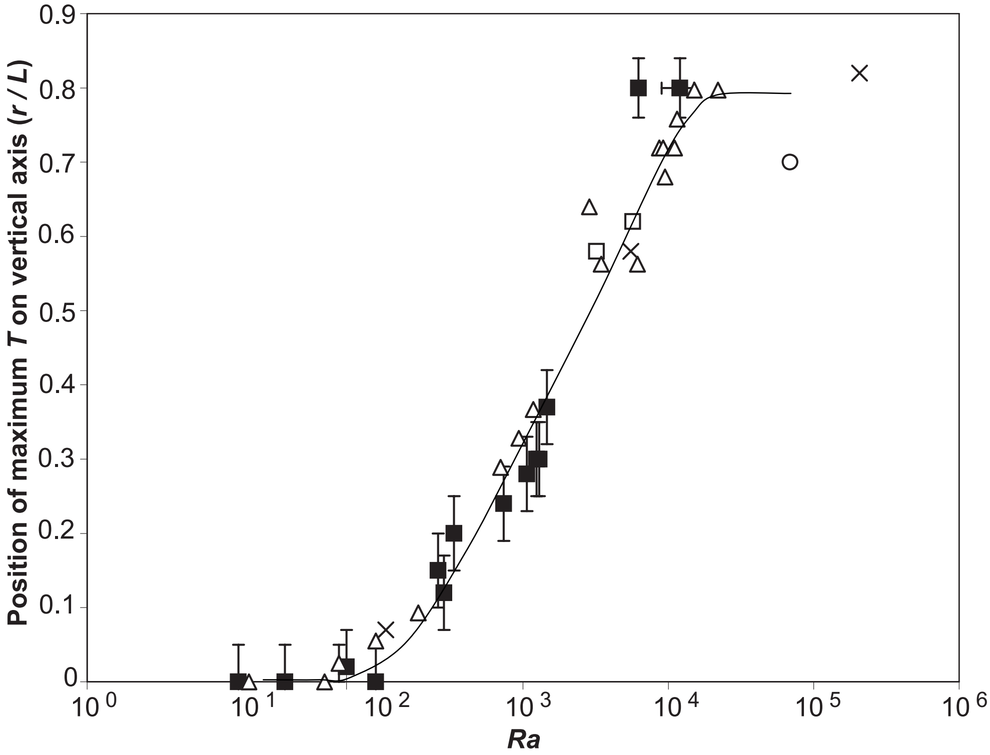

Figure 2.6. Plot of the dimensionless position of the maximum temperature on the vertical axis of the reactor, for the thermal decomposition of azomethane. The experimental results of Archer (1977) are shown (filled squares), as are the results of the numerical simulations (open triangles). The line is a best fit through the numerical results. Also shown are the results of previous numerical studies (Mitachi *et al.*, 1986; Mitachi and Igarashi, 1987; Jones, 1974) for a zeroth-order reaction occurring in a horizontal cylinder. These are the cross marks, the open circles and the open squares, respectively.

For interest, the results of other numerical studies, but of a zeroth-order reaction occurring in a horizontal cylinder (Jones, 1974; Mitachi *et al.*, 1986; Mitachi and Igarashi, 1987) have also been included. Because these studies consider a zeroth-order reaction, the temperature profiles described in Figure 2.6 are the steady-state profiles. Although the geometry of the reactors is different, qualitatively the flow patterns in each in a circular cross-section through the vertical axis are similar. These numerical results are also in good agreement with the experimental observations of Archer (1977) and the simulations described in this work, both for a spherical reactor. This is unsurprising, because at low values of *Ra*, the concentration of azomethane only decreases very slightly during the reaction, so it remains approximately spatially uniform, as shown in Figure 2.4(a) and (b). This means that there is very little spatial variation of reaction rate due to concentration effects, so in that sense the reaction is behaving as if it were zeroth-order. However, at high values of *Ra*, the numerical results for reaction in a cylinder move to the final asymptote of the position of the maximum rather gradually, whereas when azomethane reacts, this transition is more abrupt. The higher temperature rises at higher *Ra* result in the azomethane being depleted more rapidly in some parts of the reactor (Figure 2.4 (c)). This spatial variation is responsible for the deviation from the zeroth-order behaviour.

The three distinct regimes in Figure 2.6 correspond to the cases shown in Figure 2.4. There are the low and high *Ra* regimes where the position of the maximum temperature does not vary much when *Ra* is changed; also there is the intermediate regime where the position of the maximum temperature is highly dependent on *Ra*. The temperature profile along the vertical axis of the reactor at the time when the maximum temperature occurs is plotted in Figure 2.7 for a case in each of the three regimes discussed above. In fact, the cases presented in Figure 2.7 are the same as those considered in Figure 2.4.

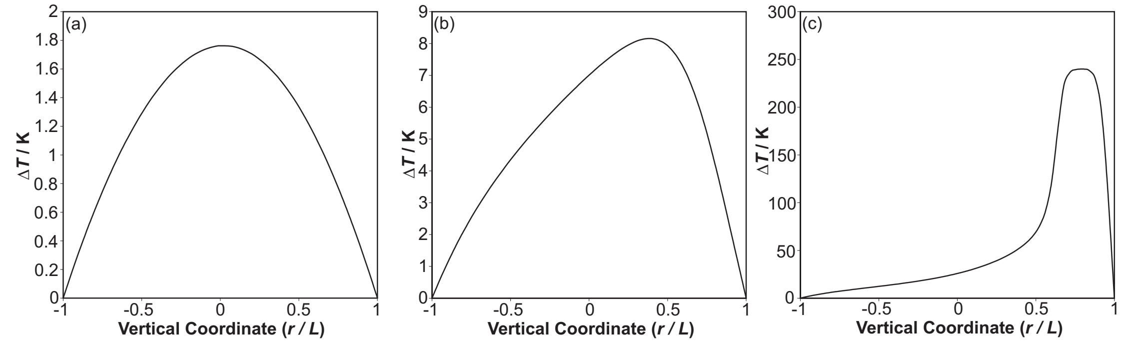

Figure 2.7. (a) Approximately symmetric temperature profile, derived through simulation, along the vertical axis of the reactor for a low *Ra*. The system considered is for *Ra* = 43 in Table 2.2. (b) Skewed temperature profile, for intermediate *Ra*, showing the maximum temperature occurring above the centre of the reactor. Here, *Ra* = 1173. (c) Peaked profile, characteristic of a large *Ra* = 21900.

As mentioned above, these three shapes for the temperature distribution were observed experimentally (Archer, 1977), as well as in the simulations. For low Rayleigh numbers (< ~ 200) the temperature distribution is approximately symmetric, as shown in Figure 2.7(a). This distribution is approximately parabolic, as described by Frank-Kamenetskii (1955). For the intermediate case ($200 < Ra < 10^4$), natural convection distorts the symmetry of the temperature distribution. Figure 2.7(b) shows a typical distribution in this region. The profile is skewed, with the highest temperature occurring above the centre of the reactor. The higher the Rayleigh number, the more skewed the profile. When *Ra* becomes sufficiently large, the hottest point in the reactor stops moving upwards. This is the third regime in Figure 2.6, when, under certain conditions, a sharply peaked profile develops, as shown in Figure

2.7(c). This type of profile typically, but not necessarily, emerges for *Ra* > 10^4. The shape of the temperature distribution in the bottom half of the reactor remains much the same as in the previous two cases. The temperature rise at the peak in Figure 2.7(c) is high (~ 250 K), because of the self-accelerating nature of the reaction in this part of the reactor. As mentioned above, the temperature profile in Figure 2.7(c) is reminiscent of what would be observed in a stabilised flame front. Archer (1977) observed experimentally that in virtually every case of such a peaked profile, the system proceeded to explosion. This effect was not observed in the simulations. The high temperature rises in the peak at the top of the vessel mean that the Boussinesq approximation (of constant density), and indeed other approximations (such as constant physical parameters) used in the numerical scheme described above, begin to break down. In fact, in the majority of the vessel the ratio $\Delta T / T_0$ remains below 0.1, which is an acceptable level for applying the Boussinesq approximation. It is only in the very high temperature region in the top of the reactor, where $\Delta T / T_0 \sim 0.4$, that the approximation breaks down. This must be borne in mind when examining the results; however, the simulations do at least give a good qualitative insight into the behaviour of the reaction at these high temperatures. The transition to explosion, observed experimentally by Archer (1977), has not been considered further in this work.

As well as studying the effect of increasing *Ra* on the position of the maximum temperature within the reactor, Archer (1977) also examined the ratio of the temperature rises at different points along the vertical axis of the reactor. This gives a measure of the asymmetry of the temperature profile. Plotted in Figure 2.8 are measurements expressed as ratios of the temperature rise at: (a) a distance 0.811 L above the centre of the reactor to the temperature rise at the centre, and (b) a distance of 0.811 L below the centre of the reactor to the temperature rise at the centre. Once again, these ratios were calculated from the measured temperature profile at the time when the maximum temperature occurred in the reactor. The results of the numerical simulations shown in Table 2.2 are also plotted, with the best fit line drawn. The numerical studies for a horizontal cylinder (Jones, 1974; Mitachi *et al.*, 1986; Mitachi and Igarashi, 1987) have also been included, where in these cases the temperature ratios were based on the steady-state temperature distribution.

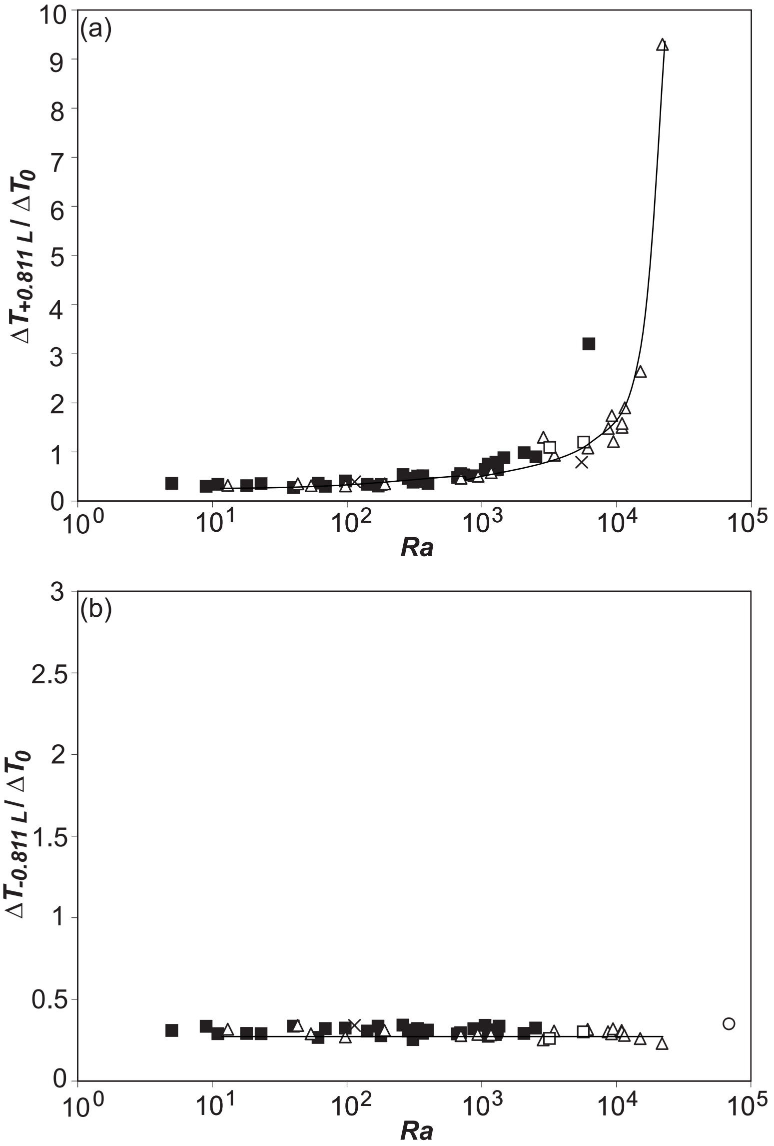

Figure 2.8. (a) Ratio of the temperature rise at 0.811 *L* above the centre of the spherical reactor to the temperature rise at the centre plotted against *Ra*. The experimental measurements of Archer (1977) are shown, as are the results of numerical simulations in Table 2.2. The line is drawn through the results of these simulations. Also shown are the results of previous numerical studies for a zeroth-order reaction occurring in a horizontal cylinder. (b) Ratio of the temperature rise at 0.811 *L* below the centre of the reactor to the temperature rise at the centre plotted against *Ra*. In both cases, the symbols are the same as for Figure 2.6.

Figure 2.8(a) shows that for low *Ra* the ratio of the temperature near the top of the reactor and at the centre is ~ 0.3. This is the value expected for an approximately parabolic distribution, as in Figure 2.7(a). When *Ra* increases above ~ 1000, the ratio begins to increase. There is good agreement between the experimental and numerical results in this region. Once *Ra* increases beyond ~ 2000 the temperature ratio increases more rapidly above unity, until for $Ra > 10^4$ the peaked profile in Figure 2.7(c) emerges, so the temperature near the top of the reactor is significantly larger than that at the centre of the reactor. Figure 2.8(a) shows this transition in both the experimental and numerical results. In fact, there is good agreement between the shapes of the experimental and numerical curves. Figure 2.8(b) shows a similar comparison for the bottom half of the reactor. It is immediately noticeable that the ratio of the temperature rise at 0.811 *L* below the centre of the reactor to the temperature rise at the centre of the reactor is independent of the Rayleigh number. Both experiments and numerics indicate that this ratio is constant at ~ 0.3. This indicates that the shape of the temperature profile in the bottom half of the reactor is largely independent of the intensity of the flow due to natural convection.

2.4.5 Comparisons for 2 NO + O_2 → 2 NO_2

Figure 2.8 gives an indication of how the temperature profile varies with *Ra*, and shows that the numerical simulations are a good representation of the temperatures measured in a spherical reactor. Unfortunately, no direct comparison can be made between the experimentally measured temperature profiles and those produced by simulation for the decomposition of azomethane, due to insufficient experimental measurements being available. However, Tyler and co-workers (Ashmore *et al.*, 1967; Tyler, 1966) have presented an experimentally measured temperature profile for the different reaction:

$$2\mathrm{NO} + \mathrm{O_2} \rightarrow 2\mathrm{NO_2}, \tag{2.32}$$

occurring in a spherical vessel with nitrogen as diluent. This reaction can be simulated, and the computed temperature profiles can be compared with the experimental results. The physical parameters were estimated using the methods described previously and the kinetics of the reaction are well established (Baulch *et al.*, 1973); these values appear in Table 2.3. It will be noticed that the rate constant has a pre-exponential factor, *Z*, which is independent of temperature, but a negative activation energy.

Figure 2.9 shows the experimentally measured temperature profile 30 s after the commencement of reaction. This corresponds to the time at which Tyler (1966) and Ashmore *et al.* (1967) made their measurements. They describe the temperature increasing rapidly initially for ~ 5 s, before cooling down slowly. This qualitative description of the initial stages of the reaction matches what was found numerically.

The situation shown in Figure 2.9 represents a snapshot of the cooling period and corresponds to *Ra* ~ 8800. Rayleigh numbers of this magnitude result in a skewed temperature profile.

Table 2.3. Physical parameters used for the simulation of the reaction between nitric oxide and oxygen, the results of which appear in Figure 2.9.

parameter	estimate	units
C_V	790 ± 40	J kg^{-1} K^{-1}
C_P	1100 ± 50	J kg^{-1} K^{-1}
q	113800 ± 1200	J mol^{-1}
Z	0.0024 ± 0.0005	m^6 mol^{-2} s^{-1}
E	-4380 ± 840	J mol^{-1}
κ	$(9.50 \pm 1.43) \times 10^{-5}$	m^2 s^{-1}
μ	$(2.30 \pm 0.35) \times 10^{-5}$	Pa s
$D_{NO,\ mixture}$	$(1.10 \pm 0.22) \times 10^{-4}$	m^2 s^{-1}
$D_{O2,\ mixture}$	$(1.05 \pm 0.21) \times 10^{-4}$	m^2 s^{-1}

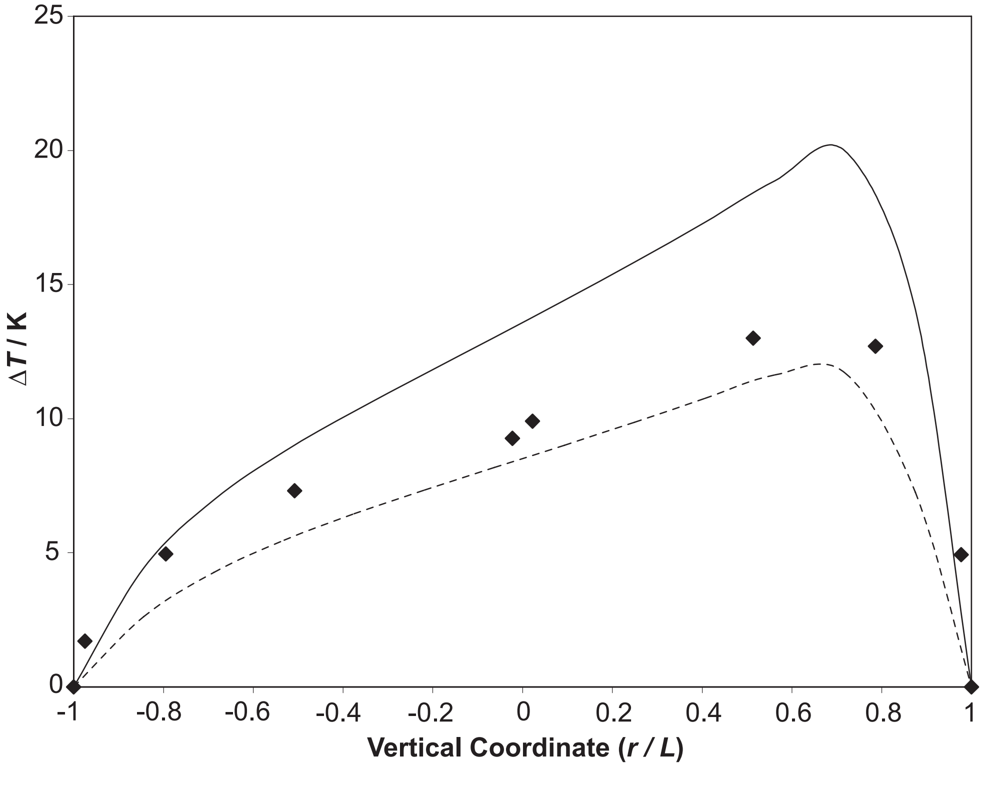

Figure 2.9. Comparison of the temperature profile measured by Tyler (1966), 30 s after the commencement of the reaction between nitric oxide and oxygen in the presence of nitrogen, with the results of numerical simulation. The reaction occurs in a spherical vessel (volume 1100 dm^3), with the wall held at 343 K. There was initially 9330 Pa of NO, 4665 Pa of O_2 and 12662 Pa of N_2. The closed diamonds are the experimental measurements. The lines show the maximum and minimum profiles calculated numerically, based on the errors in the physical parameters.

Comparison of the profiles in Figure 2.7(b) and Figure 2.9 shows the temperature distribution becoming more skewed as *Ra* increases. Also shown are the profiles of the maximum and minimum values found through simulation. These profiles were produced by taking the uncertainties in the estimates of the various physical parameters and the kinetics of the reaction into account (Table 2.3). There is clearly excellent agreement between the experimental and numerical profiles. The shape of the profile achieved through simulation is very similar to that observed experimentally, with the position of the maximum temperature being the same in both cases. The quantitative agreement between the numerical and experimental results is also very good. The experimental points lie between the maximum and minimum curves produced by simulation.

In addition to presenting the measured profile described above, Ashmore *et al.* (1967) also compared the temperature rise measured at the centre of the reactor, with that predicted by Frank-Kamenetskii (1955) for a purely conductive system, over a range of Rayleigh numbers. Frank-Kamenetskii showed that for a slow reaction below the explosive limit, the temperature rise at the centre of the reactor only depends on the value of the parameter δ. The temperature rises corresponding to specific values of δ were calculated by solving the steady state energy balance (as in Eq. (2.9)) and were tabulated by Frank-Kamenetskii (1955). In the work of Ashmore *et al.* (1967), the Frank-Kamenetskii temperature rise was normalised by the observed temperature rise, and plotted against log *Ra*. The plot presented by Ashmore *et al.* (1967) showed data for two different reaction schemes occurring in a spherical reactor with a fixed wall temperature: (i) the reaction between nitric oxide and oxygen (Eq. (2.32)) in the presence of various diluents, and (ii) the reaction between hydrogen and chlorine. That plot is reproduced in Figure 2.10. It should be noted that in the original plot (Ashmore *et al.*, 1967), *Ra* was calculated using the Frank-Kamenetskii temperature rise; however, *Ra* in Figure 2.10 has instead been calculated using the observed temperature rise at the centre of the reactor, at the time when the maximum temperature occurs in the vessel.

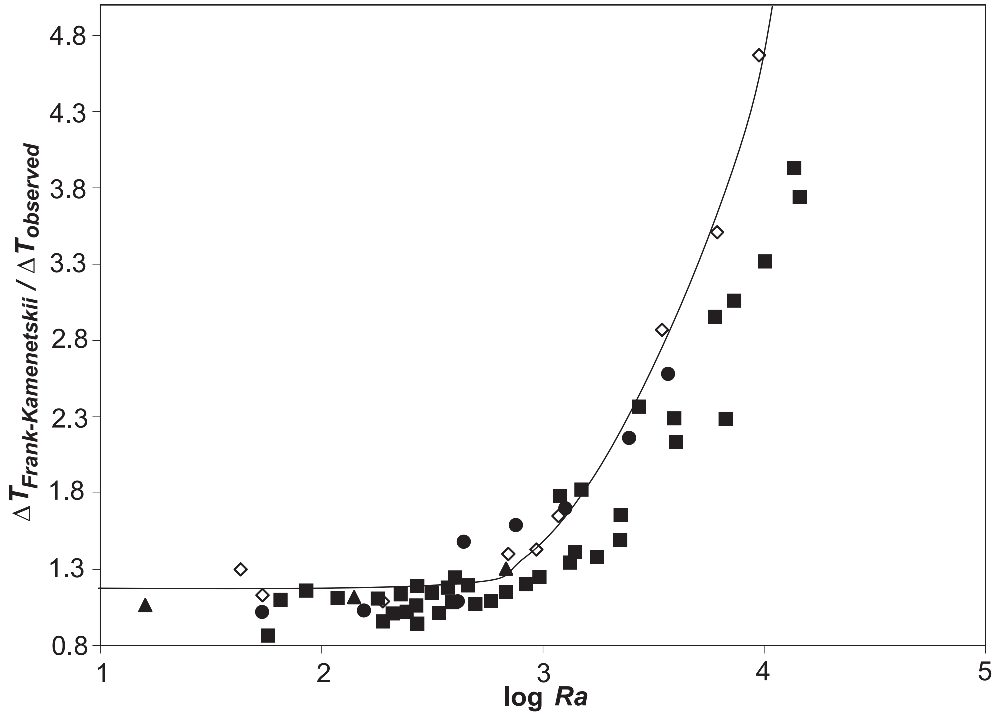

Figure 2.10. The ratio of the temperature rise in a purely conductive system to the observed temperature rise plotted against log *Ra*. The experimental results of Ashmore *et al.* (1967) for two different exothermic reactions (NO with O_2 and H_2 with Cl_2) occurring in a spherical reactor are shown, as are the experimental results of Gerri and Kaufman (1965) for the decomposition of azomethane. The results of numerical simulations for the thermal decomposition of azomethane are shown, and the best fit line is drawn through them. The filled squares are the experimental measurements for NO/O_2, the filled triangles are the measurements for H_2/Cl_2, the filled circles are measurements for the decomposition of azomethane and the open diamonds are the results of the simulations for azomethane.

Figure 2.10 very clearly shows the transition from diffusive control of transport, to a system where natural convection is dominant. This occurs at $Ra \sim 500$. Ashmore *et al*. (1967) also showed that the experimental results of Gerri and Kaufman (1965) for the thermal decomposition of azomethane followed the same trend. These points are shown in Figure 2.10, as well as the results of the numerical simulations in the present work described in Table 2.2. The values of the Frank-Kamenetskii temperature rise for the numerical cases were calculated by interpolating between the tabulated values presented by Frank-Kamenetskii (1955). There is good agreement between the results of the numerical simulations and the experimental studies of the various reactions. As well as comparing the numerics with these experimental results, it is also possible to compare the experiments with the scaling results described in section 2.3. The ordinate of Figure 2.10 compares the temperature rise for a purely conductive system with the actual temperature increase. At low *Ra*, when diffusion dominates transport, this ratio should be ~ 1. For higher Rayleigh numbers, when natural convection dominates transport, the scaling results, derived in Eqs. (2.23) and (2.25), suggest that:

$$\frac{\Delta T_{diffusion}}{\Delta T_{convection}} = \frac{0.23\dfrac{\tau_{diffusion}}{\tau_{reaction}}}{2.97\dfrac{\tau_{convection}}{\tau_{reaction}}} = 0.077\frac{\tau_{diffusion}}{\tau_{convection}} = 0.077(Ra\,Pr)^{1/2}\,. \tag{2.33}$$

The expression in Eq. (2.33) in fact over-predicts the ratio of the Frank-Kamenetskii temperature rise to the observed temperature rise, shown in Figure 2.10, by a factor of ~ 1.5. This discrepancy is most likely due to the difference between the Frank-Kamenetskii temperature rise, calculated for a zeroth-order system, and the scaling result derived in Eq. (2.23), confirmed by the experimental and numerical results for the non-zeroth order decomposition of azomethane. Nevertheless, the functional form in Eq. (2.33) is consistent with data presented in Figure 2.10. Both the numerical and experimental results indicate that the ratio of the diffusive temperature rise (calculated either using Frank-Kamenetskii's method or by Eq. (2.23)) to the observed temperature rise in a system where natural convection is important is proportional to $Ra^{1/2}$, as shown by Eq. (2.33). Such agreement between the experimental results, the numerical simulations and the analytical scaling analysis provides an excellent validation of the theoretical approach formulated at the start of this chapter.

2.5 Alterations to the Model for Sal'nikov's Reaction

The previous sections have dealt with developing a model for a simple exothermic decomposition reaction, occurring in a spherical batch reactor. The model has been validated through comparison with experimental measurements of temperature. Now the model has to be modified to allow Sal'nikov's reaction to be simulated. This is, in fact, very straightforward, because the only alteration to be made is in the species conservation Eqs. (2.2) and (2.26). For Sal'nikov's reaction, this conservation equation is written for the intermediate, A, so that an additional kinetic term appears on the right hand side of these equations to account for the production of A *via* step 1 of reaction (1.1). The equations for the conservation of energy and momentum are unaffected by the change in the kinetic scheme.

2.6 Summary

In this chapter, the results of previous experimental work investigating exothermic reactions in a closed spherical vessel have been compared with analytical and numerical techniques, which will be used below in an analysis of Sal’nikov’s reaction. The experimentally measured temperature rise at the centre of a spherical reactor, in which azomethane was decomposing thermally, was compared with the predictions of a scaling analysis of the governing equations. The forms of the scales derived, for the cases when diffusion and natural convection, respectively, control heat and mass transport, were found to be in good agreement with the experimental observations.

A numerical scheme was also developed to allow the governing equations to be solved for reaction in a spherical vessel. The results produced by this numerical scheme were found to agree well with actual measurements. The agreement of both the scaling results and the numerical simulations with experimental results is an excellent validation of both these theoretical techniques, which can now be applied with confidence to Sal’nikov’s reaction in subsequent chapters.

3 Scaling Analysis of Sal’nikov’s Reaction

3.1 Introduction

In this chapter, an initial analysis of Sal’nikov’s reaction is presented, both in the presence, and absence of natural convection. As in the previous chapter, the first technique to be applied to this problem will be a scaling analysis. Such an analysis yields important information regarding which parameters determine the behaviour of the system. The analysis presented for Sal’nikov’s reaction is more complex than that considered in the previous chapter, because of the more complex chemical scheme involved. A simple scaling analysis of Sal’nikov’s reaction was presented by Cardoso *et al.* (2004*b*); however, those results were not rigorously tested. The analysis presented in this chapter aims to improve on this initial study.

The governing equations for Sal’nikov’s reaction occurring in a spherical vessel are first presented in section 3.2. A scaling analysis is applied to these equations in section 3.3, and the form of these scales is confirmed by comparison with numerical simulations in section 3.4. The forms of the scales developed can be used to predict how the system will respond to variations in certain key process parameters, such as the radius of the reactor and the pressure of the gas. These predictions are discussed in section 3.5. Finally, in section 3.6, a comparison is made between the scaling results for Sal’nikov’s reaction and the results described in Chapter 2, for a simpler exothermic scheme.

3.2 Governing Equations

As discussed in section 1.3.3, Sal'nikov's reaction assumes a product B is generated from a precursor P *via* an active intermediate A in two consecutive first-order steps:

$$\mathrm{P} \xrightarrow{1} \mathrm{A} \xrightarrow{2} \mathrm{B} \tag{3.1}$$

Step 1 is assumed here to be thermoneutral, with E_1, the activation energy, and q_1, the exothermicity of step 1, both equal to zero. Step 2 is exothermic, with $E_2 > 0$ and $q_2 > 0$.

The reaction is assumed to occur in a closed spherical vessel of radius L, whose walls are held at a constant temperature T_0. The initial pressure and density within the reactor are taken as $\mathscr{P}_0$ and ρ_0, respectively. The equations for the conservation of species, energy and momentum can thus be stated.

The equation for conservation of the precursor species P is

$$\frac{\partial p}{\partial t} + \underline{u}.\nabla p = D_P \nabla^2 p - k_1 p\,, \tag{3.2}$$

where p is the concentration of species P, D_P is the molecular diffusivity of P, $\underline{u}$ is the velocity vector and k_1 is the first-order rate constant of step 1. As discussed in section 2.2, diffusion is assumed to be Fickian. Because the activation energy of step 1 is zero, the rate of reaction of P depends only on the concentration of P, and not on the local temperature. If P is distributed uniformly throughout the reactor initially, there is no mechanism for spatial variations of p to develop, so long as the temperature does not vary significantly from place to place, as discussed below. Because k_1 is independent of temperature, Eq. (3.2) can be rewritten in terms of a simple temporal derivative and integrated to give

$$p = p_0 \exp(-k_1 t)\,, \tag{3.3}$$

where p_0 is the initial concentration of P.

The equation for the conservation of the more reactive intermediate species A is similar in form to Eq. (2.2), which was used to model the concentration of azomethane. In this case another term needs to be included to account for the production of A in step 1 of the Sal'nikov's reaction. The equation can be written as

$$\frac{\partial a}{\partial t} + \underline{u}.\nabla a = D_A \nabla^2 a + k_1 p_0 \exp(-k_1 t) - k_2(T)a\,, \tag{3.4}$$

where a is the concentration of species A, D_A is its molecular diffusivity and k_2 is the first-order rate constant of step 2.

Conservation of energy is identical to Eq. (2.3), *i.e.*

$$\frac{C_V}{C_P}\frac{\partial T}{\partial t}+\underline{u}.\nabla T=\kappa\nabla^2 T+\frac{q_2 k_2(T)}{\rho_0 C_P}a\,. \tag{3.5}$$

Conservation of momentum is given by the Navier-Stokes equations. These take the same form as in Eq. (2.4). The equations can be simplified by adopting the Boussinesq approximation. It is shown below that usually $\Delta T << T_0$, and hence the Boussinesq approximation is appropriate; this also justifies Eq. (3.3), because the assumption that P remains spatially uniform throughout depends on there being no significant change in temperature or density inside the reactor. In the buoyancy term the variation of density is described by

$$\rho=\rho_0\left[1-\beta\left(T-T_0\right)\right], \tag{3.6}$$

The Navier-Stokes equations therefore become:

$$\frac{\partial \underline{u}}{\partial t}+\underline{u}.\nabla\underline{u}=-\frac{1}{\rho_0}\nabla\left(\mathscr{P}-\mathscr{P}_0\right)+\nu\nabla^2\underline{u}+\frac{\rho-\rho_0}{\rho_0}\underline{g}\,. \tag{3.7}$$

The final equation required is the continuity equation, which can be expressed in its incompressible form due to the adoption of the Boussinesq approximation,

$$\nabla.\underline{u}=0\,. \tag{3.8}$$

Initially, the gas in the reactor is considered to be pure P, at temperature T_0. There is no initial motion in the gas. Throughout the reaction, the temperature of the wall is held constant at T_0. This, of course, means that heat can be removed from the system at the wall. It is also assumed that the no-slip condition holds at the wall, and that there is no flux of any species at the wall. The effects of surface chemistry are therefore neglected. The initial and boundary conditions can thus be stated:

$t=0:\quad p=p_0;\;\; a=0;\;\; T=T_0;\;\; \underline{u}=0\;\;\forall\underline{x}$

At the wall: $\underline{n}.\nabla p=\underline{n}.\nabla a=0;\;\; T=T_0;\;\; \underline{u}=0\,,$ (3.9)

where $\underline{n}$ is the unit vector normal to the surface.

3.3 Scaling Analysis

As in section 2.3, the governing equations must be made dimensionless. In order to non-dimensionalise equations (3.4), (3.5), (3.7) and (3.8), the following seven dimensionless variables are defined:

$$a' = \frac{a}{a_0};\ p' = \frac{p}{p_0};\ T' = \frac{T - T_0}{\Delta T};\ \underline{u}' = \frac{\underline{u}}{U};\ \mathscr{P}' = \frac{\mathscr{P} - \mathscr{P}_0}{\rho_0 U^2};\ \underline{x}' = \frac{\underline{x}}{L}\ \text{ and }\ t' = \frac{Ut}{L}, \tag{3.10 a – g}$$

where a_0 is a characteristic concentration of species A and ΔT is the characteristic temperature rise. At this stage, these two scales are unknown, whereas p_0 and L are defined for a given system. In addition, the characteristic velocity, U, will be of the same form as Eq. (2.16), because the Navier-Stokes equations are unchanged in form from those presented in Chapter 2. Using these scales, equations (3.4), (3.5), (3.7) and (3.8), become, respectively:

$$\frac{\partial a'}{\partial t'} + \underline{u}'.\nabla' a' = \frac{D_A}{UL}\nabla'^2 a' + \frac{k_1 p_0 L}{U a_0} p' - \frac{k_{2,0} L}{U}\exp\left(\frac{\phi T'}{1 + \eta T'}\right) a', \tag{3.11}$$

$$\frac{C_V}{C_P}\frac{\partial T'}{\partial t'} + \underline{u}'.\nabla' T' = \frac{\kappa}{UL}\nabla'^2 T' + \frac{q_2 k_{2,0} a_0 L}{\rho_0 C_P U \Delta T}\exp\left(\frac{\phi T'}{1 + \eta T'}\right) a', \tag{3.12}$$

$$\frac{\partial \underline{u}'}{\partial t'} + \underline{u}'.\nabla' \underline{u}' = -\nabla' \mathscr{P}' + \frac{\nu}{UL}\nabla'^2 \underline{u}' - \frac{L\beta \Delta T T'}{U^2}\underline{g}, \tag{3.13}$$

$$\nabla'.\underline{u}' = 0 \tag{3.14}$$

where $k_{2,0}$ is k_2 evaluated at the wall temperature, T_0, and

$$\eta = \frac{\Delta T}{T_0}\ \text{ and }\ \phi = \frac{E_2 \Delta T}{R T_0^2}. \tag{3.15 a, b}$$

It is also useful at this stage to define the four characteristic timescales:

$$\tau_{step\ 1} = \frac{1}{k_1};\ \tau_{step\ 2} = \frac{1}{k_{2,0}};\ \tau_{diffusion} = \frac{L^2}{\kappa};\ \tau_{convection} = \frac{L}{U}, \tag{3.16 a – d}$$

for the various interacting phenomena in the system, namely the two steps of the reaction, diffusion of heat (which can be related to the diffusion of mass *via* a Lewis number) and finally convection. The forms of the timescales for diffusion of heat and natural convection are of the same form as defined in section 2.3. The timescales for the two steps of the reaction, however, are of a slightly different form to the reaction timescale defined in Eq. (2.14 b). The timescales in Eq. (3.16) are defined as they are from inspection of the dimensionless Eqs. (3.11) – (3.14). A comparison of the two different forms of timescale for reaction will be discussed further in section 3.6. Clearly, the relative values of the timescales in Eq. (3.16) will determine the behaviour of the system. Either diffusive or convective processes can control the transport of heat and mass and the magnitudes of ΔT and a_0 will all depend on which of these mechanisms dominates at the operating conditions of the reactor. Below, each of these regimes is examined in turn to develop the most appropriate expressions for the unknown scales in each case.

3.3.1 Transport Controlled by Diffusion

For Rayleigh numbers less than a critical value (~ 500) (Tyler, 1966), diffusion will be the dominant mechanism for the transfer of heat and mass. When diffusion dominates transport, the temperature and concentration fields are approximately spherically symmetric, with the maximum temperature occurring close to the centre of the reactor. For these low Rayleigh numbers, Eqs. (3.13) and (3.14) for the conservation of momentum can be neglected, as can the convective terms on the left hand side of Eqs. (3.11) and (3.12). In a diffusive system, the characteristic velocity, U, in Eqs. (3.11) and (3.12) is replaced by the ratio κ / L. A scale for ΔT can be found by assuming that the terms for diffusion and the generation of heat dominate in the energy equation (3.12), giving

$$\Delta T \sim \frac{q_2 k_{2,0} a_0 L^2}{\rho_0 C_P \kappa}. \tag{3.17}$$

This scaling assumes that $\tau_{diffusion}$, $\tau_{step\ 2} << \tau_{convection}$. Here, $k_{2,0}$ has been taken as a typical value of k_2.

A definition is now required for a_0. Cardoso *et al.* (2004*b*) simply defined $a_0 = p_0$ in the course of their analysis. However, their numerical results show that the concentrations of A observed at the centre of the reactor were an order of magnitude lower than p_0. This is most likely due to the formation of A in step 1 of Eq. (3.1) being much slower than the disappearance of A in step 2.

In principle, there are two alternative approaches to defining a_0, each of which will yield a different expression for ΔT. From examining the form of Eq. (3.11), it can be assumed that the term representing the generation of A in step 1 is balanced by either the diffusive term, or the step 2 term. Firstly, it is assumed that diffusion is the dominant sink term, *i.e.* $\tau_{diffusion} << \tau_{step\ 2}$. It should be noted that for a purely diffusive system (*e.g.* in microgravity), the diffusive term will not be a sink in the bulk of the vessel around the centre. This is because the concentration of A would be spherically symmetric with the lowest concentration occurring at the centre, so in fact A would diffuse inwards, thus supplying A. The constraints on the timescales, discussed above, define a region close to the $\tau_{step\ 2}$ / $\tau_{diffusion}$ axis on the regime diagram in Figure 1.5. Shown in Figure 3.1 is a two-dimensional representation of this regime diagram; the region where the inequalities for the timescales hold is region A. It has been shown previously (Fairlie and Griffiths, 2001, 2002) that in this part of the regime diagram, the reaction is very slow with only a small rise in temperature. It was also shown in these previous studies that when the reaction was slow, the concentration of A was virtually spatially uniform across the whole reactor. Fairlie and Griffiths (2001, 2002) only considered the purely diffusive limit; however, region A is in a part of the regime diagram where natural convection is very weak, and so the solutions in the presence of this weak convection would be very similar to those in the purely diffusive limit. Because the concentration is almost spatially uniform, the diffusive term in Eq. (3.11) would be ~ 0, so the kinetic terms would, in fact, dominate. It is therefore inappropriate to balance the diffusion and generation terms in Eq. (3.11).

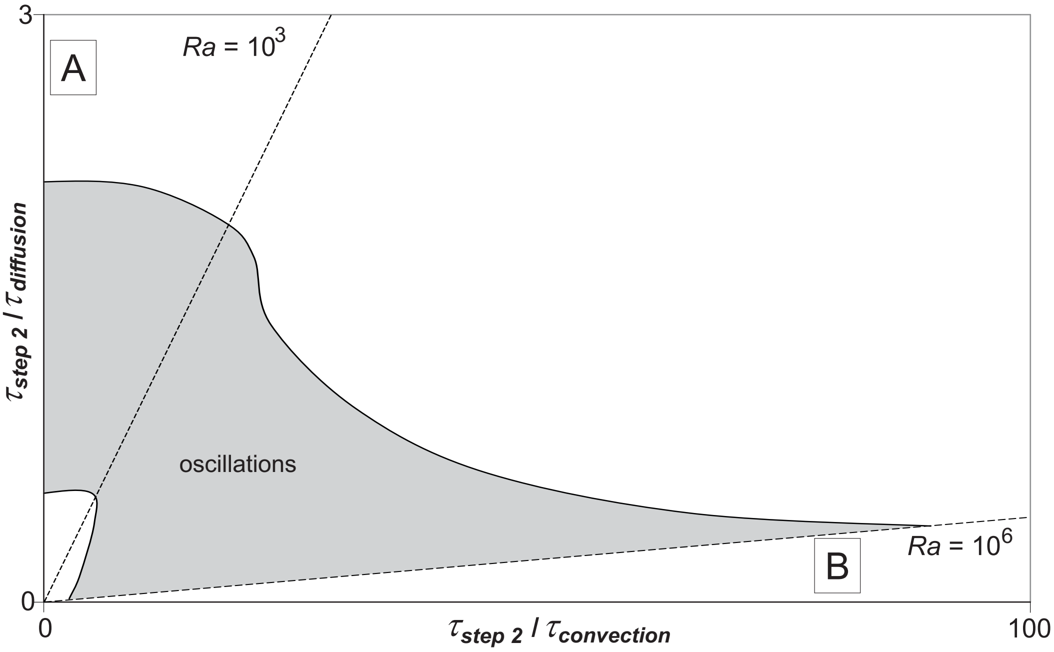

Figure 3.1. Regime diagram showing the regions of parameter space in which the different scales derived should be valid.

The second possible scale for a_0 is found by assuming that reaction in step 2 provides the dominant sink term and hence Eq. (3.11) is controlled by the kinetic terms, as discussed above. In this case

$$a_0 \sim \frac{k_1 p_0}{k_{2,0}} = p_0 \frac{\tau_{step\ 2}}{\tau_{step\ 1}}, \tag{3.18}$$

i.e. the quasi-steady state assumption, giving

$$\Delta T \sim \frac{q_2 k_1 L^2}{C_P \kappa} = \frac{\Delta T_{ad}}{\gamma} \frac{\tau_{diffusion}}{\tau_{step\ 1}}. \tag{3.19}$$

3.3.2 Transport Controlled by Convection

When the Rayleigh number rises above a critical value, natural convection becomes the dominant transport mechanism. For $10^3 < Ra < 10^6$ the convective flow is expected to be laminar (Turner, 1979). Natural convection disrupts the spherical symmetry observed when diffusion dominates transport, and leads to the formation of a hot zone above the centre of the reactor (Cardoso *et al.* 2004*a*, *b*). The scale for velocity can be defined as in section 2.3, *i.e.*

$$U \sim [\beta g L \Delta T]^{1/2}. \tag{3.20}$$

Similarly, if it is assumed that convection and generation dominate the heat Eq. (3.12) (*i.e.* $\tau_{convection}$, $\tau_{step\ 2} << \tau_{diffusion}$), a scale for ΔT can be defined as

$$\Delta T \sim \frac{q_2 k_{2,0} a_0 L}{\rho_0 C_P U}. \tag{3.21}$$

A scale for a_0 can be defined in a similar manner as in the previous section. Firstly, it is assumed that convection and generation of A dominate Eq. (3.11). Mathematically this means that $\tau_{convection} << \tau_{step\ 2}$. A scale for a_0 can therefore be defined as

$$a_0 \sim \frac{k_1 p_0 L}{U} = p_0 \frac{\tau_{convection}}{\tau_{step\ 1}}. \tag{3.22}$$

Using this definition of a_0, Eq. (3.21) becomes

$$\Delta T \sim \left(\frac{q_2 k_1 k_{2,0} L}{C_P \beta g} \right)^{1/2}. \tag{3.23}$$

These equations assume that $\tau_{convection} << \tau_{step\ 2} << \tau_{diffusion}$ and hence describe region B in the regime diagram in Figure 3.1. This scaling clearly applies to the region of the regime diagram where the natural convection generated by the reaction is turbulent. This study is only concerned with laminar natural convection, therefore these scaling results will not be considered further.

However, if $\tau_{convection} >> \tau_{step\ 2}$, so the quasi-steady state holds, the scale for a_0 is of similar form to Eq. (3.18). This yields:

$$\Delta T \sim \left(\frac{q_2}{C_P}\right)^{2/3}\left(\frac{k_1^2 L}{\beta g}\right)^{1/3}, \tag{3.24}$$

for the region where laminar natural convection dominates transport.

Table 3.1 summarises the scaling results when diffusion and laminar natural convection, respectively, dominate heat and mass transport. In order to test the scaling expressions developed in this section, a comparison is made with results obtained from full numerical simulations in section 3.4.

Table 3.1. Summary of scales developed for the diffusive and convective regimes.

Scale for a_0	Scale for ΔT
Diffusion Controls Transport	
$a_0 \sim \frac{k_1 p_0}{k_{2,0}} = p_0 \frac{\tau_{step\,2}}{\tau_{step\,1}}$	$\Delta T \sim \frac{q_2 k_1 L^2}{C_P \kappa}$
Laminar Convection Controls Transport	
$a_0 \sim \frac{k_1 p_0}{k_{2,0}} = p_0 \frac{\tau_{step\,2}}{\tau_{step\,1}}$	$\Delta T \sim \left(\frac{q_2}{C_P}\right)^{2/3}\left(\frac{k_1^2 L}{\beta g}\right)^{1/3}$

3.4 Comparison of Scaling Results with Numerical Simulations

3.4.1 Physicochemical Properties

Equations (3.4) – (3.9) were solved numerically for a spherical batch reactor with a fixed wall temperature, T_0, containing initially pure gas P, which then undergoes Sal'nikov's reaction. The equations were solved using the algorithm outlined in section 2.4.1, modified to account for Sal'nikov's reaction.

For the purpose of the numerical simulations, the thermal decomposition of di-*t*-butyl peroxide in a spherical reactor is considered. This reaction has been chosen because it can be shown to behave like Sal'nikov's reaction (3.1) under certain conditions (Gray and Griffiths, 1989; Griffiths *et al.*, 1988). These experimental studies used a semi-batch reactor, with the slow admission of the reactant into the vessel mimicking the effect of step 1 of Sal'nikov's reaction. This arrangement is suitable for studying Sal'nikov's reaction in the well-mixed limit; however, it is not suitable for cases that are not spatially uniform. This reaction has been studied numerically by Fairlie and Griffiths (2002) in both the well-mixed and zero-gravity extremes and by Cardoso *et al.* (2004*a*, *b*) when natural convection is present. The following constants were chosen to match those used by Cardoso *et al.* (2004*a*, *b*). The temperature of the wall of the spherical reactor, T_0, was held constant at 500 K and the physicochemical properties used were as follows: the initial molar density $\rho_0 = 8.2$ mol m^{-3} (corresponding to a pressure of 0.34 bar at 500 K), the heat capacity at constant volume $C_V = 190$ J mol^{-1} K^{-1}, and the exothermicity of step 2, $q_2 = 400$ kJ mol^{-1}. The base case chemistry is defined such that the rate constant $k_1 = 0.025$ s^{-1}, corresponding to $\tau_{step\ 1} = 40$ s and $k_2 = Z_2 \exp(-E_2 / R\,T)$ with $Z_2 = 2 \times 10^{15}$ s^{-1} and $E_2 / R = 18280$ K, giving $k_{2,0} = 0.265$ s^{-1}, and hence $\tau_{step\ 2} \sim 4$ s, which is an order of magnitude faster than step 1. Furthermore, the simplifying assumption that the Lewis and Prandtl numbers were unity was made. This implies that $\nu = \kappa = D_A$, *i.e.* the diffusivities of momentum, heat and chemical species were considered to be equal. In these, and all subsequent simulations, the diffusivities were assumed to remain constant when the temperature changes. The diffusivities used in the diffusive regime were of order 10^{-4} m^2 s^{-1}, and in the convective regime values of $10^{-6} - 10^{-4}$ m^2 s^{-1} were considered. Cussler (1997) suggests that values of D as low as $\sim 2 \times 10^{-6}$ m^2 s^{-1} are realistic for some of the systems under consideration.

The behaviour of the system was studied at four values of Ra, corresponding to three different areas of the 3-D regime diagram (Figure 1.5), which has as its axes ratios of the characteristic timescales in Eq. (3.16). The four cases studied were: (i) the zero gravity case, where diffusion is the only transport process and $Ra = 0$; this corresponds to the vertical plane in Figure 1.5, (ii) a case in the region where only weak convection occurs ($Ra \sim 600$), and finally two cases in the region where strong laminar convection develops ((iii) $Ra \sim 21500$ and (iv) $Ra \sim 5000$). The cases (i) – (iii) with $Ra = 0$, $Ra \sim 600$ and $Ra \sim 21500$ correspond to cases A, B and C described by Cardoso *et al.* (2004*b*). At each Rayleigh number the radius of the reactor, L, was varied; in addition, either g or κ was varied to maintain constant Ra. For the cases where diffusion is the dominant transport mechanism, g was varied and κ held constant, because the form of the scale for ΔT, as given by Eq. (3.19), is independent of g, but dependent on κ. Conversely, for the cases where convection is the dominant mode of transport, g was held constant, whilst κ was varied. Once again, this is suggested by the form of Eq. (3.24), which is independent of κ. Table 3.2 shows the ranges of L studied for each Rayleigh number, as well as the ranges of g and κ used.

To validate further the functional forms of the expressions obtained in section 3.3 through scaling, the rate constants of the base case were altered. This, of course, is a purely hypothetical action, done to confirm the mathematics. Because k_1 appears in the expressions for ΔT (Eq. (3.19) when diffusion controls and Eq. (3.24) when convection controls), a range of values was studied. Thus, the values of k_1 were varied over the range 0.0125 – 0.0375 s^{-1}. The value of k_2 was altered by arbitrarily halving the pre-exponential factor, to $Z_2 = 1 \times 10^{15}$ s^{-1}, in the Arrhenius expression. This was done to confirm that ΔT is independent of $k_{2,0}$. The final two columns in Table 3.2 show the kinetic parameters used in each case.

Table 3.2. Ranges of L, g, and κ used in the numerical simulations at each Rayleigh number, and the kinetic parameters studied in each case. The kinetic parameters were varied independently *i.e.* when k_1 was varied, $k_{2,0}$ was held at its base case value, and *vice versa*.

Ra	L / m	g / m s^{-2}	$\kappa \times 10^4$ / m^2 s^{-1}	k_1 / s^{-1}	$Z_2 \times 10^{-15}$ / s^{-1}
0	0.0025 – 0.07	0	1	0.0125, 0.025, 0.0375	1, 2
600	0.015 – 0.15	12000 – 0.12	6	0.025	2
5000	0.01 – 0.15	9.81	0.13 – 12	0.025	2
21500	0.01 – 0.15	4.9	0.066 – 4.7	0.025	2
21500	0.01 – 0.15	9.81	0.054 – 6.8	0.0125, 0.01875, 0.025, 0.0375	1, 2
21500	0.01 – 0.15	30	0.097 – 9.7	0.025	2

3.4.2 Diffusive Regime

The behaviour of the system when diffusion dominates transport is examined first, *i.e.* the cases $Ra = 0$ and $Ra \sim 600$ (in this case there is some weak flow due to natural convection). This means that, as far as Figure 1.5 is concerned, only systems on, or near, the vertical plane where only diffusion and reaction occur are considered. In Figure 3.2 is plotted the maximum temperature increase, which occurs at the centre of the reactor due to the spherical symmetry of the temperature and concentration fields, *versus* the radius of the reactor for the base case chemistry in the diffusive regime. This plot shows that ΔT exceeds 100 K when the radius, $L > 30$ mm; also the plot is typical of those seen when diffusion is the dominant transport mechanism (*i.e.* when $Ra = 0$ and $Ra \sim 600$).

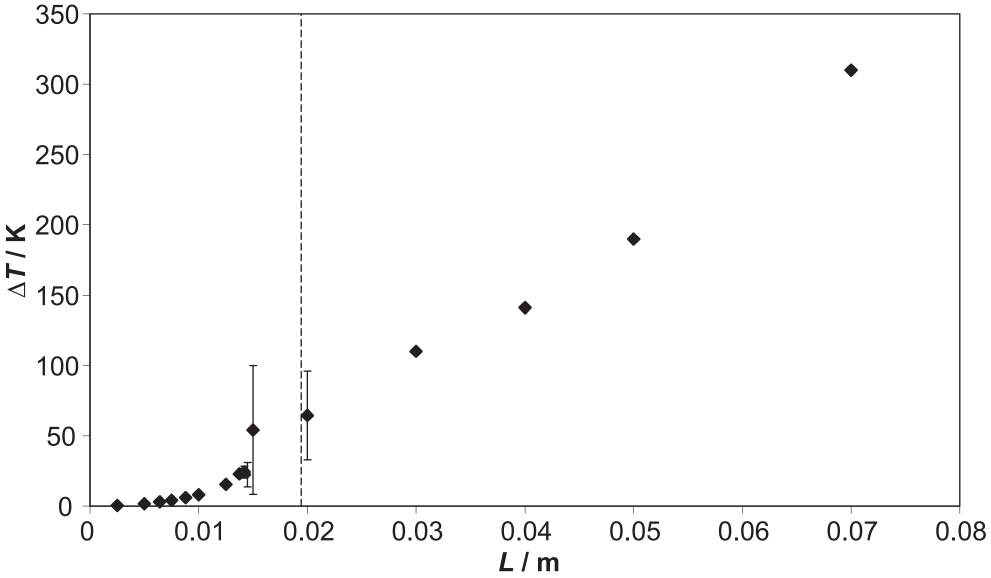

Figure 3.2. Plot of the maximum temperature rise, ΔT at the centre of the reactor *versus* L, the radius of the reactor, in the diffusive regime for the base case chemistry, $g = 0$ m s^{-2}, $\kappa = 1 \times 10^{-4}$ m^2 s^{-1}. 'Error bars' indicate the occurrence of oscillations and show their range, measured from the first peak to the first trough.

There are three identifiable regions, where the system behaves differently, as shown more clearly in Figure 3.3(a – c). The temporal development of the temperature and the concentration of A at the centre of the reactor for three different values of $\tau_{diffusion}$ are plotted. In the three cases presented, the chemistry is that of the base case *i.e.* $\tau_{step\ 1} = 40$ s and $\tau_{step\ 2} = 3.77$ s at 500 K, and $\tau_{diffusion}$ has been varied by changing the radius, L, of the reactor (in this case the graphs represent L = 10, 20 and 30 mm respectively). For a small reactor ($L < 0.01$ m in Figure 3.2), there are slow growths and decays of both the temperature and the concentration of A in time. In addition, there is only a relatively small increase in temperature (of ~ 8 K) to the maximum, so the system behaves almost isothermally. For such cases with a small

$\tau_{diffusion}$, *e.g.* in Figure 3.3(a), the temperature and concentration fields would be expected to be in effect uniform, with the exception of the thermal and concentration boundary layers at the wall. This approximate spatial uniformity decreases the magnitude of the convection and diffusion terms in Eq. (3.4) relative to that of the reaction terms. Therefore, ΔT should have the form of Eq. (3.19), *i.e.* there is a dependence on k_1, but not k_2. Indeed, the concentration and temperature fields obtained numerically were virtually uniform in these cases as can be seen in Figure 3.4.

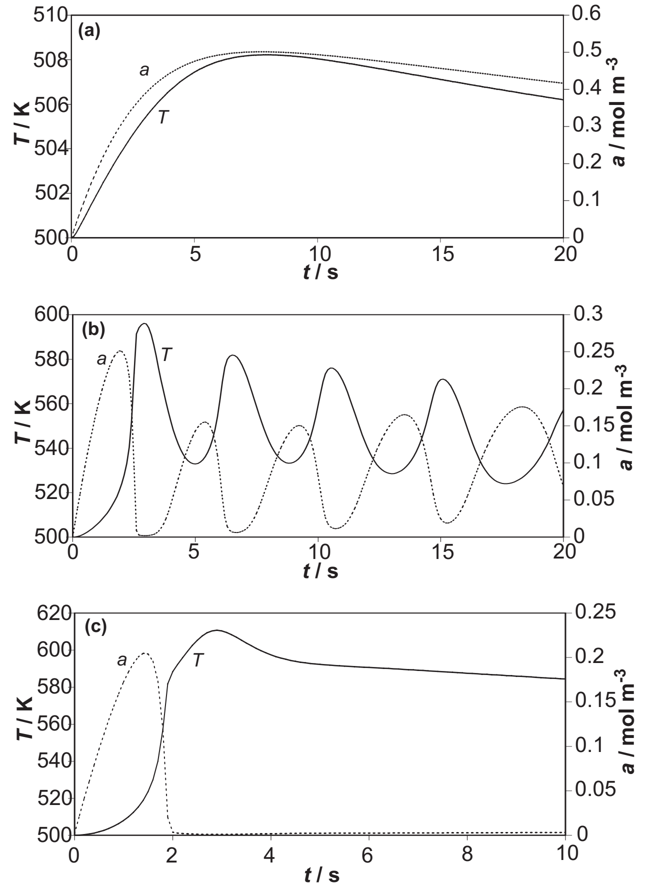

Figure 3.3. Temperature and concentration of A at the centre of the reactor plotted against time, in the diffusive regime for (a) $\tau_{diffusion}$ = 1 s; L = 10 mm, (b) $\tau_{diffusion}$ = 4 s; L = 20 mm, (c) $\tau_{diffusion}$ = 9 s; L = 30 mm, for the base case chemistry with $g = 0$ m s^{-2}, $\kappa = 1 \times 10^{-4}$ m^2 s^{-1}. The solid line shows the temperature, and the dashed line shows the concentration of A.

The temperature and concentration in Figure 3.4 only change by ~ 1%, moving from the wall to the centre of the reactor. This small variation in temperature and concentration means the system can be described as approximately spatially uniform; however, the gradients that do exist can clearly be seen in Figure 3.4. Additionally, the numerical results show that the decay in temperature and concentration (as shown by Figure 3.3(a)) is proportional to exp(– k_1 t), thus lending support to the hypothesis that k_1 is the dominant kinetic parameter in this system.

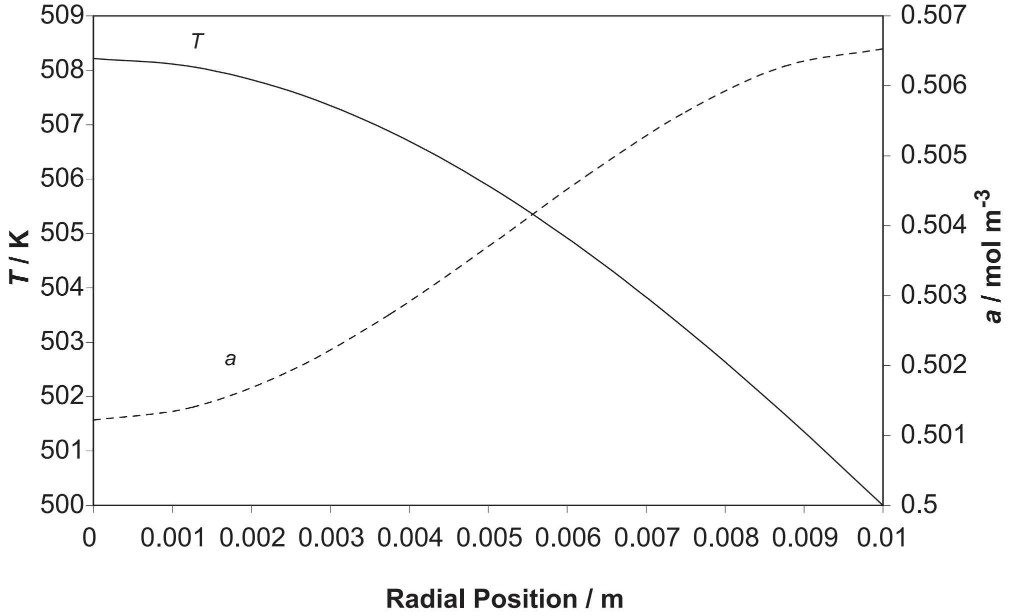

Figure 3.4. Radial profiles of the temperature and the concentration of A at t = 8 s, in the diffusive regime for $\tau_{diffusion}$ = 1 s; L = 10 mm. The solid line shows the temperature and the dashed line the concentration of A.

When the size of the reactor is increased, the system moves into a region of instability, where the temperature and the concentration of A exhibit temporal oscillations, as shown in Figure 3.3(b) for the centre of the reactor. In fact, the concentration of A oscillates in anti-phase with the temperature, as has been previously shown (Cardoso *et al.* 2004*a*, *b*). The 'error bars' in Figure 3.2 show the amplitude of the first oscillation of ΔT. The plotted point represents a time average of the first oscillation (*i.e.* the average of the temperatures at the first peak and the first trough). It was found that oscillations only occurred for reactor radii, L, in a narrow band, whose location depended on the physical and kinetic parameters used. The broken vertical line in Figure 3.2 shows the value of L for which $\tau_{diffusion} = \tau_{step\ 2}$. It seems that, when diffusion is the dominant transport mechanism, the range of L, over which oscillatory behaviour is observed, corresponds to the region where the characteristic timescales for diffusion and reaction in step 2 are of similar magnitude *i.e.* $\tau_{diffusion} \approx \tau_{step\ 2}$. This region of oscillations can be defined by a linear stability analysis. Gray and Scott (1990*b*) performed such an analysis, but for a one-dimensional diffusive system; however, the boundary conditions and geometry they studied are not appropriate to the present problem. Further work on a two-dimensional system is necessary to investigate the generality of this observation. For L > 0.03 m in Figure 3.2, the temporal evolutions of temperature and the concentration of A at the centre of the reactor change to that shown by Figure 3.3(c). Instead of the temporal oscillations, there is now an initial peak in the concentration curve, which then rapidly decays to almost zero. The temperature now rises by ~ 100 K, because of heat removal from a larger vessel being slower. The plot in Figure 3.3(c) shows an initially fast rise in temperature and then there is a distinct 'kink' in the curve (at ~ 2 s), when the concentration of the intermediate reaches a steady value, close to zero. The 'kink' in the temperature curve can be explained by examining Eq. (3.5), *i.e.* the energy conservation equation. When the concentration of A falls rapidly to virtually zero, the heat generation term in Eq. (3.5) effectively disappears. It is this swift change in the form of the governing equation that causes the observed change in the temporal development of the temperature.

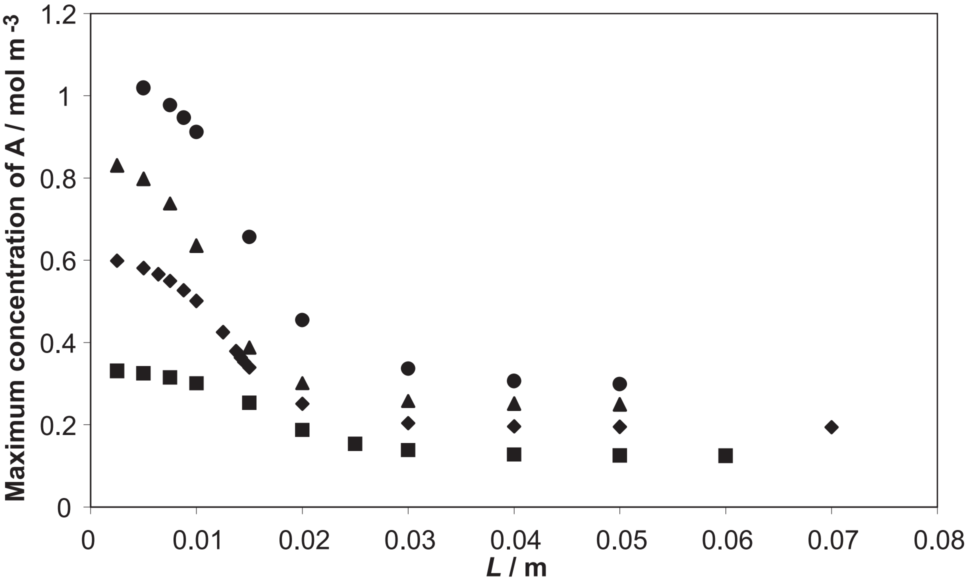

Figure 3.5. Plots of the maximum concentration of A at the centre of the reactor *versus* L, the radius of the reactor in the diffusive regime, $g = 0$ m s^{-2}, $\kappa = 1 \times 10^{-4}$ m^2 s^{-1} (filled diamond - $k_1 = 0.025$ s^{-1}, $k_{2,0} = 0.265$ s^{-1}; filled square - $k_1 = 0.0125$ s^{-1}, $k_{2,0} = 0.265$ s^{-1}; filled triangle - $k_1 = 0.0375$ s^{-1}, $k_{2,0} = 0.265$ s^{-1}; filled circle - $k_1 = 0.025$ s^{-1}, $k_{2,0} = 0.132$ s^{-1}).

In order to understand further the behaviour of the system in the diffusive regime, the computed maximum concentration of A at the centre of the reactor is plotted in Figure 3.5 against L, the radius of the reactor. It should be remembered that different expressions were derived in section 3.3 using assumptions about the dominant sources and sinks of species A in Eq. (3.11). In Figure 3.5, there is an initial decrease in the magnitude of the maximum concentration when L is increased, before it levels off at higher L. It is clear from Figure 3.5 that the maximum concentration of A depends on both k_1 and k_2, indicating that the kinetic terms dominate in Eq. (3.11), as predicted previously. Equation (3.18) for a_0, the characteristic concentration of A, suggests that it does not vary with L. This clearly fails to explain the initial curvature in Figure 3.5 at small L and does not agree with the constant value at high L. However, if Eq. (3.18) is modified to take account of the temperature dependence of k_2, a_0 takes on a similar form to those plotted in Figure 3.5. A functional dependence for ΔT of the form of Eq. (3.19) is therefore expected. This equation has been recast in dimensionless form, similar to the results in section 2.3, as

$$\gamma \frac{\Delta T}{\Delta T_{ad}} \sim \frac{\tau_{diffusion}}{\tau_{step\ 1}}. \qquad (3.25)$$

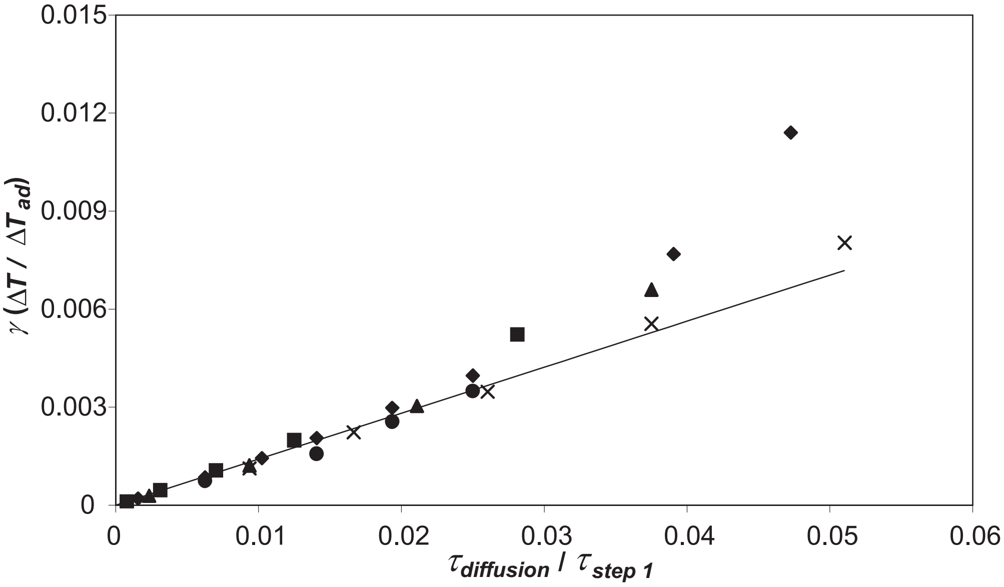

Figure 3.6. Plot of $\gamma(\Delta T / \Delta T_{ad})$ *versus* $\tau_{diffusion} / \tau_{step\ 1}$ for ‘small’ reactors in the diffusive regime. The line shown corresponds to Eq. (3.26). (filled diamond - $k_1 = 0.025$ s^{-1}, $k_{2,0} = 0.265$ s^{-1}; filled square - $k_1 = 0.0125$ s^{-1}, $k_{2,0} = 0.265$ s^{-1}; filled triangle - $k_1 = 0.0375$ s^{-1}, $k_{2,0} = 0.265$ s^{-1}; filled circle - $k_1 = 0.025$ s^{-1}, $k_{2,0} = 0.132$ s^{-1}; cross mark - $k_1 = 0.025$ s^{-1}, $k_{2,0} = 0.265$ s^{-1}, $Ra \sim 600$).

Figure 3.6 is a plot of $\gamma(\Delta T / \Delta T_{ad})$ *versus* $\tau_{diffusion} / \tau_{step\ 1}$ for small reactors. As expected, there is a good linear correlation. The line plotted represents Eq. (3.25) modified by the application of a constant factor, which was found using the least squares method. The point at which the observed value of $\gamma\ (\Delta T\ /\ \Delta T_{ad})$ begins to deviate from the linear behaviour depends on the values of the kinetic parameters used, as well as the Rayleigh number. When $Ra = 0$, the departure from linearity occurs at a lower value of $\tau_{diffusion}\ /\ \tau_{step\ 1}$, in comparison with the $Ra \sim 600$ case. The deviation from linearity is due to the transition to oscillatory behaviour. There is however good agreement for all the cases considered in the present work for $\tau_{diffusion}\ /\ \tau_{step\ 1} < 0.025$. The characteristic temperature rise for these 'small' reactors can therefore be expressed as

$$\gamma \frac{\Delta T}{\Delta T_{ad}} = \left(0.141 \pm 0.002\right) \frac{\tau_{diffusion}}{\tau_{step\ 1}}\ . \tag{3.26}$$

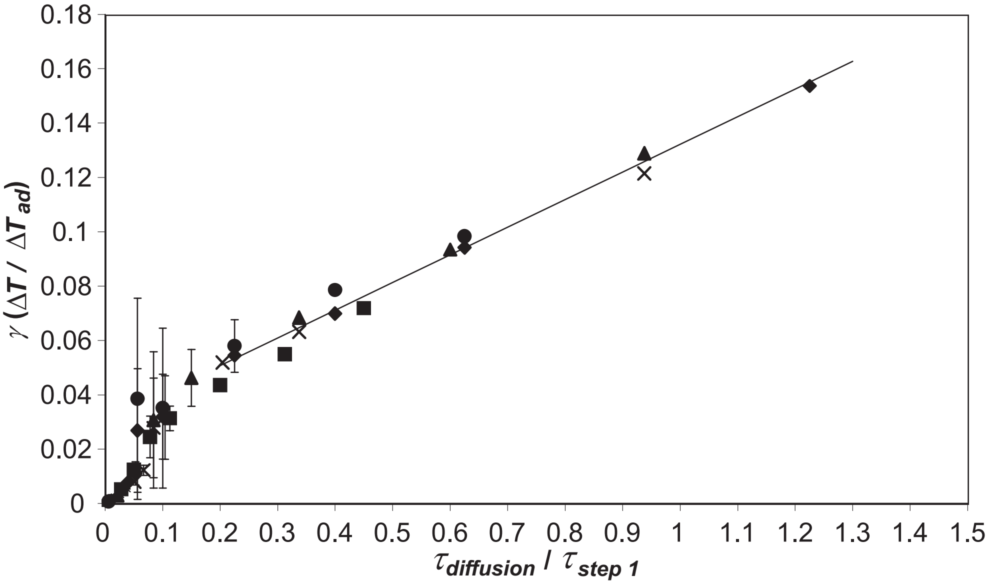

Figure 3.7. Plot of $\gamma\,(\Delta T/\,\Delta T_{ad})$ *versus* $\tau_{diffusion}\ /\ \tau_{step\ 1}$ in the diffusive regime. The line shown corresponds to Eq. (3.27). (Symbols as for Figure 3.6).

The data for all reactor sizes are plotted in Figure 3.7. Again there is good linear agreement after the transitional zone where oscillations occur ($\tau_{diffusion}\ /\ \tau_{step\ 1} > 0.2$). What is surprising is the apparent offset in the plot, so that the data for high $\tau_{diffusion}\ /\ \tau_{step\ 1}$ (*i.e.* 'large' reactors) do not extrapolate back through the origin of Figure 3.7. This can be explained by the shape of Figure 3.3(c), as discussed previously; after the observed kink in the plot of temperature in Figure 3.3(c), the concentration of A in the reactor falls to practically zero, so in effect the intermediate is destroyed by step 2 as soon as it is produced. This would mean the rate of reaction and hence the rate of heat release is determined by k_1. An expression of the form of Eq. (3.25) can then be used to describe behaviour in this region, giving the straight line shown in Figure 3.7. The offset is therefore most probably due to the region before the kink when there is still a non-trivial concentration of A within the reactor. Thus, there are two serial processes contributing to the temperature rise. Figure 3.7 indicates that the characteristic temperature rise for these larger reactors can be written as:

$$\gamma \frac{\Delta T}{\Delta T_{ad}} = (0.100 \pm 0.003) \frac{\tau_{diffusion}}{\tau_{step\ 1}} + (0.030 \pm 0.002). \tag{3.27}$$

In both cases (*i.e.* Eq. (3.26) for low $\tau_{diffusion} / \tau_{step\ 1}$ and Eq. (3.27) for high $\tau_{diffusion} / \tau_{step\ 1}$), the temperature rise is controlled by $\tau_{step\ 1}$, which is what one would expect intuitively, given that $\tau_{step\ 1}$ is an order of magnitude greater than $\tau_{step\ 2}$ in the present work. It has also been observed that the nature of the temporal evolution of the system depends on $\tau_{step\ 2}$. When $\tau_{step\ 2}$ is of similar magnitude to $\tau_{diffusion}$, oscillations are seen in the temperature and concentration fields. It should be noted, however, that the behaviour might well be different in a system, where $\tau_{step\ 1}$ and $\tau_{step\ 2}$ are of similar magnitude.

It is tempting to draw parallels between the behaviour seen in Figure 3.7, and the ignition diagram in Figure 1.1. As the ratio $\tau_{diffusion} / \tau_{step\ 1}$ increases, the system moves from a slow reaction, with relatively small temperature rises, through a region of oscillatory behaviour, into a region with much larger rises in temperature. Figure 3.3(c) shows characteristics which are similar to an explosion. There is an initial slow increase in temperature, followed by a very large and rapid increase; this is similar to an explosion following an ignition delay. The ratio $\tau_{diffusion} / \tau_{step\ 1}$ is proportional to L^2, so the sequence described could occur by increasing the size of the reactor. In addition, $\tau_{diffusion} / \tau_{step\ 1}$ is inversely proportional to κ, which is itself inversely proportional to pressure. Thus, increasing the gas pressure could move the system from a slow reaction, through an oscillatory state, into a region of rapid reaction. This change in behaviour is similar to following a horizontal path, from left to right, on Figure 1.1, moving from slow combustion, through a region of cool flames, to ignition.

3.4.3 Convective Regime

The behaviour of the system when convection is important was investigated by examining full numerical solutions for $Ra \sim 5000$ and 21500. The convective flow in these cases should be laminar. The flow-field is such that the gas rises vertically along the axis of symmetry and falls downwards close to the cooler walls, thus forming a toroidal vortex (see Figure 2.1). As mentioned previously, the spherical symmetry of the temperature and concentration fields seen in the diffusive regime are disrupted by the convective flow. In fact, a 'hot zone' forms above the centre of the reactor (Cardoso *et al.* 2004*a*, *b*). To take account of this hot zone, the temperature rise, ΔT, and the concentration of A at a point L / 2 above the centre of the reactor (*i.e.* a point three quarters of the way up the vertical axis), are examined below, instead of the values at the centre of the reactor. This gives ΔT and the concentration of A close to their maxima within the vessel. Like the diffusive region, the form of the expression for ΔT is determined by the dominant terms in Eq. (3.11) for the conservation of the intermediate A.

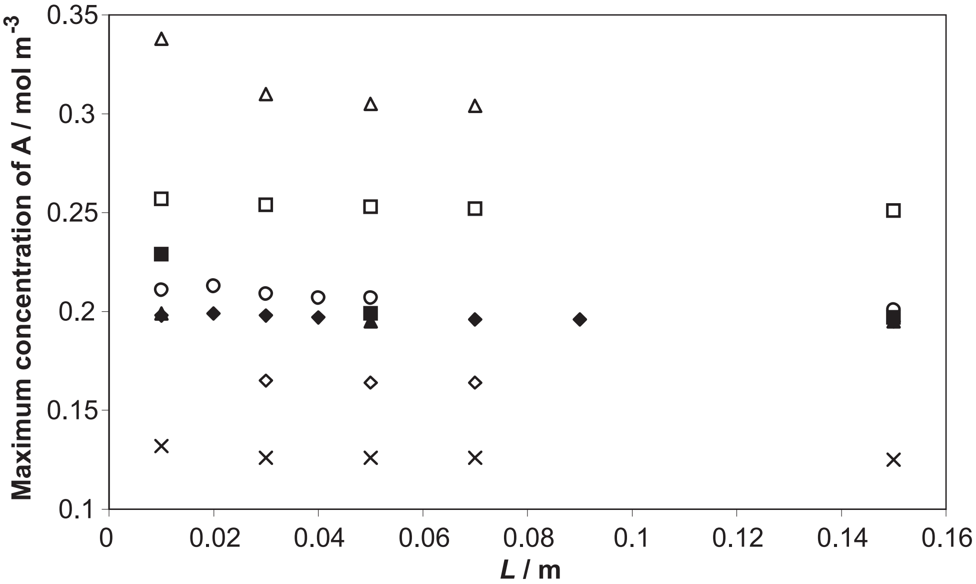

Figure 3.8. Maximum concentration of A at a distance L / 2 above the centre of the reactor plotted *versus* L, the reactor's radius in the laminar convection regime (filled diamond - $g = 9.81$ m s^{-2}, $k_1 = 0.025$ s^{-1}, $k_{2,0} = 0.265$ s^{-1}, $Ra \sim 21500$; filled triangle - $g = 4.9$ m s^{-2}; filled square - $g = 30$ m s^{-2}; cross mark - $k_1 = 0.0125$ s^{-1}; open diamond - $k_1 = 0.01875$ s^{-1}; open square - $k_1 = 0.0375$ s^{-1}; open triangle - $k_{2,0} = 0.132$ s^{-1}; open circle - $g = 9.81$ m s^{-2}, $k_1 = 0.025$ s^{-1}, $k_{2,0} = 0.265$ s^{-1}, $Ra \sim 5000$).

In Figure 3.8 is plotted the maximum concentration of A at the point $L / 2$ above the centre of the reactor *versus* the radius of the reactor for all the conditions investigated in the convective regime. Figure 3.8 shows that for any given condition, the maximum concentration is virtually constant when the radius of the reactor is increased. It is also clear that the value of this constant is independent of both the value of *Ra* (provided one remains in the laminar convection regime) and gravity. As before, it appears that what determines the maximum concentration of A are the values of the kinetic parameters k_1 and k_2, as was predicted by scaling. It is also interesting to note that the constant values of the maximum concentration of A obtained for the various combinations of k_1 and k_2 in the convective regime are the same as those for the corresponding systems in the diffusive regime. All this suggests an expression for ΔT of the form of Eq. (3.24), *i.e.* Eq. (3.11) is once again controlled by the kinetic terms.

The observed dependence of ΔT on the reactor's radius is plotted in Figure 3.9. Once again, the bars represent the magnitude of any oscillations (and show the range from the first peak to the first trough). In general, there is not a narrow region of oscillatory behaviour, as was seen for the diffusive region; instead, oscillations were generally observed across the entire range of L studied in this work. However, there is an observable change of the amplitude of the first oscillation (*i.e.* the range indicated by the bars) when the reactor is made larger. This suggests that a distinct range of reactor sizes exhibiting oscillatory behaviour could exist, the boundaries of which lie outside the values of L studied in this chapter. Figure 3.9 shows that ΔT does have a dependence on $k_{1,}$ as expected from Eq. (3.24). When k_2 is decreased, there is a slight increase in the observed ΔT, as well as an increase in the magnitude of the observed oscillations. There is significant overlap between the oscillatory ranges for $k_{2,0}$ = 0.132 s^{-1} and those for the base case chemistry. It can be concluded that to a reasonable approximation ΔT is independent of k_2, as indicated by Eq. (3.24).

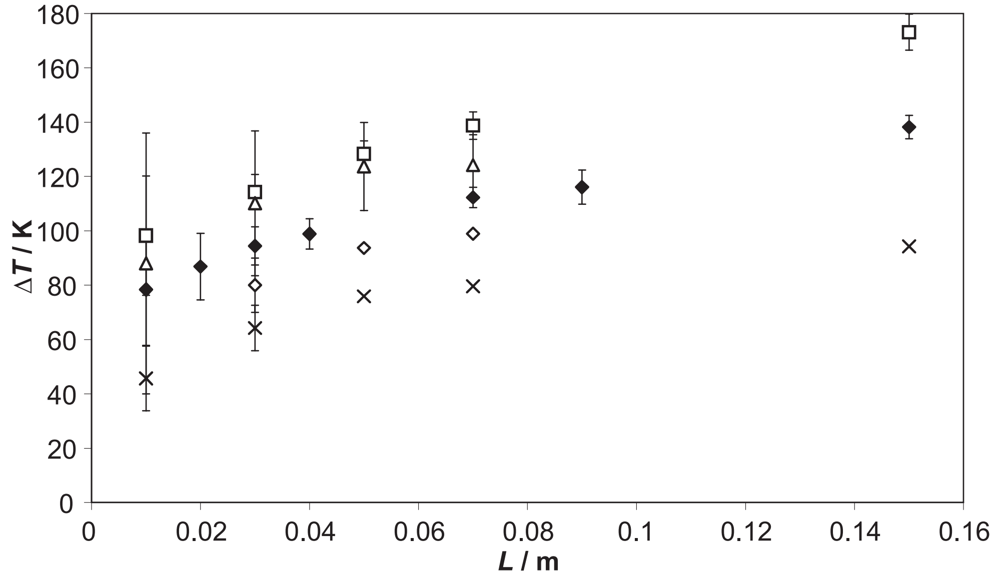

Figure 3.9. Plot of ΔT at a distance of L / 2 above the centre of the reactor, *versus* L, the radius of the reactor in the laminar convection regime. (Symbols as for Figure 3.8).

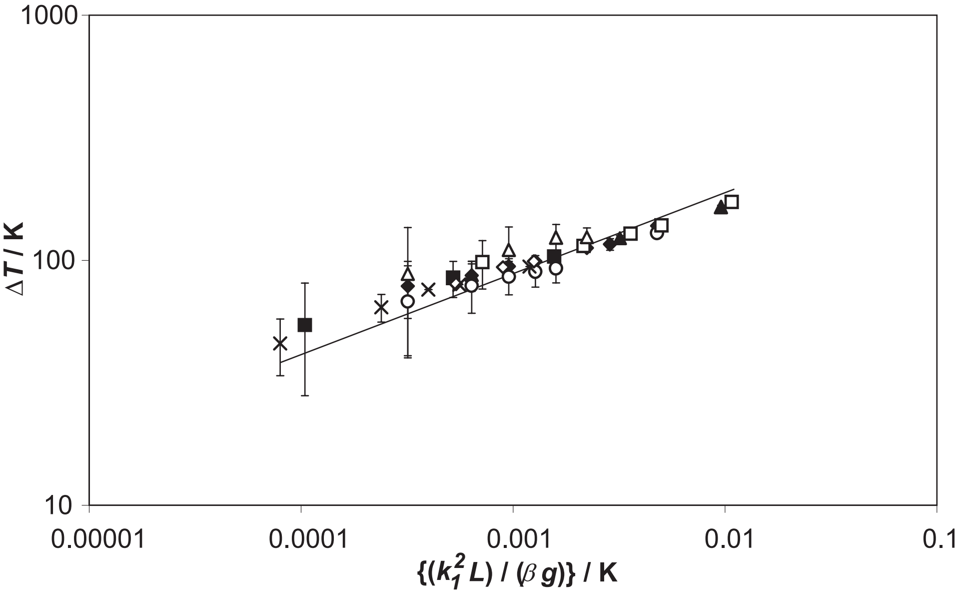

Figure 3.10. Log-log plot of ΔT at a distance L / 2 above the centre of the reactor *versus* $(k_1^2 L) / (\beta g)$ in the laminar convection regime. The line shown corresponds to Eq. (3.28). (Symbols as for Figure 3.8).

The data from all the simulations are presented on logarithmic scales in Figure 3.10. Also plotted is Eq. (3.24) modified by a constant multiplier. The result is a straight line of gradient 0.24 ± 0.01, which is less than the value of 0.33 predicted by Eq. (3.24). When the oscillatory ranges are taken into account, Eq. (3.24) does provide however, a reasonable fit to the data. The temperature rise, ΔT, can therefore be written as

$$\Delta T = (5.40 \pm 0.10)\left(\frac{\Delta T_{ad}}{\gamma}\right)^{2/3}\left(\frac{k_1^2 L}{\beta g}\right)^{1/3}. \tag{3.28}$$

The expression for ΔT in Eq. (3.28) can be substituted into Eq. (3.20) for U. Figure 3.11 shows a plot of the maximum vertical velocity at the centre of the reactor against $(g\,L^2)^{1/3}$. The velocity at the centre of the reactor was used because this generally, is where the maximum occurs. Figure 3.11 should show a linear relationship, and indeed this is the case to a reasonable approximation. The characteristic velocity, U, can therefore be defined as

$$U = (0.313 \pm 0.020)[\beta g L \Delta T]^{1/2}, \tag{3.29}$$

where ΔT is as defined in Eq. (3.28). It is striking that U reaches 0.3 m s^{-1} for $L = 0.15$ m and $g = 30$ m s^{-2}. For terrestrial gravity, the velocity in a similarly sized reactor can reach up to 0.2 m s^{-1}.

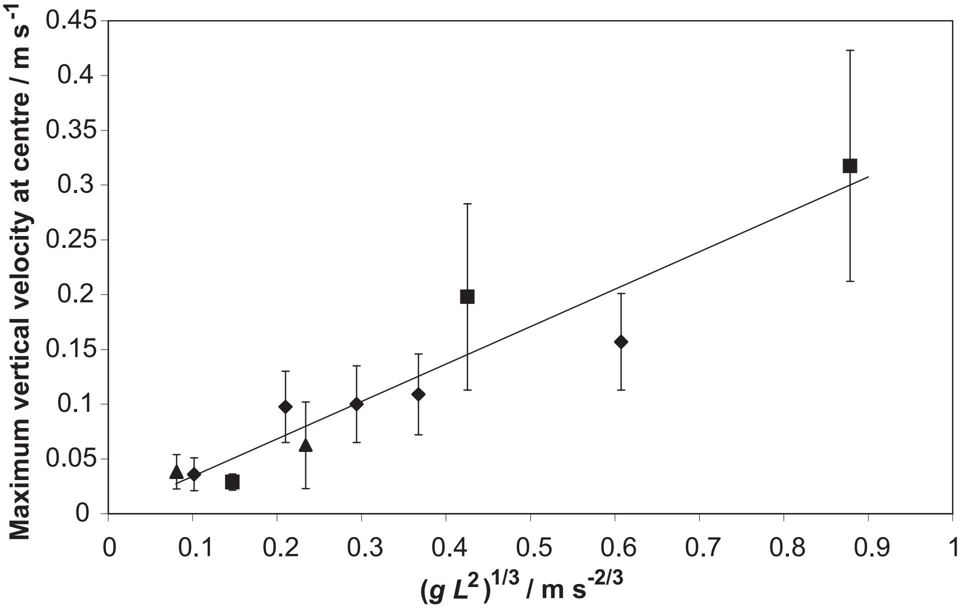

Figure 3.11. Plot of the maximum vertical velocity of the gas at the centre of the reactor, *versus* $(g\,L^2)^{1/3}$. The line shown corresponds to Eq. (3.29). (Symbols as for Figure 3.8).

This definition of U allows the calculation of $\tau_{convection}$, enabling ΔT to be expressed in terms of the characteristic timescales, $\tau_{convection}$ and $\tau_{step\ 1}$. Figure 3.12 shows $\gamma(\Delta T / \Delta T_{ad})$ as a function of $\tau_{convection} / \tau_{step\ 1}$. The expression for ΔT is then:

$$\gamma \frac{\Delta T}{\Delta T_{ad}} = (4.00 \pm 0.08)\frac{\tau_{convection}}{\tau_{step\ 1}}. \tag{3.30}$$

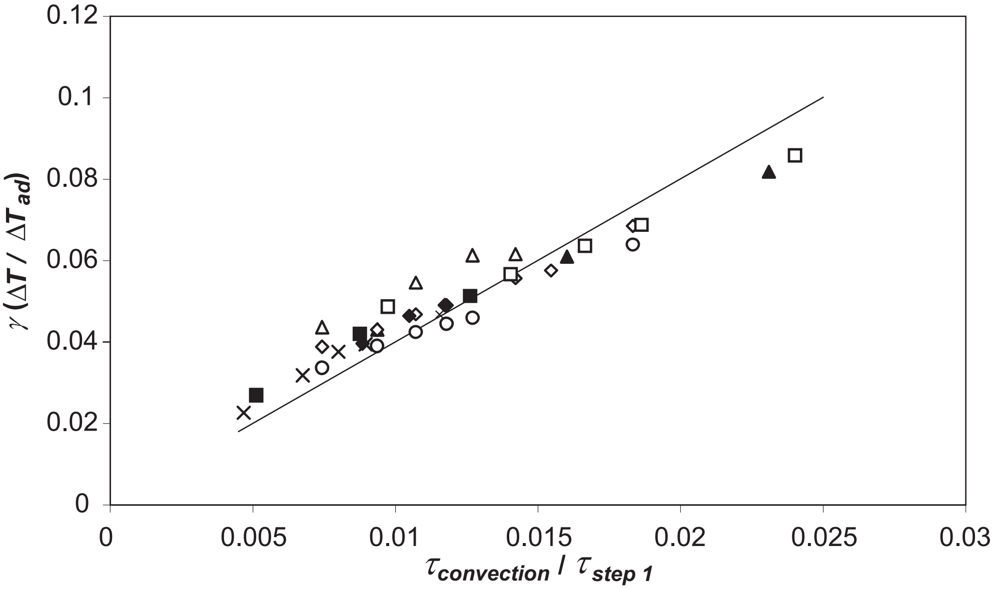

Figure 3.12. Plot of $\gamma(\Delta T/\Delta T_{ad})$ *versus* $\tau_{convection}$ / $\tau_{step\ 1}$ in the laminar convection regime. The line shown corresponds to Eq. (3.30). (Symbols as for Figure 3.8).

In the derivation of the scales in section 3.3.2, it was stated that the form of the scale for ΔT given by Eq. (3.28) would hold, when $\tau_{convection} >> \tau_{step\ 2}$. If the scale for U given by Eq. (3.29) is used, this inequality does not hold. This is because $\tau_{step\ 2}$ is calculated at 500 K, *i.e.* the wall temperature. If $\tau_{step\ 2}$ is modified to account for the increase in temperature within the reactor, the inequality does indeed hold.

As mentioned before for the diffusive region, $\tau_{step\ 1}$ is the dominant kinetic timescale in the present work. Again, it should be noted that this behaviour might well change if $\tau_{step\ 1}$ and $\tau_{step\ 2}$ are of similar order.

3.5 The Effect of Varying Process Parameters

Examination of the form of the scales developed in the previous sections, along with the expression for the Rayleigh number allows predictions to be made of how the system will respond to variations in certain process parameters. In particular, it is important to reveal the effects of pressure, reactor size and the phase of the system (*i.e.* gas or liquid) on the intensity of convection in the reactor. The effects of these changes can be plotted on a regime diagram, such as that shown in Figure 1.5. A two-dimensional representation of this diagram is presented in Figure 3.13, for constant $(\tau_{step\ 2}\,/\,\tau_{step\ 1})\,p'$.

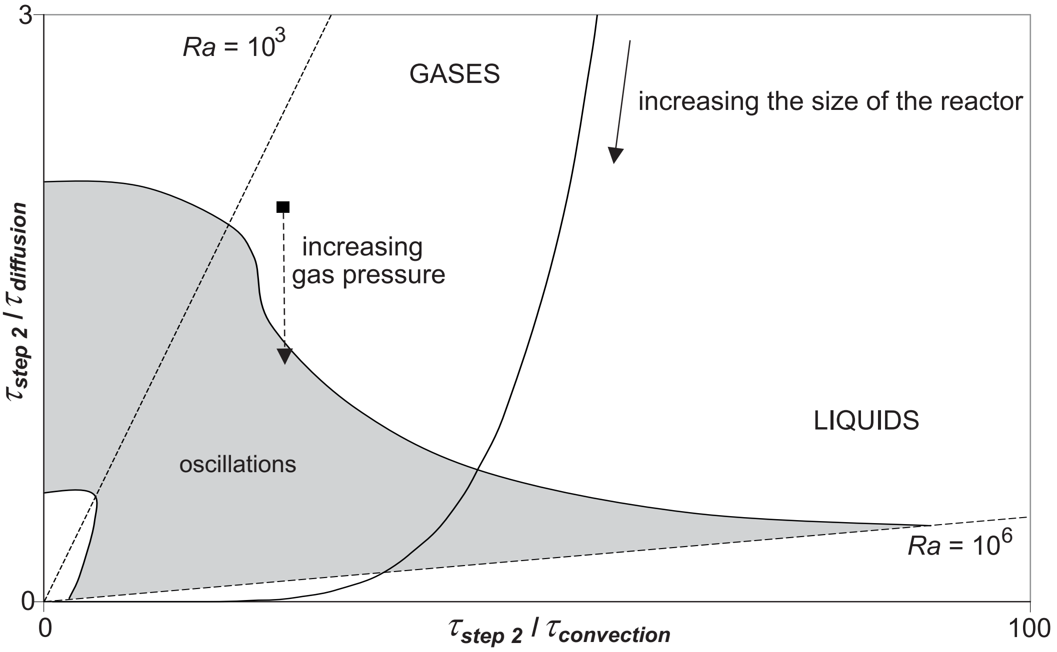

Figure 3.13. Regime diagram showing the effect on the position of the working point of increasing the gas pressure, increasing the reactor's size, and the effect of performing the reaction in the liquid-phase. The area in grey denotes approximately where the concentration of the intermediate and the temperature oscillate as in Figure 3.3(b).

Shown in Figure 3.13 are two lines of constant Ra, which represent the approximate transition from weak flow to laminar flow and from laminar flow to turbulent flow. The region in which oscillations have been observed is also included, schematically, in Figure 3.13; this region will be discussed in greater detail in section 5.2. The effect of increasing the pressure in a gas-phase reaction is considered first. The kinetic theory of gases indicates that ν and κ, the momentum and thermal diffusivities, are both inversely proportional to pressure. This means that the Rayleigh number is proportional to $\mathscr{P}^2$. Thus, increasing the pressure increases the Rayleigh number and therefore the intensity of the convective flow. A system represented by a point on the regime diagram of Figure 3.13 actually moves vertically downwards, when the pressure is increased, because the terms in the abscissa are independent of pressure. The system could accordingly move from a situation of negligible convection at low pressure, through one of laminar flow, to eventually turbulent convection, when the pressure is increased.

The effect of increasing the reactor's size is shown by the solid line in Figure 3.13 (*n.b.* $\tau_{step\,2}/\tau_{diffusion} \propto 1/L^2$; $\tau_{step\,2}/\tau_{convection} \propto 1/L^{1/3}$). It is clear from this plot that making the reactor smaller significantly reduces the Rayleigh number, thereby making diffusive processes more significant. Figure 3.13 shows that when small reactors are considered, even relatively small increases in reactor size can significantly alter the Rayleigh number, which *ex hypothesi* has an explicit dependence on L^3. There is also a dependence of ΔT on L *via* Eq. (3.19) or (3.24).

As for the effect of temperature on *Ra*, for a purely gaseous system in the convective regime, *Ra* turns out to be inversely proportional to $T_0^{11/3}$, according to the simplest version of the kinetic theory of gases. Otherwise, the main effect of temperature on the location of the working point in Figure 3.13 is *via* the exponential in the Arrhenius function for k_2. Consequently any increase in temperature reduces $\tau_{step\ 2}$ and so moves the working point towards the origin of Figure 3.13, whose abscissa and ordinate are both proportional to $\tau_{step\ 2}$.

The final effect highlighted on Figure 3.13 is the effect of moving from a reaction in the gas-phase to one in the liquid-phase. Comparing the relative magnitudes of the terms in the Rayleigh number for typical gases and liquids indicates that Rayleigh numbers will be at least an order of magnitude higher for liquid-phase systems, for similar increases, ΔT, in temperature and identical values of L. Thus comparing *Ra* for reactions with the same ΔT, g and L in water and air at normal temperature and pressure indicates that *Ra* with water is some 240 times *Ra* with air. In fact, ΔT for a reaction in the liquid-phase is likely to be only ~ 10% larger than for a reaction with the same kinetic parameters (q_2, k_1, k_2,…) in the gas-phase. The overall result is that gaseous and liquid systems occupy quite different areas of Figure 3.13. In a liquid-phase reaction, natural convection is therefore likely to be more vigorous and important than in a gas-phase reaction with similar kinetic parameters. Certainly Figure 3.13 indicates that natural convection is likely to be most important (*i.e.* turbulent) in reactors on an industrial scale, because of the dependence on L^3. Whenever natural convection is stronger, Figure 3.13 makes it clear that there is a greater likelihood of oscillations in the reactor. This is because of the quite different portions of the two axes (Figure 3.13) occupied by the region wherein oscillations occur. Thus on the vertical axis, the region for oscillations roughly extends over $0.5 < \tau_{step\ 2} / \tau_{diffusion} < 2$, whereas along the horizontal axis, oscillations occur over approximately $5 < \tau_{step\ 2} / \tau_{convection} < 90$.

3.6 Comparison with Scaling Results from Chapter 2

If the analysis presented previously is correct, the forms of the scales for the dimensionless temperature rise, defined in sections 3.4.2 and 3.4.3 for diffusive and convective control of transport, respectively, when Sal'nikov's reaction occurs in a spherical vessel (assuming $k_1 << k_2$), should be similar in form to those derived in Chapter 2 for a simpler one-step exothermic decomposition reaction. It is therefore interesting to compare the two sets of scaling results, one verified through comparison with experiments, the other through comparison with numerical simulations.

The scales derived for both reactions are proportional to the ratio of the characteristic timescale for the dominant transport mechanism, either diffusion or natural convection, and a timescale for reaction. It was mentioned in section 3.3, however, that the forms of the reaction timescales were different for the two different mechanisms. In Chapter 2, the timescale for reaction was defined as

$$\tau_{reaction} = \frac{\rho_0}{k_0 c_0^n}, \qquad (2.14\ \text{b})$$

whereas, in Eqs. (3.16 a, b) for Sal'nikov's reaction, the timescales for the two steps of the reaction were

$$\tau_{step\ 1} = \frac{1}{k_1} \text{ and } \tau_{step\ 2} = \frac{1}{k_{2,0}}. \qquad (3.16\ \text{a, b})$$

The form of $\tau_{reaction}$ defined by Eq. (2.14 b) is clearly a more general definition than those presented for Sal'nikov's reaction. It is interesting, then, to apply this more general definition to the two first-order steps of Sal'nikov's reaction. For step 1 of the reaction

$$\tau_{reaction\ 1} = \frac{\rho_0}{k_1 p_0^1} = \frac{1}{k_1} = \tau_{step\ 1}, \qquad (3.31)$$

since $\rho_0 = p_0$. Similarly, for step 2 of the reaction, using the relation in Eq. (3.18) for a_0

$$\tau_{reaction\ 2} = \frac{\rho_0}{k_{2,0} a_0^1} = \frac{\rho_0 k_{2,0}}{k_{2,0} k_1 p_0} = \frac{1}{k_1} = \tau_{step\ 1}. \qquad (3.32)$$

For both steps of Sal'nikov's reaction, the characteristic timescale defined in Eq. (2.14 b) reduces to $\tau_{step\ 1}$. This is unsurprising, since step 1 is considered to be slow, and hence the rate determining step of the reaction. Because the reactive timescales are equivalent for the simple exothermic reaction considered in Chapter 2 and Sal'nikov's scheme, the scales for the dimensionless temperature rise in each case can be compared directly.

For the low *Ra* cases presented in Chapter 2, an expression was found for the maximum temperature rise at the centre of the reactor. This was

$$\gamma \frac{\Delta T}{\Delta T_{ad}} = 0.23 \frac{\tau_{diffusion}}{\tau_{reaction}}. \tag{2.23}$$

If this expression is compared with the results for Sal'nikov's reaction for 'small' reactors, Eq. (3.26),

$$\gamma \frac{\Delta T}{\Delta T_{ad}} = 0.141 \frac{\tau_{diffusion}}{\tau_{reaction}}, \tag{3.26}$$

it can be seen that there is good agreement between the scales derived for the two different reactions. The numerical coefficients in each case are of similar order. It is also interesting to note that the experimental results shown in Figure 2.2 for the thermal decomposition of azomethane and the numerical results in Figure 3.6 for Sal'nikov's reaction show similar deviations from the linear form predicted by scaling when $\tau_{diffusion} / \tau_{reaction}$ increases above ~ 0.035. It was shown in section 2.3.2 that for azomethane, the deviation from linearity was due to the transition from a regime with slow reaction, to an explosive regime. Similarly, for Sal'nikov's reaction, the deviation from linearity is due to a change of regime, this time from a region of slow reaction to an oscillatory regime. It can be inferred, therefore, that the region of oscillations in Sal'nikov's reaction is occurring at the transition between slow reaction and explosion. This is another reassuring similarity between the behaviour exhibited by Sal'nikov's reaction and that seen in real cool flames.

A similar comparison can be made for the case where natural convection is more important. The scale derived in Chapter 2 in this case is given by Eq. (2.25):

$$\gamma \frac{\Delta T}{\Delta T_{ad}} = 2.97 \frac{\tau_{convection}}{\tau_{reaction}}. \tag{2.25}$$

The results derived in section 3.4.3 for Sal'nikov's reaction were formulated for the temperature at a distance $L / 2$ above the centre of the reactor, rather than at the centre of the reactor as was the case for Eq. (2.25). In addition, the numerical factors in these equations were derived through comparison with experimental results for *Ra* ~ 1000 – 2000. This is lower than was considered in section 3.4.3. To counter these problems, simulations were carried out in this lower range of *Ra* and the temperatures at the centre of the reactor were used to produce a modified expression for the temperature rise:

$$\gamma \frac{\Delta T}{\Delta T_{ad}} = 3.32 \frac{\tau_{convection}}{\tau_{reaction}} . \tag{3.33}$$

The agreement between the scales for the two different reaction schemes is once again reasonable. One point that does need to be borne in mind is that when Sal’nikov’s reaction occurs under the influence of natural convection, oscillations are observed over a wide range of conditions. These oscillations make it difficult to define for the system a characteristic temperature rise, which can be used in the calculation of the numerical factor in Eq. (3.33). This degree of uncertainty means that the agreement that is seen is actually better than it first appears. Nevertheless, the agreement between the scaling results in Chapter 2 and those derived in this chapter is rather good. The agreement for the two different reactions is expected, given that the constants should only depend on the geometry of the system.

Finally, the scales derived for Sal’nikov’s reaction occurring in a spherical reactor can be compared with the experimental results of Ashmore *et al.* (1967), which appear in Figure 2.10. The reactions described in this plot (nitric oxide with oxygen, hydrogen with chlorine and azomethane pyrolysis) have different orders of reaction, *e.g.* it was shown in Chapter 2 that the order of azomethane decomposition was ~ 1.4, the reaction between NO and O_2 is second order with respect to NO and first order with respect to O_2, and the reaction of hydrogen with chlorine is complex (Ashmore and Wesley, 1965; Coppersthwaite *et al.*, 1991). The fact that the experimental measurements from these different reactions show such good agreement means that the comparison of Sal’nikov’s reaction with these previous measurements is valid, and that the trends shown in Figure 2.10 are, potentially, the same for any exothermic reaction occurring in the presence of natural convection. As in section 2.4.5, the ratio of the scales for the temperature rise under the influence of diffusion and natural convection can be calculated (see Eq. (2.33)) and then compared with experimental results. The ratio of the temperature rises is

$$\frac{\Delta T_{diffusion}}{\Delta T_{convection}} = \frac{0.141 \dfrac{\tau_{diffusion}}{\tau_{reaction}}}{3.32 \dfrac{\tau_{convection}}{\tau_{reaction}}} = 0.042 \frac{\tau_{diffusion}}{\tau_{convection}} = 0.042 (Ra\, Pr)^{1/2} . \tag{3.34}$$

Equation (3.34) can be plotted against the experimental results. This is done in Figure 3.14. The agreement between the experimental, numerical and scaling results is, once again, excellent, and the transition from diffusive to convective control of transport occurs at *Ra* ~ 500. In this case the quantitative agreement between the scaling results in Eq. (3.34) and the experimental measurements is better than that found in Eq. (2.33), based on the scaling results for azomethane.

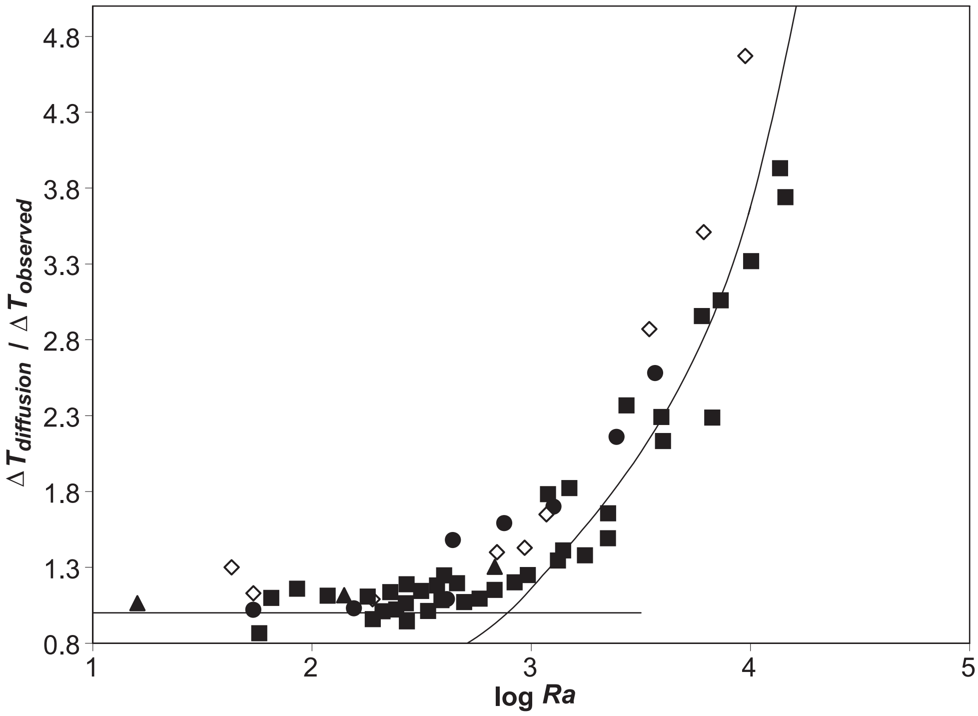

Figure 3.14. The ratio of the temperature rise in a purely conductive system to the observed temperature rise plotted against log *Ra*. The experimental results of Ashmore *et al.* (1967) for two different exothermic reactions (NO with O_2 and H_2 with Cl_2) occurring in a spherical reactor are shown, as are the experimental results of Gerri and Kaufman (1965) for the decomposition of azomethane. The results of numerical simulations for the thermal decomposition of azomethane are shown, as are lines representing a temperature ratio of 1, as would be the case in the diffusive regime, and the results of the analytical scaling analysis for Sal'nikov's reaction (Eq. (3.34)) when convection is important. The other symbols are the same as in Figure 2.10.

3.7 Summary

In this chapter, an analytical scaling analysis has been performed for Sal'nikov's reaction occurring in a spherical batch reactor. This analysis was performed for the two limiting cases where diffusion and natural convection are the dominant modes of heat and mass transfer within the reactor. The forms of these analytical scales were confirmed through comparison with numerical simulations.

It is interesting to note that different scales could be derived depending on the values of the characteristic timescales for the various interacting phenomena in the system, and the behaviour of the system is governed by the ratios of these timescales. It was found for the range of physical parameters studied, in the case of both diffusive and convective control of transport, that the characteristic concentration of the intermediate A depends only on the kinetic terms, and that the temperature rise in the reactor is proportional to the ratio of the timescales for the dominant transport mechanism to the timescale of the rate determining step of the reaction.

The scales developed yield an insight into the general behaviour of the system. The scales can therefore be used to predict how the system will respond to changes in key process parameters. The effects of varying the pressure of the gas, the size of the reactor and the temperature of the wall were all deduced. In addition, the effect of carrying out the reaction in the liquid-phase was investigated.

The scales developed in this chapter, describing the behaviour of Sal'nikov's reaction were compared with the results derived in Chapter 2 for a simpler reaction scheme. The agreement between the scaling results for both reactions was very good, and the scaling results derived for Sal'nikov's reaction showed excellent agreement with experimental measurements. This agreement between the scales derived for different reactions, and with experimental results, highlights the power of what is, essentially, quite a simple analytical technique. Despite its apparent simplicity, this method can yield significant insight into a problem.

Finally, several areas of interesting behaviour were observed, both for the case of diffusion dominated transport and natural convection dominated transport. Of particular interest were the observed oscillations. They were found in relatively narrow parameter ranges, and an understanding of what these ranges are is essential. An understanding of where oscillations occur is therefore sought in Chapters 4, 5 and 6.

4 Sal'nikov's Reaction with the Diffusion of Heat and Mass, but without Natural Convection

4.1 Introduction

When Sal'nikov's reaction occurs in a spherical vessel while diffusion controls transport, many interesting types of behaviour are seen. In Chapter 3, three distinct regions of behaviour were observed, namely: (i) a region of slow reaction, where the temperature rises were small, (ii) a region in which oscillations of the temperature and the intermediate A were observed, and (iii) a region of more rapid reaction, with a large temperature increase. These three regions are, at least qualitatively, similar to the regions of slow combustion, cool flames and explosion seen on a real ignition diagram (Figure 1.1). It was noted in section 3.4 that oscillations were observed over a very narrow range of parameters, apparently corresponding to $\tau_{diffusion} \sim \tau_{step\ 2}$; however, the generality of this observation was not explored. When considering a potentially oscillatory reaction, it is clearly of vital importance to know under what conditions oscillations occur. This chapter aims to identify a region of parameter space in which oscillations occur for the case when the transport of heat and mass is purely by diffusion. Such a system would be similar to the experimental study of cool flames carried out by Pearlman (2000) in microgravity.

Previous theoretical and numerical studies of this diffusion-reaction system have focussed primarily on either temporal oscillations or the formation of stable spatial patterns under the pool chemical approximation, where the effects of the decay of the concentration of the precursor P are ignored. Thus, Gray and Scott (1990*b*) studied, analytically, both the temporal and spatial stability of a simplified rectangular geometry in which diffusion occurs in only one dimension. Also, Forbes (1993) studied the formation of spatial patterns in a similar rectangular, pseudo-one-dimensional geometry and also in a circular geometry (Forbes, 1996). These analytical studies, whilst powerful, have been performed for geometries which are not physically significant. Fairlie and Griffiths's (2001, 2002) numerical studies of Sal'nikov's reaction in a purely diffusive system have considered some aspects of the temporal development of oscillations when the reaction occurs in a spherical vessel. It must be said that the dimensionless groups used in previous analytical studies have meant that physical interpretation of the results is problematic. Nevertheless, Fairlie and Griffiths (2001, 2002) did show numerically that there was a finite region in parameter space in which oscillations occurred; they did not, however, explore this region in any great detail. This chapter aims to completely define a region in parameter space where oscillations occur. This region can then be compared with the results of the previous analytical studies of Gray and Scott (1990*b*) in a simplified geometry. In addition to defining this region of oscillations, the non-oscillatory solutions are also to be investigated. To this end, approximate analytical solutions for the temperature and concentration of A are presented for two limiting cases of non-oscillatory behaviour.

In section 4.2, the equations governing the system when diffusion is the only transport mechanism operating are presented. A region of oscillations is defined through numerical simulations and is presented in section 4.3. In addition, this region is compared with the results of Gray and Scott's (1990*b*) analytical stability analysis. As well as comparing the results of the two methods, the two different strategies for dimensional analysis are also compared. The analysis of the non-oscillatory regions is presented in section 4.4.

4.2 Governing Equations

The governing equations take similar forms to those presented in section 3.2; however, the only transport mechanism considered is diffusion, as *e.g.* would be the case if the reaction were carried out in microgravity, so the convective terms are suppressed. Thus, the equation governing the conservation of the intermediate A can therefore be stated as:

$$\frac{\partial a}{\partial t} = D_A \nabla^2 a + k_1 p_0 \exp(-k_1 t) - k_2(T) a \,. \tag{4.1}$$

The conservation of energy can be expressed as:

$$\frac{C_V}{C_P}\frac{\partial T}{\partial t} = \kappa\nabla^2 T + \frac{q_2 k_2(T)}{\rho_0 C_P} a\,, \tag{4.2}$$

where the density, ρ_0, is considered to remain constant throughout. The assumption of constant density is, of course, a considerable simplification and this should be borne in mind when interpreting the results; however, the previous analytical (Forbes, 1993, 1996; Gray and Scott, 1990*b*) and numerical studies (Fairlie and Griffiths, 2001, 2002) of Sal'nikov's reaction occurring with purely diffusive transport processes have made the same assumption. The adoption of such an assumption also allows easier comparison with the numerical results in the presence of natural convection, when the Boussinesq approximation is applied. Comment should also be made on the inclusion of C_P, the heat capacity at constant pressure, in what is a constant volume system. Its inclusion arises from the thermal diffusivity being defined as $\kappa = k_T / (\rho\, C_P)$ to enable comparison between the results in a purely diffusive system, with those observed when convection plays a role. To achieve the required form of κ, each term in Eq. (4.2) is accordingly divided by $\rho_0\, C_P$. It is assumed that the thermal diffusivity is independent of temperature.

The boundary conditions used are the same as in the previous chapter, *i.e.*

$$t = 0: \quad p = p_0; \;\; a = 0; \;\; T = T_0; \quad \forall \underline{x}$$

$$\text{At the wall}: \; \underline{n}.\nabla p = \underline{n}.\nabla a = 0; \;\; T = T_0\,. \tag{4.3}$$

These boundary conditions are the same as those studied numerically by Fairlie and Griffiths (2001, 2002); however, the previous analytical studies (Forbes, 1993, 1996; Gray and Scott, 1990*b*) assumed that at the boundary of the region of interest, there was no heat flux.

Equations (4.1) and (4.2) can be made dimensionless by the same methods discussed previously, *i.e.* through introducing the following dimensionless variables:

$$a' = \frac{a}{a_0}; \; p' = \frac{p}{p_0}; \; T' = \frac{T - T_0}{\Delta T}; \; \underline{x}' = \frac{\underline{x}}{L} \text{ and } t' = \frac{\kappa t}{L^2}\,, \tag{4.4 a – e}$$

where L is the radius of the reactor, p_0 is the initial concentration of the precursor P, and the scales for the characteristic concentration of the intermediate A, a_0, and the temperature rise, ΔT, are of the form defined in section 3.3.1, *i.e.*

$$a_0 \sim \frac{k_1}{k_{2,0}} p_0; \;\; \Delta T \sim \frac{q_2 k_1 L^2}{C_P \kappa}\,. \tag{4.5 a, b}$$

It should be noted that in Eq. (4.4 e), the time has been made dimensionless by dividing by $\tau_{diffusion}$, instead of $\tau_{convection}$ as was done previously.

This approach differs somewhat from that used in previous studies of the well-mixed or diffusive systems, which have chosen other dimensionless groups from thermal explosion theory to reduce the governing equations. Such analyses, with some small variations, have been presented by Gray and Scott (1990*a*, *b*) and by Fairlie and Griffiths (2001, 2002). In particular, Gray and Scott presented their results in both the well-mixed (Gray and Scott, 1990*a*) and diffusive (Gray and Scott, 1990*b*) regimes in terms of the parameter-space coordinates $\mu_{G\,\&\,S} = k_1\, t_{cooling}\; p \;/\; c_{ref}$, which is a dimensionless measure of the concentration of the precursor, and $\kappa_{G\,\&\,S} = k_2\; t_{cooling}$, which is a measure of the dimensionless rate of step 2 of Sal'nikov's reaction. In the well-mixed system, $t_{cooling}$ was taken to be the Newtonian cooling time, and in the diffusive system it was taken as the Fourier timescale. The reference concentration, c_{ref}, is a large group containing kinetic terms as well as terms describing heat transfer between the system and its surroundings. The analysis presented by Gray and Scott (1990*a*, *b*) is powerful, but due to the nature of the dimensionless groups used, it is difficult to interpret the physical significance of their results. By using the simple dimensionless variables in Eqs. (4.4) and (4.5), physical interpretation of the results should be straightforward.

The governing equations can be made dimensionless using the parameters defined in Eq. (4.4). The dimensionless equations can be written in terms of the characteristic timescales for the two steps of the reaction and diffusion. These are, as before:

$$\tau_{step\,1} = \frac{1}{k_1};\; \tau_{step\,2} = \frac{1}{k_{2,0}};\; \tau_{diffusion} = \frac{L^2}{\kappa}. \tag{4.6 a – c}$$

The dimensionless governing equations therefore become

$$\frac{\partial a'}{\partial t'} = \frac{1}{Le}\nabla'^2 a' + \frac{\tau_{diffusion}}{\tau_{step\,2}}\exp\left(-t'\frac{\tau_{diffusion}}{\tau_{step\,1}}\right) - \frac{\tau_{diffusion}}{\tau_{step\,2}}\exp\left(\frac{\phi_{ad}\dfrac{\tau_{diffusion}}{\tau_{step\,1}}T'}{1+\dfrac{q_2}{C_P T_0}\dfrac{\tau_{diffusion}}{\tau_{step\,1}}T'}\right)a', \tag{4.7}$$

$$\frac{1}{\gamma}\frac{\partial T'}{\partial t'} = \nabla'^2 T' + \exp\left(\frac{\phi_{ad}\dfrac{\tau_{diffusion}}{\tau_{step\,1}}T'}{1+\dfrac{q_2}{C_P T_0}\dfrac{\tau_{diffusion}}{\tau_{step\,1}}T'}\right)a'. \tag{4.8}$$

The parameters η and ϕ, which appear in the exponentials in the dimensionless governing Eqs. (3.11) and (3.12) discussed previously, have been expanded as:

$$\phi = \frac{E_2 \Delta T}{R T_0^2} = \frac{E_2}{R T_0^2} \frac{q_2}{C_P} \frac{\tau_{diffusion}}{\tau_{step\ 1}} = \phi_{ad} \frac{\tau_{diffusion}}{\tau_{step\ 1}}, \text{ and} \tag{4.9 a}$$

$$\eta = \frac{\Delta T}{T_0} = \frac{1}{T_0} \frac{q_2}{C_P} \frac{\tau_{diffusion}}{\tau_{step\ 1}}. \tag{4.9 b}$$

The expressions for these variables have been included in the exponential terms in Eqs. (4.7) and (4.8). It is clear from the form of these equations that the behaviour of a given chemical system depends only on the two groups:

$$\frac{\tau_{step\ 2}}{\tau_{diffusion}} \text{ and } \frac{\tau_{step\ 2}}{\tau_{step\ 1}}, \tag{4.10}$$

which correspond to two of the axes on the three-dimensional regime diagram proposed by Cardoso *et al.* (2004*b*), shown in Figure 1.5. This chapter is concerned solely with the vertical plane on this diagram, defined by the axes $\tau_{step\ 2} / \tau_{diffusion}$ and $(\tau_{step\ 2} / \tau_{step\ 1})\, p'$, which corresponds to the reaction occurring in a purely diffusive system *e.g.* in microgravity. Inspection of Eq. (4.7) shows that p', the dimensionless concentration of the precursor P, is given by:

$$\exp\left(-t' \frac{\tau_{diffusion}}{\tau_{step\ 1}}\right) = \exp\left(-t' \frac{\tau_{diffusion}}{\tau_{step\ 2}} \frac{\tau_{step\ 2}}{\tau_{step\ 1}}\right). \tag{4.11}$$

Thus, for the case in which the precursor P is initially distributed uniformly within the reactor, p' is a function of the two groups in Eq. (4.10) and can therefore be eliminated from the axis of the regime diagram. It is clear that the two groups in Eq. (4.10), which can be used as parameter-space coordinates, are simple and have a well-defined physical meaning. In this regard, the approach used in this work is an attractive alternative to the method of Gray and Scott (1990*a*, *b*) described above.

4.3 Defining a Region of Temporal Oscillations

4.3.1 Numerical Simulations

The region of parameter space in which oscillations occurred was defined by performing many simulations. As in Chapter 3, the thermal decomposition of di-*t*-butyl peroxide was considered. The temperature of the wall of the spherical reactor was held constant at T_0 = 500 K and the physicochemical properties used were the same as described in section 3.4.1. The value of k_1 was varied over the range 0.0035 – 0.0375 s^{-1}, corresponding to a range for $\tau_{step\ 1}$ of ~ 26 – 285 s. The value of $k_2 = Z_2 \exp(-E_2 / R\,T)$ was taken to be that for the decomposition of di-*t*-butyl peroxide, with $Z_2 = 2 \times 10^{15}$ s^{-1} and E_2 / R = 18280 K. These values give $k_{2,0} = 0.265$ s^{-1}, and thus $\tau_{step\ 2}$ ~ 4 s. The analysis described in the previous section indicates that the behaviour of the system is defined by the ratio of the kinetic timescales (Eq. (4.10)). To test this hypothesis $\tau_{step\ 2}$ was also varied. This is, of course, a purely hypothetical action, conducted to validate the results in section 4.2. The value of $k_{2,0}$ was varied by altering the pre-exponential factor Z_2 over the range $6.3 \times 10^{13} - 2 \times 10^{15}$ s^{-1}, with E_2 / R held constant at 18280 K. This corresponds to $\tau_{step\ 2}$ ~ 4 – 120 s. Furthermore, the simplifying assumption that the Lewis number was unity was made. This implies that $\kappa = D_A$, *i.e.* the diffusivities of heat and chemical species were considered to be equal. This is approximately true for a gas, but not a liquid. For example, for an ionic reaction in water, *Le* ~ 100. Throughout this work, the values of the diffusivities were held constant at $\kappa = D_A = 1 \times 10^{-4}$ $m^2\ s^{-1}$. The value of $\tau_{diffusion}$ was therefore altered by changing the radius of the reactor, L. A similar variation in $\tau_{diffusion}$ could alternatively be achieved by keeping the radius of the vessel constant, and altering the diffusivity, as was done by Fairlie and Griffiths (2002), who considered reaction occurring in a vessel of radius 0.0492 m with diffusivities of 3×10^{-4} and 6×10^{-4} $m^2\ s^{-1}$.

4.3.2 Previous Analytical Work on a Pseudo-1-D System

An understanding of how the system behaves in different regions of parameter space is clearly very important. Principally, the region in which temporal oscillations are observed needs to be defined. Gray and Scott (1990*b*) performed a linear stability analysis on Sal'nikov's reaction occurring in a box, in which diffusion was the only transport mechanism operating. The system they studied is shown in Figure 4.1, with the reactants contained in a long and very thin box. At either end of the box (x = 0, L) there is perfect insulation so no heat can leave the system there. It was also assumed that there is no surface reaction, or other loss of chemical species from the system at these walls. Therefore, there are no-flux conditions, for both chemical species and heat, applied at the right- and left-hand ends of the box. It was also assumed that the horizontal boundaries at $y = 0$, l_0 are impermeable to the chemical species contained in the box, *i.e.* there is no flux of any chemical species across these boundaries. Heat can however be lost from the horizontal boundaries to the surroundings, under the control of a heat transfer coefficient. The box is also considered to be sufficiently thin in the y-direction for the concentration and temperature to vary only in the x-direction. This means that diffusion, of either heat or mass, can occur in only one dimension, parallel to the x-axis. In this system, oscillations can arise from thermokinetic effects, *i.e.* due to variations in the production of heat *via* the exothermic reaction and heat loss to the surroundings. In addition, oscillations can result from the diffusion of heat and mass along the thin box destabilising the system. As Gray and Scott (1990*b*) themselves point out, this situation bears little resemblance to any real situation; however, it does allow analytical solutions to be derived. It should also be said that the spherical reactor studied in this work is much more relevant to 'real' systems.

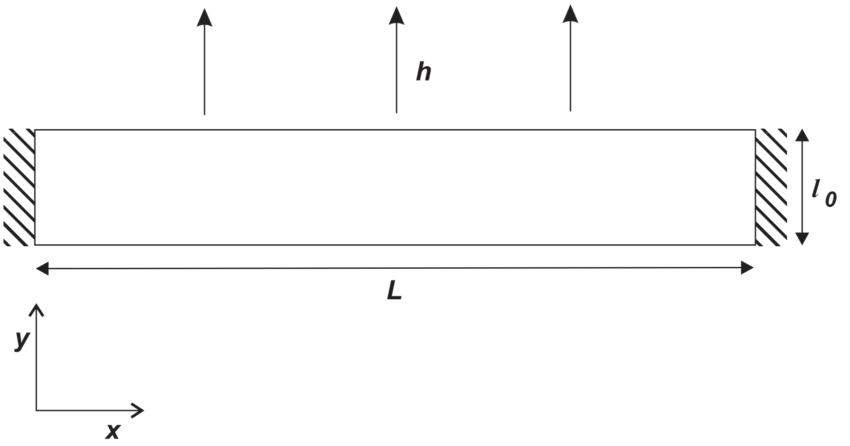

Figure 4.1. Schematic representation of the one-dimensional system considered in the analytical work of Gray and Scott (1990*b*). There is no flux of either heat or mass from the left and right hand ends. There is also no mass flux from the horizontal boundaries; however, heat is lost to the surroundings, with the rate governed by h, the heat transfer coefficient.

Whilst the spherical geometry and boundary conditions discussed below are different from those studied by Gray and Scott (1990*b*), their analytical work does provide an excellent point of reference for the numerical results described below. In the course of their stability analysis, Gray and Scott (1990*b*) were able to define a closed region in parameter space, within which the steady state solution (which can be achieved if the pool chemical approximation is applied) is unstable. In practice, this corresponds to a region where sustained temporal oscillations of the temperature and concentration of A are observed. The behaviour of the system described by Gray and Scott (1990*b*) depends on the four dimensionless parameters: $\beta_{G\,\&\,S}$, $\mu_{G\,\&\,S}$, $\kappa_{G\,\&\,S}$, and $\gamma_{G\,\&\,S}$. These dimensionless numbers can be transformed to yield expressions in terms of the ratios of timescales defined in Eq. (4.10). This transformation allows the region of instability to be plotted on the appropriate vertical plane of the regime diagram in Figure 1.5, whilst also making the results of Gray and Scott (1990*b*) easier to interpret physically. There is however a complication in this transformation of coordinates. Gray and Scott's (1990*b*) work includes a heat transfer coefficient in the derivation of the aforementioned dimensionless groups. The spherical system considered in the present work does not describe heat transfer using a transfer coefficient, and the timescales defined in Eq. (4.6) do not allow for this. To overcome this difficulty, the heat transfer coefficient is defined in terms of a Nusselt number, *i.e.*

$$h = Nu\, k_T / L\,. \tag{4.12}$$

This definition can be substituted into the definitions of the dimensionless groups in Gray and Scott's (1990*b*) work, yielding:

$$\beta_{G\&S} = 1/(Le\,\gamma);$$
$$\gamma_{G\&S} = Nu\, L/l_0\,;$$
$$\mu_{G\&S} = \frac{\phi}{\gamma\,\gamma_{G\&S}^2}\left(\frac{\tau_{diffusion}}{\tau_{step\,2}}\right)^2 \frac{\tau_{step\,2}}{\tau_{step\,1}}\,p' \quad \text{and} \tag{4.13 a – d}$$
$$\kappa_{G\&S} = \frac{1}{\gamma\,\gamma_{G\&S}}\frac{\tau_{diffusion}}{\tau_{step\,2}}\,.$$

The region of instability identified by Gray and Scott (1990*b*) was expressed in terms of the coordinates $\mu_{G\,\&\,S}$ and $\kappa_{G\,\&\,S}$, and hence can be plotted on the regime diagram of Figure 1.5 using the relations derived in Eq. (4.13 c, d). It was noted that if the axes $\tau_{step\,2}$ / $\tau_{diffusion}$ and $\tau_{step\,2}$ / $\tau_{step\,1}$ are used on the regime diagram, as defined by Cardoso *et al.* (2004*b*), the closed region of instability defined by Gray and Scott (1990*b*) becomes open because the values of the boundaries between stable and unstable solutions tend to infinity. This problem can of course be remedied by simply plotting the reciprocal of the two coordinates, *i.e.* $\tau_{diffusion}$ / $\tau_{step\,2}$ *versus* $\tau_{step\,1}$ / $\tau_{step\,2}$. Plotted in Figure 4.2 is the region of instability identified by Gray and Scott (1990*b*) for their pseudo-1-D system on the regime diagram with these inverted coordinates. The other two variables, $\gamma_{G\,\&\,S}$ and $\beta_{G\,\&\,S}$, represent adjustable parameters, which vary the size of the unstable region. The effect of varying $\gamma_{G\,\&\,S}$ is shown in Figure 4.2. Increasing

$\gamma_{G\,\&\,S}$, by having a larger Nusselt number for lateral heat transfer, or increasing the length of the box, L, or by decreasing the width, l_0, in Figure 4.1 increases the value of the ordinate of the boundary, whilst the abscissa remains constant. The value of $\beta_{G\,\&\,S}$ is fixed at ~ 1 by the physical parameters defined in section 4.3.1. When $\beta_{G\,\&\,S}$ is increased, the region of instability grows in the direction of both the ordinate and abscissa. An increase in $\beta_{G\,\&\,S}$ corresponds to a decrease in Le (= κ / D_A), the Lewis number, which indicates that there is a much larger area of instability if the molecular diffusion coefficient (D_A) is much larger than the thermal diffusivity (κ). Realistically, the Lewis number is likely to be larger than 1, therefore the region of instability will be smaller. This observation is supported by the work of Fairlie and Griffiths (2002), who looked at Le = 1, 2 and 6 for a given set of kinetic parameters. Their results showed that at the conditions chosen, increasing the Lewis number increased the rate at which the oscillations in temperature were damped away.

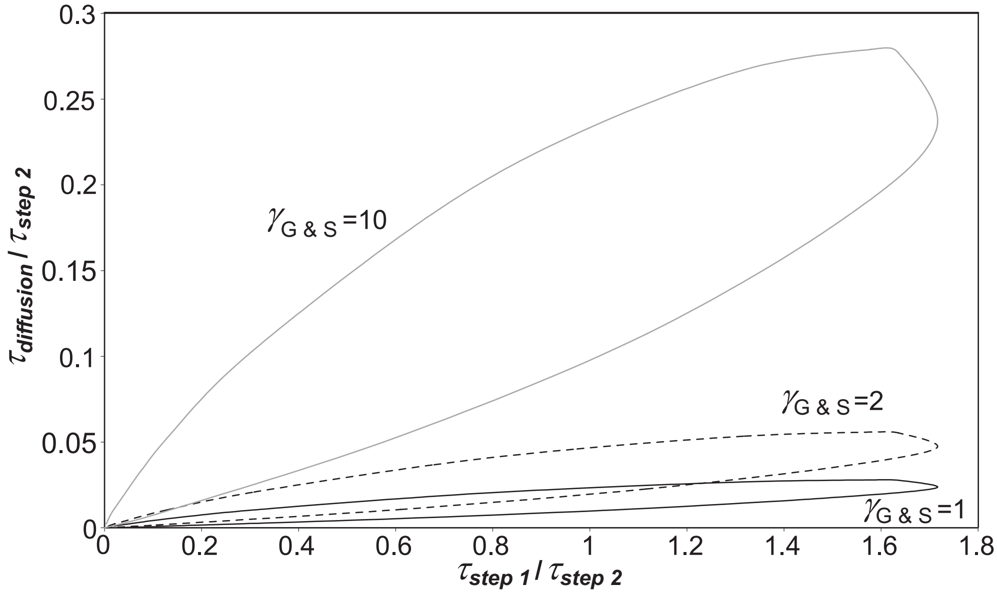

Figure 4.2. The analytically derived region of instability presented by Gray and Scott (1990*b*) for $\beta_{G\,\&\,S}$ = 0.96. In this region, sustained oscillations occur. The effect of varying the dimensionless parameter $\gamma_{G\,\&\,S}$ on the region of instability is indicated by the three different curves.

4.3.3 Regions of Oscillation in a Spherical Reactor

A series of numerical simulations was carried out in order to identify those regions on the regime diagram in which temporal oscillations in the temperature and concentration of the intermediate A occur in a spherical vessel of radius L. The approximate regions identified by performing many simulations are shown in Figure 4.3. As was the case with Gray and Scott's pseudo-1-D system (Gray and Scott, 1990*b*), closed regions of oscillations were found. The results presented in Figure 4.3 are for a system with the dimensionless groups γ, Le, ϕ_{ad} and $q_2 \ / \ C_P \ T_0$ held constant (see Eqs. (4.7) – (4.9)). Variation of these groups would result in a different region of oscillations. It should also be noted that because the Lewis number is assumed to be unity, it is likely that the oscillations observed in the simulations are a result of thermokinetic effects, that is to say the instabilities are driven by differences in local rates of heat production and loss. At low values (< 3) of $\tau_{step\ 1} \ / \ \tau_{step\ 2}$, the numerical scheme used in the simulations breaks down due to the appearance of large temperature spikes; even so, it seems reasonable to suggest that the boundaries (in Figure 4.3) identified through the simulations (for step 2 much faster than step 1) extend back to the origin, as is the case in the pseudo-1-D geometry in Figure 4.2 and in the well-mixed regime (Gray and Scott, 1990*a*). The section of the boundary which is dashed indicates the expected behaviour in the region where the numerics break down. These could be confirmed by using a different modelling technique, which is able to handle temperature spikes, *e.g.* a finite volume approach could be used. It was observed in section 3.4.2 that in the simulations run to confirm the scaling analysis, oscillations were found in a region where $\tau_{diffusion} \sim \tau_{step\ 2}$. Figure 4.3 shows that this observation was purely coincidental. The region of oscillations does, however, lie approximately in a region in which $0.04 \ \tau_{step\ 1} < \tau_{diffusion} < 0.2 \ \tau_{step\ 1}$, subject to the constraint that $\tau_{diffusion} < 4 \ \tau_{step\ 2}$. It should be noted that Figure 4.3 shows regions of damped oscillations, as well as sustained temporal oscillations, whereas Gray and Scott (1990*b*) identified a region of instability, which would correspond solely to sustained temporal oscillations (Figure 4.2). If the region of sustained oscillations in Figure 4.3 is compared with the region of instability in the pseudo-1-D system in Figure 4.2, it can clearly be seen that in the spherical system, the region is more extensive by an order of magnitude (on both axes). There are many factors which can contribute to this difference, the most obvious of which is, of course, the different geometry. The change from the pseudo-1-D system with linear geometry to one with spherical symmetry can have a dramatic impact on the progress of the reaction. There is also the difference in heat transfer to consider. The lateral heat loss, characterised by a heat transfer coefficient in the pseudo-1-D system of Gray and Scott (1990*b*), contrasts with the spherical system, inside which heat can, quite realistically, only be transferred by conduction. One further difference is in the boundary conditions. The pseudo-1-D system considers there to be no heat or mass flux at the side walls, whereas in the spherical system, heat is removed from the system at the wall because of the constant temperature condition. These effects seem to combine to ensure that the spherical system is much more unstable to temporal disturbances, and hence has a larger region in which sustained temporal oscillations are observed. The much larger region of damped oscillations in Figure 4.3 corresponds to steady state solutions which are stable. However, they would be focal in character, if a stability analysis were performed on a system with the pool chemical approximation assumed. This results in relatively small scale oscillations, which decay away very rapidly (in many cases only one oscillatory cycle was seen before steady decays in temperature and the concentration of A were observed). The results presented here, *i.e.* a relatively small region of sustained oscillations surrounded by a larger region of damped oscillations, are similar to those found by Gray and Scott (1990*a*) in the well-mixed regime. Indeed, those authors found a region of sustained oscillations surrounded by a region of damped oscillations, which was approximately an order of magnitude larger.

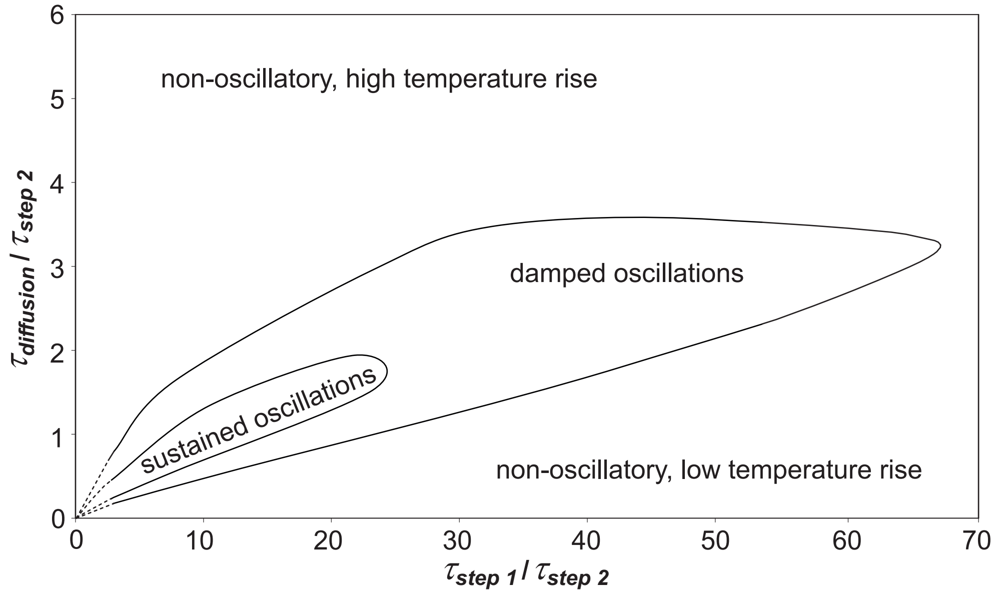

Figure 4.3. Regime diagram showing the approximate regions of oscillations, identified through numerical simulation, in the case of a spherical batch reactor. The dashed lines represent extensions of the boundaries in the region where the numerical scheme broke down.

The regions of oscillation can also be compared with the numerical results of Fairlie and Griffiths (2002), who studied the effect of varying k_1 when $L = 0.0492$ m for the cases when the diffusivities of heat and mass were first 3×10^{-4} m^2 s^{-1} and then 6×10^{-4} m^2 s^{-1}. The results they presented are reproduced on Figure 4.4, as is the nature of the temporal development of the temperature at the centre of the reactor for each case. Their results are clearly in good agreement with the region defined by the present work.

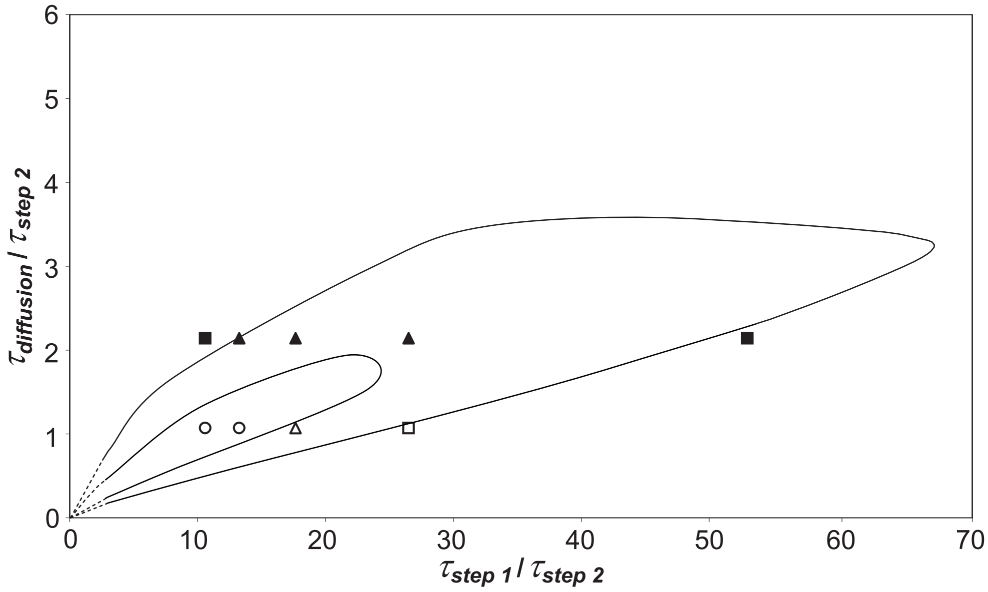

Figure 4.4. Regime diagram showing the regions of oscillations identified in Figure 4.3, and the numerical results of Fairlie and Griffiths (2002), for the case when $L = 0.0492$ m, $k_{2,0} = 0.264$ s^{-1}. The filled symbols represent the cases where the diffusivity was 3×10^{-4} m^2 s^{-1}, and the open symbols the cases where the diffusivity was 6×10^{-4} m^2 s^{-1}. In both cases the squares represent non-oscillatory solutions, the triangles represent damped oscillations and the circles sustained oscillations.

It is also interesting to observe how a point representing a given system moves in the regime diagram when the physical parameters are altered. For example, when $k_1 = 0.025$ s^{-1}, $k_{2,0} = 0.264$ s^{-1} (as it would be for the decomposition of di-*t*-butyl peroxide), $L = 0.0492$ m and $\kappa = D_A = 3 \times 10^{-4}$ m^2 s^{-1}, the values of the coordinates are $\tau_{diffusion} / \tau_{step\ 2} = 2.14$ and $\tau_{step\ 1} / \tau_{step\ 2} = 10.6$. This corresponds to the top left filled square in Figure 4.4, which is non-oscillatory. In order to move this system into an oscillatory state there are three possibilities (assuming the chemistry of step 2 is to remain unchanged): the precursor supply rate k_1 can be decreased (this corresponds to the system point moving horizontally to the right on Figure 4.4), the reactor size can be decreased or the diffusivity can be increased (through the addition of a diluent for example). The last two options correspond to the working point moving vertically downwards. By decreasing k_1 to ~ 0.02 s^{-1} the system will move into a region of the regime diagram in which damped oscillations occur. If k_1 is decreased below ~ 0.0052 s^{-1}, the system will again become non-oscillatory. It can be seen in Figure 4.4 that sustained oscillations cannot be achieved for any value of k_1, only damped oscillations occur. In order to exhibit sustained oscillations either the radius of the reactor or the diffusivity must be altered. Considering again the case where k_1 = 0.025 s^{-1}, if the radius of the reactor is reduced to ~ 0.046 m the system moves vertically downwards into a region of damped oscillatory behaviour. If the radius is reduced further, to ~ 0.0385 m, sustained oscillations emerge. These sustained oscillations continue until the radius of the reactor is reduced below ~ 0.028 m, when the behaviour reverts to damped oscillations. For a reactor of radius less than ~ 0.023 m there are no oscillations. Because the behaviour of the system is governed by the ratio $\tau_{diffusion}$ / $\tau_{step\ 2}$, similar effects to reducing the radius could be achieved by increasing the diffusivity. Thus, for a vessel with L = 0.0492 m and k_1 = 0.025 s^{-1}, damped oscillations emerge when the diffusivity is increased to ~ 3.5×10^{-4} m^2 s^{-1}, sustained oscillations emerge when the diffusivity reaches ~ 4.9×10^{-4} m^2 s^{-1}, but these revert to damped oscillations when the diffusivity is ~ 9.3×10^{-4} m^2 s^{-1} and finally the system becomes non-oscillatory when the diffusivity exceeds ~ 1.4×10^{-3} m^2 s^{-1}.

4.4 Analytical Non-Oscillatory Solutions

Whilst it is important to identify regions in parameter space where oscillations occur, inspection of Figure 4.3 shows that over the vast majority of this space, no oscillations are observed. The behaviour of the system in these regions with no oscillation also merits further study. It was noted in section 3.4.2 that three distinct types of temporal behaviour are exhibited by this system. These are presented in Figure 3.3, which shows the development of the temperature and the concentration of A at the centre of the reactor. For 'slow' reactions, which occur close to the $\tau_{step\ 1}$ / $\tau_{step\ 2}$ axis (*i.e.* $\tau_{diffusion}$ / $\tau_{step\ 2}$ is small) of the regime diagram of Figure 4.3, there is a slow growth and subsequent decay of the temperature and the concentration of A, as shown in Figure 3.3(a). The increase in temperature is very small (~ 8 K). It is observed that the concentration in the reactor is virtually uniform spatially at any time throughout the course of the reaction. Upon moving vertically upwards in Figure 4.3 (*i.e.* increasing $\tau_{diffusion}$ / $\tau_{step\ 2}$), a region of instability is entered resulting in oscillations. Shown in Figure 3.3(b) is a solution exhibiting sustained oscillations, as would be expected if the steady state of the corresponding pool chemical system were unstable. For values of $\tau_{diffusion}$ / $\tau_{step\ 2}$ above the region of oscillations in Figure 4.3, a third type of behaviour is seen. This is shown by Figure 3.3(c); there is an initial increase in the concentration of A, which then rapidly decays to almost zero. The temperature increases quickly initially, followed by a period of slower increase after the concentration has fallen to virtually zero. The temperatures reached in this region are considerably higher (~ 110 K in Figure 3.3(c)) than those seen for 'slower' reactions. This is not surprising, because this region of behaviour corresponds to larger reactors, with higher ratios of volume to surface area, so more heat can accumulate in the system.

The region of oscillatory behaviour, characterised by Figure 3.3(b), was identified in the previous section. The two other cases are now considered, and through appropriate simplification of the governing equations, approximate analytical solutions are sought for these two non-oscillatory cases.

4.4.1 Non-Oscillatory Solutions for a Low Temperature Rise with a Small $\tau_{diffusion}$ / $\tau_{step\ 2}$

As discussed above, the solution for small values of $\tau_{diffusion}$ / $\tau_{step\ 2}$ takes the form of a slow growth and decay of the temperature and concentration of A. It was also noted that, with diffusion faster than reaction, the concentration of A was virtually uniform throughout the whole reactor. This means that the diffusive term in the governing equation, Eq. (4.7), is small and can therefore be ignored. Also, because the temperatures reached in the reactor are relatively small (< 10 K increase generally), the exponential term in Eqs. (4.7) and (4.8), representing the Arrhenius temperature dependence of step 2 of Sal'nikov's reaction can be simplified:

$$\exp\left(\frac{\phi_{ad}\dfrac{\tau_{diffusion}}{\tau_{step\ 1}}T'}{1+\dfrac{q_2}{C_P T_0}\dfrac{\tau_{diffusion}}{\tau_{step\ 1}}T'}\right)\approx 1 \quad \text{, since } T' << 1 \tag{4.14}$$

The governing equations, assuming spherical symmetry therefore become in this situation:

$$\frac{\partial a'}{\partial t'} = \frac{\tau_{diffusion}}{\tau_{step\ 2}} \exp\left(-t' \frac{\tau_{diffusion}}{\tau_{step\ 1}} \right) - \frac{\tau_{diffusion}}{\tau_{step\ 2}} a' , \tag{4.15}$$

$$\frac{1}{\gamma} \frac{\partial T'}{\partial t'} = \frac{1}{r'^2} \frac{\partial}{\partial r'} \left(r'^2 \frac{\partial T'}{\partial r'} \right) + a' . \tag{4.16}$$

Equation (4.15) can be rewritten in terms of an ordinary derivative and solved to give:

$$a' = \frac{\tau_{step\ 1}}{\tau_{step\ 1} - \tau_{step\ 2}} \left(\exp\left(-t' \frac{\tau_{diffusion}}{\tau_{step\ 1}} \right) - \exp\left(-t' \frac{\tau_{diffusion}}{\tau_{step\ 2}} \right) \right). \tag{4.17}$$

for the evolution of the concentration within the reactor. Equation (4.17) can then be substituted into Eq. (4.16) to obtain a solution for the evolution of the temperature within the reactor:

$$\begin{aligned} T' = \sum_{n=1}^{\infty} & \frac{2\,\tau_{step\ 1}\,\gamma \exp\left\langle -(n\pi)^2 t'\gamma \right\rangle \cos(n\pi)\sin(n\pi r')}{n\pi r'(\tau_{step\ 1} - \tau_{step\ 2})\left((n\pi)^2 \gamma\tau_{step\ 1} - \tau_{diffusion}\right)\left((n\pi)^2 \gamma\tau_{step\ 2} - \tau_{diffusion}\right)} \times \\ & \left\{ \left[1 - \exp\left\langle (n\pi)^2 \gamma t' - t' \frac{\tau_{diffusion}}{\tau_{step\ 2}} \right\rangle \right] \tau_{step\ 2}\tau_{diffusion} \right. \\ & \left. + \tau_{step\ 1} \left[\exp\left((n\pi)^2 \gamma t'\right) \left((n\pi)^2 \gamma\tau_{step\ 2} \exp\left\langle -t' \frac{\tau_{diffusion}}{\tau_{step\ 2}} \right\rangle + \left(\tau_{diffusion} - (n\pi)^2 \gamma\tau_{step\ 2}\right) \exp\left\langle -t' \frac{\tau_{diffusion}}{\tau_{step\ 1}} \right\rangle \right) - \tau_{diffusion} \right] \right\} . \end{aligned} \tag{4.18}$$

These expressions for the dimensionless concentration of A and the dimensionless temperature rise can now be compared to the results of numerical simulations. This is done in Figure 4.5(a) for the concentration, and in Figure 4.5(b) for the temperature rise, at the centre of the reactor for increasing time. These results are for a system with $\tau_{diffusion}$ / $\tau_{step\ 2}$ = 0.017 and $\tau_{step\ 1}$ / $\tau_{step\ 2}$ = 10.6. There is excellent agreement between the analytical and numerical solutions in both cases.

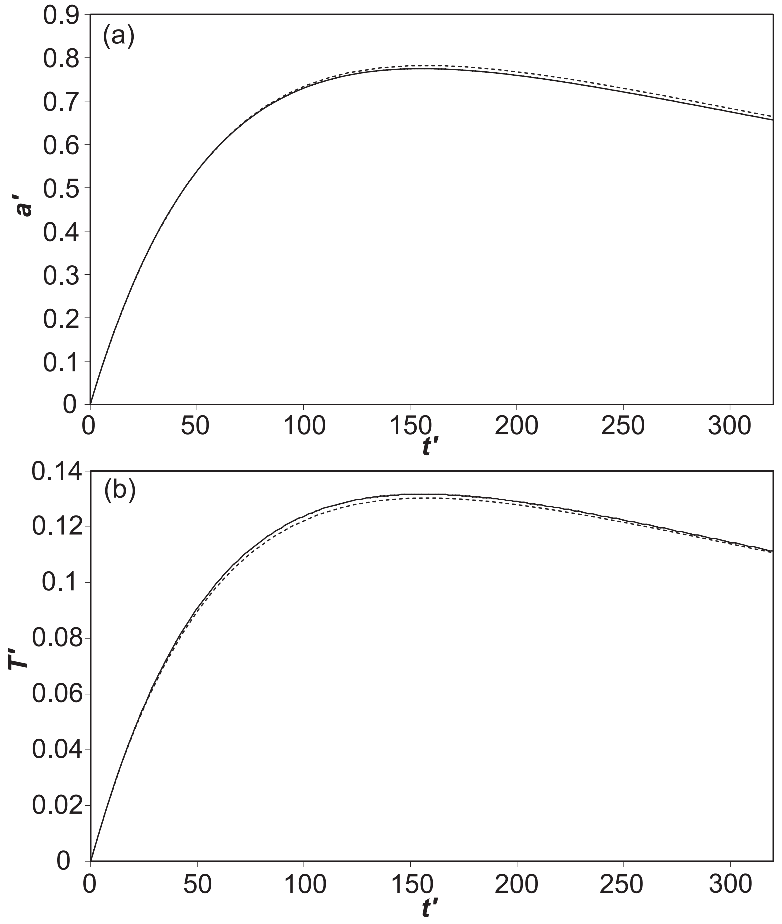

Figure 4.5. Comparison of the analytical (dashed line) and numerical (solid line) solutions for (a) the dimensionless concentration of A, and (b) the dimensionless temperature rise, at the centre of the reactor for the case where $\tau_{diffusion} / \tau_{step\ 2} = 0.017$ and $\tau_{step\ 1} / \tau_{step\ 2} = 10.6$. In the numerical solution $L = 0.0025$ m, $\kappa = 1 \times 10^{-4}$ m^2 s^{-1}, $k_1 = 0.025$ s^{-1} and $k_{2,0} = 0.264$ s^{-1}.

A comparison is made of the spatial form of the solutions in Eqs. (4.17) and (4.18) in Figure 4.6 with the numerically derived spatial solutions at two values of t'. Once again there is excellent agreement between the analytical and numerical results with the discrepancy between the two being ~ 1%. The forms found in Eqs. (4.17) and (4.18) prove to be good approximations to the full solution of the governing equations when $\tau_{diffusion} / \tau_{step\ 2} < \sim 0.1$. When the value increases much beyond this limit, the temperature rise in the reactor is such that the approximation in Eq. (4.14) breaks down.

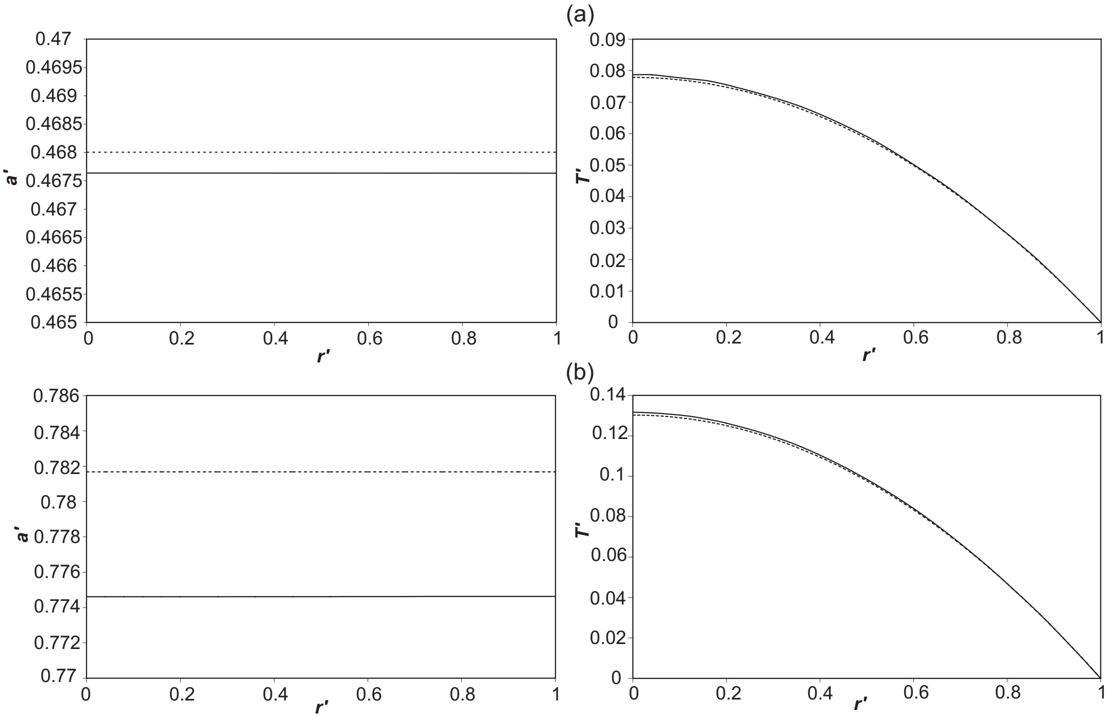

Figure 4.6. Comparison of the dimensionless spatial temperature and concentration profiles when $\tau_{diffusion} / \tau_{step\ 2} = 0.017$ and $\tau_{step\ 1} / \tau_{step\ 2} = 10.6$, at two distinct times: (a) $t' = 40$ and (b) $t' = 152$. The solid line represents the numerical solution and the dashed line the analytical solution. The conditions for the numerical solution are the same as in Figure 4.5.

4.4.2 Non-Oscillatory Solution for a High Temperature Rise with a Large $\tau_{diffusion} / \tau_{step\ 2}$

At larger values of $\tau_{diffusion} / \tau_{step\ 2}$, the simple approximations used in the previous section are not valid, because the exponential term in the Arrhenius equation becomes highly significant due to the much larger temperature rise; also the concentration of A in the reactor deviates from the approximate spatial uniformity seen in section 4.4.1. The form of the temporal solution seen in Figure 3.3(c) is also more complex, with an initial rapid increase in the concentration of A, followed by a sharp decline to almost zero. After this time, the concentration remains at approximately zero at the centre of the reactor. There are therefore two distinct temporal regions of behaviour, which can also be seen in the evolution of the temperature. There is an initial fast rise in temperature, whilst the concentration of A in the reactor is significant; however, when the concentration of A falls to virtually zero, there is a distinct change of slope in the plot of temperature against time in Figure 3.3 (c). Given that there are two regions of behaviour, the first of which is a 'temporal boundary layer', and that solutions are sought for extreme values of $\tau_{diffusion}$

/ $\tau_{step\ 2}$, this problem takes the form of a singular perturbation problem (see *e.g.* Varma and Morbidelli, 1997). This method involves asymptotic expansion of the dependent variables, *i.e.*

$$a'(r',t')=\sum_{n=0}^{\infty}\varepsilon^n a'_n(r',t')=a'_0+\varepsilon\, a'_1+O(\varepsilon^2), \text{ and} \tag{4.19}$$

$$T'(r',t')=\sum_{n=0}^{\infty}\varepsilon^n T'_n(r',t')=T'_0+\varepsilon\, T'_1+O(\varepsilon^2), \tag{4.20}$$

where ε is a small parameter determined from inspecting the governing Eqs. (4.7) and (4.8). These were rewritten in terms of the two coordinates of the regime diagram, namely $\tau_{diffusion}$ / $\tau_{step\ 2}$ and $\tau_{step\ 1}$ / $\tau_{step\ 2}$, by making the substitution:

$$\frac{\tau_{diffusion}}{\tau_{step\ 1}}=\frac{\tau_{diffusion}}{\tau_{step\ 2}}\frac{\tau_{step\ 2}}{\tau_{step\ 1}}. \tag{4.21}$$

Solutions are sought when $\tau_{diffusion}$ / $\tau_{step\ 2}$ tends to infinity, so the small parameter, ε, is therefore defined as:

$$\varepsilon\equiv\tau_{step\ 2}\big/\tau_{diffusion}. \tag{4.22}$$

Given the values of $\tau_{step\ 1}$ / $\tau_{step\ 2}$ over which oscillations occur (shown in Figure 4.3) the following definition

$$\tau_{step\ 2}\big/\tau_{step\ 1}=m\varepsilon, \tag{4.23}$$

where *m* is of order unity, was also made.

The singular perturbation method involves substituting the expansions (Eqs. (4.19) and (4.20)) into the governing equations and then collecting terms of similar order, with respect to the small parameter ε. These sub-problems can then be solved for each term in the asymptotic expansion. This method is useful in handling systems in which there are boundary layers. In this case there is a temporal boundary layer at t' = 0. The method involves considering an outer solution, corresponding to the conditions away from the boundary layer, and an inner solution, which deals with the boundary layer. A composite solution is then found by matching the two solutions at the edge of the boundary layer. The present work is only concerned with finding the $O(\varepsilon^0)$ terms, *i.e.* a'_0 and T'_0, in Eqs. (4.19) and (4.20); all higher order terms are neglected.

4.4.2.1 Outer solution

Equations (4.19) – (4.23) were substituted into Eqs. (4.7) and (4.8) in order to find the outer solution. Furthermore, the simplifying assumption that

$$\exp\left(\frac{\phi_{ad}mT'}{1+\dfrac{q_2}{C_PT_0}mT'}\right)\approx\exp(\phi_{ad}mT'), \tag{4.24}$$

was made, because in general $\frac{q_2}{C_PT_0}mT' << 1$. Solving for concentration yields a_0' for the outer solution as:

$$a_0'^o=\frac{\exp(-mt')}{\exp(\phi_{ad}mT_0'^o)}. \tag{4.25}$$

The expression derived in Eq. (4.25) was found without the application of the no-flux boundary condition at the wall of the vessel. This indicates that there is a concentration boundary layer at the wall. This has been ignored in the present analysis, so the solution will be valid in the middle region of the reactor, but not in the thin boundary layer at the wall. Equation (4.8) for the temperature reduces to:

$$\frac{1}{\gamma}\frac{\partial T_0'^o}{\partial t'}=\frac{1}{r'^2}\frac{\partial}{\partial r'}\left(r'^2\frac{\partial T_0'^o}{\partial r'}\right)+\exp(-mt'), \tag{4.26}$$

with the boundary conditions

$$\begin{aligned}&\frac{\partial T_0'^o}{\partial r'}(0,t')=0\\&T_0'^o(1,t')=0\end{aligned} \tag{4.27}$$

The initial condition depends on a matching of the inner and outer solutions and so is unknown at this stage.

4.4.2.2 Inner solution

For the inner expansion a stretching transformation is applied, *i.e.* the substitution

$$\omega=t'/\varepsilon, \tag{4.28}$$

is made in the governing equations. Considering first the concentration equation, the equation for $O(\varepsilon^0)$ gives:

$$\frac{\partial a_0'^i}{\partial \omega} = 1 - a_0'^i \exp\left(\phi_{ad} m T_0'^i\right),$$
$$a_0'^i(r',0) = 0 \tag{4.29}$$

A similar analysis for the temperature reveals that $T_0'^i$ = 0. This result can be substituted back into Eq. (4.29) yielding the inner solution for concentration:

$$a_0'^i = 1 - \exp(-\omega). \tag{4.30}$$

Equations (4.7), (4.8), (4.19), (4.20) and (4.28) suggest that the non-dimensional boundary layer thickness is of the order ε. Hence:

$$t_{boundary\ layer} = t'_{boundary\ layer}\ \tau_{diffusion} = \frac{\tau_{step\ 2}}{\tau_{diffusion}} \tau_{diffusion} = \tau_{step\ 2}\,. \tag{4.31}$$

4.4.2.3 Composite solution

To produce a solution which is valid across the whole region of interest, the inner and outer solutions must be combined. In general, this is done by adding the two solutions together and subtracting the common part in the overlapping region. This common part is defined as:

$$\lim_{\omega \to \infty}(\text{inner solution}) = \lim_{\varepsilon \to 0}(\text{outer solution}), \tag{4.32}$$

where this constraint also ensures that the solutions match at the edge of the boundary layer. This rule can most easily be applied to the composite solution for temperature. Because the inner solution for the temperature is zero, this implies that the missing initial condition in Eq. (4.27) is simply $T_0'^o$ = 0 at t' = 0. Using this additional condition, Eqs. (4.26) and (4.27) can be solved giving

$$T_0'^c = T_0'^o = \sum_{n=1}^{\infty} \frac{2\gamma \cos(n\pi)\sin(n\pi r')\exp(-mt')\left(\exp\left(t'\left[m-(n\pi)^2\gamma\right]\right)-1\right)}{r'\left((n\pi)^3\gamma - mn\pi\right)}, \tag{4.33}$$

where m, as defined by Eqs. (4.22) and (4.23), is

$$m = \tau_{diffusion} / \tau_{step\ 1}\,. \tag{4.34}$$

The solution for T' is therefore

$$T' = T_0'^c + O(\varepsilon). \tag{4.35}$$

It is interesting to note that the sole dimensionless group influencing the behaviour of the temperature dependence is the ratio of the timescales for diffusion and step 1 of the reaction. This is in general agreement with the scaling work presented in Chapter 3, where this ratio was found to determine the maximum temperature rise within the reactor. Similarly, the composite solution for the concentration of A can be found to be:

$$a_0'^c = \frac{\exp(-mt')}{\exp\left(\phi_{ad} m T_0'^o\right)} + \left(1 - \exp\left(-\frac{t'}{\varepsilon}\right)\right) - 1 = \frac{\exp(-mt')}{\exp\left(\phi_{ad} m T_0'^o\right)} - \exp\left(-\frac{t'}{\varepsilon}\right). \tag{4.36}$$

As in Eq. (4.35) for temperature, it can be said that

$$a' = a_0'^c + O(\varepsilon). \tag{4.37}$$

The predictions of the analytical expressions derived above are compared with the results of numerical simulations in Figures 4.7 and 4.8. The simulations were performed for a value of ε (=$\tau_{step\ 2}$ / $\tau_{diffusion}$) of 0.0052, and m = 0.57.

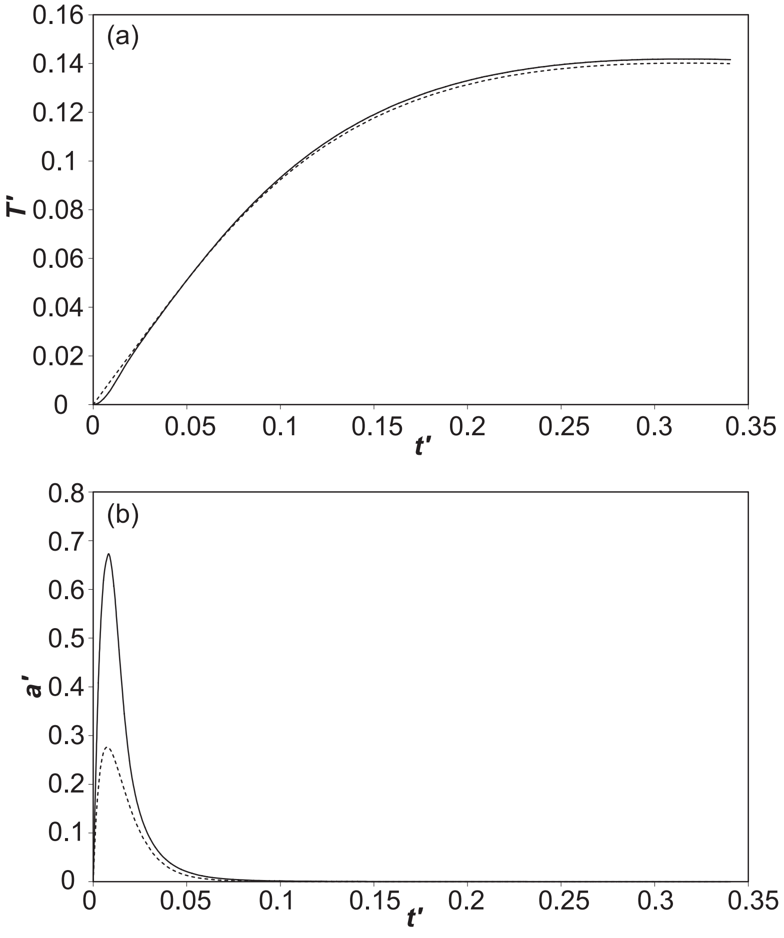

Figure 4.7. Comparison of the analytical (dashed line) and numerical (solid line) solutions for (a) the dimensionless temperature rise, and (b) the dimensionless concentration of A, at the centre of the reactor for the case where ε (=$\tau_{step\ 2}$ / $\tau_{diffusion}$) of 0.0052, and m (= $\tau_{diffusion}$ / $\tau_{step\ 1}$) = 0.57. In the numerical solution L = 0.085 m, κ = 1 × 10^{-5} m^2 s^{-1}, k_1 = 0.000795 s^{-1} and $k_{2,0}$ = 0.264 s^{-1}.

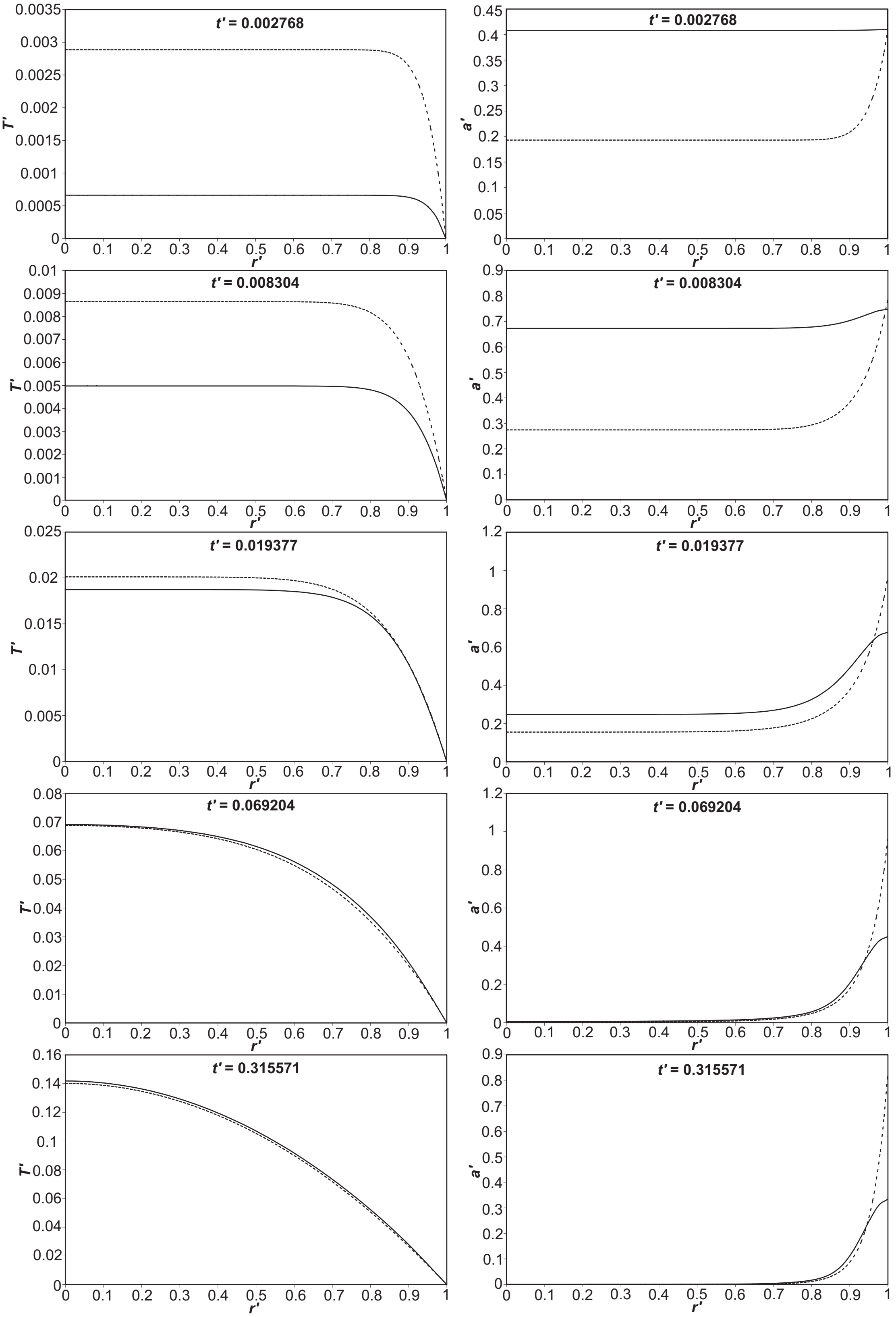

Figure 4.8. Comparison of the dimensionless spatial temperature and concentration profiles when ε ($=\tau_{step\ 2}$ / $\tau_{diffusion}$) of 0.0052, and *m* (= $\tau_{diffusion}$ / $\tau_{step\ 1}$) = 0.57 for increasing values of *t'*. These values appear at the top of each plot. The solid line represents the numerical solution and the dashed line the analytical solution. The conditions for the numerical solution are the same as for Figure 4.7.

Shown in Figure 4.7 are comparisons of the temporal development of (a) the temperature, and (b) the concentration of A at the centre of the reactor. There is excellent agreement between the analytical form for the temperature presented in Eq. (4.33) and the result of simulations. The largest discrepancy between the analytical and numerical solutions is at the start of the reaction, within the temporal boundary layer. This discrepancy would probably be remedied by the inclusion of higher order terms. Figure 4.7(b) shows a comparison of Eq. (4.36) for the concentration of A and the results from simulation. Once again, it is clear that for large values of time, beyond the temporal boundary layer, the agreement between the analytical and numerical solutions is excellent. Within the boundary layer, however, there is again a significant difference between the two solutions. The higher order terms, neglected in the analysis above, are clearly important within the temporal boundary layer. The calculation of these higher order terms is not trivial, and has therefore not been included in the present work.

Comparison can also be made of the spatial forms predicted by the analytical solutions above. Such a comparison is made in Figure 4.8 for five increasing values of t'. For small time, $t' < t'_{boundary\ layer}$, the discrepancy between the analytical and numerical forms of both the temperature and the concentration is evident. The overall shape of the temperature profile predicted by Eq. (4.33) is correct, but the magnitudes of numerical and analytical predictions differ. The simulations show that the concentration is approximately constant over the whole of the reactor. The analytical solution predicts a much larger spatial variation within the reactor with the concentration at the wall being roughly double that at the centre of the reactor. For larger times, when $t' \sim t'_{boundary\ layer}$, the analytical and numerical solutions begin to show better agreement, and for $t' > t'_{boundary\ layer}$, in the region corresponding to the outer solution, the agreement is excellent. However, there is disparity between the analytical and numerical solutions for large times at the wall, where the prediction of the concentration from the analytical solution is clearly wrong. The form predicted by Eq. (4.36) violates the no-flux boundary condition at the wall as expected. This implies that a further spatial concentration boundary layer is present at the wall. The work described above could therefore be extended to take account of this additional boundary layer; however, the form predicted by Eq. (4.36) is valid over the majority of the vessel ($r' < 0.95$), so this has not been considered in the present work.

The above comparison is, of course, for a very small value of $\varepsilon\,(=0.0052)$, which corresponds to large values of $\tau_{diffusion}$ / $\tau_{step\ 2}$ (~200) in the regime diagram of Figure 4.3. This is obviously a considerable way from the region of oscillations. For that reason, a comparison with a simulation much closer to the region of oscillations was also made. The agreement is inevitably poorer, because when $\tau_{diffusion}$ / $\tau_{step\ 2}$ is decreased, ε is increased and hence the higher order terms in Eqs. (4.35) and (4.37) are likely to play a much more significant role. The simulation used for comparison had ε (=$\tau_{step\ 2}$ / $\tau_{diffusion}$) = 0.15, and m = 0.63; the resulting temperatures at the centre of the reactor are presented in Figure 4.9. This case is much closer to the region of oscillations identified in Figure 4.3.

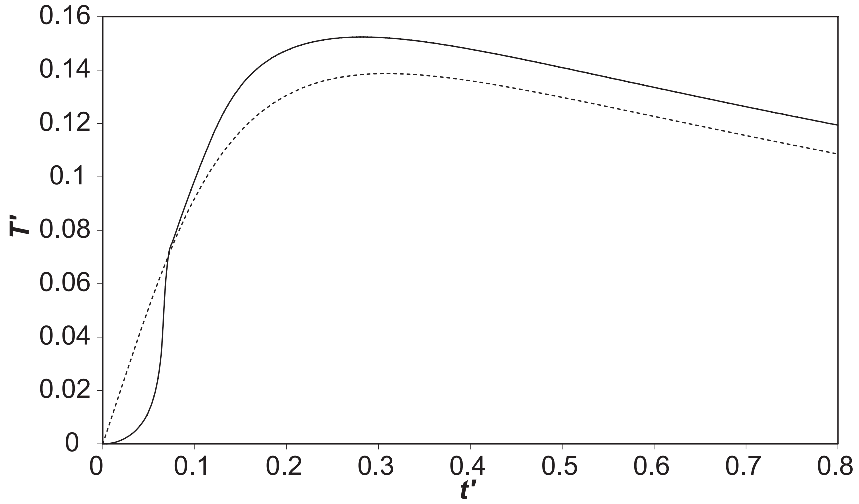

Figure 4.9. Comparison of the analytical (dashed line) and numerical (solid line) solutions for the temperature at the centre of the reactor when ε = 0.15, and m = 0.63. In the numerical solution L = 0.05 m, $\kappa = 1 \times 10^{-4}$ m^2 s^{-1}, k_1 = 0.025 s^{-1} and $k_{2,0}$ = 0.264 s^{-1}.

It is not surprising that in the temporal boundary layer, the analytical expression for concentration in Eq. (4.36) does not agree with the simulated results. Even when ε is two orders of magnitude smaller, the higher order terms are significant. Beyond the temporal boundary layer, Eq. (4.36) does provide a reasonable representation of the results of the simulation. Figure 4.9 shows a comparison of the analytical and numerical solutions for the temperature. The agreement is clearly not as good as for a smaller ε, but the analytical expression is still reasonable; there is, for example, only ~ 10% difference between the analytically derived maximum temperature, and that found by simulation. The largest apparent discrepancy is once again within the temporal boundary layer. The shape of the two curves is clearly different, but the temperature increase within the boundary layer is the same in both cases. Once again, the inclusion of higher order terms would probably correct the shape of the analytical solution in this region.

4.4.3 Oscillatory Solutions

The region in which oscillations are found falls at the transition between the two non-oscillatory cases discussed in sections 4.4.1 and 4.4.2. Whilst no analytical approximations have been sought in this region, it is possible to make some general observations. For example, it is interesting to note that the oscillatory solutions display characteristics of both the low temperature and high temperature reactions described in the previous sections.

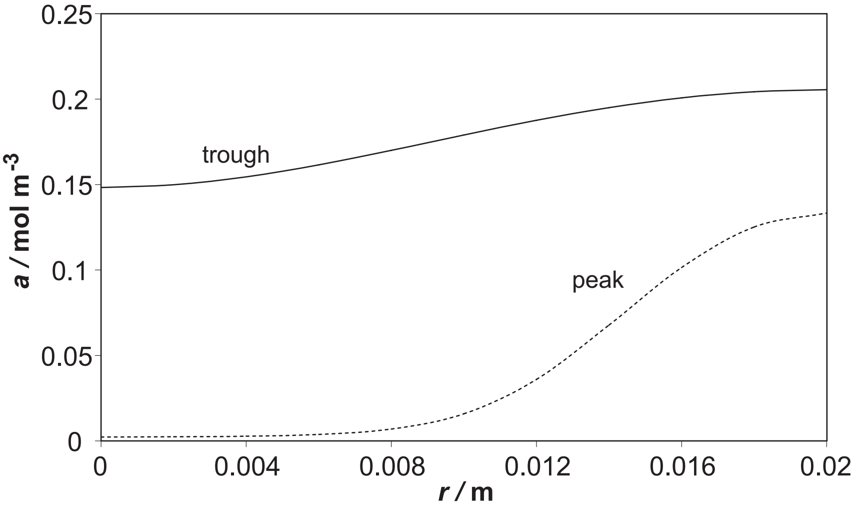

Figure 4.10. Spatial concentration profiles near the first peak and the first trough of an oscillatory cycle in temperature. In this case $L = 0.02$ m, $\kappa = 1 \times 10^{-4}$ m^2 s^{-1}, $k_1 = 0.025$ s^{-1} and $k_{2,0} = 0.264$ s^{-1}. The concentration profile for the temperature peak occurring at $t = 3.1$ s is shown as the dashed line, and the concentration profile at the temperature trough at $t = 5.1$ s is shown as a solid line.

Figure 4.10 shows the radial concentration profiles for the first peak and trough in the temperature in an oscillatory solution. At the first trough in the temperature, the concentration is virtually uniform spatially. This is similar to the behaviour discussed in section 4.4.1 for the non-oscillatory, low temperature rise reaction, as characterised by Figure 4.6. At the first peak in temperature, the concentration in the central portion of the reactor is virtually zero; however, it does increase near the wall. This behaviour is similar to that seen in Figure 4.8 and discussed in section 4.4.2 for the non-oscillatory, high temperature rise reaction. The oscillatory solutions occur at the transition between the two forms of non-oscillatory solutions discussed above, but interestingly show features of both of them.

4.5 Summary

This chapter has examined the behaviour of Sal'nikov's reaction, occurring in a spherical reactor in the absence of natural convection. A closed region in parameter space in which oscillations occur was defined by performing a series of numerical simulations. This region was found to be considerably larger than that defined by Gray and Scott (1990*b*) analytically, for a pseudo-one-dimensional geometry. This difference is probably due to the differing geometries of the systems considered, as well as to the differing modes of heat transfer considered in each case. In addition to identifying the region of parameter space in which oscillations occur, approximate analytical solutions were sought and found for two limiting types of non-oscillatory behaviour. The predictions of the new solutions were compared with the results of full numerical solutions, and the comparisons were favourable in each case. It was also observed that the oscillatory solutions exist at the transition between these two, non-oscillatory, cases and that the oscillatory solutions exhibit characteristics of both of these limiting cases.

The work presented in this chapter yields significant insight into the behaviour of Sal'nikov's reaction occurring in the presence of diffusion only. Similar insight is now sought for the case where natural convection plays a role. This analysis is presented in Chapter 5.

5 Sal’nikov’s Reaction with Natural Convection

5.1 Introduction

Chapter 4 dealt with oscillations when diffusion was the only transport mechanism. When natural convection occurs, the behaviour is more complex. This chapter examines the behaviour of Sal’nikov’s reaction when convection is significant. Specifically, a region in parameter space where oscillations occur should be identified. This is vitally important for gaining insight into the interaction of natural convection and the thermokinetic oscillations potentially produced by Sal’nikov’s reaction. A well defined region of oscillations is also important in the context of the discussions presented in section 3.5 regarding the effect of varying process parameters, such as the size of the reactor and the pressure. It is necessary to know how changing these parameters alters the behaviour of the system, and as was discussed previously, even small changes in the key process parameters can significantly alter the location of the working point locating a system in the regime diagram (Figure 1.5, Figure 3.13).

In addition to defining a region of oscillations in section 5.2, some of the interesting behaviour observed when Sal’nikov’s reaction occurs in the presence of varying intensities of natural convection is also discussed. In section 5.3, the characteristic behaviour in different areas of the regime diagram is examined. This highlights a very interesting feature of the oscillations when natural convection becomes more intense; quite oddly the oscillations in the temperature and the concentration of the intermediate A oscillate in-phase in the bottom half of the reactor. This contrasts with the behaviour seen in the well-mixed limit (*e.g.* Gray and Scott, 1990*a*) and in the purely diffusive limit, as discussed in section 3.4.2. Such occurrences are explored further in Chapter 6.

5.2 Defining a Region of Temporal Oscillations

A region in the regime diagram in Figure 1.5 in which oscillations occur under the influence of natural convection is to be found. Consider a system with reaction, diffusion and convection; this system is represented as a point (C) in the general 3-D regime diagram shown in Figure 1.5. As reaction progresses, p' decreases and hence the working point, locating the system on the diagram, moves along a line parallel to the $(\tau_{step\ 2} / \tau_{step\ 1})\ p'$ axis. However, if step 1 is much slower than step 2, p' decreases slowly and the pool chemical approximation is valid. Thus, it may be assumed that p' is approximately constant. Under these conditions the working point does not move in the 3-D diagram. This is true in general for step 1 of Sal'nikov's reaction being very slow. For the specific case considered in this work, *i.e.* with the precursor P being initially uniformly distributed throughout the reactor and remaining thus as the reaction proceeds, a similar analysis to that shown in Eq. (4.11) for the purely diffusive regime can be performed, thereby showing that p' can be removed from the axis of the regime diagram. Attention can therefore be focused on the 2-D plane, defined by the $\tau_{step\ 2} / \tau_{diffusion}$ and $\tau_{step\ 2} / \tau_{convection}$ axes (for a constant value of $\tau_{step\ 2} / \tau_{step\ 1}$), containing the working point. It was shown in Chapter 4 that in the diffusive limit, oscillations occurred over a finite range of $\tau_{step\ 2} / \tau_{diffusion}$. The $\tau_{step\ 2} / \tau_{diffusion}$ axis of the 2-D regime diagram corresponds to the diffusive limit, so this finite range of oscillations should be defined on this axis. Similarly, a closed region of parameter space in which oscillations occur for the well-mixed case was identified by Gray and Scott (1990*a*). The well-mixed limit corresponds to the $\tau_{step\ 2} / \tau_{convection}$ axis of the 2-D diagram. If a coordinate transform were performed, similar to that outlined in section 4.3.2, the oscillatory region could be mapped onto the regime diagram in Figure 1.5. It seems logical to conclude, therefore, that the region of oscillations when natural convection plays a role would join these two limiting cases.

The region of oscillations was defined by carrying out a series of many simulations, solving numerically the governing Eqs. (3.4) – (3.9). It should be noted that these simulations were for $Ra < 10^6$. Only the region of oscillations in the presence of weak and laminar natural convection is therefore considered. As before, the thermal decomposition of di-*t*-butyl peroxide was used as the model for step 2 of Sal'nikov's reaction, corresponding to $\tau_{step\ 2} \sim 4$ s. For all the simulations k_1 was held constant at 0.025 s^{-1}, therefore $\tau_{step\ 1}$ = 40 s. Different regions of the regime diagram were explored by varying the radius of the reactor, L, the acceleration due to gravity, g, and the thermal diffusivity, κ. It was again assumed throughout that $Le = Pr = 1$.

The results of these simulations are shown on the 2-D regime diagram in Figure 5.1. It should be noted that in calculating the value of $\tau_{convection}$ for points on this diagram, Eq. (3.24) was used for ΔT, and Eq. (3.20) was used for U, *i.e.* the forms of the scales used did not include the numerical factors calculated in section 3.4.3. The Rayleigh number was calculated using the expression:

$$Ra = 5.40\frac{\left(\tau_{step\ 2}/\tau_{convection}\right)^2}{\left(\tau_{step\ 2}/\tau_{diffusion}\right)^2}, \tag{5.1}$$

where the numerical factor comes from Eq. (3.28), calculated in section 3.4.3, and therefore ensures that the Rayleigh numbers calculated in this manner are similar to those observed in the simulations.

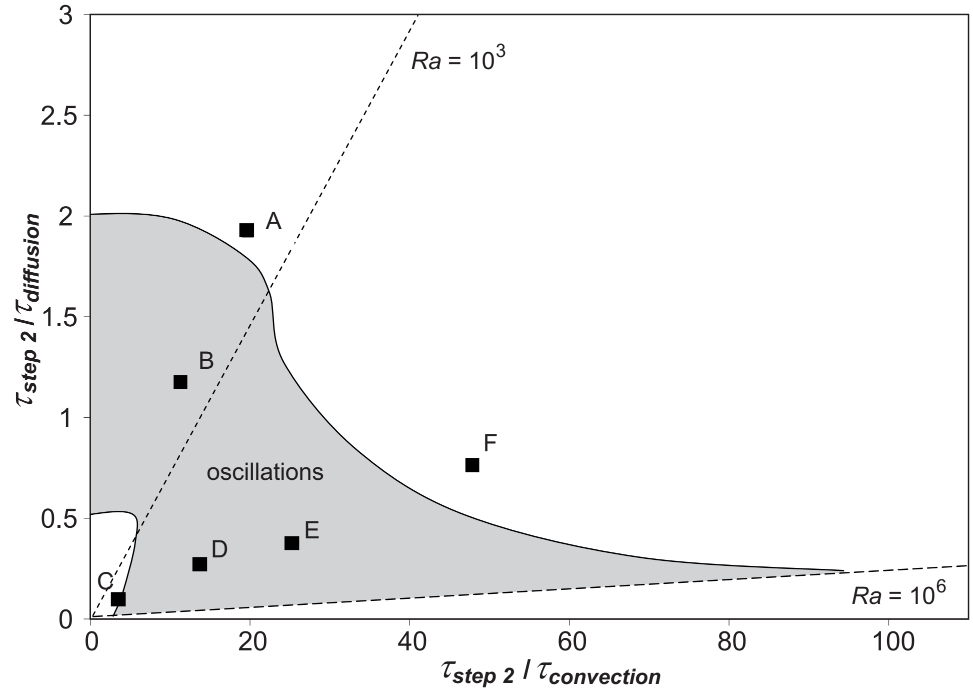

Figure 5.1. Two-dimensional representation of the regime diagram in Figure 1.5, for $\tau_{step\ 2} / \tau_{step\ 1}$ = 0.094. The shaded region shows where oscillations in the temperature and concentration of A occur. Also shown are two lines of constant Ra, corresponding to the approximate transition from weak flow to laminar flow ($Ra = 10^3$), and from laminar flow to turbulent flow ($Ra = 10^6$). The points A – F marked on the diagram correspond to the situations discussed in section 5.3.

The region in which oscillations were observed is shaded. If this region of oscillations is considered, it is clear that there are two distinct sections, namely that when $Ra < 10^3$, when diffusion is still dominant, and when $Ra > 10^3$ and natural convection becomes much more significant. When $Ra < 10^3$, the boundaries between the non-oscillatory and oscillatory solutions remain at an approximately constant value of $\tau_{step\ 2} / \tau_{diffusion}$ for increasing $\tau_{step\ 2} / \tau_{convection}$. These boundaries in the region of oscillations are in good agreement with the results in section 4.3.3 for a purely diffusive system. When Ra reaches ~ 10^3, there is a sharp change in the shape of the region of oscillations. This change is obviously due to natural convection superceding diffusion as the dominant transport mechanism. The fact that this change is observed at a Rayleigh number of just below 10^3 provides further confirmation that the model being used in the numerical simulations is capturing the principal physical processes correctly. The experimental observations of Tyler (1966) and Ashmore *et al.* (1967), discussed previously, showed that natural convection becomes significant when Ra is just below 10^3. When Ra exceeds 10^3, the shape of the oscillatory region is dramatically different. It is evident that oscillations occur over a very wide range of $\tau_{step\ 2} / \tau_{convection}$. This is consistent with the observation made in section 3.4.3 that oscillations occur over a much wider range of parameters when natural convection controls transport than when diffusion dominates transport. It is interesting to note that as Ra increases, the region of oscillations defined in Figure 5.1, increases significantly in size. As alluded to previously, the turbulent regime has not been considered in the present work. Obviously, as natural convection becomes turbulent, the degree of mixing in the reactor will increase. This will significantly affect the behaviour of the system. It would be interesting to see if there is a sharp change in the shape of the oscillatory region at the transition to turbulence, similar to that seen in Figure 5.1 at the transition from weak or no flow, to laminar convection. The region of oscillations defined in Figure 5.1 is, of course, for a fixed value of $\tau_{step\ 2} / \tau_{step\ 1}$, so in fact only represents a cross-section of a general 3-D space in which oscillations occur. A map of this 3-D space could be built up by performing simulations at different values of $\tau_{step\ 2} / \tau_{step\ 1}$; however, there is no reason to believe that the general shape of the 2-D cross-sections would be any different. The boundaries of the system on the axes, represented by regions of stability in the purely diffusive and well-mixed limits, would change according to the value of $\tau_{step\ 2} / \tau_{step\ 1}$, but it seems likely that the region joining these two limiting cases, *i.e.* the region in which natural convection is significant, would be of similar shape to that seen in Figure 5.1.

As one might expect, the oscillatory behaviour seen within the region defined in Figure 5.1 is not consistently identical throughout the different areas of the diagram. Various types of behaviour are seen, depending on the location in the regime diagram. The different types of behaviour observed are discussed in the next section, and in addition, the non-oscillatory regions are also examined.

5.3 Identifying Different Regions of Behaviour

5.3.1 Numerical Results

Figure 5.2 shows the development of the temperature and the concentration of A in a vertical cross-section through the centre of the reactor as time progresses, for the six cases highlighted on Figure 5.1. Details of these six cases appear in Table 5.1. Each case is characteristic of a different region of behaviour in the regime diagram; these will be discussed in turn.

Table 5.1. Details of cases A – F shown on the regime diagram in Figure 5.1.

case	L / m	g / m s^{-2}	$\kappa \times 10^4$ / m^2 s^{-1}	$\tau_{step\ 2}$ / $\tau_{convection}$	$\tau_{step\ 2}$ / $\tau_{diffusion}$
A	0.05	70	13	19.65	1.96
B	0.05	15	7.5	11.75	1.13
C	0.05	0.5	0.5	3.78	0.08
D	0.01	4.9	0.066	13.84	0.25
E	0.01	30	0.097	25.33	0.37
F	0.01	200	0.2	47.68	0.75

Case A is in the non-oscillatory region when $Ra < 10^3$. In this part of the regime diagram, the temperature shows a very slow growth and subsequent decay. This behaviour is evident in Figure 5.2, which shows that the temperature rise caused by the heating effect of the reaction is relatively small, and that the concentration of A remains virtually spatially uniform throughout the course of the reaction. This behaviour is very similar to that seen in section 4.4.1 for the non-oscillatory, low temperature rise solutions in the purely diffusive case. This similarity is expected given that case A is in a region of the regime diagram where diffusion controls heat and mass transfer, and it was shown previously that the non-oscillatory, low-temperature rise solutions occurred in the purely diffusive case for values of $\tau_{step\ 2}$ / $\tau_{diffusion}$ which were similar to those for case A.

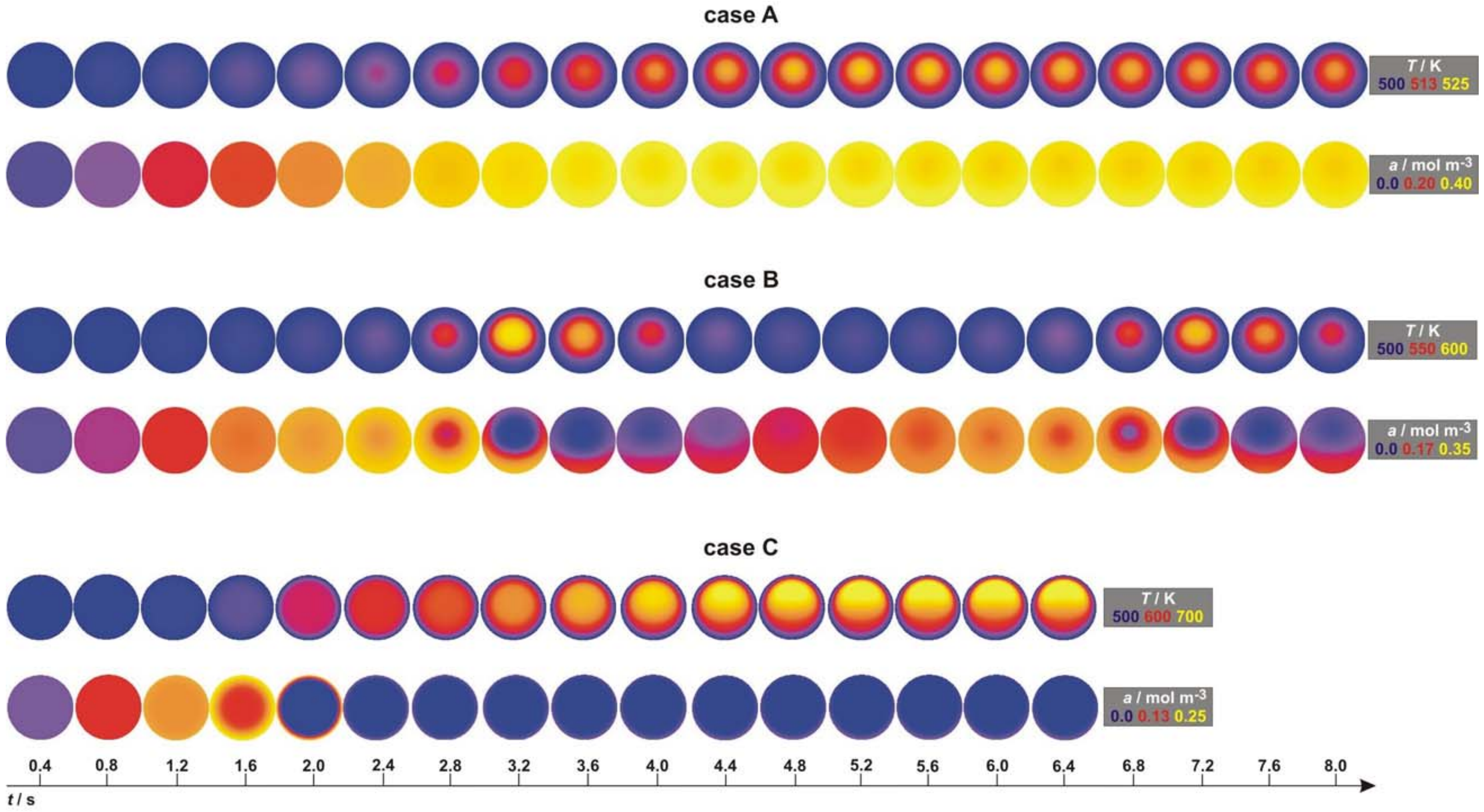

Figure 5.2(a). Development of the temperature (top) and concentration of A (bottom) for a vertical cross-section through the centre of the reactor for cases A – C. The progress of the reaction is shown for 8 s for cases A and B, and for 6.4 s for case C. The frames are separated by 0.4 s.

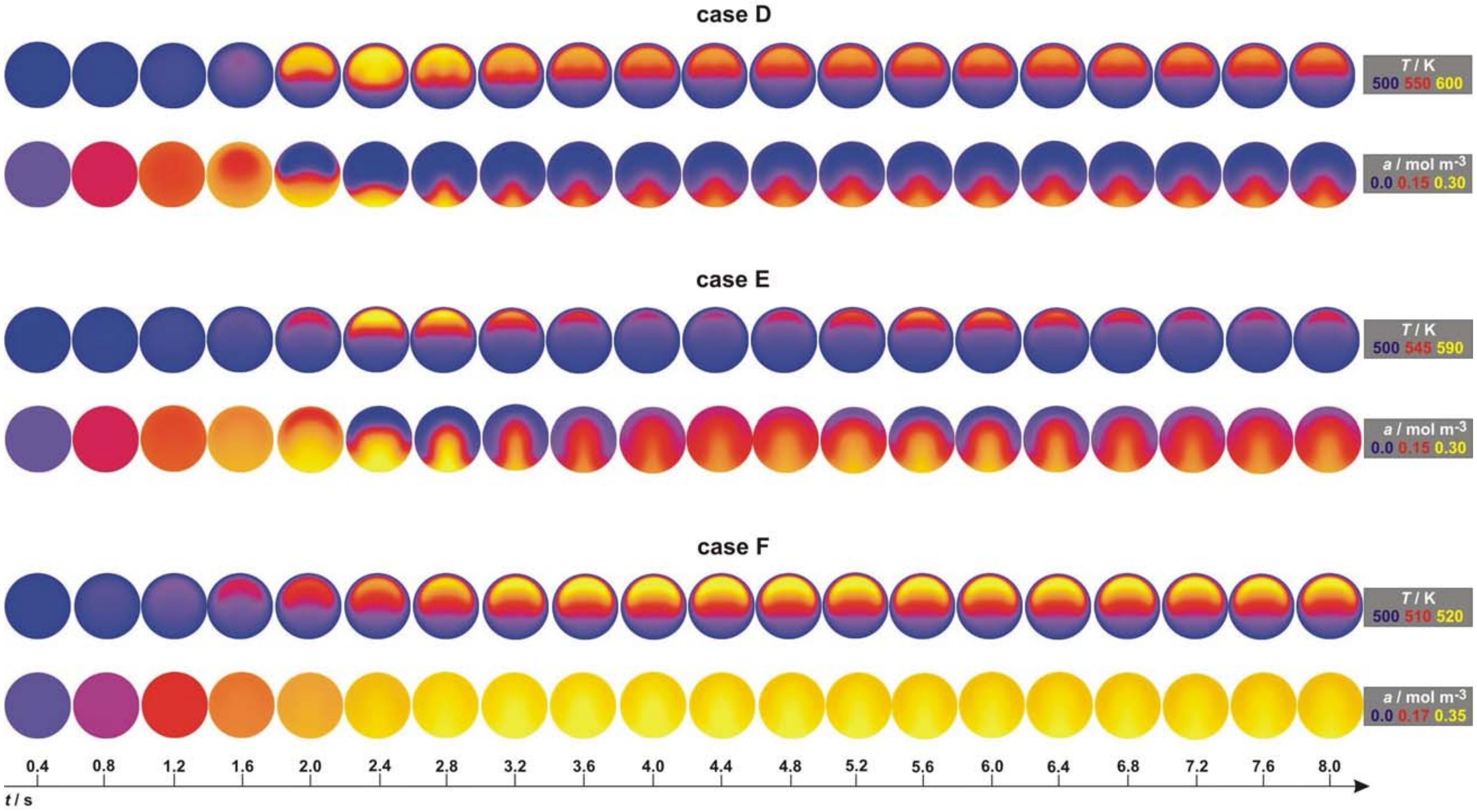

Figure 5.2(b). Development of the temperature (top) and concentration of A (bottom) for a vertical cross-section through the centre of the reactor for cases D – F. The progress of the reaction is shown for 8 s. The frames are separated by 0.4 s.

Despite occurring in a part of the regime diagram where diffusion is the dominant transport mechanism, the effects of weak natural convection can still be seen in case A in Figure 5.2. The spherical symmetry that would be expected in a purely diffusive system, such as those discussed in Chapter 4, has clearly been disrupted. The hot zone near the centre of the reactor has clearly been shifted upwards slightly, due to the influence of the weak convective flow. The spatial form of the solutions will be discussed further in section 5.3.3.

If the value of $\tau_{step\ 2} / \tau_{diffusion}$ is lowered with *Ra* kept below ~ 10^3, the system moves from the non-oscillatory state, typified by case A, into a region of oscillations. Case B is typical of a region of sustained oscillations. Figure 5.2 clearly shows that for case B, the temperature rise is far larger than for the slow reaction in case A. The concentration field is also far more complex than in case A; there is significant spatial variation. As before, the effects of the weak natural convection are evident in the disruption of the spherical symmetry and it is clear that in the hottest region of the reactor, the temperature and the concentration of A are oscillating in approximately anti-phase. These anti-phase oscillations are, of course, very similar to those seen in the well-mixed and purely diffusive limits. At the bottom of the reactor, the temperatures are slightly lower than those in the top half of the reactor, and consequently, the bottom half of the reactor is slightly richer in A.

Between cases A and B is a region of damped oscillations. When $\tau_{step\ 2} / \tau_{diffusion}$ is reduced further, the system moves through another region of damped oscillations, before again becoming non-oscillatory. This behaviour is very similar to the non-oscillatory, high temperature rise regime described in section 4.4.2. The behaviour seen in this area of Figure 5.1 ($Ra < 10^3$) is, as described above, very similar to the behaviour seen for the purely diffusive system. This is entirely predictable given that diffusion is still dominating transport. The effects of natural convection are limited to a disruption of the spherical symmetry seen in the purely diffusive limit, although this effect is relatively small until the Rayleigh number approaches the transition value.

When *Ra* increases above 10^3, there are further interesting regions of behaviour. Case C is in a similar area of the regime diagram to the non-oscillatory, high temperature rise solutions, as discussed in section 4.4.2; however, the Rayleigh number is higher (~ 10^4), thus convection is having a significant influence on the progress of the reaction. It is interesting to note that the temperature and concentration fields shown for case C in Figure 5.2 at small times (< ~ 3 s) are almost symmetric; however, this symmetry is disrupted by the natural convection which does develop at larger times. It can be seen that for $t > 3$ s, the temperature profile becomes more skewed, with the hot zone moving upwards in the reactor. Eventually, a degree of stratification in the temperature is evident, as would be expected in a system where natural convection is important. As was the case in the non-oscillatory, high temperature rise regime in the purely diffusive limit, the temperature rises are considerably larger than those seen in the oscillatory region in Figure 5.1, and after an initial increase in the concentration of A, it falls to virtually zero throughout the reactor except within a thin layer at the wall.

When $\tau_{step\ 2} / \tau_{convection}$ increases, the system moves into the region where oscillations are observed. When natural convection is significant, the oscillatory behaviour is more complex, and there is a notable difference between this and the behaviour seen in the purely diffusive case. Case D is typical of the oscillatory behaviour seen in the region on the regime diagram defined by $\tau_{step\ 2} / \tau_{diffusion} < 0.5$ and $5 < \tau_{step\ 2} / \tau_{convection} < 15$. In contrast to case C, it is evident from Figure 5.2 that natural convection is significant throughout the time period considered. The hot zone initially forms above the centre of the reactor and subsequently a high degree of stratification of the temperature can be seen. It is interesting to compare the horizontal temperature contours seen in case D in Figure 5.2, which are most obvious at the centre of the reactor, with the shape of cool flames at terrestrial conditions. Foster and Pearlman (2006) describe terrestrial cool flames as being horizontal flame fronts with a slight upward curvature in the centre of the reactor, and a slight downward curvature near the walls. This is qualitatively similar to the shape of the temperature contours in Figure 5.2. The concentration field is clearly more complex in this case. The top of the reactor is quickly depleted of A. This zone of depletion spreads down the walls of the vessel due to the toroidal flow pattern. Near the bottom of the reactor, there is a small region around the vertical axis which is rich in A due to the lower temperatures in this part of the vessel. Some small scale oscillations in the temperature and the concentration of A can be seen for case D in Figure 5.2; however, it is difficult to discern their exact nature due to their relatively small scale. It is also interesting to look at the temperature distribution at $t = 2.8$ s. Consider the temperature along the horizontal axis of the reactor, moving out from the centre. Near the vertical axis, the temperature is at a maximum, then upon increasing the radius, the temperature of the gas drops. When the radius is increased further the temperature once again increases, before decreasing to the wall temperature in the boundary layer. This variation in temperature is clearly due to the flow patterns in the reactor. The cooler regions, about halfway between the vertical axis and the wall, correspond to the areas of the reactor where the 'eye' of the toroidal flow field (Figure 2.1(a)) would be found. The region of higher temperature near the wall is probably due to the influence of the hotter gas flowing downwards near the wall.

When $\tau_{step\ 2} / \tau_{convection}$ is increased beyond ~ 15, a new region of behaviour is observed, which exhibits more well-defined oscillations. This region is typified by case E in Figures 5.1 and 5.2. The temperature fields seen in Figure 5.2 for case E are similar to those seen in case D. The high temperature region is more confined to the top of the reactor. This is, of course, due to the more intense natural convection. At first glance, the oscillations in the temperature and the concentration of A are confined to the hot region in the top half of the reactor. In the much cooler lower half of the reactor, the variations in temperature and concentration are much smaller in magnitude. The smaller hot zone allows the region rich in A around the vertical axis to move further up the reactor than in case D.

When the system moves towards the upper boundary between oscillatory and non-oscillatory behaviour, the oscillations observed become much more heavily damped. They do, however, remain qualitatively similar to those seen in case E. Eventually, the system moves into a region of parameter space where no oscillations occur. In this region, the solutions are similar to case F in Figures 5.1 and 5.2. The concentration of A remains virtually spatially uniform throughout; there is only a very slight decrease in the concentration near the top of the reactor for $t > 5$ s. In this regard, case F is very similar to case A, which is also in a region of slow reaction. However, cases A and F do differ in the temperature distribution. The influence of natural convection is clear in case F in Figure 5.2. The hot zone initially forms well above the centre of the reactor and a high degree of stratification in the temperature develops. This difference between cases A and F is observed despite the fact that both cases exhibit temperature rises of similar magnitude.

The pictures of the concentration fields in Figure 5.2 allow some qualitative comparison of the behaviour in different regions. The salient differences are more easily seen by examining first the temporal development of the temperature and the concentration of A at the centre of the reactor for each of the cases A – F, and then the spatial development as the reaction proceeds. These comparisons are made, in turn, below.

5.3.2 Temporal Development of the Temperature and Concentration of A at the Centre of the Reactor

The temporal development of the six cases A – F is shown in Figure 5.3. Case A is in the non-oscillatory region when $Ra < 10^3$. The slow growth and subsequent decay in the temperature and concentration of A, discussed above, are evident in Figure 5.3(a). The temperature rises are reasonably small (~ 20 K in case A). Comparison of Figure 5.3(a) and Figure 3.3(a) shows just how similar the temporal evolution of the temperature and the concentration of A are to those seen in the non-oscillatory, low temperature rise limit for the purely diffusive case.

Case B, shown in Figure 5.3(b), is typical of the region of sustained oscillations, which is found approximately when $1.5 < \tau_{step\ 2} / \tau_{diffusion} < 1$. These boundaries are once again very similar to those shown in Figure 4.3 for the diffusive regime. This region of sustained oscillations is very similar to that seen in the purely diffusive case.

Case C is located in a part of the regime diagram where natural convection should be significant ($Ra \sim 10^4$). Despite this, the temporal development of the temperature and the concentration of A at the centre of the reactor (Figure 5.3(c)) are remarkably similar in shape to what they would be in the purely diffusive case. The reason for this was discussed above. Over the first 3 s of the reaction, the temperature and concentration profiles in Figure 5.2 show approximate radial symmetry. This is because the temperature rise in the vessel is insufficient to generate natural convection. Indeed, natural convection only becomes significant after ~ 3 s. At this time, however, the concentration of A has risen to its peak and then subsequently fallen back to almost zero.

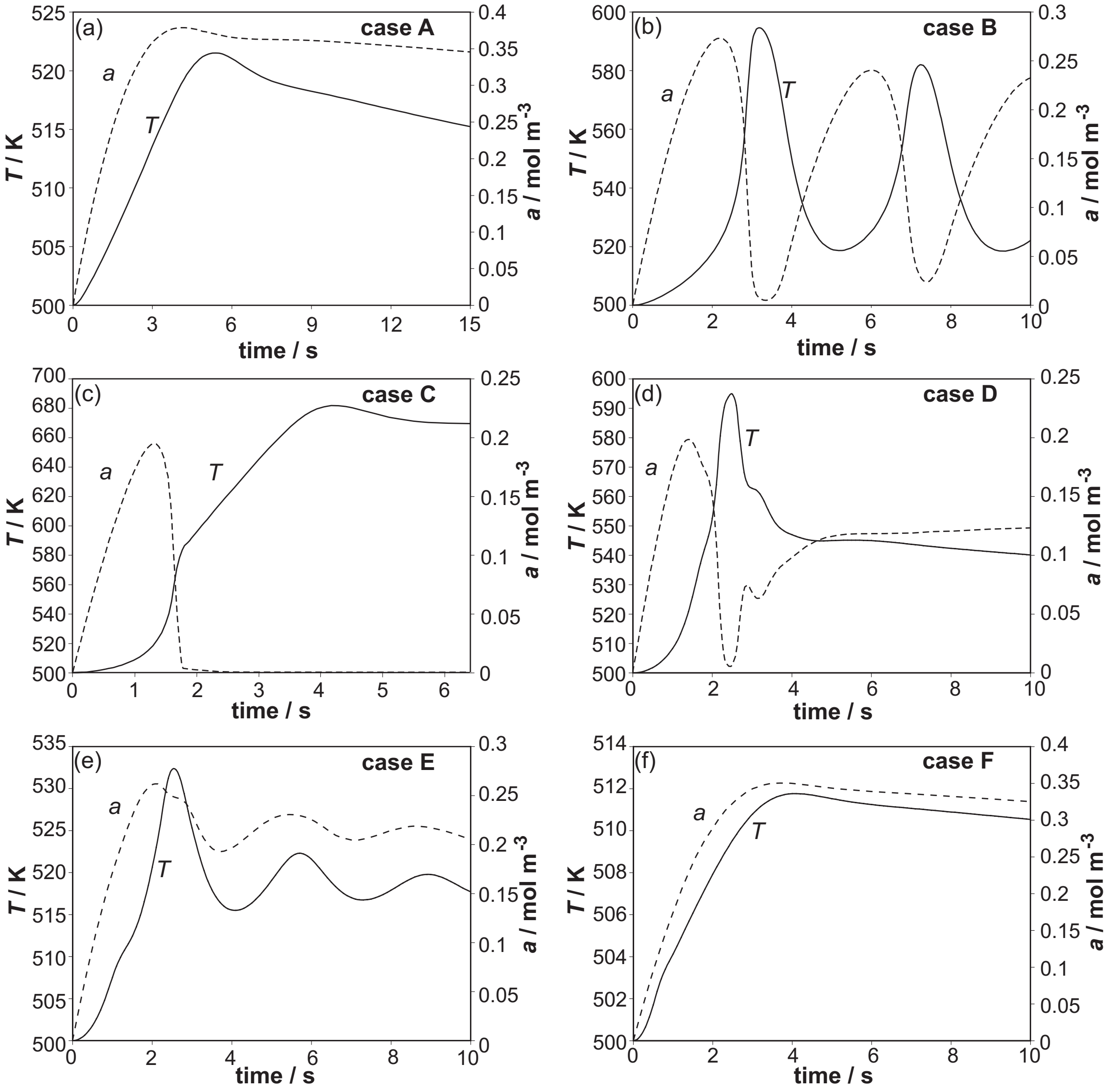

Figure 5.3. Plots showing the temporal development of the temperature and the concentration of the intermediate A at the centre of the reactor, for cases A – F on the regime diagram in Figure 5.1. Details of the parameters used in the simulations appear in Table 5.1. In each case, the temperature is the solid line and the concentration of A is the dashed line.

The first oscillatory case considered in which natural convection is important is case D, shown in Figure 5.3(d). The oscillatory behaviour is evidently more complex, and there is a notable difference between this and the behaviour seen in the purely diffusive case. The temporal development of the temperature and the concentration of A, shown in Figure 5.3(d), is unlike anything presented previously. The temperature increases rapidly initially, reaching its peak after ~ 2.5 s. The temperature rise is large (~ 95 K) as would be expected given the proximity of this region to the non-oscillatory, high temperature rise solutions in the regime diagram. Whilst the temperature increases, the concentration of A first increases, and then decreases rapidly. So far, this behaviour is similar to what has been observed previously. However, after reaching the peak temperature, the system begins to cool, and the concentration increases, until at ~ 3 s the temperature goes through an inflexion, before continuing downwards. At the same time there is a very small-scale oscillation in the concentration of A, which then continues increasing. After this time, the temperature falls, before increasing very slightly at ~ 5.5 s, then resumes a steady decline. The behaviour exhibited in this case is typical of the solutions in this part of the regime diagram. These all exhibit very small oscillations in temperature over a long timescale, but also show shorter timescale effects, such as the inflexion in temperature. These effects often take the form of an inflexion in the temperature curve, or there is a small-scale oscillation in the temperature before it either keeps increasing or decreasing. Similar effects to this can be seen in the thermocouple traces in the experimental work of Archer (1977). The fact that these small-scale inflexions or oscillations occur in the experimental measurement of a non-oscillatory decomposition reaction suggests that these small-scale oscillations are due to the fluid mechanics, rather than the oscillatory nature of the reaction. It is interesting to compare the period of the small-scale oscillation in the concentration of A seen at $t \sim 3$ s in Figure 5.3(d), with the magnitude of $\tau_{convection}$. For case D, $\tau_{convection} \sim 0.3$ s, which is very similar in magnitude to the period of the oscillation in a.

Case E was shown in Figure 5.2 to exhibit anti-phase oscillations in the top half of the reactor; however, no discernible oscillations could be seen lower down the reactor. It is noticeable in Figure 5.3(e) that the temperatures measured at the centre of the reactor are significantly lower in case E, than those seen in case D, and in the diffusive limit. It is also evident that there are indeed oscillations in the temperature and the concentration of A. The oscillations have a much smaller amplitude than those seen in the diffusive limit. These smaller amplitude oscillations are typical of those seen at the centre of the region of oscillations defined in Figure 5.1. What is perhaps most surprising about case E is that the temperature and concentration are oscillating in-phase at the centre of the reactor. This is in stark contrast to any of the oscillatory solutions presented previously, either in the diffusive or well-mixed limits, where only (approximately) anti-phase oscillations occurred. This effect is intriguing, and will be discussed further in Chapter 6.

The final case, F, shown in Figure 5.3(f) is non-oscillatory and the temporal development of the temperature and the concentration of A are similar to those in Figure 5.3(a) for case A. There is, once again, a slow growth and decay of both temperature and concentration, and the maximum temperature rise is very small (~ 12 K). Where the two cases do differ, of course, is in the spatial structure, which can be seen from Figure 5.2.

It is interesting to note that natural convection appears to have very little effect on the temporal development of the temperature and concentration in the reactor in the regions of the regime diagram in which the reaction is non-oscillatory (cases A, C and F). However, natural convection does play a significant role in the oscillatory solutions (cases B, D and E), where the behaviour can be complex. The complexities introduced by natural convection will be further discussed below when the spatial development of the temperature and the concentration of A in the reactor is considered in greater detail.

5.3.3 Spatial Development of the Temperature and the Concentration of A

The six cases considered above show a variety of different forms in the temporal development of the temperature and the concentration of A. In addition to this, Figure 5.2 also shows that there are considerable differences in the spatial structure of the temperature and concentration fields. To highlight these differences, temperature and concentration profiles along the vertical and horizontal axes are presented, as time progresses, for each of the cases A – F.

5.3.3.1 Case A

The vertical profiles of the temperature and the concentration of A appear in Figure 5.4. Part (a) shows how the temperature varies along the vertical axis of the reactor over the course of the first 8 s of the reaction. It can clearly be seen that over the first 3 s of reaction, the temperature is approximately symmetric. This is, of course, expected because case A is in the region of the regime diagram where diffusion dominates. After 3 s, the effect of the weak natural convection that is occurring becomes evident. The location of the maximum temperature does gradually begin to move up the reactor. When the temperature reaches its maximum (at $t \sim 5$ s), the maximum temperature is located above the centre of the reactor. In fact, the location of the maximum is at $y \sim 0.55$ m, where y is the vertical distance measured from the bottom of the reactor. The maximum temperature is therefore $\sim 0.1\ L$ above the centre. After reaching its maximum temperature, the gas in the reactor cools slowly, with the point of maximum temperature remaining above the centre.

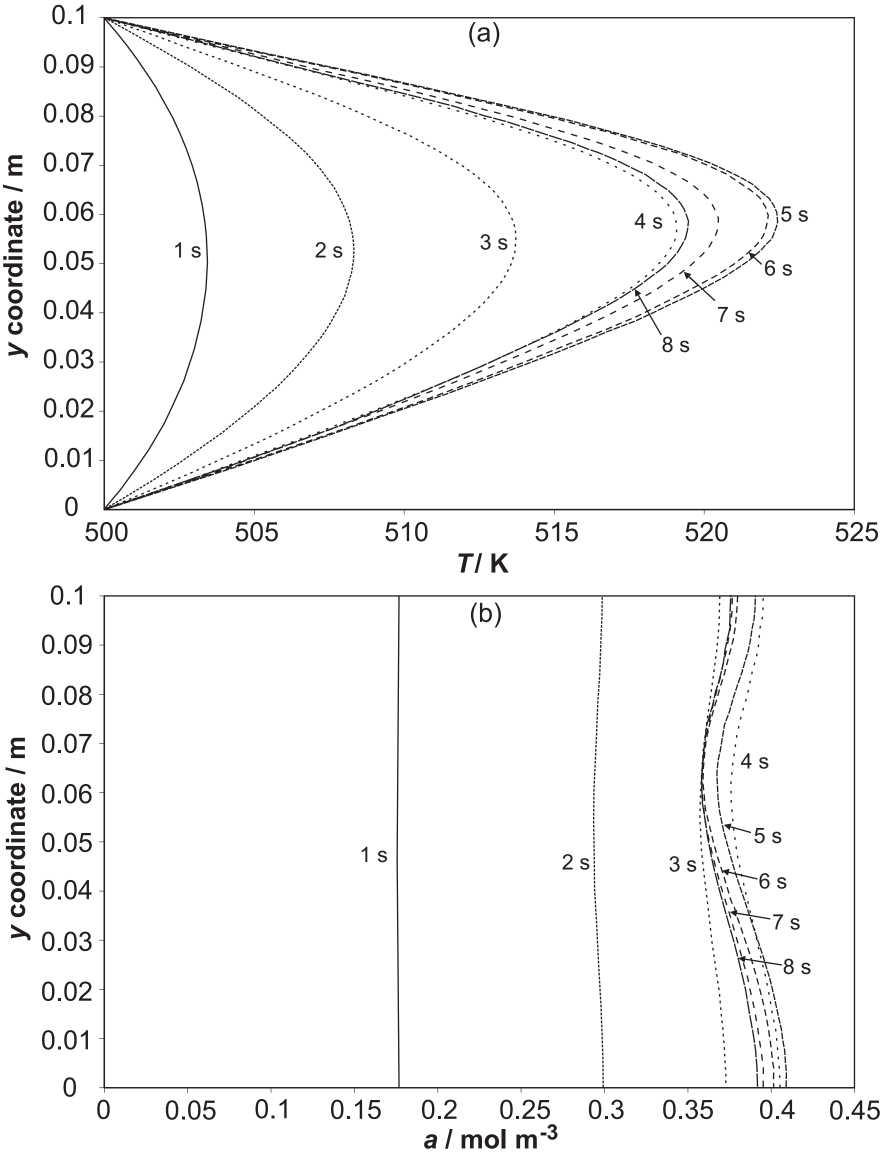

Figure 5.4. (a) The temperature profiles along the vertical axis of the reactor for case A. Lines are shown for the temperature every second for 8 s. The vertical position is measured from the very bottom of the reactor. (b) Profiles of the concentration of A along the vertical axis every second for 8 s.

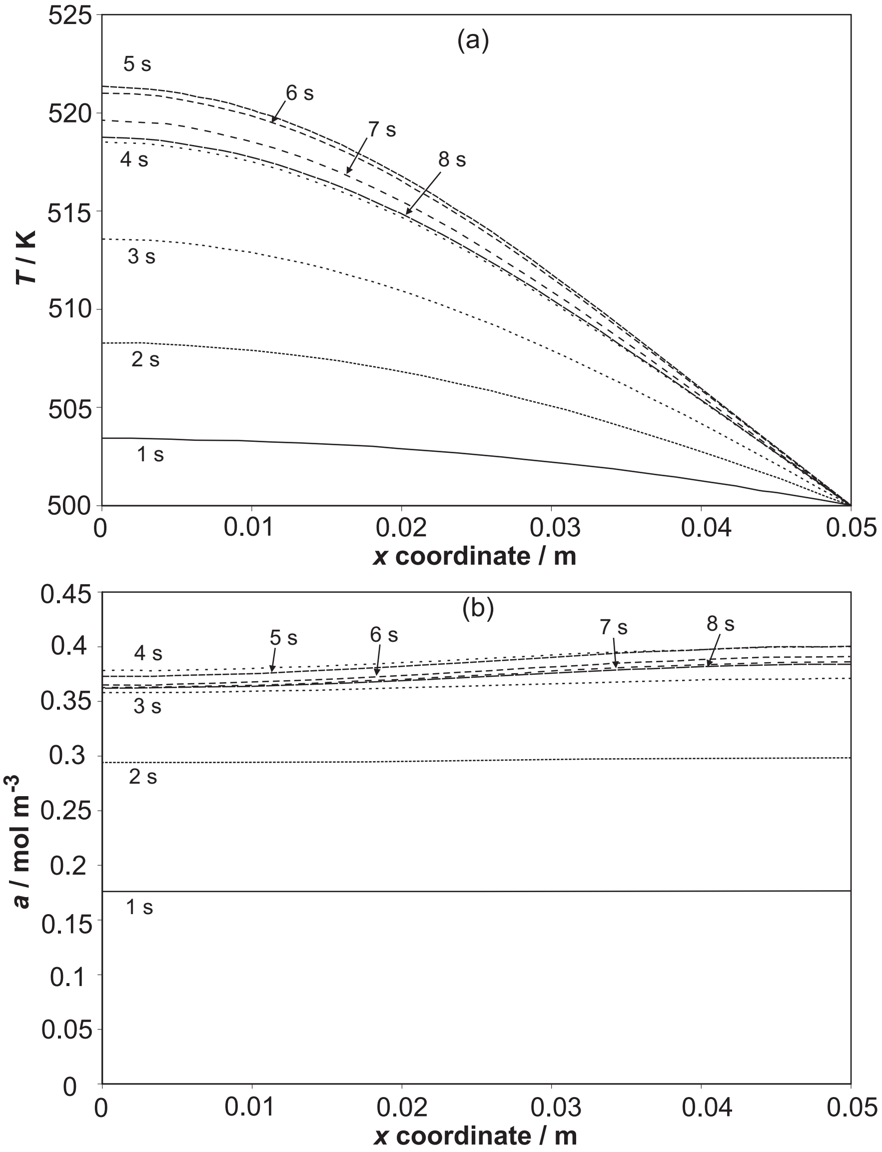

Figure 5.5. (a) Profile of the temperature along the horizontal axis of the reactor for increasing time for case A. (b) Profile of the concentration of A along the horizontal axis of the reactor for increasing time for case A. In both cases, the coordinate *x* is measured horizontally, from the centre of the reactor.

The development of the vertical concentration profile is shown in Figure 5.4(b). The concentration in the reactor can be seen to increase slowly. It is also evident that the concentration of A is virtually spatially uniform over the course of the first 2 – 3 s of the reaction, as was remarked upon in section 5.3.1. Figure 5.4(b) does show that there is some spatial variation in the concentration of A for larger times. As one would expect, the concentration is lowest in the hottest region of the reactor. Indeed, at $t = 6$ s, it can be seen that the concentration of A in the hot zone of the reactor is ~ 10% lower than that at the wall. It is also interesting to see that for $t > 4$ s, the concentration of A at the wall remains approximately constant, whereas in the hot zone above the centre of the reactor, the rate of depletion is much higher.

As well as examining the vertical profiles, the distributions of the temperature and the concentration of A along the horizontal axis of the reactor are also considered. The temperature and concentration profiles are shown, respectively, in Figure 5.5(a) and (b). The shapes of the profiles shown in Figure 5.5 are very similar to those seen previously in the purely diffusive limit, as shown in Figure 3.4. The temperature is, of course, highest at the centre of the reactor and decays monotonically when the radius is increased. The concentration of A is virtually uniform across the whole reactor; however, the concentration is marginally lower at the centre of the reactor than it is near the wall.

5.3.3.2 Case B

Case B is in the region of sustained oscillations when diffusion dominates transport. Figure 5.6 shows the variation of (a) the temperature and (b) the concentration of A with vertical position on the axis of the reactor. The initial development of the temperature profile is similar to that seen in case A, in that for the first 2 s the distribution is approximately symmetric, before it skews slightly at larger times. It is noticeable that the temperature rises in this case are significantly larger than those seen in case A. It is also interesting to see that there is clearly variation in the position of the maximum temperature at different times in the oscillatory cycle. For example, when the temperature reaches its first maximum at $t \sim 3$ s, the maximum temperature is found at $y = 0.06$ m, whereas at the first trough in the temperature, the maximum is found lower down the reactor at $y = 0.055$ m. The development of the concentration of A along the vertical axis, shown in Figure 5.6(b), is very different to that seen in case A. The concentration is initially spatially uniform; however, as the temperature in the hot zone of the reactor increases, the rate of depletion of A in this part of the reactor also increases. Between 2 and 3 s, the concentration of A in the top half of the reactor falls from its highest value to almost zero very rapidly. It can also be seen that in the next oscillatory cycle, the concentration rises to very close to its initial maximum value, and is very nearly spatially uniform. As was the case with the location of the maximum temperature, the location of the minimum concentration of

A can also be seen to shift up and down as time progresses. For example, at the first trough in concentration at t = 3 s (corresponding to the first peak in the temperature), the minimum concentration of A is found at y = 0.065 m, whereas at the next peak in the concentration at t = 6 s, the minimum concentration is found much closer to the centre of the reactor at y = 0.055 m. Finally, it is also interesting to note from Figure 5.6(b) that the concentration of A at the bottom of the reactor is significantly higher than that at the top for a large part of the time period considered. This is, of course, due to the weak natural convection skewing the temperature field.

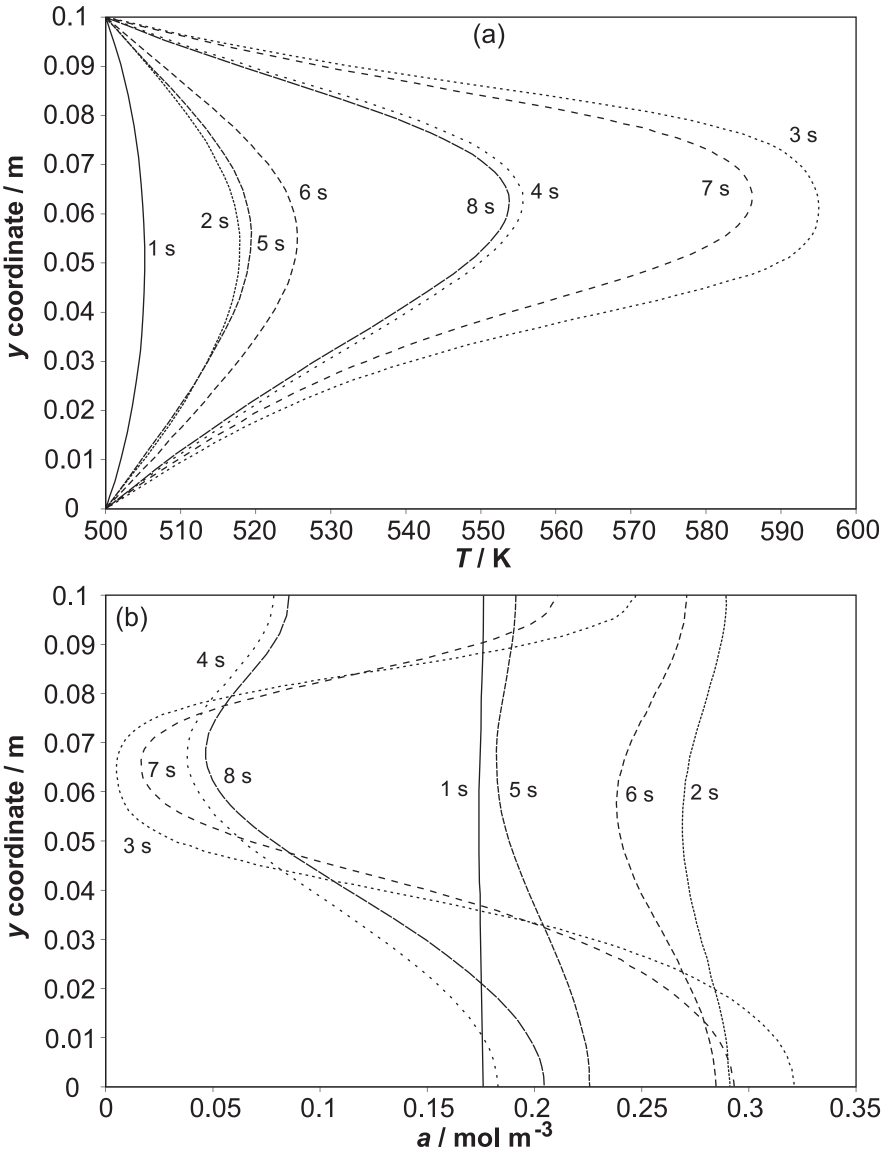

Figure 5.6. (a) The temperature along the vertical axis of the reactor for increasing values of time for case B. (b) Profiles of the concentration of A along the vertical axis for case B for increasing time.

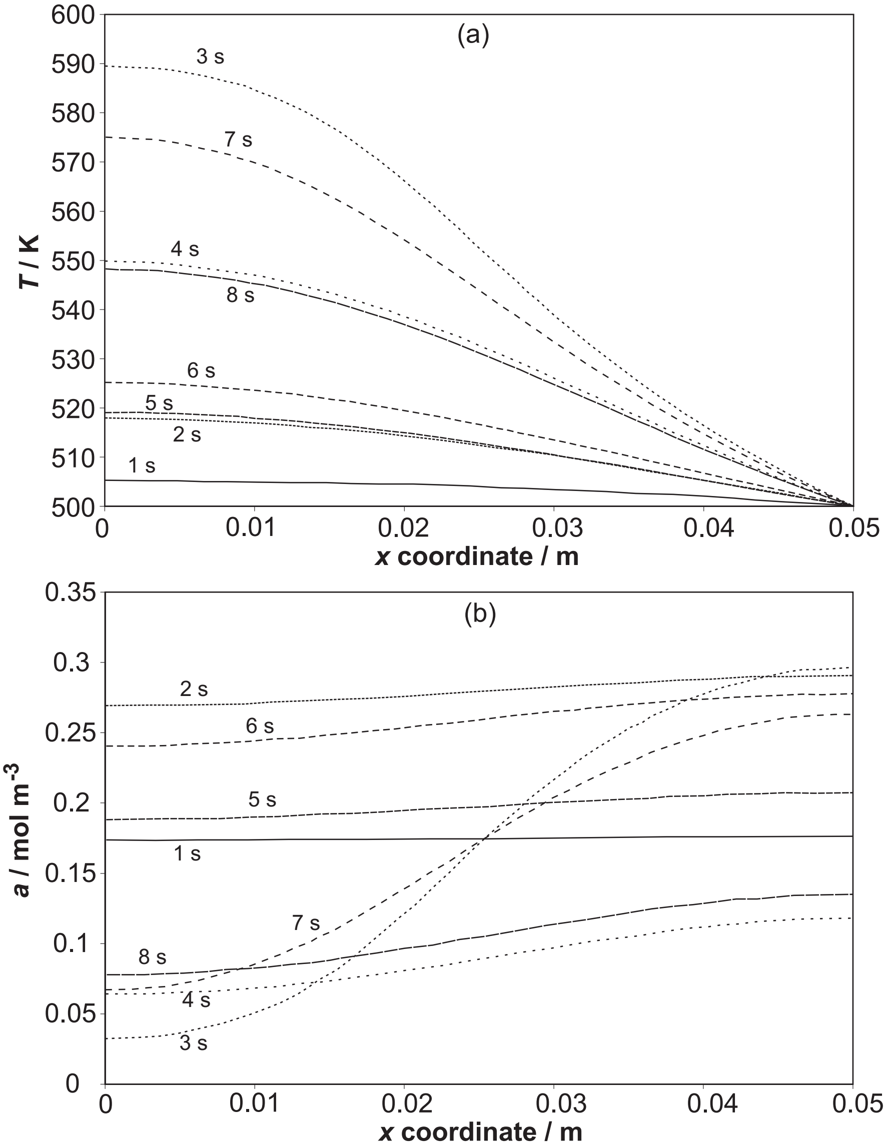

Figure 5.7. (a) Profile of the temperature along the horizontal axis of the reactor for increasing time for case B. (b) Profile of the concentration of A along the horizontal axis of the reactor for case B for increasing time.

The variation of the temperature and the concentration of A along the horizontal axis are shown in Figure 5.7. The temperature profiles are very similar to those seen in Figure 5.5(a) for case A, although it is interesting to note that there is an inflexion in the profiles with the largest temperature rises, upon moving away from the centre of the reactor (*e.g.* at $t = 3$ s). These horizontal temperature profiles are very similar, as expected, to those seen in the oscillatory cases in the purely diffusive regime. The concentration profiles show that the system is oscillating between a case where the concentration is virtually spatially uniform, with the concentration of A at the centre of the reactor being only marginally smaller than that at the wall and a case where the concentration near the centre of the reactor is near zero, whilst the concentration at the wall is significantly higher. This is exactly the same behaviour as was seen in Figure 4.10 for the cases with sustained oscillations in the purely diffusive limit.

5.3.3.3 Case C

Case C is the first case considered in which natural convection plays a significant role. The maximum value of Ra is ~ 10^4, which is well into the region in which laminar natural convection is significant. Case C is in a region of the regime diagram close to the non-oscillatory, high temperature rise regime in the diffusive limit. The vertical profiles of temperature and concentration of A are shown in Figure 5.8 and the horizontal profiles in Figure 5.9. It was noted in section 5.3.1 that over the first 2 – 3 s of the reaction, the temperature and concentration fields were approximately symmetric. This is confirmed in Figures 5.8 and 5.9. The vertical temperature profiles over the first 3 s in Figure 5.8(a) are virtually symmetrical. The shapes of the temperature distributions are also very interesting. There is a large region in the centre of the reactor where the temperature is increasing virtually uniformly. This can be seen in both Figure 5.8(a) for the vertical profile and Figure 5.9(a) for the horizontal profile. There is therefore a region of constant temperature around the centre of the reactor with a narrow boundary layer near the wall. The shapes of these temperature profiles at small times are virtually identical to those seen in Figure 4.8 for the non-oscillatory, high temperature rise case in the diffusive limit. The development of the concentration profiles are also very similar to what is seen in the purely diffusive limit. The concentration is approximately spatially uniform as it increases initially, but then it very rapidly drops to virtually zero in the bulk of the vessel, with the only significant amounts of A being found in the cooler boundary layer near the wall.

When t increases beyond ~ 3 s, the effects of natural convection are evident. In the vertical temperature profile in Figure 5.8(a) the symmetry that was seen for small times is lost and the temperature profile becomes highly skewed, with the highest temperature occurring very close to the top of the reactor. The effects of convection can also be seen in Figure 5.8(b). The concentration in the boundary layer at the top of the reactor drops as time progresses, but at the bottom, the concentration in the boundary layer increases. This is due to the skewing of the temperature profile, with the intermediate A being depleted in the hotter top section of the reactor, and accumulating in the cooler bottom section of the reactor.

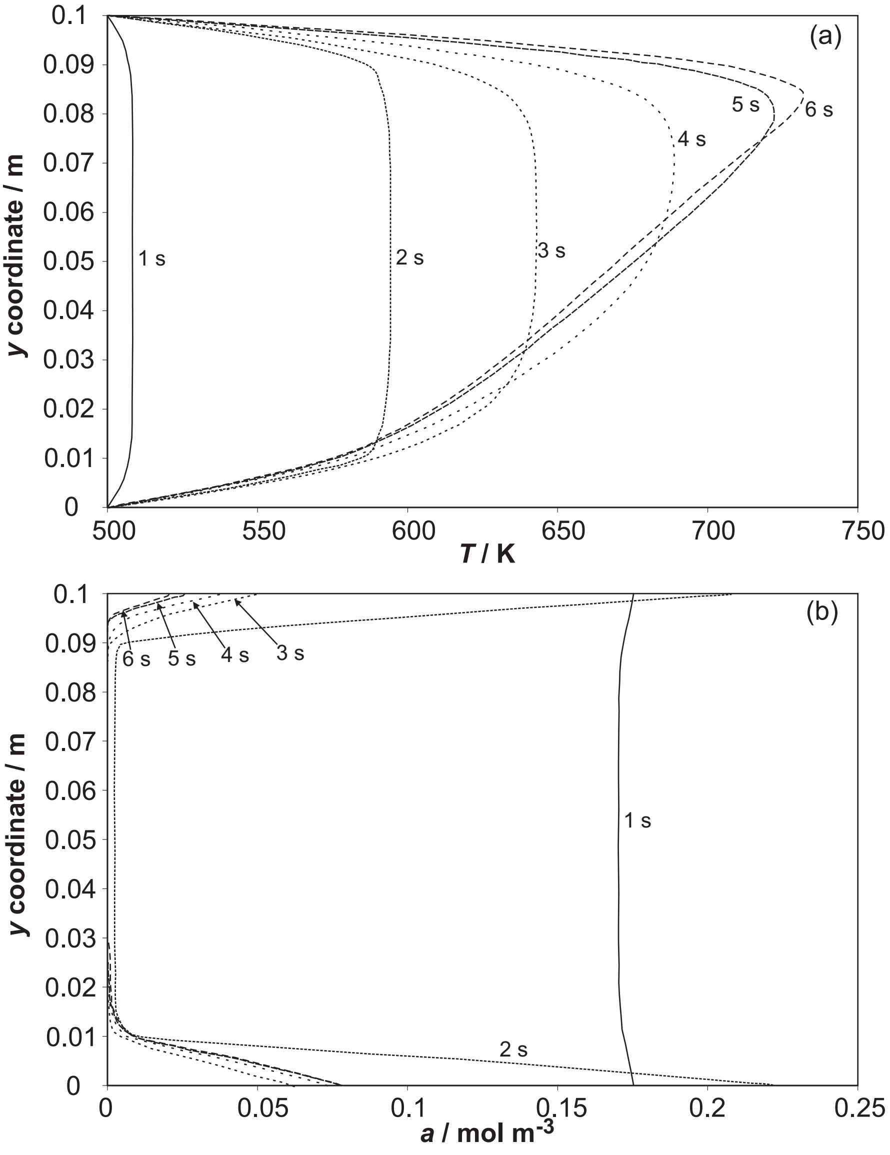

Figure 5.8. (a) The temperature along the vertical axis of the reactor for increasing time for case C. (b) Profiles of the concentration of A along the vertical axis for case C for increasing time.

The effects of natural convection can also be seen in the horizontal temperature profile in Figure 5.9(a), although these effects are far more subtle than those seen in the vertical profile. Initially, the temperature is constant over a large part of the horizontal axis of the reactor, as described previously. At $t = 4$ s, when natural convection is just starting to take effect, the temperature profile shows much more curvature, *i.e.* there is no region of uniform temperature around the centre of the reactor. For greater t, natural convection is significant and the maximum temperature on the horizontal axis decreases slightly. What is interesting is that the temperature is once again virtually constant along a significant fraction of the horizontal axis. The temperature distribution when natural convection becomes significant is therefore dependent on the vertical position, but does not vary significantly with horizontal position. The emergence of this vertical stratification in the temperature is a classic feature of a system in which natural convection is significant, but not extreme.

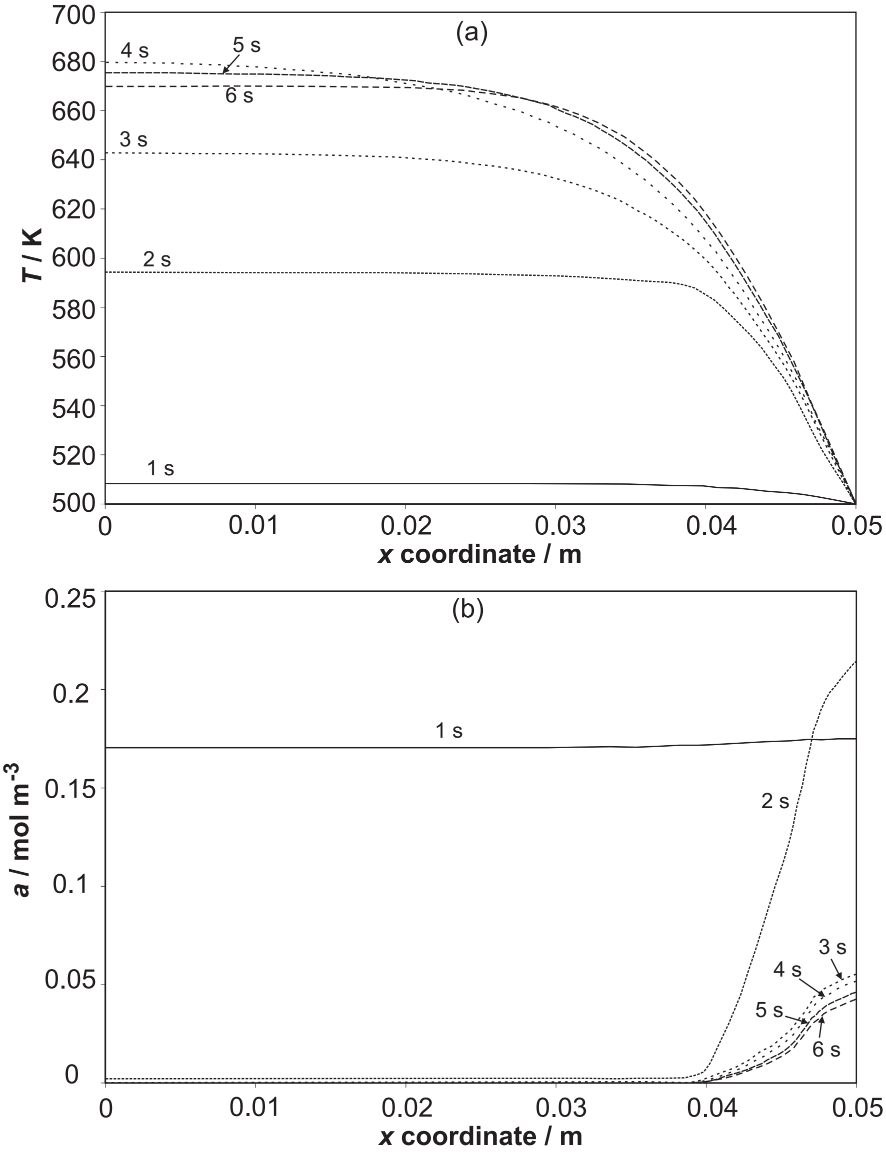

Figure 5.9. (a) Profile of the temperature along the horizontal axis of the reactor for increasing time for case C (b) Profile of the concentration of A along the horizontal axis of the reactor for case C for increasing time.

It was discussed above that natural convection only becomes significant after ~ 3 s. This is more clearly demonstrated if an estimate of the magnitude of the convective term in Eq. (3.5), describing the conservation of energy, at the centre of the reactor is examined. This appears in Figure 5.10. Over the first 3 s of the reaction, the convection term is virtually zero. After 3 s, there is a very large increase in the magnitude of the term as natural convection becomes important. The fact that natural convection does not develop is probably due to the shape of the temperature profile, shown in Figure 5.8(a). Initially, the temperature is virtually uniform over the bulk of the vessel, so the temperature gradients, which cause natural convection, are too small to cause significant motion of the gas. The fact that the temperature rise in much of the reactor is uniform suggests that the generation term in Eq. (3.5) is dominant initially, with the convection term only becoming significant at larger times.

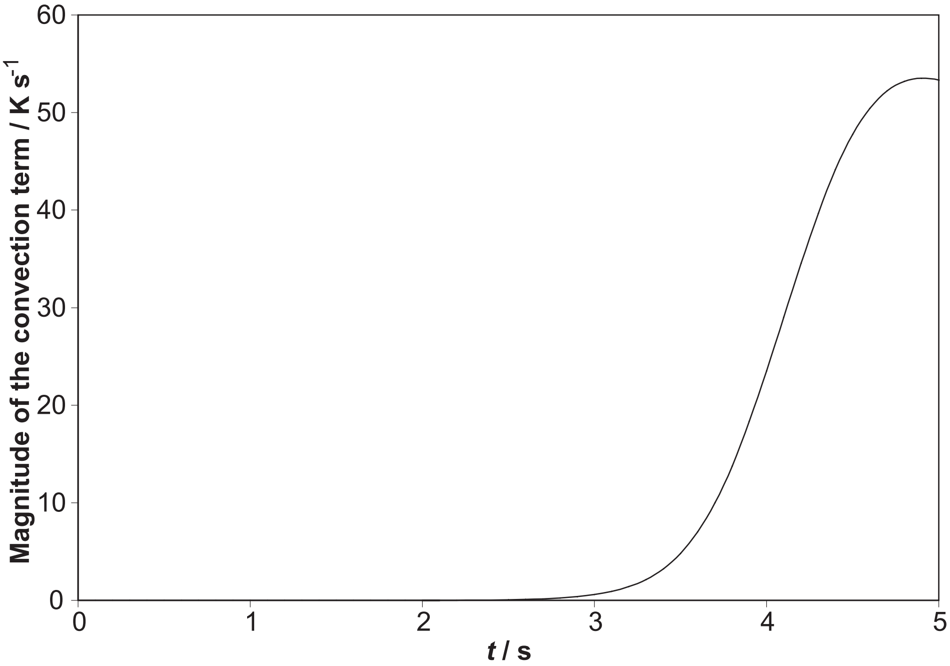

Figure 5.10. Development of the convective term in Eq. (3.5) at the centre of the reactor for case C.

This induction time for natural convection is obviously an important property in these systems. It is especially important for explosive systems, because it is possible that a system could explode before natural convection has had a chance to develop to cool the system. Merzhanov and Shtessel (1973) compared the induction time for explosion with an expression for the induction time for convection:

$$\tau_i = 70 Ra^{-2/3} Pr^{5/6} . \tag{5.2}$$

It should be noted that this expression was developed through the study of natural convection in a plane layer of inert fluid, heated from below. It is not clear whether this expression was derived theoretically or empirically. Equation (5.2) suggests that the induction time for natural convection is only a function of the Rayleigh number, with higher *Ra* having lower induction times. A cursory inspection of the numerical results discussed in this chapter suggests that this is not the case for this system, which includes chemical reaction. It is sensible to assume that the kinetics of the reaction would also play a role in determining the induction time for natural convection. The form of the expression for the induction time when reaction is important has, however, not been considered further in this work.

5.3.3.4 Case D

Case D showed some interesting behaviour in Figure 5.3(d), with small scale oscillations in the concentration of A at the centre of the reactor and an inflexion in the temperature curve. The vertical temperature and concentration profiles are shown in Figure 5.11. In contrast to case C, it is clear from Figure 5.11(a) that natural convection becomes significant at a much lower value of t. A skewed temperature profile quickly develops with the maximum temperature in the top half of the vessel. It is curious to note that at t = 2.5 s, which is when the temperature reaches a maximum, the peak in the vertical temperature profile broadens significantly. This is different from any of the conditions considered previously, either for Sal'nikov's reaction or the simpler decomposition reaction considered in Chapter 2. This peak broadening is short lived, and as the gas cools, the temperature profile more closely resembles the skewed profiles seen previously.

Inspection of Figure 5.11(b) for the vertical concentration profile shows that there are two distinct regions in the reactor. There is the relatively cool region at the bottom of the reactor, which is rich in the intermediate A, and then there is the hot zone at the top of the reactor where the concentration of A is virtually zero. The peak broadening effect is also evident; at t = 2.5 s, it can be seen that the region in which the concentration of A in the reactor is close to zero extends much further down the reactor than at any other time. It is this broadening of the temperature peak which causes the unusual shape of the temperature *versus* time curve in Figure 5.3(d). The time at which the broadening of the temperature peak in Figure 5.11(a) occurs is the same as the time when the maximum temperature is reached in Figure 5.3(d). The expansion of the temperature peak in Figure 5.11(a) begins at ~ 2 s; this corresponds to the first inflexion in the temperature curve in Figure 5.3(d), which can be seen at this time. The temperature profile returns to the more familiar skewed form after ~ 3 s, which corresponds to the second, more obvious inflexion in the temperature curve.

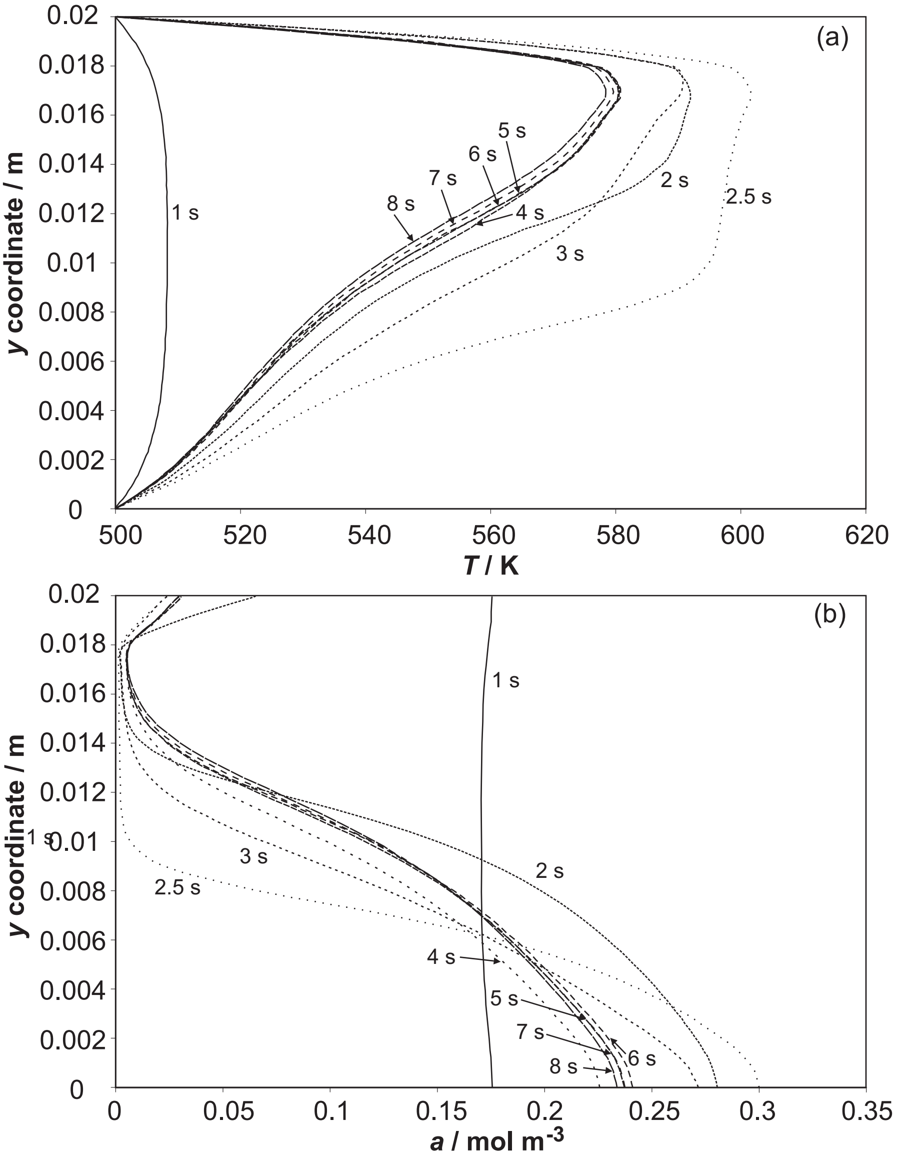

Figure 5.11. (a) The temperature along the vertical axis of the reactor for increasing values of time for case D. (b) Profiles of the concentration of A along the vertical axis for case D for increasing time.

The forms of the horizontal temperature and concentration profiles are also very interesting. These are shown in Figure 5.12. It can clearly be seen from Figure 5.12(a) that there is very little variation in the temperature over about 70% of the horizontal axis. There is generally a very slight decrease in temperature, moving out from the centre of the reactor initially. The temperature then increases slightly, before falling to the wall temperature in the boundary layer. The maximum in the horizontal temperature profile is due to the flow patterns within the reactor. The temperature is higher due to the hotter gas flowing downwards from the top half of the reactor. The widening of the temperature peak can once again be identified in Figure 5.12(a) at 2.5 s, where the temperature at the centre of the reactor shows a very large increase from that at 2 s, whilst the rest of the gas along the horizontal axis heats up considerably less.

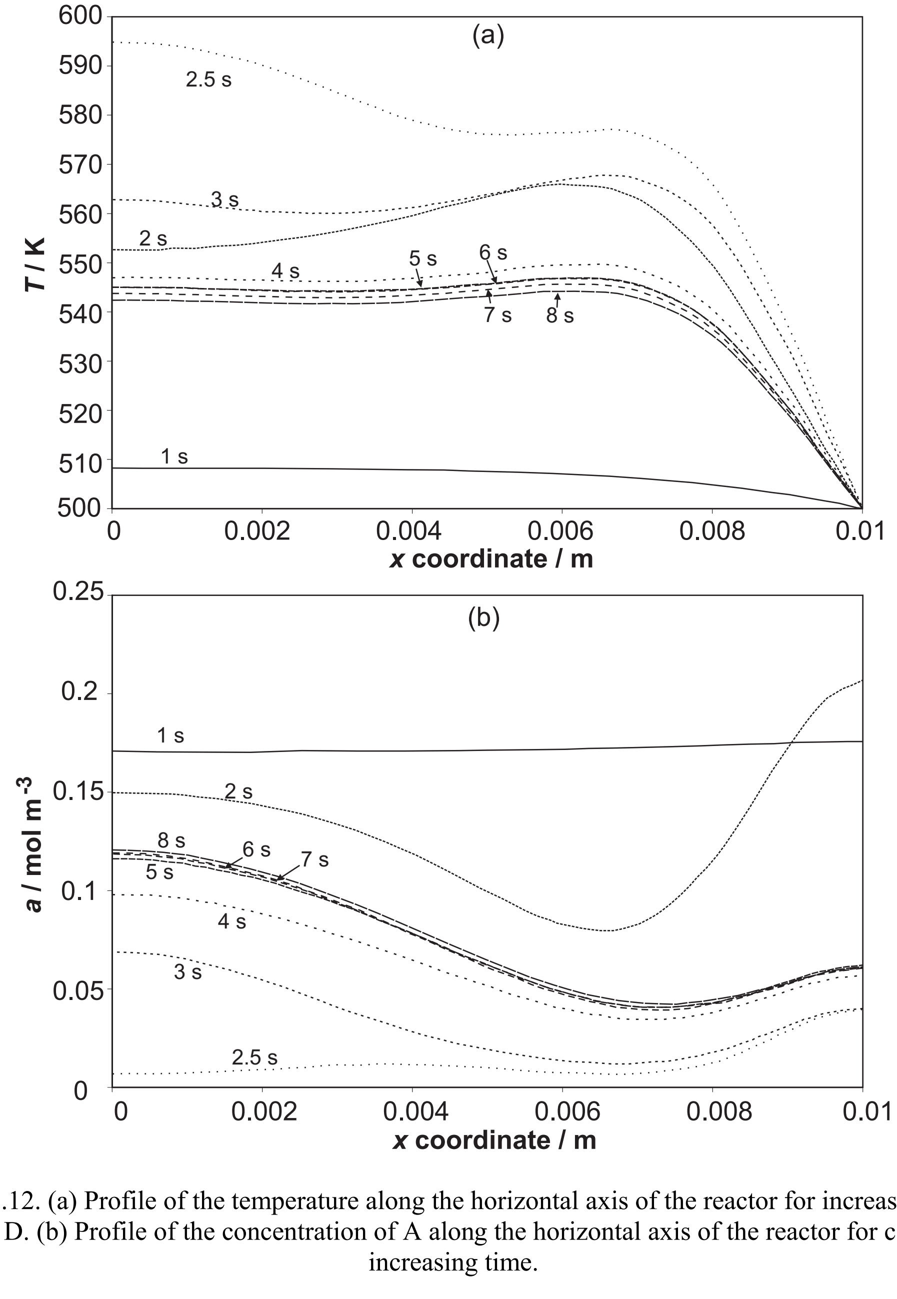

Figure 5.12. (a) Profile of the temperature along the horizontal axis of the reactor for increasing times for case D. (b) Profile of the concentration of A along the horizontal axis of the reactor for case D for increasing time.

The shapes of the concentration profiles along the horizontal axis in Figure 5.12(b) are markedly different from anything seen previously. As usual, the concentration increases uniformly along the horizontal axis initially, but as the reaction proceeds, the concentration profile changes shape. A minimum develops in the concentration profile. This is again due to the influence of the hot gas descending from the top half of the reactor, which has been depleted of A. Eventually, the horizontal profile develops such that the highest concentration of A is at the centre of the reactor, and the concentration falls as the distance from the vertical axis is increased. This concentration profile is in stark contrast to those seen previously, particularly in the diffusive limit, where the concentration is always lowest at the centre of the reactor and increases on moving toward the wall.

5.3.3.5 Case E

Figure 5.3(a) showed that case E exhibited small scale, in-phase oscillations in the temperature and the concentration of A at the centre of the reactor. Figure 5.13 shows the development of the vertical temperature and concentration profiles. The temperature profile is highly skewed, but does not show any of the peak broadening seen in case D. It is interesting to note that the region of the reactor in which the concentration of A is depleted is confined to a very small region near the top of the reactor. In fact, there is very little variation of the concentration of A over the bottom three quarters of the vertical axis. It is also interesting to compare the extent to which the intermediate A is depleted in the hot zone of the reactor with what was seen in Figure 5.11 for case D. Despite both cases having similar rises in temperature in the hot zone, case E shows a much smaller drop in the concentration of A in this part of the reactor. This is most likely due to the increased intensity of convection supplying A more efficiently to the hot zone in the reactor. Finally, the large scale anti-phase oscillations in the concentration and temperature can clearly be identified at the top of the reactor, and there is also some evidence of the smaller scale, in-phase oscillations further down the reactor.

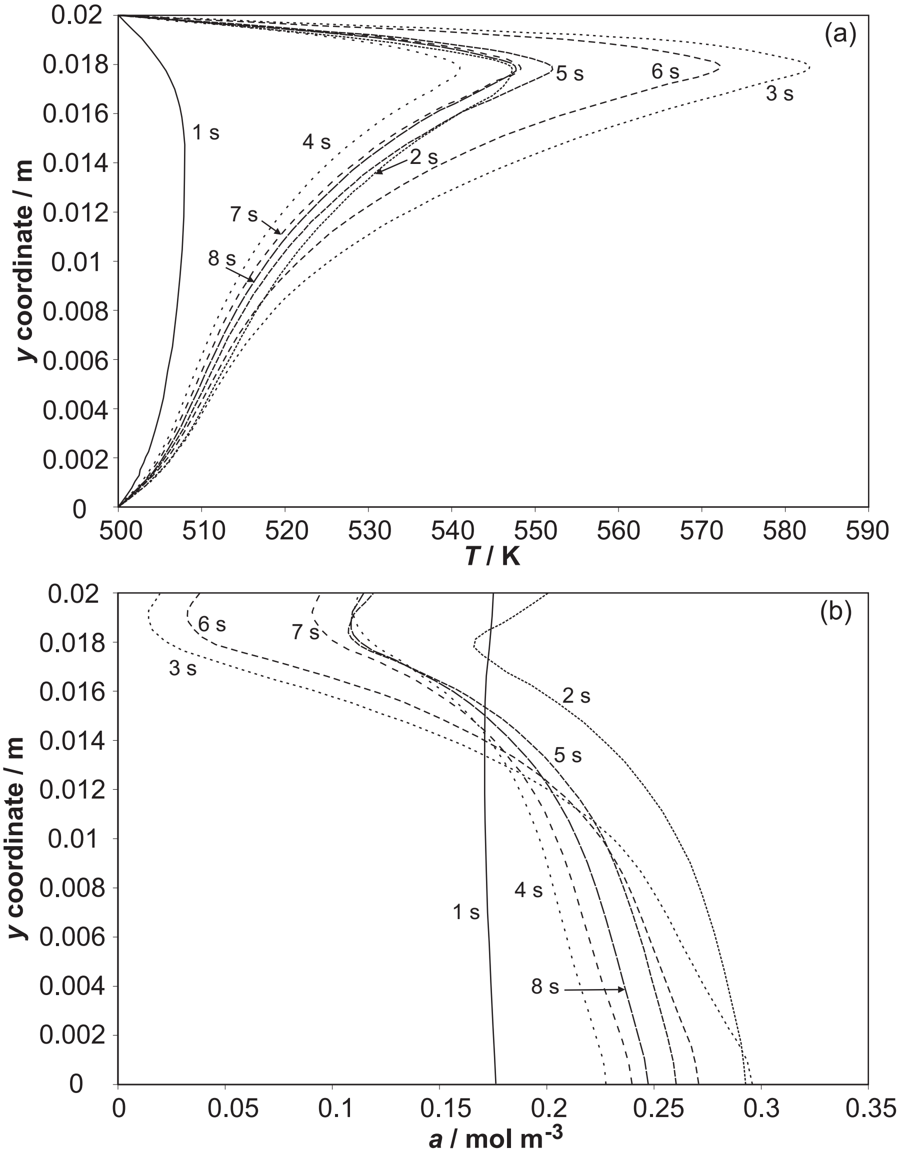

Figure 5.13. (a) The temperature along the vertical axis of the reactor for increasing time for case E. (b) Profiles of the concentration of A along the vertical axis for case E for increasing time.

The horizontal temperature and concentration profiles, shown in Figure 5.14, are very similar in form to those seen for case D, with the temperature being approximately constant over half the radius. As with case D, the temperature then increases due to the influence of the descending hot gas, before decreasing in the boundary layer to the wall temperature. The concentration profiles show that the concentration is highest at the centre of the reactor and decreases on moving outwards toward the wall. At some times there is a minimum in the concentration profile, close to, but not at, the wall. Once again this is due to the influence of the descending hot gas near the wall of the reactor.

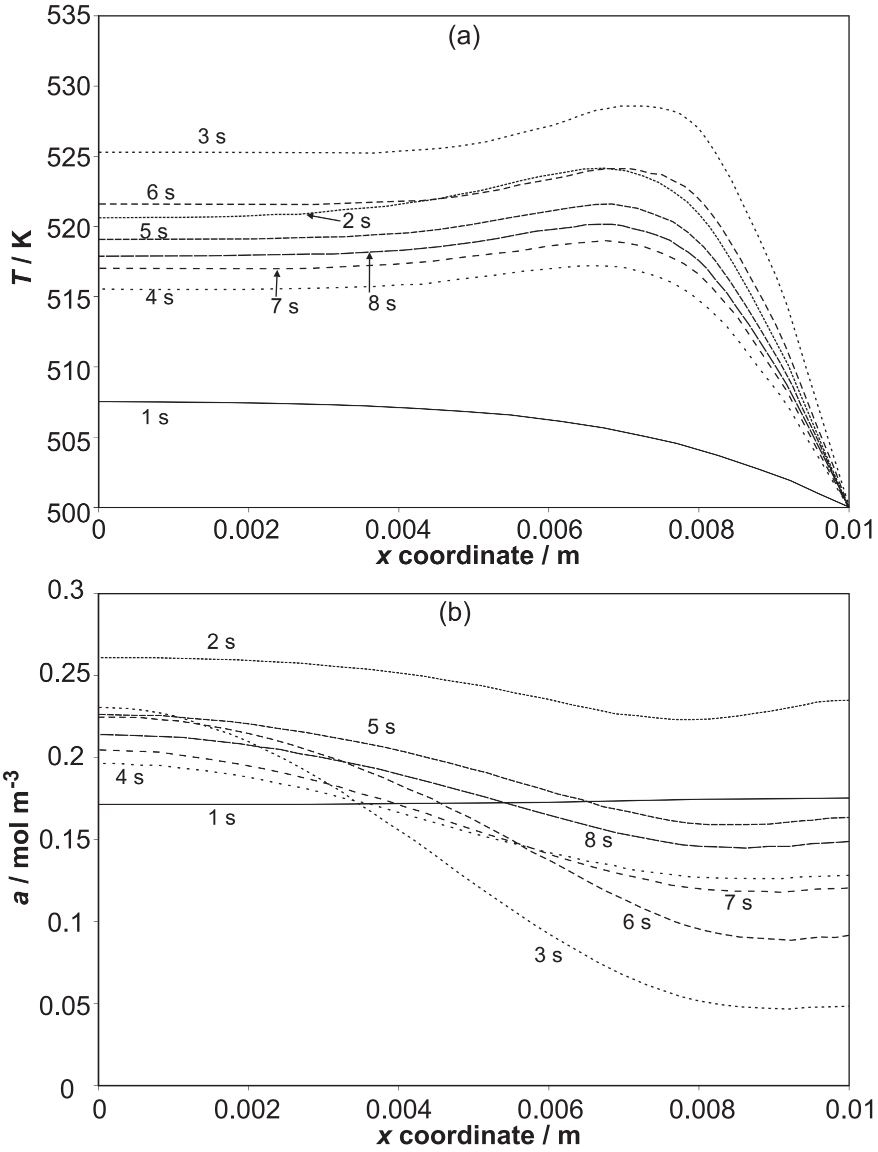

Figure 5.14. (a) Profile of the temperature along the horizontal axis of the reactor for increasing time for case E. (b) Profile of the concentration of A along the horizontal axis of the reactor for case E for increasing time.

5.3.3.6 Case F

Case F is in a region of the regime diagram in which no oscillations are observed. In fact, it can be seen from Figure 5.3 that the temporal developments of the temperature and the concentration of A are very similar to that in case A, and consequently the non-oscillatory low temperature rise regime in the purely diffusive limit. Comparison of Figure 5.4(a) for case A and Figure 5.15(a), which shows the temperature profile along the vertical axis of the reactor for case F, shows that despite having similar evolution of the temperature at the centre of the reactor, the spatial forms of the solutions are quite different, due entirely of course to the presence of significant natural convection in the latter case. In case F the temperature profile is highly skewed, whereas in case A, the profile is approximately symmetric. Despite the difference in the temperature profiles, comparison of Figure 5.15(b), showing the variation of the concentration of A along the vertical axis, with Figure 5.4(b) for case A shows that the concentration profiles are similar. There is in fact very little variation of the concentration of A along the vertical axis for either case. Of course, for case F, the concentration at the top of the reactor is slightly less than at the bottom, due to the skewed temperature profile, but the variation is minimal.

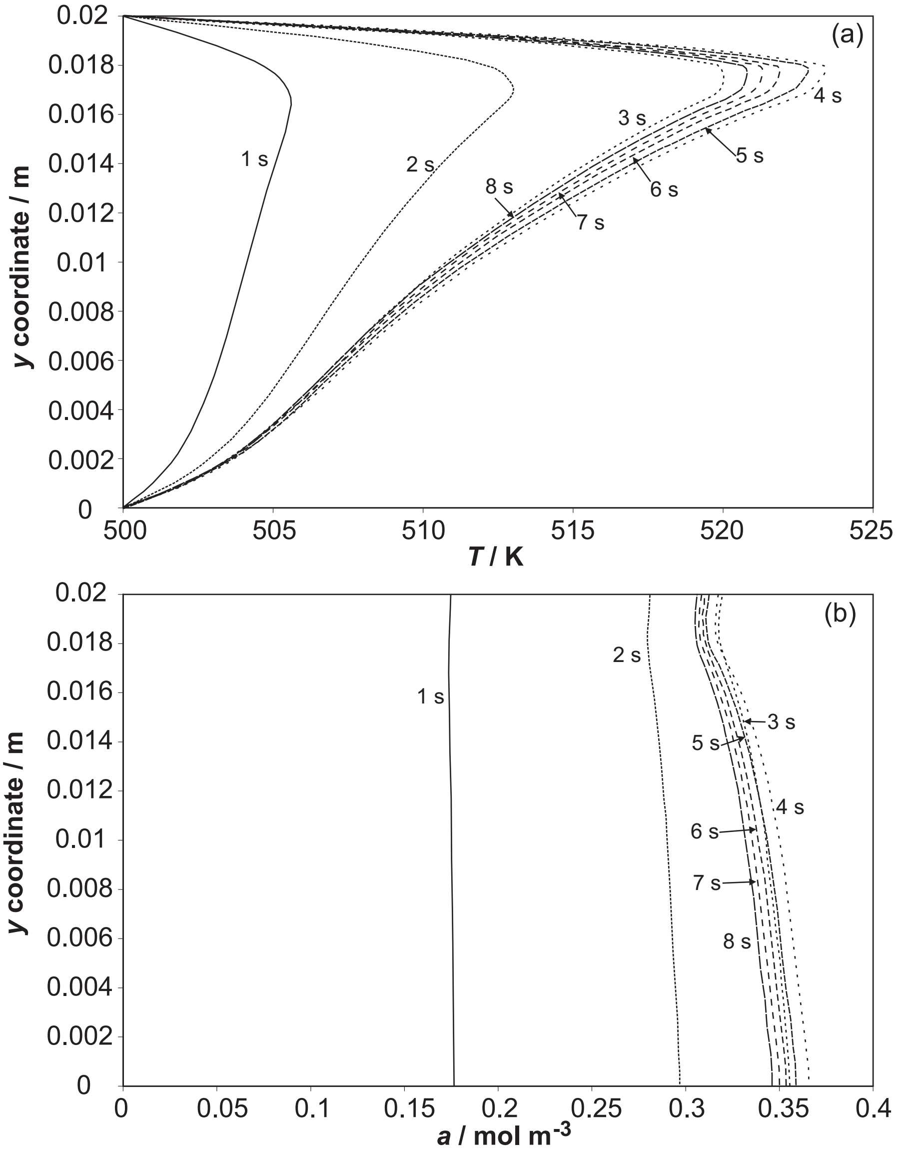

Figure 5.15. (a) The temperature along the vertical axis of the reactor for increasing time for case F. (b) Profiles of the concentration of A along the vertical axis for case F for increasing time.

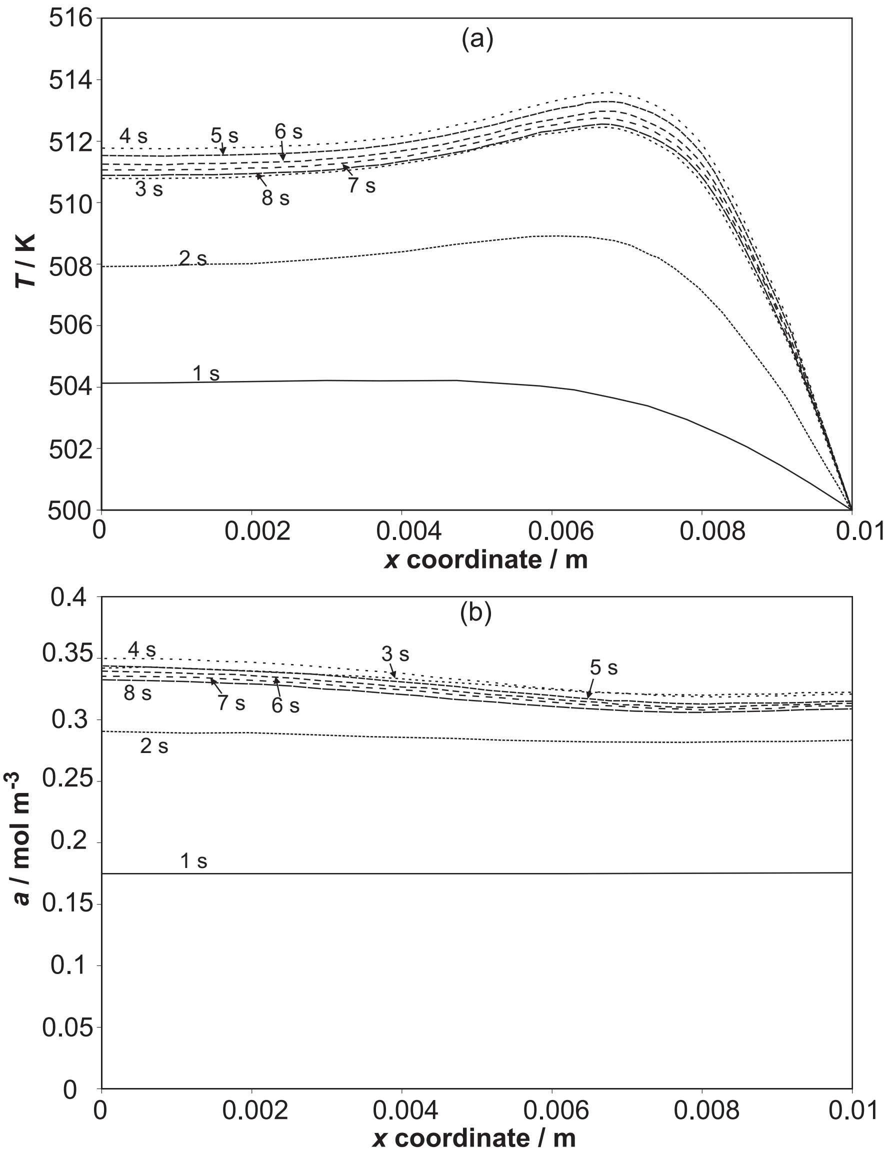

Figure 5.16. (a) Profile of the temperature along the horizontal axis of the reactor for increasing time for case F. (b) Profile of the concentration of A along the horizontal axis of the reactor for case F for increasing time.

Figure 5.16 shows the profiles of the temperature and the concentration of A along the horizontal axis for case F. The shape of the temperature profiles is very similar to those in cases D and E, and therefore very different to those seen in the other slow reaction regime in case A. Again, it is clear that there is very little spatial variation in the concentration of A, but it is worth pointing out that the concentration is highest at the centre of the reactor and then decreases towards the wall. This is the opposite of what was seen in case A and in the diffusive limit, where the concentration was always at its lowest at the centre of the reactor.

5.3.3.7 Position of the Maximum Temperature for Cases A – F

It was shown in Chapter 2 that the position of the maximum temperature on the vertical axis of the reactor varied with Rayleigh number (Figure 2.6). It is interesting to compare the variation of the position of the maximum temperature derived by Archer (1977) experimentally, and in Chapter 2 of this work numerically, for the thermal decomposition of azomethane, with the results for Sal'nikov's reaction, described above. Figure 5.17 shows the best fit line through the simulated points in Chapter 2, giving the variation of the position of the maximum temperature along the vertical axis of the reactor, with Rayleigh number. As before, *Ra* has been calculated using the temperature rise at the centre of the reactor at the same time as the maximum temperature occurred in the vessel. It should be remembered that the results of the simulations showed good agreement with Archer's (1977) experimental results (see Figure 2.6). Also plotted are points representing cases A – F, discussed above. The simulations for Sal'nikov's reaction agree very well with the results, both experimental and numerical, for the decomposition of azomethane.

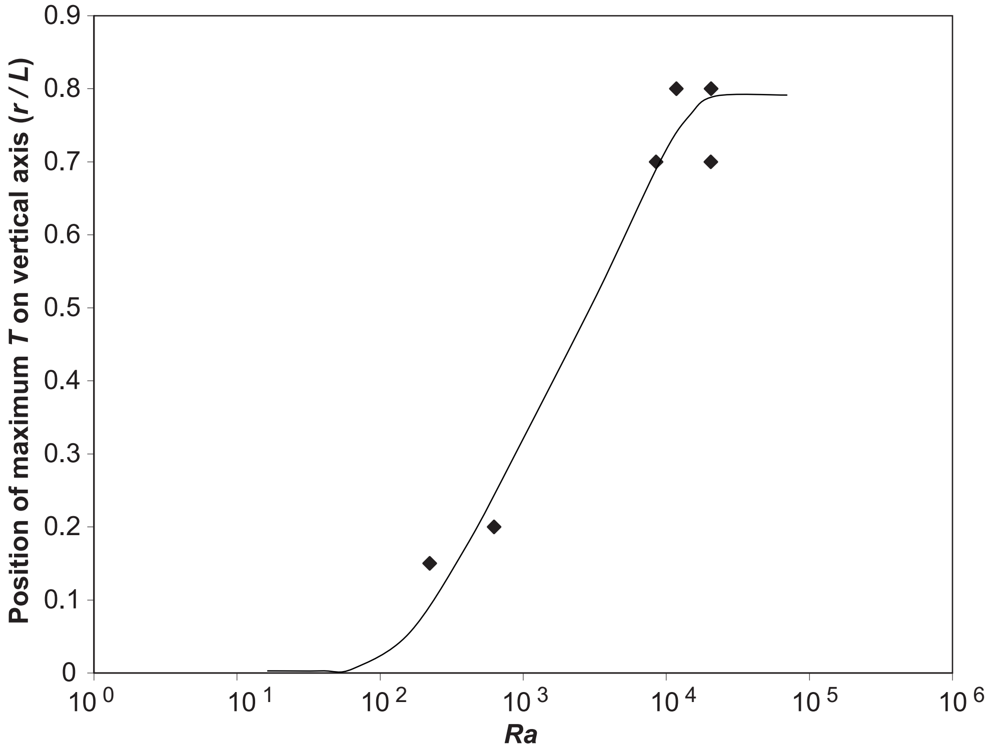

Figure 5.17. Variation of the dimensionless position of the maximum temperature along the vertical axis of the reactor with *Ra*. The line is the best fit through the simulated points in Figure 2.6 for the thermal decomposition of azomethane. The diamonds correspond to cases A – F, discussed above.

5.4 Summary

The behaviour of Sal'nikov's reaction has been examined under the influence of natural convection to determine the region on the regime diagram, for fixed $\tau_{step\ 2}$ / $\tau_{step\ 1}$, in which oscillations occur. The region found could be split into two distinct areas, one for $Ra < 10^3$, where diffusion dominates transport, and one when $10^3 < Ra < 10^6$, when laminar convection dominates. There was a very noticeable change in shape of the region of oscillations around the critical value of $Ra \sim 10^3$, when natural convection supercedes diffusion as the principal means of heat and mass transport. As one might have anticipated, when diffusion dominated transport, the boundaries between oscillatory and non-oscillatory solutions are largely independent of $\tau_{step\ 2}$ / $\tau_{convection}$, and agreed well with the values found in the purely diffusive limit in Chapter 4. When natural convection was important, the oscillations occurred over a wider range of parameters, and the width of the oscillatory region increased with *Ra*.

In addition to defining a region of oscillations, the different types of behaviour in different parts of the regime diagram were discussed. In general, it was observed that the inclusion of natural convection led to a number of different types of behaviour. In most cases the spatial temperature and concentration fields were far more complex than those seen in the absence of natural convection. Specifically, it was shown that for the non-oscillatory cases with relatively small increases in temperature, the temporal evolution of the temperature and the concentration of A at the centre of the reactor was similar, regardless of the degree of convection present. In addition, it was shown that in this region of slow reaction, the concentration of A remained virtually spatially uniform at Rayleigh numbers sufficient to generate significant natural convection. This is similar to the diffusive case. Natural convection did, however, have an impact on the shape of the temperature profile along the vertical axis of the reactor. The profile becomes more skewed as *Ra* is increased. Some curious behaviour was also observed when oscillations occurred in the presence of natural convection. It was found that at the centre of the reactor, the temperature and the concentration of A oscillated in-phase. This is very different to what is seen in the well-mixed and purely diffusive limits, and will be discussed in more detail in Chapter 6. Finally, for the non-oscillatory high temperature rise solutions with natural convection, the forms of the solutions were found to be initially very similar to those seen in the purely diffusive limit. This is because it takes some time for sufficient temperature gradients to develop to induce significant natural convection.

Finally, the degree to which natural convection skewed the vertical temperature profile in the simulations of Sal’nikov’s reaction was compared with the experimental and numerical results for the decomposition of azomethane, presented in Chapter 2. The agreement between the behaviour for the two different reactions was found to be very good.

6 The Effect of Natural Convection on the Phase of the Oscillations

6.1 Introduction

It was noted in Chapter 5 that for case E, the oscillations in the temperature and the concentration of A were in-phase at the centre of the reactor. A similar effect was seen by Cardoso *et al.* (2004*b*); they, however, chose not to pursue the reasons for this. It is not intuitively obvious why there should be in-phase oscillations. The anti-phase oscillations seen in the well-mixed or purely diffusive regimes are more expected. These oscillations arise, because, as the temperature increases, the rate of step 2 of Sal'nikov's reaction increases, therefore causing the rate of destruction of the intermediate to increase, so reducing the concentration. Thus, the temperature will increase and the concentration decrease. Eventually, a point will be reached when the rate of heat production from the reaction goes down because the intermediate has been depleted. Heat loss then dominates heat production, so the temperature drops. As the temperature drops the rate of step 2 decreases, until the rate of production of A by step 1 is greater than the rate of its destruction in step 2. At this point the temperature is going down, and the concentration is rising. The cycle can then repeat, causing oscillations. Natural convection can clearly disrupt this cycle, causing in-phase oscillations. This effect is investigated below.

6.2 Numerical Method

The region of oscillations identified in the previous chapter was investigated by carrying out a series of simulations. Table 6.1 shows the values used in each of the sixteen runs considered; cases 2 and 16 correspond, respectively, to cases B and D presented by Cardoso et al. (2004*b*). Estimates of *Ra* and the values of $\tau_{step\ 2} / \tau_{convection}$ and $\tau_{step\ 2} / \tau_{diffusion}$ are shown in Table 6.1.

Table 6.1. Details of the 16 cases considered. The highlighted entries show the cases discussed in detail.

case	L / m	g / m s^{-2}	$\kappa \times 10^4$ / m^2 s^{-1}	Ra	$\tau_{step\ 2} / \tau_{convection}$	$\tau_{step\ 2} / \tau_{diffusion}$
1	0.02	0	1	0	0	0.94
2	**0.05**	**9.81**	**6**	**680**	**10.21**	**0.91**
3	**0.05**	**30**	**6**	**1445**	**14.81**	**0.91**
4	0.05	50	6	2030	17.56	0.91
5	0.03	4.9	1.5	1260	9.60	0.63
6	0.03	9.81	1.5	2000	12.10	0.63
7	0.03	30	1.5	4210	17.56	0.63
8	0.01	1.5	0.13	1960	9.33	0.49
9	0.01	4.9	0.13	4300	13.85	0.49
10	0.01	9.81	0.13	6835	17.45	0.49
11	0.02	3	0.4	3300	9.33	0.38
12	0.02	9.81	0.4	7280	13.85	0.38
13	0.02	20	0.4	11700	17.56	0.38
14	**0.01**	**30**	**0.097**	**25900**	**25.33**	**0.37**
15	0.02	9.81	0.33	10700	13.85	0.31
16	0.05	1962	1	8.45×10^5	59.69	0.15

All the cases in Table 6.1 exhibited temporal oscillations in the temperature and the concentration of the intermediate. Three of these cases are discussed in detail below; their behaviour is typical of that of the other 13 cases studied, which are summarised later. The cases presented in detail are case 2, which is in the region of the regime diagram where diffusion controls transport, and cases 3 and 14, which are in the region where laminar convection is the controlling mechanism. Of these three cases, case 14 typifies the region in which oscillations at the top of the reactor are anti-phase, whereas at the bottom they are in-phase; consequently, it is considered in the greatest detail. In each case, plots of the temperature and the concentration of A, whilst the reaction proceeds, are shown (in Figures 6.1, 6.3 and 6.4) at five points in the reactor. These plots provide a profile along the reactor's vertical and horizontal axes and were chosen as follows: on the vertical axis the points are at distances y = 0.5 L, L (*i.e.* the centre of the reactor) and 1.5 L from the bottom of the reactor. On the horizontal axis the points are located a distance of x = 0.25 L, and 0.75 L from the vertical axis. The coordinates of each point appear in the top right corners of the plots, relative to the origin, which is defined as being on the vertical axis of the reactor, at the very bottom. For cases 2 and 14, *i.e.* the cases displaying anti-phase oscillations throughout the reactor, and in-phase behaviour in the bottom of the reactor respectively, a term by term analysis of the governing equations is also presented.

6.3 Anti-Phase Oscillations Throughout the Reactor

Case 2 in Table 6.1 typifies the area in the regime diagram where the oscillations in the temperature and the concentration of A are in anti-phase throughout the reactor. The Rayleigh number is 680 and hence natural convection is just starting to become significant. Figure 6.1 shows the temporal development of the temperature and the concentration of A at the five points within the reactor. It is clear that the temperature and concentration are everywhere oscillating out-of-phase, as discussed above, with the concentration leading the temperature. This, almost anti-phase oscillation throughout the reactor, is similar to that seen in the well-mixed case (Gray and Scott, 1990*a*). It is interesting to note that although diffusion is the dominant mode of transport, the effects of the very weak convective motion can still be seen in Figure 6.1. The top portion of the reactor is clearly hotter than the bottom section. This contrasts with what is seen when diffusion is the only transport mechanism (*i.e.* in microgravity), where the temperature field is spherically symmetric. The weak convection present in case 2 has caused the hot zone in the reactor to be shifted above the centre, thus disrupting the spherical symmetry.

The rates of chemical reaction and transport of species A, as well as the generation and transport of heat, into and out of a local elemental control volume are now considered in detail. This is done by analysing the magnitudes of the convective, diffusive and reactive terms in the equations for the conservation of chemical species A and thermal energy, as a function of time. Figure 6.2(a) shows each of the terms in the equation for the dimensionless concentration of A, *i.e.*

$$\frac{\partial a'}{\partial t'} + \underbrace{\underline{u}'.\nabla' a'}_{convection} = \underbrace{\frac{1}{Le}\frac{\tau_{convection}}{\tau_{diffusion}}\nabla'^2 a'}_{diffusion} + \underbrace{\frac{\tau_{convection}}{\tau_{step\ 2}}p' - \frac{\tau_{convection}}{\tau_{step\ 2}}\exp\left(\frac{\phi T'}{1+\eta T'}\right)a'}_{reaction}. \tag{6.1}$$

Figure 6.2(b) shows each of the terms in the dimensionless energy equation,

$$\frac{1}{\gamma}\frac{\partial T'}{\partial t'} + \underbrace{\underline{u}'.\nabla' T'}_{convection} = \underbrace{\frac{\tau_{convection}}{\tau_{diffusion}}\nabla'^2 T'}_{diffusion} + \underbrace{\exp\left(\frac{\phi T'}{1+\eta T'}\right)a'}_{reaction}. \tag{6.2}$$

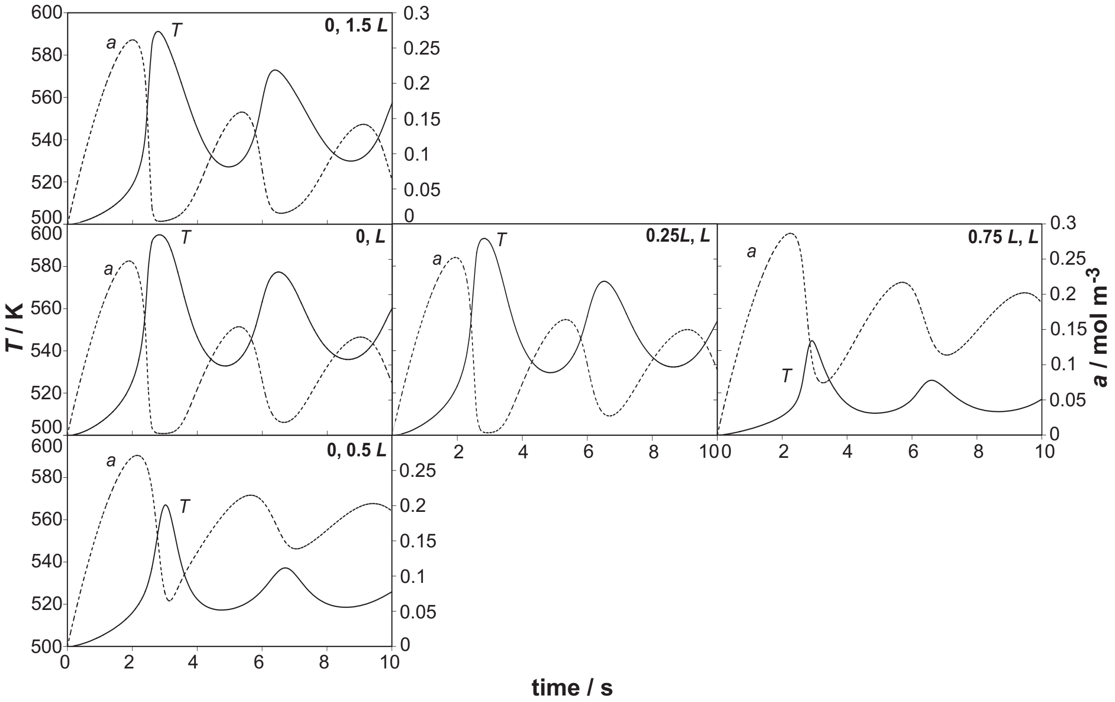

Figure 6.1. Plots of the temperature and concentration of A at five locations within the reactor as a function of time, for case 2. The numbers in the top right corner of each plot are the coordinates of the location considered, relative to the origin which is defined to be at the bottom of the reactor, on the vertical axis. The plots are arranged schematically to indicate their relative positions in the reactor. The solid lines show the temperature and the dashed lines the concentration of A.

At the top of the reactor, the convective and diffusive terms in the concentration equation are positive, while the net reactive term, which combines steps 1 and 2 of the reaction, is negative. This means that species A is transported into the control volume by diffusion and transported out by convection; these two transport mechanisms result in a net inflow of intermediate A. It should be recalled that A is generated in step 1 and consumed in step 2 of the chemical reaction; thus a negative reactive term means that there is a net depletion of A. It can be concluded therefore, that at the top of the reactor, transport by both diffusion and convection supplies species A, which is consumed by chemical reaction. The magnitudes of the terms in the temperature equation show that the heat generated by this chemical reaction is transported out of the control volume by diffusion, *i.e.* thermal conduction.

At the bottom of the reactor, diffusion, of both species A and heat, has a small role after the first oscillation. Species A is transported by convection into a control volume and is consumed by chemical reaction. The heat generated locally is removed mainly by convection.

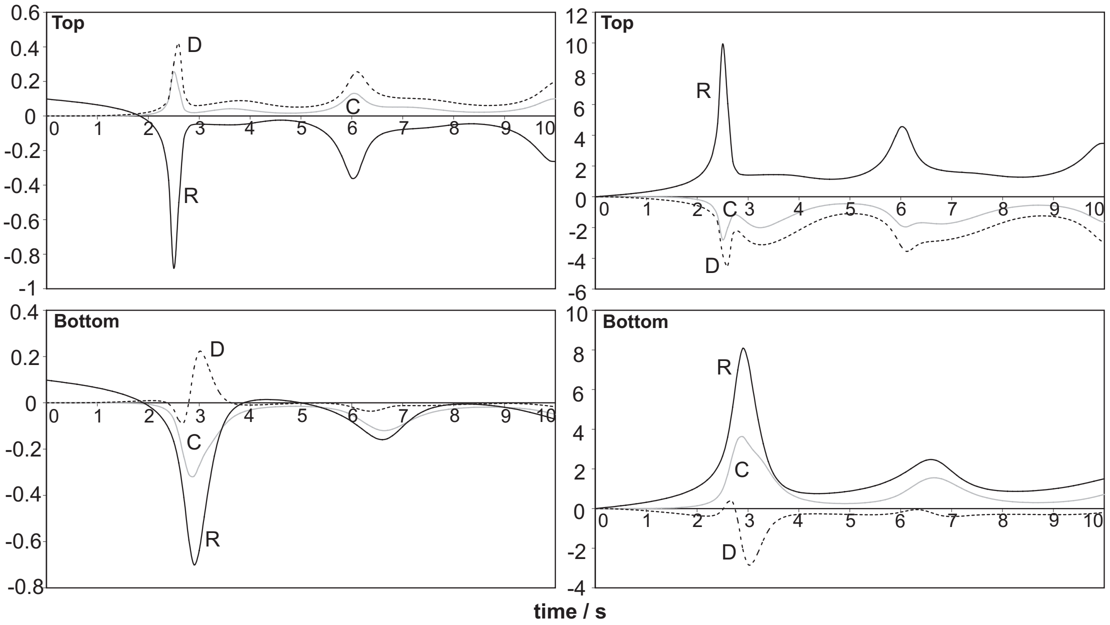

(a) concentration **(b) temperature**

Figure 6.2. Temporal evolution of the convective, diffusive and reactive terms in (a) the concentration equation, Eq. (6.1), and in (b) the energy equation, Eq. (6.2), for case 2. Note that time is dimensional for ease of comparison with Figure 6.1. In each case, the black line is the reaction term (R), the grey line is the convective term (C), and the dashed line is the diffusive term (D).

6.4 Transition from Anti- to In-Phase Oscillations

For case 3, the value of *g* was increased to 30 m s^{-2} (see Table 6.1), thus increasing the Rayleigh number to 1445; the effects of natural convection are now more significant, due to the higher value of *Ra*. Plots of the temperature and concentration of A at the five specified points in the reactor are shown in Figure 6.3. It can be seen that the behaviour at the top of the reactor is similar to that shown in case 2, *i.e.* the concentration of A and the temperature are oscillating approximately in anti-phase. However, in the bottom section of the reactor, the difference in phase (measured arbitrarily between the second peaks in both curves) is 0.6 s compared with 1.2 s at the top of the reactor. Clearly, the phase difference in this case depends on the position in the reactor.

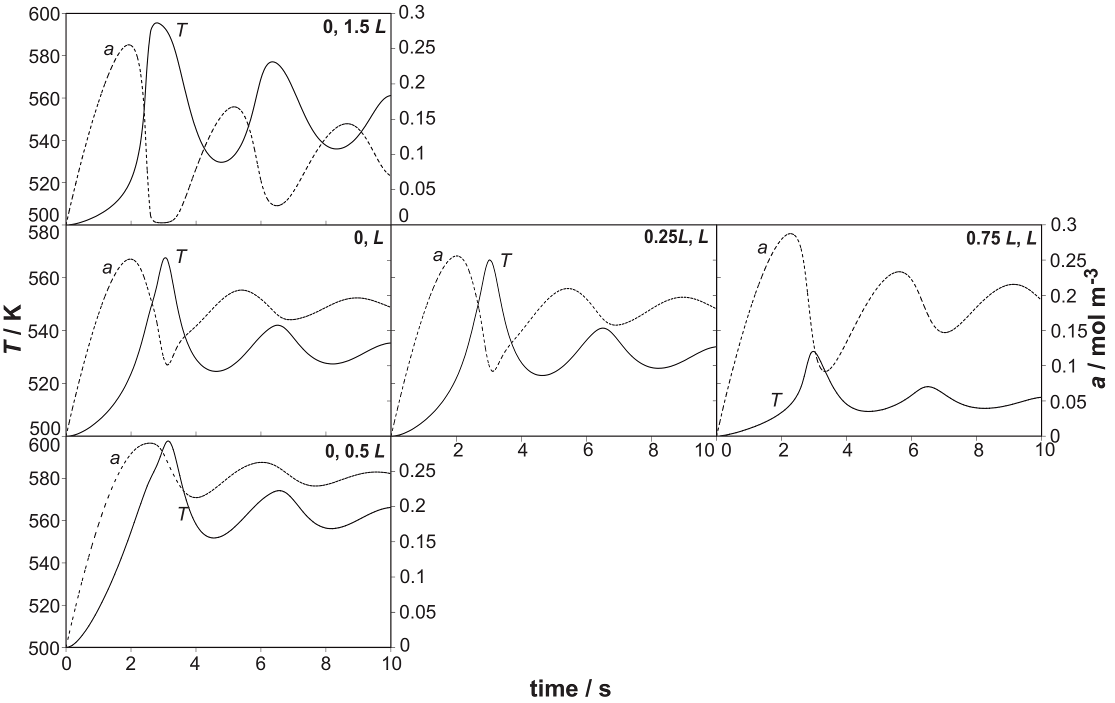

Figure 6.3. Plots of the temperature and concentration of A at the specified points within the reactor for case 3.

6.5 In-Phase Oscillations in the Bottom of the Reactor

The final case presented in detail (case 14) has a Rayleigh number of ~ 2.6 × 10^4, *i.e.* it is well within the region where laminar convection is the dominant transport mechanism. Like cases 2 and 3, in the hot zone in the top section of the reactor, the temperature and concentration of A oscillate almost in anti-phase, as shown in Figure 6.4. At the centre of the reactor, the phase difference is 0.2 s compared with 1 s in the top section. In the bottom of the reactor the temperature and the concentration of A are oscillating in-phase, but with relatively small amplitudes. This behaviour mirrors that observed by Cardoso et al. (2004*b*) in their case D (case 16 in Table 6.1). What is also interesting to note is how the phase difference behaves with increasing radial position along the horizontal axis. Thus, Figure 6.4 shows that at the centre of the reactor, the temperature and the concentration of A oscillate, virtually, in-phase. However, at larger radial positions, the concentration and temperature plots become out-of-phase. At a radius of 0.75 *L*, the temperature lags the concentration by 0.9 s. The temperature plots at all points along the horizontal axis are nearly identical. Thus, the magnitude of the temperature varies significantly in the vertical direction, but very little in the horizontal direction. Such stratification is expected in systems with moderate convection, because it corresponds to maximum gravitational stability.

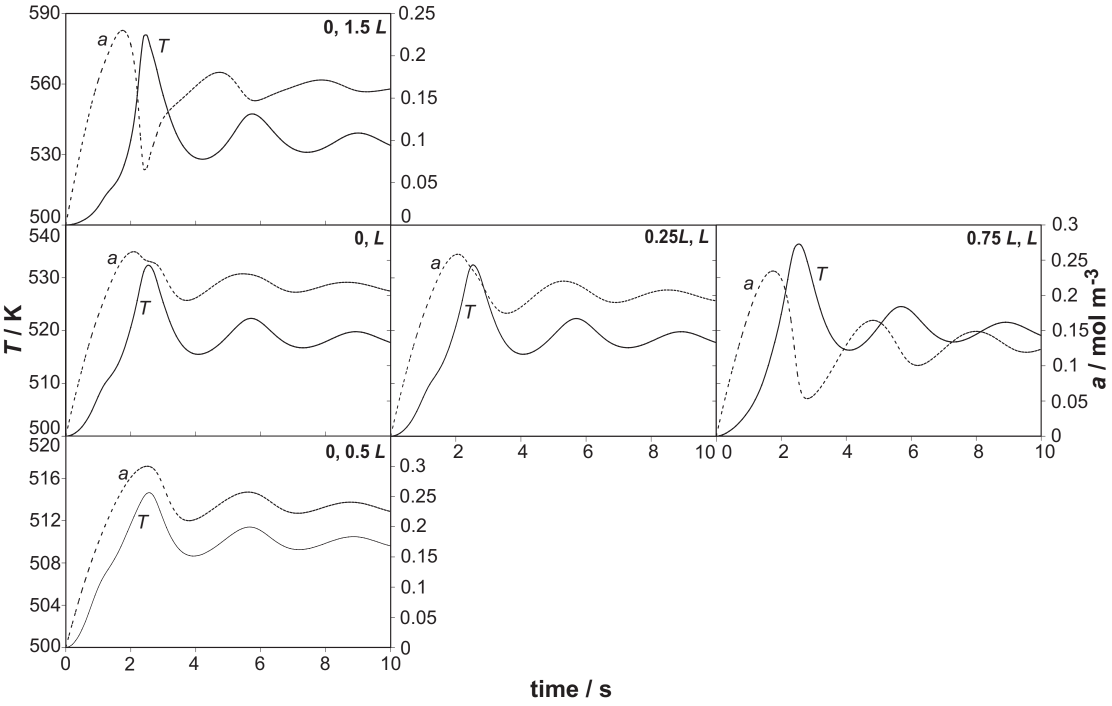

Figure 6.4. Plots of the temperature and concentration of A at the specified points within the reactor for case 14.

This temperature stratification can also be seen in Figure 6.5, which shows the concentration of A, and the temperature on a vertical cross section through the axis of the reactor at 0.4 s intervals, whilst the reaction proceeds. Figure 6.5 clearly shows the two distinct regions of behaviour observed previously in Figure 6.4. At the top of the reactor the anti-phase oscillations in concentration and temperature are evident. It is also apparent that the temperature in this region is considerably higher than in the bottom of the reactor at all times, and that the amplitude of the oscillations is larger. In the bottom section of the reactor, where the temperatures are relatively low, the in-phase oscillations cannot be seen clearly due to their relatively small magnitude; however, it is clear that the concentration of A in this lower part of the reactor is significantly higher, and the temperature significantly lower, than at the top, throughout the course of the reaction. It is also noticeable from Figure 6.5 that, whilst cold fluid descends at the wall, there is a significant increase in the concentration of the intermediate A.

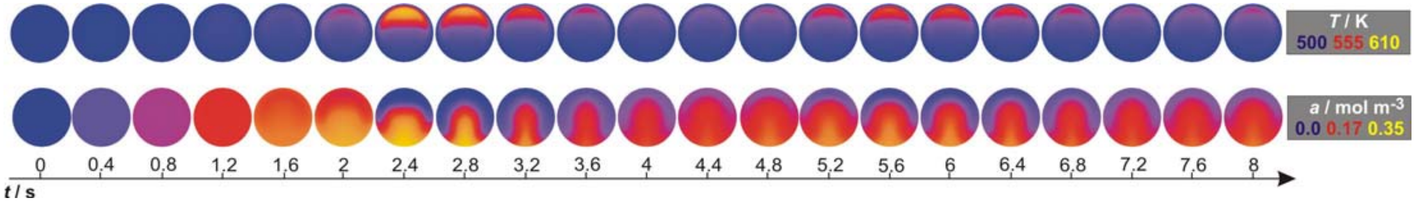

Figure 6.5. Evolution of the temperature (top) and the concentration of A (bottom) in the reactor, for case 14. The frames occur at regular intervals of 0.4 s, over the course of 8 s.

This effect is highlighted more clearly in Figure 6.6, which shows how the temperature and concentration of A vary in a notional element of gas, whilst it is circulating in the flow for case 14. Figure 6.6(b) shows y, the vertical distance above the bottom of the reactor. In this case the element is initially stationary at a position (0.3 L, L), *i.e.* it is on the horizontal axis of the reactor, and slightly removed from the vertical axis. Figure 6.6(b) allows the duration of each complete flow loop to be estimated by looking at the time when the element moves upwards past its initial y coordinate. The end points of these circuits are shown by the broken vertical lines in Figure 6.6(a). Three such loops are shown. Initially, the element moves slowly upwards, and the temperature increases only very slightly. This results in the production of A in step 1 of Sal'nikov's reaction being favoured over its destruction in step 2. A small peak in temperature is observed at ~ 1.2 s as the element moves through the hottest point in the reactor (at the top). The fluid then descends at the wall and remains at a low temperature, with A accumulating. When the element begins to rise, near the vertical axis, the temperature increases rapidly and, conversely, the concentration decreases, because step 2 now dominates at this higher temperature. Once through the hot zone, the fluid cools to near the wall temperature and, once more, significant accumulation of A is observed, whilst this cooler fluid descends. It is interesting to note that the difference in temperature between the hot zone at the top of the reactor, and the cool regions at the wall and at the bottom is very large (~ 80 K as seen in Figure 6.5), and also that the fluid element spends only a small amount of time under the influence of the hot zone. Figure 6.6(a) also clearly shows the effect of the large temperature oscillations at the top of the reactor. The first major temperature peak at ~ 2.4 s reaches ~ 590 K, whereas the second major peak (corresponding to the third time the particle passes through the hot zone) at ~ 4.1 s only reaches ~ 540 K. What is interesting is the effect this has on the concentration of A when the element reaches the bottom of the reactor. After passing through the much hotter first peak, the concentration of A in the element is ~ 0.19 mol m^{-3} at the bottom of the reactor, whereas after passing through the hot zone during the next cycle, now at a lower temperature, the concentration at the bottom is ~ 0.24 mol m^{-3}. It should be noted that the difference between these values is of similar magnitude to that of the oscillations in the bottom section of the reactor.

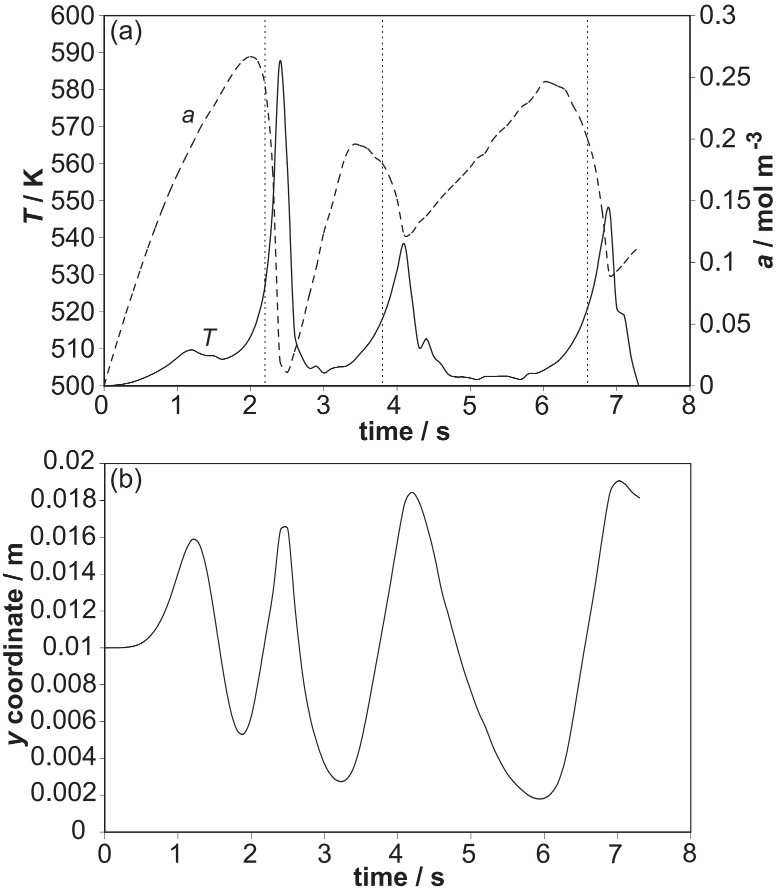

Figure 6.6. (a) The evolution of the temperature (solid line) and the concentration of A (dashed line) within a notional fluid element as it is tracked through the flow field generated by natural convection in case 14. The element begins at a location (0.3 *L*, *L*). The broken lines indicate the time taken for the element to return to its starting point. (b) The *y* coordinate of the fluid element as it moves around the reactor.

The magnitudes of the convective, diffusive and reactive terms in Eq. (6.1) for the conservation of chemical species A and in Eq. (6.2) for energy, as a function of time, are now analysed for case 14. Figure 6.7(a) shows each of the terms in Eq. (6.1); Figure 6.7(b) shows each of the terms in Eq. (6.2).

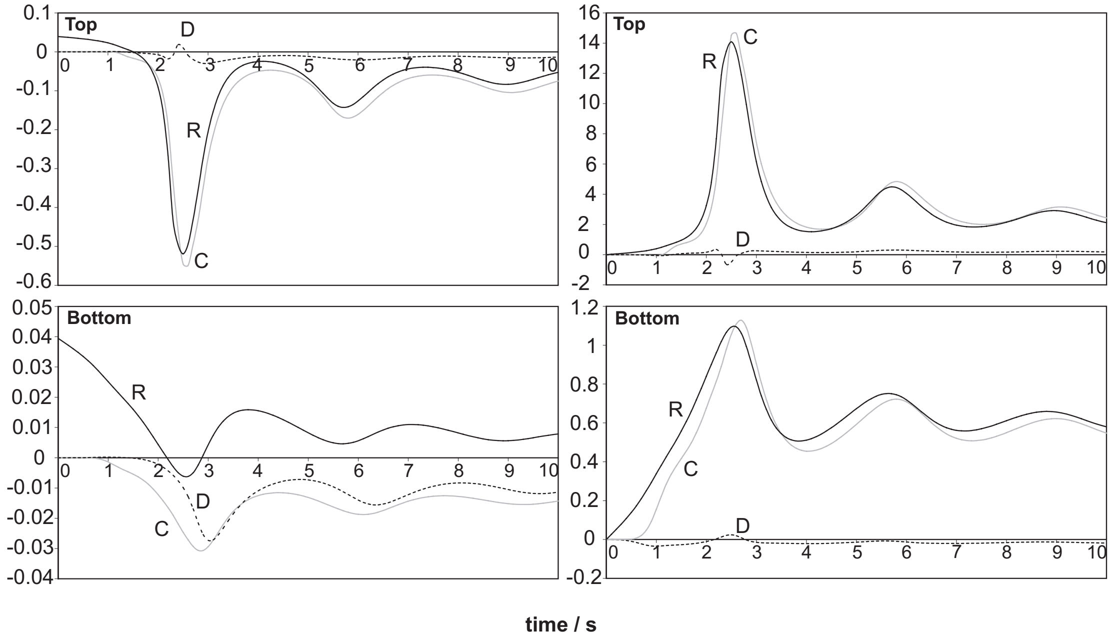

(a) concentration **(b) temperature**

Figure 6.7. Temporal evolution of the convective, diffusive and reactive terms in (a) the concentration Eq. (6.1), and in (b) the energy Eq. (6.2), for case 14. Note that time is dimensional for ease of comparison with Figure 6.4. In each case, the black line is the reaction term (R), the grey line is the convective term (C), and the dashed line is the diffusive term (D).

At the top of the reactor, the transport of both species A and heat by diffusion is much smaller than by convection. It is concluded that convection supplies A, which reacts locally in step 2. The heat generated by this chemical reaction is removed by convection. This situation is similar to that already described for case 2; the transport processes (diffusion, convection or both) combine to locally supply A for chemical reaction and remove the heat released by reaction.

At the bottom of the reactor, the behaviour is strikingly different from that found in case 2. The reactive term is now positive, almost at all times, instead of negative. This means that species A is locally generated, rather than being depleted by chemical reaction. This generation of species A by chemical reaction, as well as its transport by convection into the control volume, are balanced by diffusion of A out of the control volume. The heat generated by chemical reaction is transported away by convection, because the term for the diffusion of heat is relatively small in Eq. (6.2) for the temperature.

6.6 General Trends

Some general trends are apparent from comparing the above three cases. It is interesting to note that the frequency of the oscillations in each case is similar, which may be seen in Figures 6.1, 6.3 and 6.4. Gray and Scott (1990*a*) showed that in the well-mixed case, the frequency of oscillations is given by $\omega_0 = (\phi - 1)^{1/2}$, with $\phi = E_2 \Delta T / R T_0^2$. Inserting the relevant parameters for cases 2, 3 and 14 into this expression leads to a predicted oscillatory frequency of ~ 2 rad s^{-1}, which is in reasonable agreement with that observed in this study. Of course, this is only a very approximate calculation given that cases 2, 3 and 14 are not well-mixed. It is also clear from Figures 6.1, 6.3 and 6.4 that the phase of the temporal development of temperature is almost independent of position in the reactor, *i.e.* the peaks and troughs in the temperature occur at approximately the same times throughout the reactor. However, the phase of the oscillations in the concentration of A does depend on position in the reactor. This implies that the changing phase difference between the concentration and temperature curves is due to the concentration curve shifting. This should be a result of a change in the balance of the terms in the concentration equation, from point to point within the reactor. If the ‘anti-phase’ oscillations in each case are compared (*i.e.* the whole of case 2 and the top sections of the reactor in cases 3 and 14), it is clear that these oscillations occur at higher temperatures and have a greater amplitude than the ‘in-phase’ oscillations. At all points considered in case 2 (see Figure 6.1), the temperature peaks at ~ 590 K, and the peak-to-peak change of the first oscillation (measured from the first peak to the first trough) is ~ 60 K. Similar ranges are found in the hot zones in the top section of the reactor in cases 3 and 14. Lower down the reactor in cases 3 and 14, however, the temperatures are considerably lower. For example, in the bottom section of the reactor in case 3 (Figure 6.3), the temperature reaches a peak value of only ~ 525 K, with the peak-to-peak range of the first oscillation being ~ 12 K. This is seen again in case 14 (Figure 6.4), where the bottom section of the reactor is relatively cool and only exhibits small oscillations in the temperature and the concentration of A. Therefore there is a change in behaviour, from case 2, where the whole reactor is ‘hot’ and the temperature and concentration oscillate out-of-phase, through a transitional stage (case 3), to a situation as in case 14, where the reactor can, in effect, be split into a ‘hot’ zone at the top of the reactor, in which temperature and concentration oscillate out-of-phase, and a ‘cold’ zone at the bottom, where the smaller oscillations are in-phase. These ‘hot’ and ‘cold’ zones can be easily identified in Figure 6.5, showing the evolution of temperature and concentration of A for case 14.

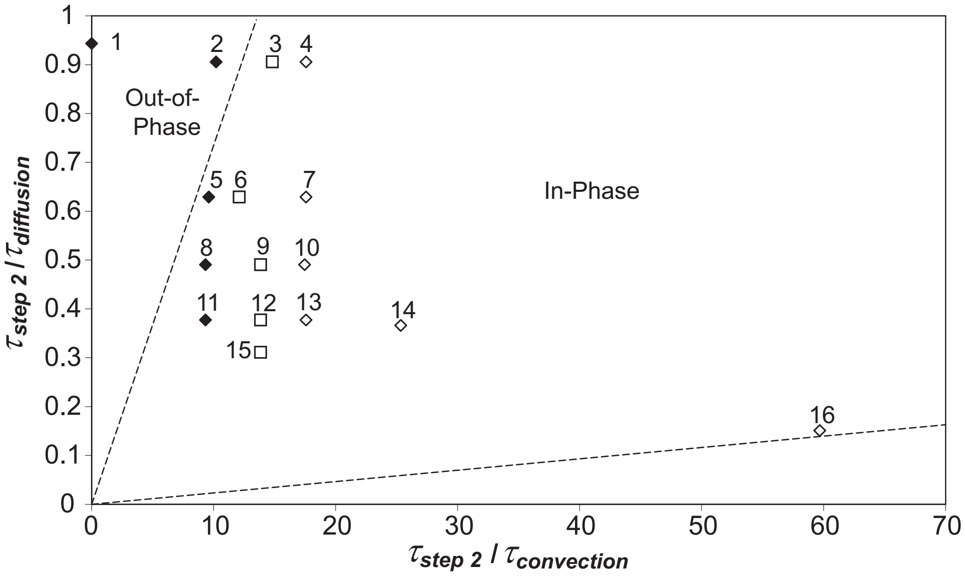

Figure 6.8. Regime diagram showing the sixteen cases considered. The closed diamonds represent the case where oscillations always occurred out-of-phase; the open diamonds represent those cases where in-phase oscillations were observed at some point in the reactor; the open squares represent the transitional cases where a shift in the phase difference was observed.

In order to understand this transition, complete computations for all sixteen cases presented in Table 6.1 were done to characterise fully the observed oscillations. Figure 6.8 shows these sixteen points plotted on the regime diagram of Figure 5.1. The closed diamonds represent the cases where the oscillations in the temperature and the concentration of A are out-of-phase at all points in the reactor (as typified by case 2). At the other extreme, the open diamonds show the cases where the observed oscillations were in-phase in the bottom half of the reactor (*e.g.* case 14). The open squares represent the transition between these two extremes, *i.e.* there is some shift in the phase difference between the temperature and concentration plots, but the oscillations cannot be described as being in-phase (*e.g.* case 3). Figure 6.8 clearly shows that the transition from out-of-phase oscillations everywhere, to oscillations in-phase in the bottom half of the reactor depends on the value of $\tau_{step\ 2} / \tau_{convection}$ (but not on $\tau_{step\ 2} / \tau_{diffusion}$), with the transition occurring at a value of ~ 10 – 15. In other words, in-phase oscillations are observed when the characteristic timescale for convection is an order of magnitude faster than the timescale for step 2 of Sal’nikov’s reaction.

The in-phase oscillatory behaviour above is a result of a complex interaction between chemical kinetics, and the transport of heat and mass by natural convection and diffusion. It occurs when the oscillations in temperature have relatively small amplitude, so that the supply of A by step 1 dominates the depletion of A in step 2 throughout the whole cycle of an oscillation in temperature. The reactive term in Eq. (6.1) is then always positive, as is the case for the reactive term in Eq. (6.2) for the temperature. The evolution of the concentration of intermediate and temperature during one cycle of such an oscillation can be followed. Whilst the intermediate A is produced in step 1, its concentration rises. Species A is then consumed in step 2, which is exothermic, so the temperature rises. Because this second step has an Arrhenius temperature-dependence, it is self-propagating. While the temperature increases, the convective velocity also increases according to Eq. (3.22). The rate of generation of A then slows down due to the rate of step 2 increasing, and hence the rate of heat generation also slows down. The temperature accordingly begins to fall when the rate of heat removal by convection exceeds the rate of generation in the second step of the reaction. When the temperature falls, removal of intermediate A by diffusion overtakes the supply by convection and chemical reaction. When the temperature becomes so low that the rate at which heat is convected away is less than the rate of heat generation by chemical reaction, the temperature starts to increase. As the temperature increases, the supply of A by convection increases, beginning the cycle again.

Also noted in case 14 was the fact that the oscillations appeared to become out-of-phase at locations farther from the centre of the reactor. This is due to the flow patterns within the reactor. Away from the centre of the reactor, the flow is less influenced by the axial up-flow of cool, intermediate-rich gas around the vertical axis of the reactor and more influenced by the relatively hot gas, with a low concentration of A, which moves from the top half of the reactor into the boundary layer. It is therefore unsurprising that the in-phase oscillations, which typify the former, are less evident on moving further away from the axis. The effect of the flow in the boundary layer can clearly be seen in plots of concentration in Figure 6.5. At the top of the reactor, a horse-shoe shaped region of similar concentration can be seen at all times. This particular shape occurs due to the influence of the flow at the walls.

6.7 Summary

It was seen in Chapter 5 that under certain conditions, the oscillations in the temperature and the concentration of A at the centre of the reactor could be in-phase instead of anti-phase, as is the case in the well-mixed and purely diffusive limits. The conditions under which these in-phase oscillations emerge were investigated. It was found that oscillations in the temperature and the concentration of the intermediate A could occur in-phase in the bottom section of the reactor when $\tau_{step\ 2} / \tau_{convection}$ is increased beyond 15. It is believed that these differences in phase at various points inside the reactor are due to a complex interaction of the convective flow, the kinetics of Sal'nikov's reaction, and the diffusion of both heat and the intermediate species.

7 Conclusions and Recommendations for Future Work

7.1 Conclusions

This work aimed to study the influence of natural convection on a simplified model of cool flames, namely Sal'nikov's reaction, by means of numerical simulation in conjunction with simple analytical techniques. The main conclusions derived from this study are summarised below.

7.1.1 Model Development and Comparison with Previous Experimental Measurements

A model of a simple exothermic reaction occurring in a spherical vessel was formulated in Chapter 2. This was done to compare the results of previous experimental work with the analytical and numerical results from this study. Such a comparison could not directly be made for Sal'nikov's reaction, due to the lack of both experimental measurements, and a suitable chemical analogue for this system. In fact, comparisons were made between experimental measurements of the temperature when a one-step exothermic reaction occurs in a spherical vessel and the results of a scaling analysis of the governing equations, and also numerical simulation. It was found that for the two limiting cases where the transport of heat and mass within the reactor is controlled by either diffusion or natural convection, there was excellent agreement between the experimental measurements and both the simulations and the analytical scales. These scales showed that the temperature rise within the reactor is proportional to the ratio of the characteristic timescales for the dominant transport mechanism (*i.e.* diffusion or natural convection) and chemical reaction. It was also observed that the linear form predicted by scaling broke down in the diffusive limit as the system approached the transition from slow reaction to explosion. The location of this transition was compared with the classical theory of Frank-Kamenetskii (1955), and the agreement was found to be very good.

The measured temperature profile along the vertical axis of the reactor was compared with the results of numerical simulations. Experiments showed that the position of the maximum temperature within the reactor depends on the Rayleigh number, with the maximum temperature occurring higher up the reactor for higher values of Ra. This variation of the point of maximum temperature inside the reactor was also seen in the results of the numerical simulations, and the experimental and numerical results showed excellent agreement. It was also found that the temperature profile measured experimentally for an exothermic reaction proceeding in a spherical reactor agreed very well with that deduced through simulation, both in terms of the shape of the temperature distribution, and the magnitude of the temperature rise. Finally, comparison of experimental results for three different exothermic reactions with both numerical and analytical results was made. The agreement between the three techniques proved to be excellent, and showed the onset of natural convection occurring at $Ra \sim 500$.

The pleasing agreement between the experimental measurements and both the analytical and numerical results proved that the model developed here to describe the system was correctly capturing the principal physical processes occurring in the reactor. These methods could then be applied, with confidence, to the analysis of Sal'nikov's reaction.

7.1.2 Scaling Analysis of Sal'nikov's Reaction

The techniques developed and tested in Chapter 2 for a simple one-step reaction were next applied to Sal'nikov's reaction. The first to be applied was scaling analysis, which yielded significant insight into the general behaviour of the system. Scales were developed in Chapter 3 for the characteristic concentration of the intermediate A and the temperature rise for a gas undergoing Sal'nikov's reaction, $P \rightarrow A \rightarrow B$, in a closed vessel; moreover the most appropriate form for these scales was compared with the results of numerical simulations. Examining the regions where diffusion and natural convection were in turn the dominant transport mechanism revealed that in both cases the characteristic concentration of the intermediate, a_0, was controlled by the kinetic terms, *i.e.* the quasi-steady-state hypothesis is often established on a timescale shorter than those for the other physical processes.

When diffusion was controlling transport, three distinct regions of behaviour were observed. For 'small' reactors, the temperature and concentration fields showed a slow rate of growth and decay, and the fields were virtually spatially uniform. In fact, the system behaved fairly similarly to the isothermal case. However, the characteristic temperature rise scaled as $\tau_{diffusion} / \tau_{step\ 1}$. When the size of the reactor was increased, a region in which the temperature and concentration profiles exhibited temporal oscillations was observed. For 'larger' reactors, the temporal profiles ceased to be oscillatory. Once again, the temperature rise scaled as $\tau_{diffusion} / \tau_{step\ 1}$; however, the data for these 'large' reactors did not extrapolate back through the origin. This is due to the rapid change in form of the equation governing the conservation of energy, when the concentration of the intermediate A falls to almost zero, during the course of Sal'nikov's reaction in a 'large' vessel.

When natural convection controls transport, oscillations were observed over a wide range of reactor sizes. The simulations indicated that the characteristic temperature rise scaled as $\tau_{convection} / \tau_{step\ 1}$. This means that in both the diffusive and convective regimes, the temperature rise scales as the ratio of the timescales for the controlling transport mechanism and the rate-determining step of the reaction.

Using these scales, along with order of magnitude arguments, predictions have been made as to how the system will respond to changes in process parameters, such as gas pressure, the size of reactor and if the reaction is conducted in the liquid-phase. It has been shown that natural convection is favoured by a high pressure in gas-phase reactions, and by a larger reactor. Because liquids have different physical properties, reactions in the liquid-phase develop more intense convection than gas-phase reactions with similar kinetic parameters. This effect is mainly due to the higher density of liquids, the principal effect of which is on the thermal diffusivity, κ.

Finally, the scaling results achieved for Sal'nikov's reaction occurring in a spherical reactor could be compared with those found in Chapter 2 for the thermal decomposition of azomethane. It was found that there was good agreement between the scales for the dimensionless temperature rise due to each of the two reaction schemes considered. This agreement highlights the power of what is, essentially, a relatively simple analytical technique. It was also shown that the scaling results for Sal'nikov's reaction agreed very well with previous experimental observations made when an exothermic reaction proceeds in a spherical vessel.

7.1.3 The Behaviour in the Absence of Natural Convection

One of the most important aims of a study of any potentially oscillatory reaction must be to define a region in parameter space in which oscillations occur. Such an analysis was performed in Chapter 4, for the simpler case when natural convection is entirely absent. Regions of the regime diagram where oscillations occur were identified through numerical simulation. These results were compared with previous analytical work on a pseudo-one-dimensional system. It was found that in this case with spherical symmetry, the region of parameter space in which sustained oscillations occurs is considerably larger than in the 1-D case. This was attributed to the differing geometries of the systems considered, as well as the differing modes of heat transfer considered in each case. In addition to identifying the region of parameter space in which oscillations occur, approximate analytical solutions were found for two limiting types of non-oscillatory behaviour. The predictions of the new solutions were compared with the results of full numerical solutions, and the comparisons were favourable in each case. It was also observed that the oscillatory solutions exist at the transition between these two non-oscillatory cases, and that the oscillatory solutions exhibit characteristics of both these limiting cases.

7.1.4 The Behaviour in the Presence of Natural Convection

Chapter 5 dealt with the more complex problem of defining a region of oscillations when natural convection plays a role. This was done for a two-dimensional slice of the general three-dimensional regime diagram. There were two distinct parts to the region of oscillations defined through simulation. For $Ra < 10^3$, when convection is weak and diffusion still largely dominates, the boundaries of the oscillatory region were virtually independent of $\tau_{step\ 2} / \tau_{convection}$, and had similar values to those found in the purely diffusive limit. When Ra increased beyond 10^3, there was a very distinct change in the shape of the region of oscillations, and the width of the region grew as *Ra* increased.

The different behaviour seen in different parts of the regime diagram was also explored. It was found that the temporal behaviour in the non-oscillatory regions of the regime diagram was very similar in form to that seen previously in the purely diffusive limit. The spatial development of the non-oscillatory cases did show some differences depending on the extent to which natural convection was present. The most obvious difference is in the shape of the temperature profile along the vertical axis, which becomes skewed when natural convection is significant. Different oscillatory behaviours were also observed. It was seen that for *Ra* less than 10^3, the oscillations tended to have much larger amplitudes than those when convection was significant. A region of complex oscillatory behaviour was identified for $\tau_{step\ 2} / \tau_{diffusion} < 0.5$ and $5 < \tau_{step\ 2} / \tau_{convection} < 15$. The results in this region were qualitatively similar to previous experimental measurements, and it is possible that these effects are due to the influence of natural convection, as opposed to the thermokinetic oscillations exhibited by Sal'nikov's reaction. Perhaps the most interesting observation is that when natural convection becomes more significant, the oscillations in the temperature and the intermediate A were in-phase. This is in contrast to the purely diffusive and well-mixed limits, where only anti-phase oscillations are seen.

It was found in Chapter 6 that the oscillations could either effectively be in anti-phase throughout the reactor, or the reactor could be divided into two regions, with a hot zone at the top of the reactor, where oscillations occurred in anti-phase, and a cool zone in the bottom of the reactor, where these oscillations were in-phase. Which of these possibilities occurs depends on the relative values of the characteristic timescales for step 2 of Sal'nikov's reaction and natural convection. When $\tau_{step\ 2} / \tau_{convection} < 10$, the oscillations are in anti-phase throughout the reactor, and when $\tau_{step\ 2} / \tau_{convection}$ is increased beyond 15, the phase difference between the plots of temperature and the concentration of A against time disappears. It was also seen that the in-phase oscillations were confined to a region around the vertical axis in the lower half of the reactor and that away from the vertical axis, the oscillations once again become out-of-phase. It is believed that these differences in phase at various points inside the reactor are due to a complex interaction of the convective flow, the kinetics of Sal’nikov’s reaction, and the diffusion of both heat and the intermediate species.

7.1.5 General Conclusions

The work described in this study represents the first comprehensive investigation of the effects of natural convection on a simplified model of cool flames, *i.e.* Sal’nikov’s reaction. The variety of behaviour exhibited by this relatively simple reaction has been very rich, and the work carried out has highlighted how natural convection can complicate the behaviour of this relatively straightforward reaction. It was interesting to note that both in the absence and presence of natural convection, the system could move from a region of slow reaction, with relatively small temperature rises, through a region of oscillations, to a region of rapid reaction with very sizeable rises in temperature. This behaviour is qualitatively similar to that seen in hydrocarbon oxidation, despite the simplified reaction scheme, where the system moves from slow combustion, through cool flames, to explosion. The fact this behaviour can be reproduced by such a simple reaction serves to highlight the insight that Sal’nikov had when he first proposed the model.

Perhaps the most significant aspect of the current work to highlight is the analytical techniques used. The choice of dimensionless groups, in combination with the scaling analysis, showed that the behaviour of the system is largely governed by the ratios of the characteristic timescales for the various interacting phenomena. This analysis is both simple and elegant, yet still provides a highly significant physical insight into the behaviour of the system.

7.2 Recommendations for Future Work

7.2.1 Cool Flames with Natural Convection

The work described in this thesis represents an initial study of the effects of natural convection on cool flames. There is therefore considerable scope for this work to be extended.

7.2.1.1 Stability analysis

It would be highly desirable to be able to identify regions in parameter space in which oscillations occur, for Sal'nikov's reaction, by analytical methods. The results discussed in sections 4.3 and 5.2 provide an insight, but an analytically defined region of stability would yield further significant information. Hitherto, such an analysis has only been satisfactorily carried out in the limit of perfect mixing, and in a notional one-dimensional system, in which diffusion dominated. There is therefore considerable scope for improving the analysis of a purely diffusive system and as yet, no such analysis has been carried out when natural convection also plays a role. Such a study would yield important insight into how the interaction of fluid mechanics, heat transfer and chemical kinetics can produce oscillations.

7.2.1.2 Different reaction schemes

In addition, it would be interesting to study alternative, and more complex, kinetic schemes. It is a logical step to try and build up the complexity of the model to try and capture more types of behaviour, such as delayed and two-stage ignition, as exhibited in the low temperature combustion of hydrocarbons. These models include chemical feedback, in addition to the thermal feedback seen in Sal'nikov's reaction. The chemical feedback arises through the inclusion of 'branching' reactions, as well as high and low temperature mechanisms. The study of more complex reaction schemes will of course bring the model closer to reality, but in addition it will also help to answer the important question of whether it is thermal or chemical effects which are most significant in the generation of oscillations. To date, this is a question which has remained unanswered, even in the well-mixed limit. Methods similar to those discussed in this work could be applied to the study of, initially, the Gray and Yang model (section 1.3.4) and then to more complex reduced schemes, such as the 'Shell' model (section 1.3.6). The work presented here provides a solid foundation for the study of these more complex schemes, which will yield further insight into the interaction of natural convection and cool flames.

7.2.1.3 Different geometries

In addition to changing the chemistry of the system, the geometry considered could also be varied. Much of the analytical analysis described in this work does not assume anything about the geometry of the system, and so could easily be compared with numerical results from other geometries. In fact, only the empirical constants that appear in the scales developed in this work should be affected by the geometry. It would also be desirable to extend the model to include inflow and outflow, thus bringing the study closer to certain technological applications of cool flames.

7.2.1.4 Developing the model

There is considerable scope to examine the effects of certain key assumptions made in the previous analysis. The principal example of this is the Boussinesq approximation, which states that the density of the fluid being investigated only varies in the buoyancy term of the Navier-Stokes equations. This approximation is widely used in the study of buoyant systems and depends on there being only a relatively small change in temperature within the fluid concerned. This is a constraint which is rarely mentioned in the literature. The system considered in this work is often at the upper limit of applicability of the approximation, so it would be useful to study the effects of not using the Boussinesq approximation, but instead, allowing the density to vary in other important terms of the governing equations. In addition, there is also scope to improve the numerical scheme used in the simulations, because it experiences problems when there are very steep changes in the variables, as discussed in section 4.3. Alternative modelling approaches could be investigated to try and solve this problem. It would also be interesting to extend the model to compute the luminescence exhibited by real cool flames. Of course, this luminescence will depend on both the temperature and concentration fields, but comparisons with the experimentally observed luminescence are important as these are often the only experimental observations made.

7.2.1.5 Turbulence

One further area, which is likely to be of significant interest, is the study of turbulent natural convection, and examining its effect on the development of cool flames. This has not been considered in the present work, but the above analysis has indicated that turbulence is very likely in large industrial reactors.

7.2.2 Other Reactions with Natural Convection

As well as highlighting further areas of study in relation to the interaction of cool flames and natural convection, this work has also raised a number of questions regarding the interaction of natural convection and other exothermic reactions. In Chapter 2, a simple exothermic decomposition reaction was considered. This reaction could, potentially, cause an explosion. The results in Chapter 2 were compared with Frank-Kamenetskii's (1955) classic theory of explosion in a purely diffusive system. This theory assumes a zeroth-order reaction. This assumption is unrealistic under certain circumstances. The classic theory can therefore be extended to look at more realistic reaction schemes, and possibly also to describe more complex schemes, such as Sal'nikov's reaction.

Whilst explosion in the purely diffusive limit is well understood, there has been remarkably little attention paid to the effect that natural convection, which of course would be present in any real system, has on the transition to explosion. The few studies that there have been (*e.g.* Merzhanov and Shtessel, 1973) have merely extended the diffusive theory by studying the variation of δ_{cr} for the onset of explosion. Whilst this can yield some insight into the effects of natural convection on explosion, a more fundamental approach could yield far greater understanding of the mechanisms involved. The study could again be extended to cover reactions of order greater than zero, although this would also necessitate a clarification of the somewhat unsatisfactory definition of an explosion used in previous studies. These have considered a system to be explosive if there is an upwards inflexion in the temperature curve at the centre of the reactor. If a higher order reaction occurs, this is an insufficient condition to define an explosion, because the rate of heat production is reduced as the concentration of the reactant decreases. This effect provides an extra level of control, which could prevent thermal runaway.

All previous numerical studies of the effects of natural convection on thermal explosion have applied the Boussinesq approximation. Whilst this assumption is likely to be more valid for explosions in liquid systems, it is unsatisfactory for the description of explosions in gaseous systems. Some of the problems associated with the Boussinesq approximation in relation to gaseous explosions were discussed in Chapter 2. In order to successfully model thermal explosions in a system with natural convection, an alternative modelling strategy must be sought, which takes account, to some degree, of the compressibility of the gas.

Finally, it was seen in Chapter 5, that the induction time for natural convection to develop can be important. To date, no study has examined how this induction time varies for a system involving chemical reaction. This is important because it is possible, for example, for the induction time for convection to be greater than the ignition delay, therefore explosion would occur before natural convection could get going. This would be undesirable if the heat removal by natural convection was to be used as a method of suppressing explosion.

References

Archer, W.H., 1977. *Heat transfer mechanisms in exothermic reactions*. Ph.D. Thesis, University of Manchester Institute of Science and Technology.

Ashmore, P.G., Tyler, B.J., Wesley, T.A.B., 1967. Experimental investigations of conductive and convective heat transfer in relation to thermal ignitions. *Eleventh Symposium (International) on Combustion*. The Combustion Institute, Pittsburgh, PA, pp. 1133 – 1140.

Ashmore, P.G., Wesley, T.A.B., 1965. A test of thermal-ignition theory in autocatalytic reactions. *Tenth Symposium (International) on Combustion*. The Combustion Institute, Pittsburgh, PA, pp. 217 – 226.

Bardwell, J., Hinshelwood, C., 1951. The cool flame of methyl ethyl ketone. *Proceedings of the Royal Society A*, **205**, 375 – 390.

Baulch, D.L., Drysdale, D.D., Horne, D.G., Lloyd, A.C., 1973. *Evaluated Kinetic Data for High Temperature Reactions*, Vol. 2, Butterworths, London, pp. 285 – 300.

Buda, F., Glaude, P.A., Battin-Leclerc, F., Porter, R., Hughes, K.J., Griffiths, J.F., 2006. Use of detailed kinetic mechanisms for the prediction of autoignitions. *Journal of Loss Prevention in the Process Industries*, **19**, 227 – 232.

Buda, F., Bounaceur, R., Warth, V., Glaude, P.A., Fournet, R., Battin-Leclerc, F., 2005. Progress towards a unified detailed kinetic model for the autoignition of alkanes from C_4 to C_{10} between 600 and 1200 K. *Combustion and Flame*, **142**, 170 – 186.

Bull, D.C., Pye, D.B., Quinn, C.P., 1977. Autoignition and cool-flame behaviour in a convective system. *Combustion and Flame*, **28**, 207 – 211.

Camilleri, P., Marshall, R.M., Purnell, H., 1975. Arrhenius parameters for the unimolecular decompositions of azomethane and n-propyl and isopropyl radicals and for methyl radical attack on propane. *Journal of the Chemical Society, Faraday Transactions 1*, **71**, 1491 – 1502.

Cardoso, S.S.S., Kan, P.C., Savjani, K.K., Hayhurst, A.N., Griffiths, J.F., 2004*a*. The computation of the velocity, concentration and temperature fields during a gas-phase oscillatory reaction in a closed vessel with natural convection. *Combustion and Flame*, **136**, 241 – 245.

Cardoso, S.S.S., Kan, P.C., Savjani, K.K., Hayhurst, A.N., Griffiths, J.F., 2004*b*. The effect of natural convection on the gas-phase Sal'nikov reaction in a closed vessel. *Physical Chemistry Chemical Physics*, **6**, 1687 – 1696.

Coppersthwaite, D.P, Griffiths, J.F., Gray, B.F., 1991. Oscillations in the H_2 + Cl_2 reaction: experimental measurements and numerical simulation. *Journal of Physical Chemistry*, **95**, 6961 – 6967.

Cox, R.A., Cole, J.A., 1985. Chemical aspects of the autoignition of hydrocarbon – air mixtures. *Combustion and Flame*, **60**, 109 – 123.

CSIRO, 2000. *Fastflo Tutorial Guide*, (version 3), CSIRO, Australia.

Cussler, E.L., 1984. *Diffusion: Mass Transfer in Fluid Systems*, Cambridge University Press, Cambridge, pp. 112 – 113.

Cussler, E.L., 1997. *Diffusion, mass transfer in fluid systems*, 2nd edition, Cambridge University Press, Cambridge, pp. 102–111

Davy, H., 1817. Some new experiments and observations on the combustion of gaseous mixtures, with an account of a method of preserving a continued light in mixtures of inflammable gases and air without flame. *Philosophical Transactions of the Royal Society of London*, **107**, 77 – 85.

Dumont, T., Ge´nieys, S., Massot, M., Volpert, V.A., 2002. Interaction of thermal explosion and natural convection: critical conditions and new oscillating regimes. *SIAM Journal on Applied Mathematics*, **63**, 351–372.

Dixon-Lewis, G., 1979. Kinetic mechanism, structure and properties of premixed flames in hydrogen – oxygen – nitrogen mixtures. *Philosophical Transactions of the Royal Society of London, Series A*, **292**, 45 – 99.

Emeléus, H.J., 1926. The spectra of phosphorescent flames of carbon disulphide and ether. *Journal of the Chemical Society*, 1926, 2948 – 2951.

Emeléus, H.J., 1929. The light emission from the phosphorescent flames of ether, acetaldehyde, propaldehyde, and hexane. *Journal of the Chemical Society*, 1929, 1733 – 1739.

Fairlie, R., Griffiths, J.F., 2001. A numerical study of spatial structure during oscillatory combustion in closed vessels in microgravity. *Faraday Discussions*, **120**, 147 – 164.

Fairlie, R., Griffiths, J.F., 2002. Oscillatory combustion in closed vessels under microgravity. *Mathematical and Computer Modelling*, **36**, 245 – 257.

Fairlie, R., Griffiths, J.F., Hughes, K.J., Pearlman, H., 2005. Cool flames in space: experimental and numerical studies of propane combustion. *Proceedings of the Combustion Institute*, **30**, 1057 – 1064.

Forbes, L.K., 1990. Limit-cycle behaviour in a model chemical reaction: the Sal’nikov thermokinetic oscillator. *Proceedings of the Royal Society A*, **430**, 641 – 651.

Forbes, L.K., 1993. One-dimensional pattern formation in a model of burning. *Journal of the Australian Mathematical Society Series B*, **35**, 145 – 173.

Forbes, L.K., 1996. Stationary circular target patterns in a surface burning reaction. *Journal of Engineering Mathematics*, **30**, 471 – 486.

Foster, M., Pearlman, H., 2006. Cool flames at terrestrial, partial, and near-zero gravity. *Combustion and Flame*, **147**, 108 – 117.

Frank-Kamenetskii, D.A., 1955. *Diffusion and Heat Exchange in Chemical Kinetics* (translated by N. Thon), Princeton University Press, Princeton, pp. 202 – 266.

Fuller, E.N., Ensley, K., Giddings, J.C., 1969. The effect of structure on collision cross sections. *Journal of Physical Chemistry*, **73**, 3679 – 3685.

Fuller, E.N., Schettler, P.D., Giddings, J.C., 1966. New method for prediction of binary gas-phase diffusion coefficients. *Industrial and Engineering Chemistry*, **58**(5), 18 – 27.

Gray, B.F., 1969*a*. Unified theory of explosions, cool flames and two-stage ignitions. Part 1. *Transactions of the Faraday Society*, **65**, 1603 – 1613.

Gray, B.F., 1969*b*. Unified theory of explosions, cool flames and two-stage ignitions. Part 3. *Transactions of the Faraday Society*, **65**, 2133 – 2137.

Gerri, N.J., Kaufman, F., 1965. The explosive decomposition of azomethane. *Tenth Symposium (International) on Combustion*. The Combustion Institute, Pittsburgh, PA, pp. 227 – 235.

Gray, B.F., Roberts, M.J., 1988. Analysis of chemical kinetic systems over the entire parameter space I. The Sal'nikov thermokinetic oscillator. *Proceedings of the Royal Society A*, **416**, 391 – 402.

Gray, P., Griffiths, J.F., 1989. Thermokinetic combustion oscillations as an alternative to thermal explosion. *Combustion and Flame*, **78**, 87 – 98.

Gray, P., Griffiths, J. F., Hasko S. M., 1984. Ignitions, extinctions and thermokinetic oscillations accompanying the oxidation of ethane in an open system (continuously stirred tank reactor). *Proceedings of the Royal Society A*, **396**, 227 – 255.

Gray, P., Griffiths, J.F., Moule, R.J., 1974. Thermokinetic oscillations accompanying propane oxidation. *Faraday Symposia of the Chemical Society*, **9**, 103 – 113.

Gray, P., Kay, S.R., Scott, S.K., 1988. Oscillations of an exothermic reaction in a closed system I. Approximate (exponential) representation of Arrhenius temperature-dependence. *Proceedings of the Royal Society A*, **416**, 321 – 341.

Gray, P., Scott, S.K., 1990*a. Chemical Oscillations and Instabilities*. Clarendon Press, Oxford, pp. 83 – 111.

Gray, P., Scott, S.K., 1990*b. Chemical Oscillations and Instabilities*. Clarendon Press, Oxford, pp. 264 – 291.

Gray, B.F., Yang, C.H., 1965. On the unification of the thermal and chain theories of explosion limits. *Journal of Physical Chemistry*, **69**, 2747 – 2750.

Griffiths, J.F., 1985*a*. Thermokinetic oscillations in homogeneous gas-phase oxidations, in: Field, R.J., Burger, M. (Eds.), *Oscillations and travelling waves in chemical systems*. Wiley, New York, pp. 529 – 564.

Griffiths, J.F., 1985*b*. Thermokinetic interactions in simple gaseous reactions. *Annual Review of Physical Chemistry*, **36**, 77 – 104.

Griffiths, J.F., 1995. Reduced kinetic models and their application to practical combustion systems. *Progress in Energy and Combustion Science*, **21**, 25 – 107.

Griffiths, J.F., 2004. Why cool flames are a hot prospect. *New Scientist*, **2450**, 28 – 29.

Griffiths, J.F., Felton, P.G.; Gray, P., 1973. Heat-release rates accompanying the non-isothermal oxidation of organic compounds. *Fourteenth Symposium (International) on Combustion*. The Combustion Institute, Pittsburgh, PA, pp. 453 – 462.

Griffiths, J.F., Gray, B.F., Gray, P., 1971. Multistage ignition in hydrocarbon combustion: temperature effects and theories of non-isothermal combustion. *Thirteenth Symposium (International) on Combustion*. The Combustion Institute, Pittsburgh, PA, pp. 239 – 248.

Griffiths, J.F., Kay, S.R., Scott, S.K., 1988. Oscillatory combustion in closed vessels: theoretical foundations and their experimental verification. *Twenty-second Symposium (International) on Combustion*. The Combustion Institute, Pittsburgh, PA, pp. 1597 – 1607.

Griffiths, J.F., Phillips, C.H., 1990. Experimental and numerical studies of the combustion of ditertiary butyl peroxide in the presence of oxygen at low pressures in a mechanically stirred closed vessel. *Combustion and Flame*, **81**, 304 – 316.

Griffiths, J.F., Scott, S.K., 1987. Thermokinetic interactions: fundamentals of spontaneous ignition and cool flames. *Progress in Energy and Combustion Science*, **13**, 161 – 197.

Griffiths, J.F., Sykes, A.F., 1989. Numerical studies of a thermokinetic model for oscillatory cool flame and complex ignition phenomena in ethanal oxidation under well-stirred flowing conditions. *Proceedings of the Royal Society A*, **422**, 289 – 310.

Hartmann, L., Lucka, K., Köhne, H., 2003. Mixture preparation by cool flames for diesel-reforming technologies. *Journal of Power Sources*, **118**, 286 – 297.

Halstead, M.P., Kirsch, L., Prothero, A., Quinn, C.P., 1975. A mathematical model for hydrocarbon autoignition at high pressures. *Proceedings of the Royal Society A*, **346**, 515 – 538.

Halstead, M.P., Kirsch, L., Quinn, C.P., 1977. The autoignition of hydrocarbon fuels at high temperatures and pressures – fitting of a mathematical model. *Combustion and Flame*, **30**, 45 – 60.

Halstead, M.P., Prothero, A., Quinn, C.P., 1970. A model for cool-flame behaviour. *Journal of the Chemical Society D: Chemical Communications*, 1150 – 1151.

Halstead, M.P., Prothero, A., Quinn, C.P., 1971. A mathematical model of the cool-flame oxidation of acetaldehyde. *Proceedings of the Royal Society A*, **322**, 377 – 403.

Halstead, M.P., Prothero, A., Quinn, C.P., 1973. Modelling the ignition and cool-flame limits of acetaldehyde oxidation. *Combustion and Flame*, **20**, 211 – 221.

Jones, D.R., 1973. The dynamic stability of confined, exothermically reacting fluids. *International Journal of Heat and Mass Transfer*, **16**, 157 – 167.

Jones, D.R., 1974. Convective effects in enclosed, exothermically reacting gases. *International Journal of Heat and Mass Transfer*, **17**, 11 – 21.

Kagan, L., Berestycki, H., Joulin, G., Sivashinsky, G., 1997. The effect of stirring on the limits of thermal explosion. *Combustion Theory and Modelling*, **1**, 97–111.

Kay, S.R., Scott, S.K., 1988. Oscillations of simple exothermic reactions in a closed system. II. Exact Arrhenius kinetics. *Proceedings of the Royal Society A*, **416**, 343 – 359.

Knox, J.H., 1967. The interpretation of cool flame and low-temperature combustion phenomena, in: Ashmore, P.G., Dainton, F.S., Sugden, T.M. (Eds.), *Photochemistry and Reaction Kinetics*. Cambridge University Press, Cambridge, pp. 250 – 286.

Liang, C.H., Mou, C.Y., Lee, D.J., 2003. Dynamic behaviour and sensitivity of a skeleton thermokinetic model for acetaldehyde oxidation. *Chemical Engineering Science*, **58**, 4173 – 4184.

Lignola, P.G., Reverchon, E., 1987. Cool flames. *Progress in Energy and Combustion Science*, **13**, 75 – 96.

Matos da Silva, J., Hermann, I., Mengel, C., Lucka, K., Köhne, H., 2004. Autothermal reforming of gasoline using a cool flame vaporizer. *AIChE Journal*, **50**, 1042 – 1050.

Melvin, A., 1969. The development of cool flames in propane – oxygen mixtures. *Combustion and Flame*, **13**, 438 – 439.

Merzhanov, A.G., Shtessel, E.A., 1971. Thermal explosion in reacting liquid systems in the presence of thermal convection. *Combustion, Explosion and Shock Waves*, **7**, 58 – 65.

Merzhanov, A.G., Shtessel, E.A., 1973. Free convection and thermal explosion in reactive systems. *Astronautica ACTA*, **18**, 191–199.

Mitachi, K., Aoki, K., Kitamura, K., Komatsu, N., 1986. Natural convection of heat generating fluid within horizontal cylinder. *Bulletin of JSME*, **29**, 2547 – 2553.

Mitachi, K., Igarashi, M., 1987. Unsteady natural convection of heat-generating fluids in a horizontal cylinder. *JSME International Journal*, **30**, 1099 – 1105.

Müller, U.C., Peters, N., Liñan, A., 1992. Global kinetics for n-heptane ignition at high pressures. *Twenty-second Symposium (International) on Combustion*. The Combustion Institute, Pittsburgh, PA, pp. 777 – 784.

Naidja, A., Krishna, C.R., Butcher, T., Mahajan, D., 2003. Cool flame partial oxidation and its role in combustion and reforming of fuels for fuel cell systems. *Progress in Energy and Combustion Science*, **29**, 155 – 191.

Newitt, D.M., Thornes, L.S., 1937. The oxidation of propane. Part I. The products of slow oxidation at atmospheric and at reduced pressures. *Journal of the Chemical Society*, 1656 – 1665.

Pearlman, H., 1997. Excitability in high-Lewis number premixed gas combustion. *Combustion and Flame*, **109**, 382 – 398.

Pearlman, H., 2000. Low-temperature oxidation reactions and cool flames at Earth and reduced gravity. *Combustion and Flame*, **121**, 390 – 393.

Pearlman, H.G., Ronney, P.D., 1994*a*. Near-limit behaviour of high-Lewis number premixed flames in tubes at normal and low gravity. *Physics of Fluids*, **6**, 4009 – 4018.

Pearlman, H.G., Ronney, P.D., 1994*b*. Self-organized spiral and circular waves in premixed gas flames. *Journal of Chemical Physics*, **101**, 2632 – 2633.

Pekalski, A.A., Zevenbergen, J.F., Pasman, H.J., Lemkowitz, S.M., Dahoe, A.E., Scarlett, B., 2002. The relation of cool flames and auto-ignition phenomena to process safety at elevated pressure and temperature. *Journal of Hazardous Materials*, **93**, 93 – 105.

Perkin, W.H., 1882. Some observations on the luminous incomplete combustion of ether and other organic bodies. *Journal of the Chemical Society*, **41**, 363 – 367.

Reddy, J.N., Gartling, D.K., 1994*a*. *The Finite Element Method in Heat Transfer and Fluid Dynamics*. CRC Press, Boca Raton, Florida, pp. 25 – 78.

Reddy, J.N., Gartling, D.K., 1994*b*. *The Finite Element Method in Heat Transfer and Fluid Dynamics*. CRC Press, Boca Raton, Florida, pp. 166 – 167.

Reid, R.C., Prausnitz, J.M., Poling, B.E., 1987*a*. *The Properties of Gases and Liquids*, 4th edition, Mcgraw-Hill, New York, pp. 404 – 417.

Reid, R.C., Prausnitz, J.M., Poling, B.E., 1987*b*. *The Properties of Gases and Liquids*, 4th edition, Mcgraw-Hill, New York, pp. 530 – 535.

Riblett, E.W., Rubin, L.C., 1937. The thermal decomposition of azomethane. *Journal of the American Chemical Society*, **59**, 1537 – 1540.

Rice, O.K., 1940. The role of heat conduction in thermal gaseous explosions. *Journal of Chemical Physics*, **8**, 727 – 733.

Richardson, S.M., Saville, G., Griffiths, J.F., 1990. Autoignition – occurrence and effects. *Transactions of the Institution of Chemical Engineers Part B*, **68**, 239 – 244.

Sal'nikov, I.E., 1949. Contribution to the theory of the periodic homogeneous chemical reactions. *Zhurnal Fizicheskoi Khimii*, **23**, 258 – 272.

Sawerysyn, J.P., Tourbez, H., Bridoux, M., Lucquin, M., 1973. Observations and records of oxidation and combustion phenomena by photoelectric image devices, in: Weinberg, F.J. (Ed.), *Combustion Institute European Symposium*, Academic Press, London, pp. 729 – 734.

Scott, S.K., Wang, J., Showalter, K., 1997. Modelling studies of spiral waves and target patterns in premixed flames. *Journal of the Chemical Society – Faraday Transactions*, **93**, 1733 – 1739.

Sheinson, R.S., Williams, F.W., 1973. Chemiluminescence spectra from cool and blue flames: electronically excited formaldehyde. *Combustion and Flame*, **21**, 221 – 230.

Shtessel, E.A., Priytkova, K.V., Merzhnaov, A.G., 1971. Numerical solution to the problem of a thermal explosion taking account of free convection. *Combustion, Explosion and Shock Waves*, **7**, 137 – 146.

Sidhu, H.S., Forbes, L.K., Gray, B.F., 1995. Analysis of the unified thermal and chain branching model of hydrocarbon oxidation. *Proceedings of the Royal Society A*, **449**, 493 – 514.

Stiles, P.J., Fletcher, D.F., 2001. The effect of gravity on the rate of a simple liquid-state reaction in a small, unstirred cylindrical vessel. *Physical Chemistry Chemical Physics*, **3**, 1617–1621.

Stiles, P.J., Fletcher, D.F., Morris, I., 2001. The effect of gravity on the rates of simple liquid-state reactions in a small, unstirred cylindrical vessel: part II. *Physical Chemistry Chemical Physics*, **3**, 3651–3655.

Trotman-Dickenson, A.F., 1955. *Gas Kinetics: an introduction to the Kinetics of Homogeneous Gas Reactions*, Butterworths Scientific Publications, London, pp. 69 – 71.

Turner, J.S., 1979. *Buoyancy Effects in Fluids*. Cambridge University Press, Cambridge, pp. 207 – 250.

Tyler, B.J., 1966. An experimental investigation of conductive and convective heat transfer during exothermic gas phase reactions. *Combustion and Flame*, **10**, 90 – 91.

Tyler, B.J., Tuck, A.F., 1967. Heat transfer to a gas from a spherical enclosure: measurements and mechanism. *International Journal of Heat and Mass Transfer*, **10**, 251 – 253.

Ubbelohde, A.R., 1935. Investigations on the combustion of hydrocarbons I – The influence of molecular structure on hydrocarbon combustion. *Proceedings of the Royal Society A*, **152**, 354 – 378.

Varma, A., Morbidelli, M., 1997. *Mathematical Methods in Chemical Engineering*, Oxford University Press, Oxford, pp. 611–686.

Wang, X., Mou, C.Y., 1985. A thermokinetic model of complex oscillations in gaseous hydrocarbon oxidation. *Journal of Chemical Physics*, **83**, 4554 – 4561.

Yang, C.H., 1969. Two-stage ignition and self-excited thermokinetic oscillation in hydrocarbon oxidation. *Journal of Physical Chemistry*, **73**, 3407 – 3413.

Yang, C.H., Gray, B.F., 1969*a*. On the slow oxidation of hydrocarbons and cool flames. *Journal of Physical Chemistry*, **73**, 3395 – 3406.

Yang, C.H., Gray, B.F., 1969*b*. Unified theory of explosions, cool flames and two stage ignitions. Part 2. *Transactions of the Faraday Society*, **65**, 1614 – 1622.

Yang, C.H., Gray, B.F., 1969*c*. The determination of explosion limits from a unified thermal and chain theory. *Eleventh Symposium (International) on Combustion*. The Combustion Institute, Pittsburgh, PA, pp. 1099 – 1106.

Zienkiewicz, O.C., Taylor, R.L., 1989. *The Finite Element Method*, vol. 1, 4th edition. McGraw-Hill, London, pp. 206 – 259.

Appendix: Outline of the Finite Element Method

Introduction

In this section, a brief overview of the finite element method, which has been used in the numerical simulations described previously, is given. In addition, some of the features of Fastflo, the software package used in this work, are discussed and more details of the solution methods used are given. More comprehensive accounts of the mathematical background of the finite element method can be found in the literature, *e.g.* Reddy and Gartling (1994*a*), Zienkiewicz and Taylor (1989).

The Finite Element Method

The finite element method is a powerful computational technique which can be used in the solution of differential and integral equations. The method belongs to the class of weighted-residual methods, which assume that the solution of a differential equation can be represented as a linear combination of unknown coefficients, c_j, and appropriately chosen functions, ϕ_j, over the entire domain of the problem. The parameters, c_j, can then be determined such that the differential equation is satisfied. The functions, ϕ_j, are called trial or basis functions. The general solution to the differential equation can therefore be written as:

$$u(x, y, \ldots) = \sum_{j=1}^{J} c_j \phi_j (x, y, \ldots). \tag{A.1}$$

In conventional weighted-residual methods, it is difficult to generate trial functions that satisfy all the boundary conditions. This problem is particularly important given that most real world problems are defined on regions which are geometrically complex. It is difficult then to achieve a solution with acceptable errors unless *J* in Eq. (A.1) is made very large. The finite element method seeks to overcome this problem by sub-dividing the domain into an assemblage of simple geometric shapes for which it is possible to systematically generate the trial functions needed in the solution of the differential equations by weighted-residual methods.

The details of the finite element method are discussed below in terms of a simple example, as presented by Reddy and Gartling (1994*a*). The example considered is finding the steady state temperature distribution $T(x,y)$ in a two-dimensional orthotropic medium Ω, with boundary Γ. The governing equation is:

$$-\left[\frac{\partial}{\partial x}\left(k_{11}\frac{\partial T}{\partial x}\right)+\frac{\partial}{\partial y}\left(k_{22}\frac{\partial T}{\partial y}\right)\right]=Q, \tag{A.2}$$

subject to the boundary conditions

$$T=\hat{T}(s) \text{ on } \Gamma_T, \tag{A.3}$$

$$\left(k_{11}\frac{\partial T}{\partial x}n_x+k_{22}\frac{\partial T}{\partial y}n_y\right)+q_c=q(s) \text{ on } \Gamma_q, \tag{A.4}$$

where Γ_T and Γ_q are disjoint portions of the boundary and q_c represents a convective transport term.

The finite element mesh contains nodes, and the values of the unknown function at the nodes can replace the unknown coefficients in Eq. (A.1). The unknown function can then be written as:

$$T(x,y)\approx T^e(x,y)=\sum_{j=1}^{n}T_j^e\phi_j^e(x,y), \tag{A.5}$$

where T^e is an approximation of the temperature over a single element, T_j^e denote the values of the function T^e on the nodes of the element, ϕ_j^e are the trial (interpolation) functions associated with the element and n is the number of nodes in the element. The form of the functions, ϕ_j^e, depend on the number of nodes in the element, and on its shape. Generally, the trial functions used are low order polynomials. These can readily be found from interpolation theory. The use of the function values on the nodes as unknown parameters ensures that the solution is continuous across element boundaries. The most commonly used trial functions are either linear or quadratic functions. The higher the order of the polynomial used, the better the interpolation is on the same grid. Functions of higher order are seldom used, however, due to the high computational cost involved.

The nodal values in Eq. (A.5) must be determined such that the approximate solution satisfies the boundary conditions. This is achieved in a weighted-integral sense over the element, leading to *n* algebraic equations for the nodal values. This set of algebraic equations is found by examining the residual of Eq. (A.2) when the element approximation T^e is used. The residual is multiplied by a weighting function, *w*, and integrated over the element, *i.e.*

$$\int_{\Omega^e} w\left[-\frac{\partial}{\partial x}\left(k_{11}\frac{\partial T^e}{\partial x}\right)-\frac{\partial}{\partial y}\left(k_{22}\frac{\partial T^e}{\partial y}\right)-Q\right]dV = 0\,, \tag{A.6}$$

where the terms in the square brackets represent the residual of Eq. (A.2). Setting the integral equal to zero forces the residual to zero, in a spatially averaged sense.

Making use of integration by parts and the divergence theorem, Eq. (A.6) can be rewritten as:

$$\int_{\Omega^e}\left(\frac{\partial w}{\partial x}k_{11}\frac{\partial T}{\partial x}+\frac{\partial w}{\partial y}k_{22}\frac{\partial T}{\partial y}-wQ\right)dV-\oint_{\Gamma^e} w\left(k_{11}\frac{\partial T}{\partial x}n_x+k_{22}\frac{\partial T}{\partial y}n_y\right)ds = 0\,,\text{ or}$$

$$\int_{\Omega^e}\left(k_{11}\frac{\partial w}{\partial x}\frac{\partial T}{\partial x}+k_{22}\frac{\partial w}{\partial y}\frac{\partial T}{\partial y}-wQ\right)dV-\oint_{\Gamma^e} wq_n ds = 0\,. \tag{A.7}$$

Different choices of the weighting function give different methods, such as the point collocation method and the subdomain collocation method (Zienkiewicz and Taylor, 1989). The most commonly used method, and that used by Fastflo, is the Galerkin method, which assumes that the weighting functions are the same as the trial functions. If the finite element approximation in Eq. (A.5) is substituted into Eq. (A.7), assuming that *w* and ϕ are identical yields:

$$\sum_{j=1}^{n} K_{ij}^e T_j^e = Q_i^e + q_i^e\,, \tag{A.8}$$

where the coefficients are given by:

$$K_{ij}^e = \int_{\Omega^e}\left(k_{11}\frac{\partial \phi_i^e}{\partial x}\frac{\partial \phi_j^e}{\partial x}+k_{22}\frac{\partial \phi_i^e}{\partial y}\frac{\partial \phi_j^e}{\partial y}\right)dV\,, \tag{A.9}$$

$$Q_i^e = \int_{\Omega^e} Q\phi_i^e dV \text{ and } q_i^e = \oint_{\Gamma^e} q_n \phi_i^e ds\,. \tag{A.10}$$

These equations can then be solved for each element, subject to the constraint that the primary variable (in this case temperature) and the secondary variable (heat flux) are continuous across an element boundary.

Benefits of Fastflo and Details of the Algorithm Used

Benefits of Fastflo

Fastflo is a general PDE solver, which uses the Galerkin method to solve systems of equations. The fact that it is a general solver means that the main advantage the package has is that it is very flexible, both in terms of the equations it can solve, and because users have a great deal of control of the algorithm used to solve the equations. In addition, Fastflo has its own internal mesh generator, so there no need to specify the mesh by hand. At the same time, it is possible to import meshes generated in other packages, which can be useful for complex geometries.

Another of the key features of Fastflo is that it uses its own language, *Fasttalk*, which is concise and easy to use, meaning that time-consuming programming in languages like FORTRAN is avoided. The use of the *Fasttalk* language also allows users a great deal of control over how the equations are solved and what processes are performed on the data. This means users are not constrained to a fixed menu of techniques and applications.

Algorithm

Details of the algorithm used were presented in Chapter 2; however, some of the decisions made require further discussion. Because this work has considered a transient system, temporal discretisation was required. The most commonly used time integration methods are part of a one-parameter family, called the θ-family of approximation. This gives an expression for the temporal derivative of a function as:

$$u_{n+1} = u_n + \Delta t\left[(1-\theta)\dot{T}_n + \theta\dot{T}_{n+1}\right],\ 0 \le \theta \le 1. \tag{A.11}$$

For different values of the parameter θ, several well-known time approximation schemes are obtained. A forward difference scheme is defined by $\theta = 0$, and a backwards difference scheme by $\theta = 1$. A backwards difference scheme was used in this work because, in contrast to the forward difference scheme, the method is unconditionally stable. A simple backwards difference scheme was chosen over more complex unconditionally stable schemes, such as Crank-Nicolson or Galerkin, due to its simplicity.

In order to linearise the governing equations, Picard's method was used. This uses successive substitution to solve the equations. This method has a reasonably large radius of convergence, but can be slow to converge (Reddy and Gartling, 1994*b*). This method was chosen, once again, due to its simplicity and also due to the large radius of convergence.

Details of the Mesh Used

Fastflo's unstructured triangular mesh generator was used to produce the 2-D mesh on which the governing equations were solved. A 2-D mesh was sufficient because of the adoption of an axisymmetric condition about the vertical axis of the reactor. The mesh was concentrated at four points where it was felt greater spatial resolution would be required. A typical mesh appears in Figure A.1.

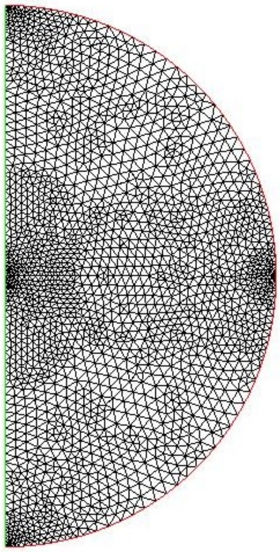

Figure A.1. Typical mesh used in the simulations.